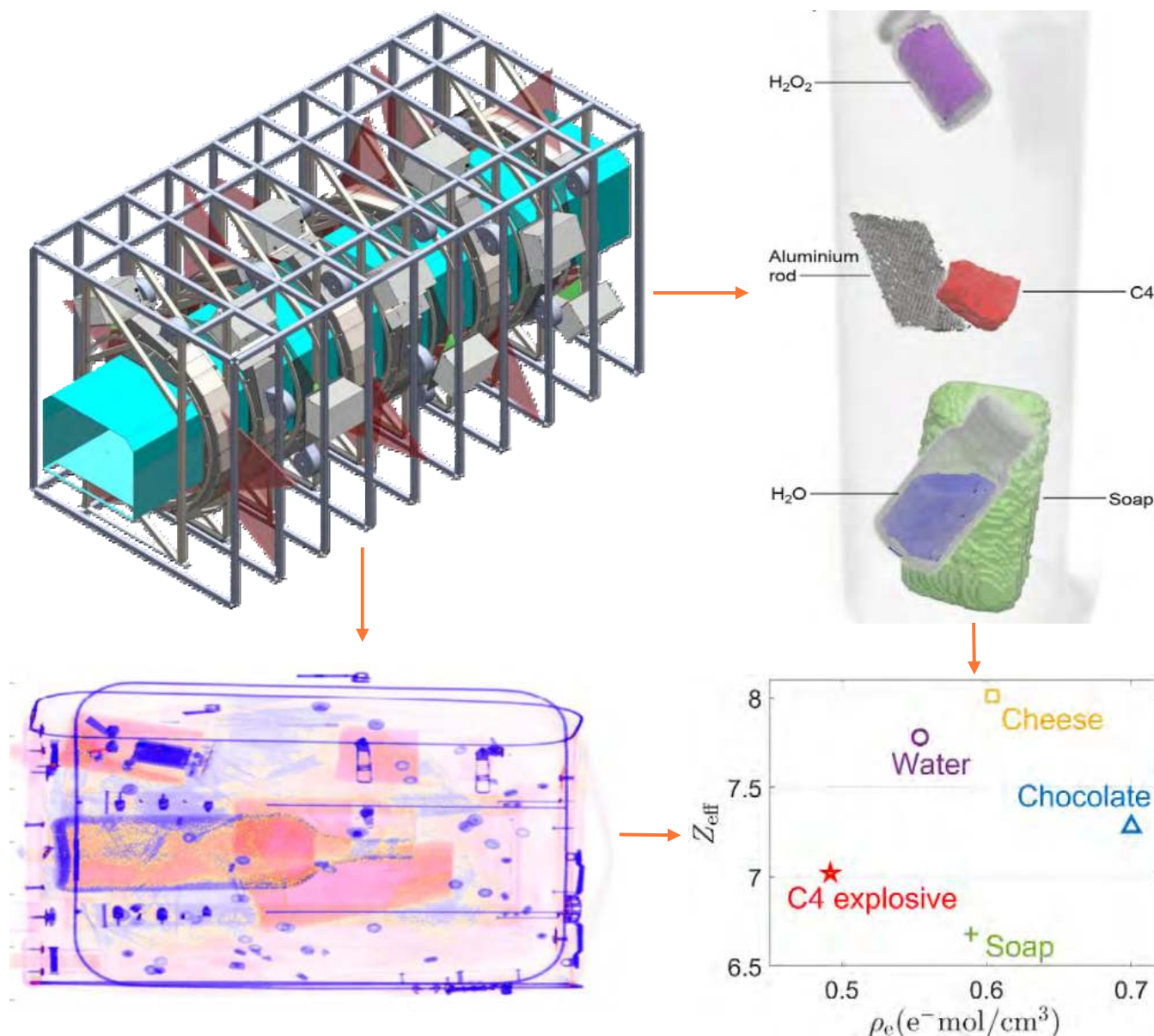


# Spectrally joint reconstruction and material classification from multi-energy CT



**Doniyor Jumanazarov**

PhD Thesis

October 2021

**Academic Advisors:**

Henning Friis Poulsen

Ulrik Lund Olsen

Mihai IOVEA

# Contents

---

<b>Abstract</b>	<b>iv</b>
<b>Acknowledgements</b>	<b>vi</b>
<b>1 Introduction</b>	<b>1</b>
1.1 About the project . . . . .	1
1.2 Thesis Overview . . . . .	1
<b>2 Background</b>	<b>4</b>
2.1 Conventional X-ray computed tomography . . . . .	4
2.1.1 The principles of X-ray attenuation . . . . .	5
2.1.2 The Beer Lambert law . . . . .	7
2.1.3 The limitations of conventional single energy CT . . . . .	8
2.2 Dual-energy CT . . . . .	8
2.2.1 Dual basis function decomposition . . . . .	9
2.2.2 Electron density and effective atomic number . . . . .	10
2.2.3 The limitations of dual-energy CT . . . . .	12
2.3 Spectral CT . . . . .	12
2.4 Statement of problem for the thesis . . . . .	13
2.5 Thesis objectives . . . . .	14
<b>3 Data acquisition and data pre-processing step</b>	<b>17</b>
3.1 Overview of the overall workflow . . . . .	17
3.2 Experimental setup and materials . . . . .	17
3.3 Photon counting detectors . . . . .	22
3.4 Correction of detector's spectral response . . . . .	24
3.5 LAC extraction and setting low- and high-energy thresholds . . . . .	28
3.6 Energy channels rebinning . . . . .	29
<b>4 Joint reconstruction</b>	<b>34</b>
4.1 Fundamentals of tomographic reconstruction . . . . .	34
4.1.1 Projection data . . . . .	34
4.1.2 Conventional channel-by-channel reconstructions . . . . .	36
4.2 The state-of-the-art joint reconstruction . . . . .	38
4.2.1 State-of-the-art literature review . . . . .	38

---

4.2.2	TNV joint reconstruction . . . . .	39
4.2.3	$L_\infty$ -VTV joint reconstruction . . . . .	42
<b>5</b>	<b>Methods to material classification</b>	<b>46</b>
5.1	SIMCAD classification method . . . . .	46
5.1.1	Calibration step . . . . .	46
5.1.2	Calculation of material features . . . . .	47
5.2	BMD classification method . . . . .	48
5.2.1	Basis material decomposition . . . . .	48
5.2.2	Curve fitting and calculation of the material feature . . . . .	49
<b>6</b>	<b>Results</b>	<b>51</b>
6.1	Results of the Paper A . . . . .	51
6.1.1	A brief introduction . . . . .	51
6.1.2	Main results . . . . .	52
6.2	Results of the Paper B . . . . .	54
6.2.1	A brief introduction . . . . .	54
6.2.2	Main results . . . . .	55
6.3	Results of the Paper C . . . . .	60
6.3.1	A brief introduction . . . . .	60
6.3.2	Main results . . . . .	61
6.4	Results of the Paper D . . . . .	62
6.4.1	A brief introduction . . . . .	62
6.4.2	Main results . . . . .	62
<b>7</b>	<b>Discussion and Outlook</b>	<b>67</b>
<b>8</b>	<b>Conclusion</b>	<b>71</b>
	<b>Bibliography</b>	<b>73</b>
	<b>APPENDIX</b>	<b>84</b>
	Paper A . . . . .	84
	Paper B . . . . .	97
	Paper C . . . . .	114
	Paper D . . . . .	133

# Abstract

---

X-ray computed tomography (CT) is a popular technique for non-destructive examination of the interior of an object in medical diagnosis and security applications. This technique can reconstruct a high-resolution three-dimensional (3D) image of the object from projection data collected at different angles. The emergence of energy-discriminating photon counting detectors (PCD) has paved the way to spectral (or multi-energy) X-ray CT which can simultaneously retrieve the linear attenuation coefficients (LAC) of materials as function of photon energy with polychromatic sources. The extraction of LACs at multiple energies can potentially enhance material separation than the traditional energy-integrating or dual energy detectors. This thesis presents a new joint reconstruction algorithm and new classification methods which can classify materials into energy-independent features such as electron density ( $\rho_e$ ) and effective atomic number ( $Z_{\text{eff}}$ ). The methods and the algorithm developed to address the challenges of spectral CT for security applications are briefly explained below.

First, we propose a material classification method using a dual basis function decomposition which is based on the fact that the LAC of any material can be accurately reproduced by a linear combination of material- and energy-dependent components. The method requires a calibration phase to register the energy-dependent basis functions of the decomposed LACs by employing a set of reference materials. Materials are then classified into  $\rho_e$  and  $Z_{\text{eff}}$ , while these two parameters can completely identify the materials that may be found in the luggage. The method is explored in the broad range of  $6 \leq Z_{\text{eff}} \leq 23$  that includes the most materials important in explosive detection. Our method outperforms another state-of-the-art method called SRZE, providing up to 32 times better time efficiency for the image reconstruction with similar performance.

Second, we present a new joint reconstruction algorithm called  $L_\infty$ -norm-based vectorial total variation ( $L_\infty$ -VTV), which utilizes the increased information from spectral LACs. The algorithm is tested for experimental data acquired with the low signal-to-noise ratios (SNR) and few projections. It is demonstrated that the algorithm can outperform another state-of-the-art joint reconstruction in terms of reconstruction quality and classification from such data.

Third, how the correction step for spectral distortions in a PCD influences the resulting material classification is analyzed. This is because the spectra measured with PCDs are usually distorted by charge accumulation artifacts, such as pileup of photons

---

and charge sharing between detector pixels.

Fourth, we develop another classification method using a basis material decomposition which is based on the fact that the LAC of any material can be correctly restored by a linear combination of equivalent thicknesses and LACs of several basis materials. The method requires a calibration phase in which a set of reference materials are measured to compute corresponding equivalent thicknesses. Equivalent thicknesses of the scanned unknown objects are found, and their  $Z_{\text{eff}}$  values are calculated by interpolation or extrapolation with respect to the reference materials. This method shows better accuracy in estimating  $Z_{\text{eff}}$  than the first classification method mentioned above, when the number of projections is decreased or the data SNR is decreased. Both methods do not require *a-priori* knowledge of the sample.

In the thesis, we address some challenges of spectral CT. First, the division of photon counts into many energy bins significantly reduces data SNR in each bin. Second, if the widths of energy bins are lower than detector's energy resolution, classification performance may not be improved further. Lastly, reconstructing many individual energy bins is computationally expensive. Therefore, the experimental data is rebinned into smaller numbers of energy bins prior to reconstruction, which are optimized for each developed method in terms of classification performance.

# Acknowledgements

---

First of all, I would like to express my deep gratitude to my research supervisors, Henning Friis Poulsen, Ulrik Lund Olsen and Mihai IOVEA. Your invaluable comments, continuous support, and patience during my PhD study have led me into the academic world, and helped me to succeed. Prof. Poulsen, I would like to thank you for your useful comments on the papers and the thesis. Ulrik, I really appreciate your genuinely friendly way of welcoming me to Denmark and assistance, and weekly face-to-face and online supervision meetings throughout these three years. Mr. IOVEA, your continuous support and face-to-face supervision during the two-year external stay at Accent Pro 2000 s.r.l. in Romania has been invaluable, always with a good advice and a positive attitude. I would also like to thank Matteo Busi who has worked closely with me and helped to polish my writings for the first paper, and have answered countless questions.

I also want to express my gratitude to everyone in the MUMMERING network for interesting workshops and meetings all over Europe, where I have learned a lot about tomography. Special thanks to Jens Wenzel Andreasen, Hanne Lauritzen, Heidi Adler Berggren and Elisabeth Boelskifte for their wonderful efforts to organise these events. I would also like to thank my ESR colleague, Jakeoung Koo for his friendship and great collaboration during these three years, especially with development of image reconstruction algorithms. I wish to extend a special thanks to my other MUMMERING ESR friends who have made me feel at home away from home: Elise Otterlei Brenne, Poulami Ganguly, Shiva Hosseinnejad, Qiongyang Chen, Sotirios Magkos, Azat Slyamov, Robert Auenhammer, Anuj Prajapati, Abdellatif Saadaldin, Jisoo Kim, David Marchant, and Rasmus Munk. I am grateful for sharing your knowledge, insightful discussions and memorable moments together. Being part of the MUMMERING network has been a great experience.

Last but not least, I would like to deeply thank my loving family. My father, Rustam Jumanazarov and my mother, Rano Rahmanova have been a constant source of support and encouragement. My grandmother, Bipashsha Saidmametova has been proud of me, and always wished me success, giving me the confidence. My younger sisters, Oysha Abdullayeva and Fatima Abdullayeva have supported me. My father's younger brother, Olimboy Jumanazarov, and my wife's parents, Alibek Qurbonov and Gulandom Jumanazarova were always there for me all along the way. I greatly thank my dear wife, Asalkhon Alimova for understanding me and cheering me on. You always

---

prepared delicious meals and dishes which helped me to have a lot of extra time for doing research and writing papers. The support of my family always protected me from external social problems, allowing me to focus just on my research and work. I owe you all my personal achievement and development which have guided me to where I am now.





# Introduction 1

---

In this thesis, with focus on security applications we develop new material classification methods and image reconstruction algorithms from spectral (or multi-energy) X-ray Computed Tomography (CT). Spectral CT with a polychromatic source uses energy-sensitive single photon counting detectors, and extracts the linear attenuation coefficients of materials as a function of photon energy with a single data collection. The different data correction techniques and optimization of energy thresholds in the energy spectrum are implemented to enhance the developed methods. The various challenges of spectral CT for security applications are addressed. The developed algorithms and methods are compared with their state-of-the-art competitors using spectral CT scans.

## 1.1 About the project

The work introduced in the thesis is performed in the context of a multi-disciplinary project, MUltiscale, Multimodal and Multidimensional imaging for EngineerRING (MUMMERING) funded by EU Horizon Marie Skłodowska-Curie Innovative Training Network (ITN) with the grant number 765604. MUMMERING covers the whole pipeline of electron beam and X-ray tomography from data collection and image reconstruction to finite element modelling and material characterization. This project trained 15 early stage researchers (ESRs) benefiting from the participation in the different host and secondment institutions. The original title of the thesis was "2D/3D multimodal analysis for X-ray security applications".

## 1.2 Thesis Overview

Chapter 2 explains background on single, dual and multi-energy CT, and addresses the objectives of the thesis. Chapter 3 presents data acquisition and data-processing techniques before performing image reconstructions. Chapter 4 describes new joint reconstruction algorithms which are implemented for improving classification performance from few CT projections and increased noise levels. Chapter 5 introduces

new classification methods for spectral CT which are based on the different attenuation decomposition models. The main results from the appended papers are given in Chapter 6. Discussion of the results and some suggestions for future work are presented in Chapter 7. In Chapter 8 we draw a conclusion. Lastly, four papers are added in the appendix section.

This thesis consists of an extended summary and the following appended papers:

- **Paper A:**

Doniyor Jumanazarov, Jakeoung Koo, Matteo Busi, Henning. F. Poulsen, Ulrik L. Olsen and Mihai Iovea. System-independent material classification through X-ray attenuation decomposition from spectral X-ray CT, NDT and E International 116 (2020) 102336. DOI: 10.1016/j.ndteint.2020.102336.

In this work, we present a system-independent material classification method through attenuation decomposition (SIMCAD). The method adopts the dual basis function decomposition model introduced by Alvarez et al. [1] for multi energies, and estimates electron density and effective atomic number of a material from energy-resolved attenuation coefficients.

- **Paper B:**

Doniyor Jumanazarov, Jakeoung Koo, Jan Kehres, Henning. F. Poulsen, Ulrik L. Olsen and Mihai Iovea. Material classification from sparse spectral X-ray CT using vectorial total variation based on L infinity norm. Submitted for publication.

This work presents the joint reconstruction with  $L_\infty$  norm based vectorial total variation regularization ( $L_\infty$ -VTV). This is implemented to handle artifacts due to using few projections and low signal-to-noise ratios in each energy bin. It uses the correlations between different energy bins and simultaneously reconstructs the multi-channel images instead of reconstructing each energy bin separately. This is tested against another state-of-the-art joint, Total Nuclear Variation (TNV) and bin-by-bin reconstructions using the experimental data.

- **Paper C:**

Doniyor Jumanazarov, Jakeoung Koo, Henning. F. Poulsen, Ulrik L. Olsen and Mihai Iovea. The significance of the spectral correction of photon counting detector response in material classification from spectral x-ray CT, Proc. SPIE 11771, Quantum Optics and Photon Counting 2021, 117710J (18 April 2021); doi: 10.1117/12.2589290.

This paper explores how the correction of detector's spectral response is important in material classification. This is because detector effects such as charge sharing and

pulse pile up effects result in the spectral distortions of the spectra measured by photon counting detectors.

- **Paper D:**

Doniyor Jumanazarov, Jakeoung Koo, Henning. F. Poulsen, Ulrik L. Olsen and Mihai Iovea. Method for system-independent material classification through basis material decomposition from spectral X-ray CT. Submitted for publication.

In this work, we present a classification method based on a basis material decomposition (BMD). The distorted spectra caused by photon counting detector artifacts are corrected, and effective atomic number of a material is estimated from spectral CT.

# Background 2

---

## 2.1 Conventional X-ray computed tomography

The conventional 2D transmission radiography technique is currently used for security screening in airports. They produce good 2D x-ray images of the luggage. With CT systems, the classification of illegal objects is performed through shape recognition and the physical features of materials. However, this technique has the main limitation [2, 3] that it cannot differentiate between a thin layer of highly attenuating material (high- $Z$ ) and a thick layer of low attenuating material (low- $Z$ ). This is called the effect of superimposition that can mask the presence of potential threats such as explosives and illicit materials. More specifically, a low attenuating explosive like a plastic explosive could be hidden behind strong absorber that appears highly dark in the image. As a result, single energy X-ray computed tomography (CT) scanners were introduced to resolve this problem. These scanners generate single energy images that approximate the density values of scanned object.

CT setup is composed of an X-ray source, a detector and a sample holder. 2D cross-sectional images of the sample are reconstructed from the data collected by irradiating the sample from various angles, for which we use the term of *projection*. X-ray beam is projected through the sample on to the detector surface. A stack of 2D images creates a 3D image of the sample, giving detailed images of the internal structures. The ability of CT system to capture information from the third spatial dimension and to estimate material property solve the problem of occlusion in 2D radiography scanning. This provides better performance in automatically discovering explosives in the luggage. CT projections are performed during the synchronous rotation of the X-ray source and detector around the static sample. The sample itself is sometime rotated while the source and detector are fixed in laboratory-based setups. Conventional CT has been widely used as a non-destructive testing and evaluation technique in security, medical and many industrial applications.

X-rays are generated by an X-ray tube, composed of a cathode and an anode in vacuum [4]. The cathode is heated up to generate free electrons due to the thermionic effect. The electrical field created by a high voltage potential between the cathode

and anode accelerate electrons that hit a metal target at the anode. The most of input energy by incoming electrons are converted into heat inside the x-ray tube, and a very small part of the energy is converted into X-ray photons. The source radiation spectrum, called the Bremsstrahlung, consists of polychromatic beam with a wide energy spectrum. The energy interval of the X-ray spectrum is usually controlled by changing the maximum acceleration voltage that defines the peak energy of the spectrum and is represented in the unit of kVp. Metal filters can also be mounted in front of the source to control it. The number of photon counts or the intensity of the produced spectrum, is regulated by the anode current.

A broad range of X-ray detectors are available, some detectors measure only overall beam flux or count rate, while others count individual photons [5]. Collimators are often placed in front of the detectors to decrease the amount of incident scattered photons.

### 2.1.1 The principles of X-ray attenuation

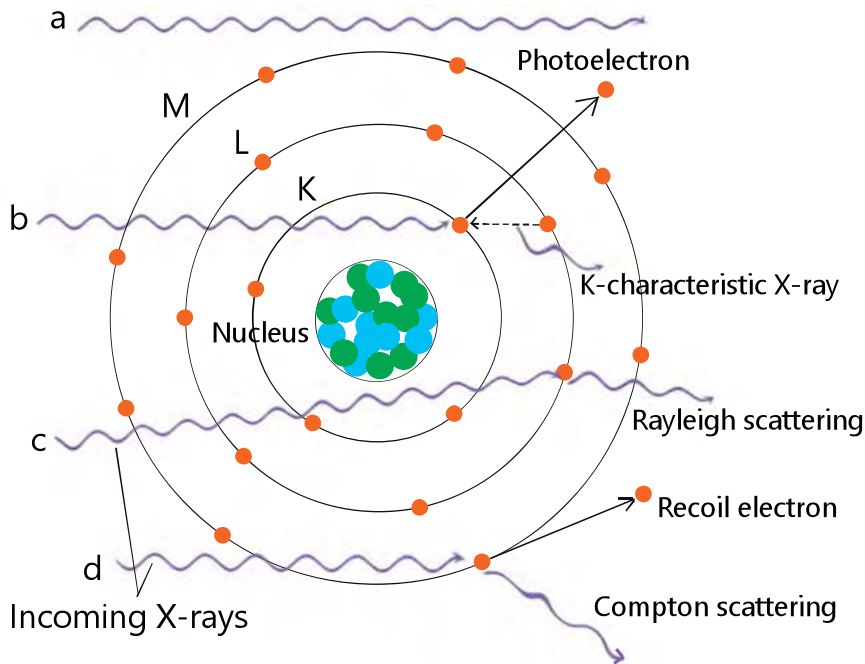
CT systems reconstruct a voxelized image of the distribution of the linear attenuation coefficients (LAC) within an object, denoted by  $\mu$ . X-ray attenuation occurs when photons penetrate the object, some photons are scattered, while some are absorbed due to interaction with the matter particles. Within the photon energy range used in CT (approximately from 20 keV to 160 keV), the interaction between X-rays and matter is dominated by photoelectric absorption at low energies and Compton scattering at high energies. Each interaction is independent, and the total LAC is the sum of the contributions of these interactions to the attenuation, which change with material and energy.

Fig. 2.1 illustrates the main mechanisms of X-ray and matter interactions. Photoelectric absorption is the process in which incident photon kicks out an electron from a lower shell of an atom to free state. Therefore, the photon is absorbed giving its energy to the orbital electron. The only condition for the absorption is that the photon should have more energy than the binding energy of the bound electron. The kinetic energy of the kicked electron is locally transferred to the lattice in the form of heat. The position abandoned by the electron is filled by other electrons from outer shells or, in the event of solids, by electrons from the band. Due to this recombination process, characteristic X-ray fluorescence lines may appear in the spectrum. If the radiation energy of the characteristic X-ray fluorescence is sufficient to kick out another electron in the more far shells from the nucleus, and the new free electron that left the atom is called an Auger electron. Auger electrons have same kinetic energies. This physical phenomenon is usually called radiation-free transition or internal conversion.

Compton (incoherent) scattering is the process in which X-ray photon collides with the weakly bound outer shell electrons (valence or quasi-free electron) or free electrons, and is deflected from incident beam. As a result, the wavelength of the scattered photon increases while its energy decreases. The Compton electron removed

from the atom is called a secondary electron. Both the scattered photon and Compton electron may have sufficient energy to go through next ionizing interactions.

Coherent or Rayleigh scattering is a phenomenon in which the scattering nucleus re-emits a beam when it is excited by the incoming radiation, and the emitted beam points in different direction than the incident beam. This is an elastic scattering without energy transfer in which the incoming and the scattered beam have the same wavelength. It occurs when the scattering nucleus is small in relation to the wavelength of the incoming beam. The Coherent scattering contribution is relatively small within the CT energy region, and it is often ignored in the total LAC.



**Figure 2.1:** Schematic illustration of X-ray interactions with matter. a) Some X-rays do not interact with matter and pass through. b) In photoelectric absorption mechanism an incident photon deposits its full energy to a binding electron of an atom, which is kicked out from its shell. The resulting hole is occupied by an outer shell electron which leads to X-ray emission called X-ray fluorescence. c) Rayleigh scattering is interaction with electron that occurs without energy transfer, and only deflects the trajectory of the incident beam. d) In incoherent Compton scattering an incident photon gives a part of its energy to an unbound electron that leaves the atom, and is deflected with the reduced energy.

Fig. 2.2 presents the contributions of different interactions to the total attenuation between 30 keV and 140 keV, exemplified for water and aluminum. The Compton component does not almost change with energy, whereas the photoelectric component varies strongly. Thus, the photoelectric and Compton components dominate the attenuation mechanism in the energy range related to medical and baggage CT systems.

Bragg and Peirce (1914) [7], Owen (1919) [8] and Richtmyer and Warburton (1923)

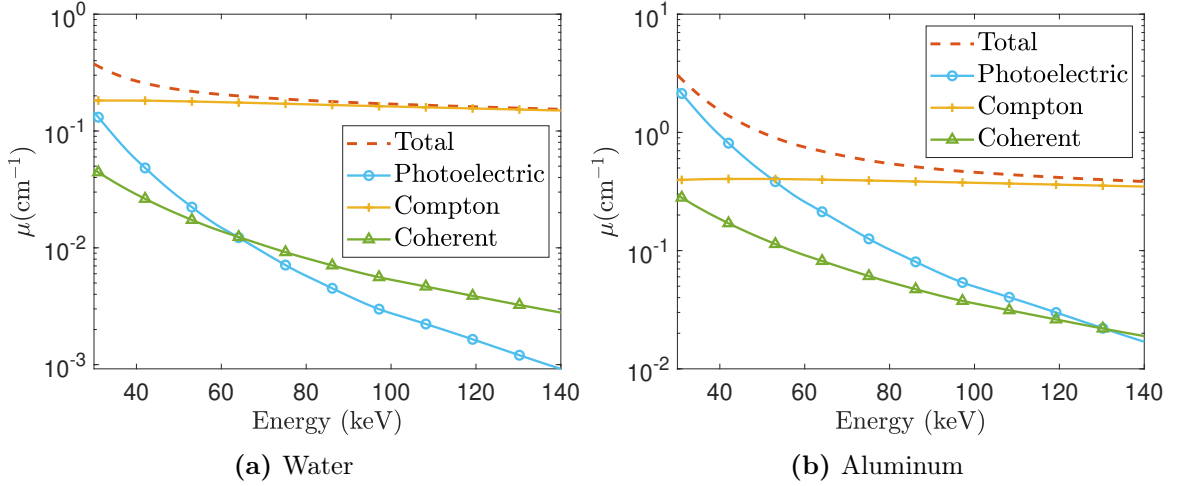


**Figure 2.2:** LAC at different photon energies with the components of photoelectric absorption, Compton scattering and coherent scattering, for water and aluminum. The data is obtained from NIST database [6]. Note the logarithmic scale in the y-axis.

[9] proposed the hypothesis of how photon interactions depend on atomic number ( $Z$ ) of matter, which has been applied in many radiation studies [10].

### 2.1.2 The Beer Lambert law

This scattering and absorption processes are quantified through the LAC. The quantity of photons transmitted through the matter without interaction depends on the photon energy, and density, atomic number and thickness of matter. To derive LAC we assume that X-ray is propagating along the path  $s$  from the source to the detector, and after passing a very small distance  $ds$  through a material, the small decrease in photon flux  $I(y)$  is defined as

$$dI = -\mu(s)I(s)ds.$$

By integrating from initial photon flux  $I_0$  to final transmitted photon flux  $I$  along the whole thickness of the material,  $d$ , as

$$\int_{I_0}^I \frac{dI}{I(s)} = - \int_0^d \mu(s)ds,$$

thus we obtain the Beer Lambert law that defines the transmitted photon flux for energy  $E$  as

$$I(E) = I_0(E) \exp \left( - \int_0^d \mu(s, E)ds \right). \quad (2.1)$$

The initial photon flux  $I_0$  is defined with the flat-field measurement, i.e. the projection measured by the detector without a sample, also referred as the source spectrum or the system's spectral response.

### 2.1.3 The limitations of conventional single energy CT

Conventional CT suffers from three main limitations. First, commercially available CT scanners are equipped with energy-integrating detectors that capture only the overall beam flux rather than single photons. Therefore, the transmitted signal is integrated over all energy range, and they ignore the energy dependence of LAC described in Eq.2.1. Thus, the energy spectrum information is lost at the detectors during the signal integration. As a result, conventional CT reconstruction appears with the so-called beam-hardening artifacts. This is due to the fact that the LAC usually decreases as the X-ray energy increases, and the low energy photons are more absorbed, and the beam becomes sharper in high energy photons as it passes through the sample. Placing a thin sheet of metal (e.g. aluminum or copper) filter in front of the source can reduce the beam-hardening artifacts by decreasing the energy spectrum width, as the filter absorbs more low energy photons. However, the filtering reduces the beam flux, resulting in higher noise levels. The beam-hardening effect affects reconstruction quality and leads to the appearance of cupping artifacts and a loss of image contrast. Second, conventional CT reconstructs the averaged LAC of an object at single energy over a broad energy spectrum. This means that some materials that are different can have the same averaged LAC for single energy due to overlapping over the wide energy range, and it results in poor material specificity. Finally and more importantly, this technique measuring LAC at just single energy cannot determine the chemical composition of materials. The measured LAC is an energy-dependent feature of a material, and thereby dependent on the scanner specifics such as the source spectrum or filters. This makes the technique system-dependent. These limitations result in higher false alarm rates linked to threat detection, which require additional labor resources to carefully check the luggage. Therefore, there is a need to decrease the false alarm rate for these systems in order to decrease the labor expenses.

## 2.2 Dual-energy CT

To overcome the disadvantages of conventional CT in material separation, many studies have been done to estimate energy-independent material features, using Dual-energy CT. Dual-energy CT scanners measure two various spectra used to extract the material's LAC at low- and high- mean energies that are overlapping. The data is acquired as consecutive scans with different source accelerating voltages and filters in order to have the different energy peak of spectrum, or as a single scan with dual-energy sandwich detectors [11].

Dual-energy CT is able to quantitatively characterize materials via electron density  $\rho_e$ , and effective atomic number  $Z_{\text{eff}}$  of scanned objects, based on the measurement of the energy dependence of the attenuation. Classification of materials into two parameters significantly improves detection ability. For example, water and the explosive ANFO (Ammonium Nitrate and fuel oil) can possess indistinguishable



densities, however, they have very different effective atomic numbers [12]. Therefore, a dual energy CT scanner can better separate water and ANFO. It has been proved that dual-energy radiography systems that measure both atomic number and density can also reach a lower false alarm rate for threat detection compared to systems that measure only density [13–15]. Therefore, dual-energy CT is currently the state-of-the-art technique for the material characterization in security applications, and radiotherapy and medical diagnosis [12, 16–30]. The estimation of  $\rho_e$  and  $Z_{\text{eff}}$  has increased the contrast of soft human tissues even though they have overlapping attenuation properties [23, 31, 32].

### 2.2.1 Dual basis function decomposition

The LAC can be generally represented as a linear combination of multiple basis functions (i.e. as multiple dimensions of attenuation vector space) as [33, 34]

$$\mu(E_k) = a_1 f_1(E_k) + a_2 f_2(E_k) + \dots + a_N f_N(E_k), \quad (2.2)$$

where  $a_i$  denote the corresponding material-dependent coefficients,  $f_i(E_k)$  are energy-dependent basis functions, and  $i = 2, 3, \dots, N$ ,  $k = 2, 3, \dots, K$ , with  $N$  and  $K$  being the total number of basis functions and energy bins, respectively. The coefficients  $a_i$  are evaluated and usually employed as the material properties. The basis functions can just represent a mathematical formulation without a physical meaning, or represent physical models, such as the Photoelectric absorption and Compton scattering, or LACs of multiple basis materials [35]. Alvarez (1982) [33] studied the dimensionality of the LAC vector space in the above general decomposition model, using the Singular Value Decomposition (SVD) theorem, a mathematical tool from matrix algebra [36]. For diagnostic applications with dual-energy CT, they found that the decomposition into two dimensions (i.e. into two basis functions) can be sufficient to accurately approximate LACs. Moreover, they showed that the LACs of materials with K-edge absorption such as iodine contrast agent can be properly fitted with three basis functions. The K-edge is a sudden increase in the LAC taking place at an incident photon energy larger than the binding energy of the atomic K-shell electron. This physical effect is used in medical CT to separate contrast agents from body tissues and other materials [37].

Several alternatives for the basis functions have been proposed however, the dual basis function decomposition proposed by Alvarez and Macovski [1] that can accurately represent the LAC was the innovative approach towards the development of dual-energy CT. Using materials without K-edges within the CT energy range of 30–200 keV, they accurately decomposed the LAC into a dual set of basis functions, defined by

$$\mu(E) = a_1 f_1(E) + a_2 f_2(E), \quad (2.3)$$

where  $a_1$  and  $a_2$  are the material-dependent coefficients,  $f_1(E)$  and  $f_2(E)$  are the energy-dependent basis functions which approximate the photoelectric absorption and

Compton scattering components, respectively.  $f_1(E)$  is defined as  $f_1(E) = 1/E^3$ .  $f_2(E)$  is also called the Klein-Nishina function, defined by

$$f_2(\varepsilon) = \frac{1 + \varepsilon}{\varepsilon^2} \left( 2 \frac{1 + \varepsilon}{1 + 2\varepsilon} - \frac{\ln(1 + 2\varepsilon)}{\varepsilon} \right) + \frac{\ln(1 + 2\varepsilon)}{2\varepsilon} - \frac{1 + 3\varepsilon}{(1 + 2\varepsilon)^2}, \quad (2.4)$$

and  $\varepsilon = E/511$  keV ( $\varepsilon = E/m_e c^2$ ) denotes the reduced energy of the incoming photon. For the materials with the K-edge discontinuity in the LACs, the energy range below the K-edge should be truncated in order to be able to use the dual basis function decomposition.

The quantities of  $a_1$  and  $a_2$  coefficients are defined based on how photons interact with matter. Alvarez et al. [1] showed empirically that the coefficients,  $a_1$  and  $a_2$  can be approximately determined through mass density ( $\rho$ ), atomic number ( $Z$ ) and atomic mass ( $A$ ) of an element as

$$a_1 \approx K_1 \frac{\rho}{A} Z^n, \quad a_2 \approx K_2 \frac{\rho}{A} Z \quad (2.5)$$

where  $K_1$  and  $K_2$  are constants, and  $n$  is the exponent for photoelectric absorption component in the attenuation decomposition (per atom). Inserting  $a_1$  and  $a_2$  from Eq. 2.5 in Eq. 2.3 we obtain the LAC decomposed into material- and energy-dependent components as

$$\mu(E) = \frac{Z}{A} \rho (Z^{n-1} p(E) + c(E)), \quad (2.6)$$

where

$$p(E) = K_1 \frac{1}{E^3}, \quad c(E) = K_2 f_{\text{KN}}(E). \quad (2.7)$$

In this work, we define  $p(E)$  and  $c(E)$  as photoelectric absorption and Compton scattering basis functions, respectively. The basis functions are empirically found from experimental fit to data.

### 2.2.2 Electron density and effective atomic number

X-ray attenuation is proportional to an electron density of a material [38]. The electron density represents the number of electrons per unit volume (electron – mole/cm<sup>3</sup>) and is correlated with mass density ( $\rho$ ), atomic number ( $Z$ ) and atomic mass ( $A$ ) of an element as follows:

$$\rho_e = \frac{Z}{A(Z)} \rho, \quad (2.8)$$

For a compound that is composed of  $N$  total different elements  $i$  each with a number of atoms,  $\alpha_i$ , the electron density can be defined as

$$\rho_e = \frac{\sum_{i=1}^N \alpha_i Z_i}{\sum_{i=1}^N \alpha_i A_i} \rho, \quad (2.9)$$

where  $A_i$  and  $Z_i$  denote atomic mass and atomic number for each element,  $i$ , respectively. For compounds, the atomic number is described with effective atomic number,  $Z_{\text{eff}}$ , which is correlated with the atomic numbers of the elements in the compound and with their corresponding proportions. A now classical parameterization for  $Z_{\text{eff}}$  was presented by Mayneord (1937) [39] and Spiers (1946) [40] as

$$Z_{\text{eff}} = \sqrt[l]{\sum_{i=1}^N r_i Z_i^l}, \quad (2.10)$$

where  $N$  is the number of elements that compose a compound,  $Z_i$  designates the atomic number for each element,  $i$ , and  $r_i$  is the relative electron fraction of an element,  $i$ , which is computed as

$$r_i = \frac{\alpha_i Z_i}{\sum_{j=1}^N \alpha_j Z_j},$$

where  $\alpha_i$  is the number of atoms that possess atomic number  $Z_i$ .

No single definition of  $Z_{\text{eff}}$  can accurately describe the variation of Rayleigh scattering and photoelectric absorption cross sections in the attenuation coefficients over the set of materials and energy range of medical and baggage CT scanning (approximately between 10 keV and 150 keV) [10, 40–47]. In this energy range the Compton interaction occurs with relatively unbound electrons. Consequently, the Compton scattering cross section is independent of the chemical composition of materials being scanned, and only related to X-ray energy [41]. Therefore, the exponent  $l$  is optimized based on the material, source spectrum and system features. In the literature, this parameter,  $l$  typically varies between 2.94 and 3.8 depending on experimental fits for different CT scanners. Even though Eq. 2.10 disregards the Rayleigh scattering contribution, the Lehnmann parameterization defines  $Z_{\text{eff}}$  quite well because the total cross section is mostly dominated by photoelectric absorption and Compton scattering for the set of our materials and detector's energy range [44, 47]. Therefore, in the Paper A in the appendix the exponent value of  $l = 3.8$  being from the original Lehnmann parameterization is used for calculating the reference  $Z_{\text{eff}}$  values of materials [48]. However, when the dependence of the classification performance on exponent  $l$  was estimated based on the relative deviations, we found that the optimal range of  $l$  was between 7.2 and 10.5, and  $l = 8.0$  gave the minimum relative deviation [48]. Nevertheless, in the Paper A we kept the value of  $l = 3.8$  to preserve consistence with the previously published works. In the Paper B, C and D presented in the appendix, we employed the value of  $l = 8.0$  being optimal with the set of our materials, source spectrum and detector response.

Inserting Eq. 2.9 in Eq. 2.6 we obtain a decomposed LAC for a compound as

$$\mu(E) = \rho_e (Z_{\text{eff}}^{n-1} p(E) + c(E)). \quad (2.11)$$

### 2.2.3 The limitations of dual-energy CT

The dual-energy CT has two main limitations. First, they usually employ dual sandwiched energy integrating detectors consisting of two layers of scintillator-photodiode, separated by a metal filter. The low- and high-energy spectrums of X-ray beam absorbed by the first and second layers, respectively, are overlapping which leads to poor energy separation. Second, the dual-energy CT extracts only two mean LACs averaged over wide low- and high-energy spectrums, and this limits its potential for further improving classification performance. Moreover, material classification with dual-energy detectors may be system-dependent, i.e. being dependent on the system components such as source spectrum, materials for filtration, and detector efficiency [49]. Recently, Azevedo et al. [50] presented the System-Independent  $\rho_e/Z_{\text{eff}}$  (SIRZ) method that estimates  $(\rho_e, Z_{\text{eff}})$  from dual-energy CT, independent of the instrument. For  $Z_{\text{eff}}$  values between 6 and 20, and energies up to 200 keV, the SIRZ showed that the accuracy and precision error were lower than 3% and 2% for estimating  $\rho_e$  and  $Z_{\text{eff}}$ , respectively. Champley et al. [51] have developed the method further (SIRZ-2). These methods require the calibration of the detector's spectral response by employing a set of reference materials. The assumptions in these methods leads to some limitations. For example, it cannot estimate materials with K-edge discontinuities in the LAC, and the correction of the beam-hardening effect being dependent on the source spectrum and detector's spectral response remains a challenge.

## 2.3 Spectral CT

The development of cadmium telluride (CdTe) photon-counting detectors (PCD) has established the foundation for Spectral CT [52, 53]. This technique is also called as multi-energy X-ray CT in the literature. PCDs can separate the energy of the incident photons and simultaneously capture a band of energy-dependent material features by employing certain thresholds to gather and digitize the photon counts. PCDs have shown a great potential to improve diagnostic and radiation therapy imaging [54, 55]. Compared to dual-energy CT, spectral CT with single acquisition can extract energy-discriminated LACs at multiple energy bins and is proved to significantly enhance material separation [56]. Therefore, spectral CT has attracted significant interest within the security [57–59] and medical applications [60–65]. X-ray radiography research in explosive detection showed that PCDs outperform dual-layer sandwich detectors with relatively poorer energy discrimination in improving classification performance [66–69].

Busi et al. [70] have implemented the principle of the SIRZ method in Spectral CT and presented the Spectral  $\rho_e/Z_{\text{eff}}$  Estimation (SRZE) method, which measures system-

independent material features ( $\rho_e$ ,  $Z_{\text{eff}}$ ) directly from the spectral LACs. The SRZE method reaches the optimal classification performance at 64 energy bins, and relies on the accurate extraction of spectral LAC curves. The estimation accuracy decreases for low  $Z_{\text{eff}}$  materials because of detector response artifacts at lower energies, where the contrast of these materials is also greatest. Brambilla et al. [58] proposed a method for material classification from spectral CT based on basis material decomposition, which defines a material's LAC as a linear combination of basis materials' LACs with corresponding equivalent thicknesses. This method requires a calibration step to capture the detector's spectral response for a set of basis materials with different thicknesses, and only estimates  $Z_{\text{eff}}$ . The calibration step makes the method system-dependent because of the dependence on the source spectrum, filtration and detector's response. The concepts of basis material decomposition of LACs were presented in Refs. [44, 71, 72].

## 2.4 Statement of problem for the thesis

Airport scanners are constructed based on trade-offs between data processing speed, reconstruction quality and computer cost. They usually use channel-by-channel iterative reconstruction algorithms with sufficient number of projections. As of today, modern multi-energy scanners mostly have sources and detectors placed on a rotating disk denoted by Gantry [73]. Scanners constructed with a fixed detector have the superiority of being mechanically stable, and can have a longer detector's exposure time. Therefore, they can support a larger signal-to-noise ratio (SNR) during capturing the projections than a scanner with a rotating disk. However, separate sources and detectors for each projection are usually required for a fixed gantry setup. Using several photon counting detectors means the relatively high cost than conventional single or dual-energy detectors. Therefore, employing the lowest possible number of detectors is highly desired, which means a very limited number of projections for the image reconstruction. The advanced reconstruction algorithms should be used to overcome reconstruction artifacts caused by using few projections, and achieve good material recognition. Moreover, using few numbers of projections gives the reduced computation time for reconstructions, which increases throughput. Fig. 2.3 illustrates such a multi-energy scanner with fixed detectors and sources, built in the 3D Imaging Center at Technical University of Denmark. Detector records are received by an image reconstruction computer and are converted into slice images that go to a computer for the image analysis. The luggage bag moves on a conveyor belt of the system that moves continuously and is synchronized with the ability of the data acquisition. After the luggage is reconstructed and classified, the luggage is segmented into individual objects and labelled for potential threats and non-threats, as illustrated in Fig. 2.4. An alarm situation is automatically triggered if any suspicious regions in the luggage are found, and then the luggage needs to be reviewed by human operator.

I list the following problems that can be addressed in this thesis. First, for a

fixed gantry setup there is a need for decreasing the necessary number of projections in order to reach lower cost of detectors and higher throughput of scanned objects. This is because a faster boarding time for passengers should be achieved while they can leave their laptops, electronics and liquids in their luggage.

Second, the state-of-the-art (SRZE) classification method in Spectral CT requires a large number of energy bins for the optimal classification [70]. Because the required image reconstruction is time costly, it is a disadvantage if all energy bins from the detector should be reconstructed separately. To overcome this, we can consider how to develop a new classification method that can achieve the best performance with reduced number of energy bins. In spectral CT, we have a possibility of rebinning energy bins into bi-energy bins which are non-overlapping and can be widely separated. Therefore, we can investigate the chance of improving classification by optimizing the thresholds of the bi-energy bins in the energy spectrum.

Third, while photon counting detectors are better than traditional energy integrating detectors, they require correction of detector's spectral distortions that can limit the resulting classification accuracy. Therefore, we should analyze how the correction algorithm is important in classifications.

Fourth, spectral CT suffers from reduced SNR due to increased number of energy bins resolved by the energy sensitive detector. We should minimize this inherent issue of reconstruction artifacts by incorporating additional information consisting of the correlations between multi energy data, using a new joint reconstruction algorithm.

Fifth, the multi-energy scanners have a disadvantage that they use small detectors to have good spatial resolution of the image, i.e. the minimum size of features that can be resolved by the image analysis system. For a given source-to-detector distance and a given source power, a reduced detector size results in reduced detector SNR and thus introduces more noise to the signal due to lower photon statistics. A loss in SNR can be restored by employing a more powerful source. Raising the source current increases the photon emission rate, and thereby the captured signal, which can in turn compensate the loss. However, this comes at a cost with the following disadvantages; extra power expenses of the source, decreased source lifetime, and extra power expenses for cooling increased heat. Therefore, we should develop a new reconstruction algorithm to address the last two problems, which can be achieved by capturing additional information in spectral dimension.

## 2.5 Thesis objectives

Based on the problems laid out above, the main objectives of the thesis can be summarized as follows:

- Study how the different steps of the overall data-processing workflow impact the final material classification and how to improve the classification performance.

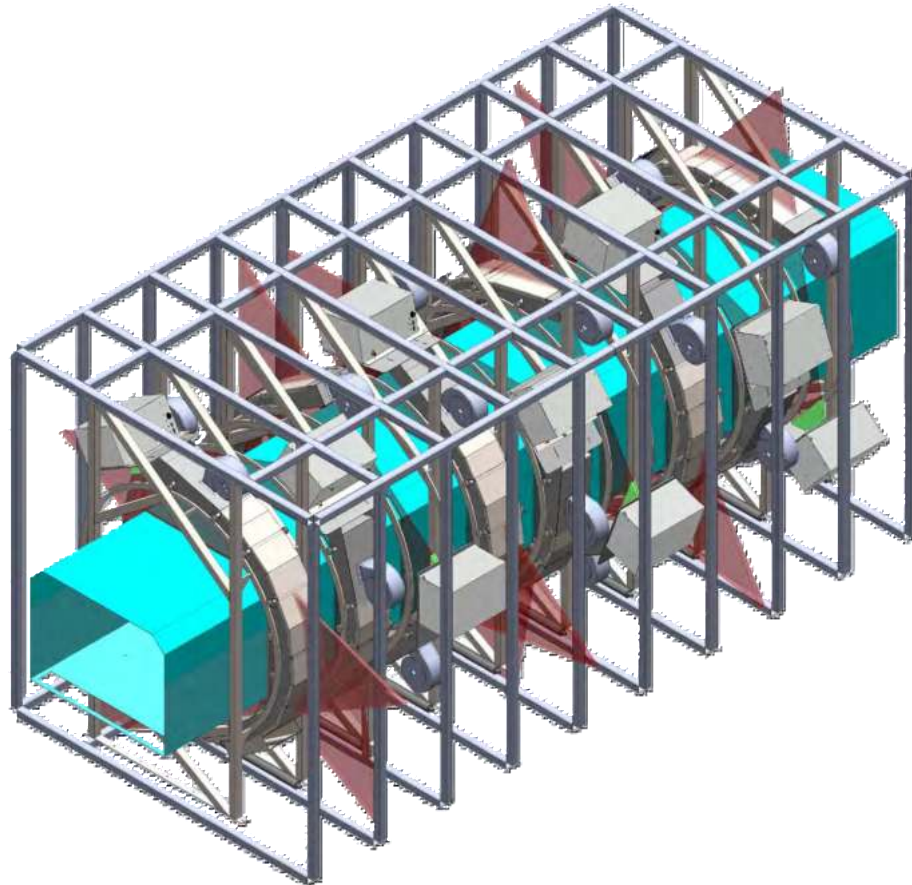


**Figure 2.3:** Illustration of a multi-energy scanner with fixed detectors and sources for explosive detection, constructed in the 3D Imaging Center at Technical University of Denmark.

The examples can be the correction step for spectral distortion in the multi-energy detector and the reconstruction step.

- Develop a new method(s) for material classification based on spectral CT which can accurately retrieve material properties without *a-prior* knowledge on the complex sample. Explore how to reduce and optimize the number of multiple energy bins for the best performance.
- Develop an image reconstruction algorithm(s) that can handle reconstruction artifacts caused by using few CT projections and low SNR in each energy bin, exploiting additional information in the spectral dimension.

The above strategies have set the scope of this thesis. The thesis is not just a summary of the results of experiments, but new image reconstruction algorithms and classification methods based on applied mathematics are introduced and optimized, and their performances are tested using real experimental datasets.

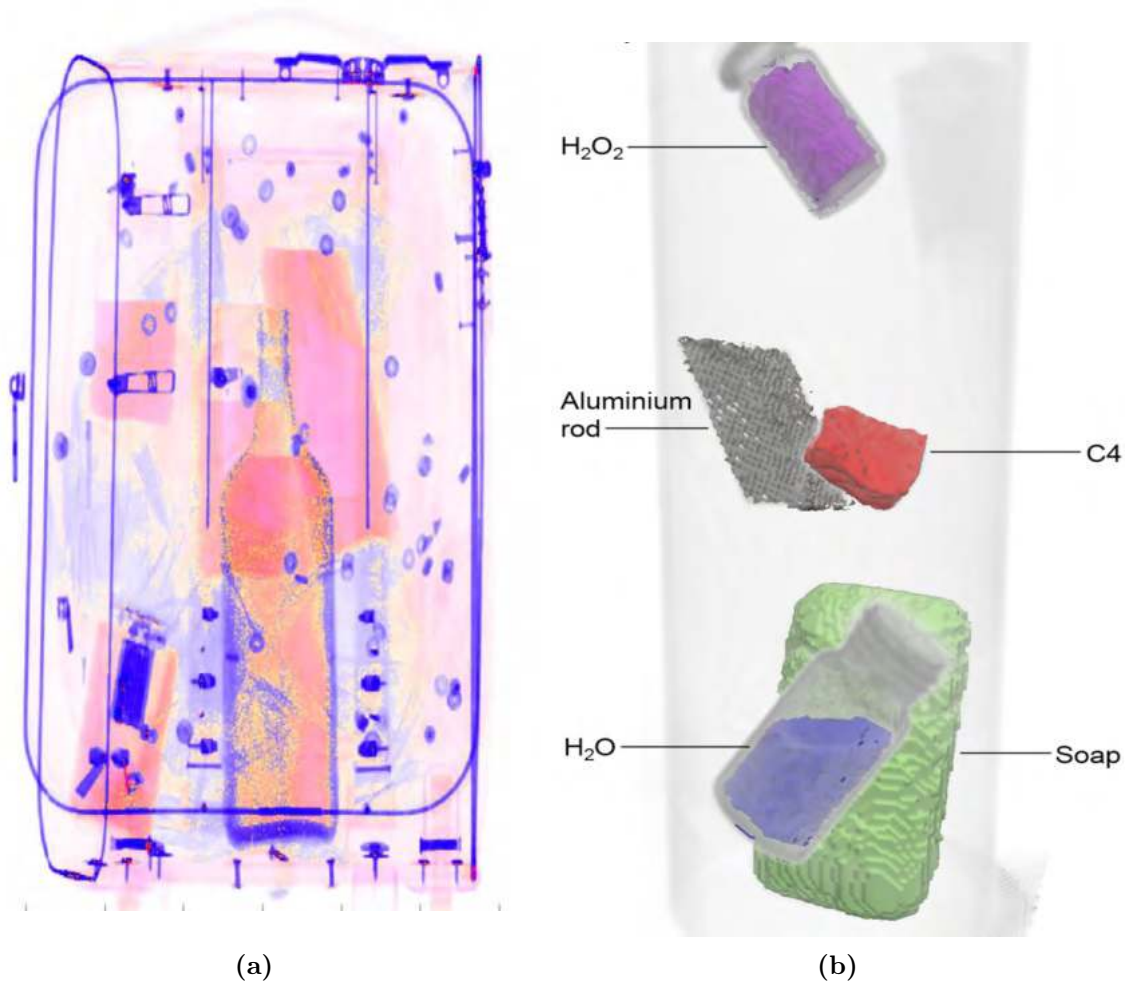


**Figure 2.4:** 3D image reconstructions of the luggage scanned with the multi-energy scanner illustrated in Fig. 2.3. The reconstructions are segmented into individual objects for explosive detection.



# Data acquisition and data pre-processing step 3

---

This chapter introduces data acquisition and data pre-processing steps before image reconstruction. Image reconstruction is performed for energy bins between low- and high-energy thresholds in the source spectrum, which are set to exclude bins with photon starvation and spectral distortion existent even after correction of detector response for spectral distortions.

## 3.1 Overview of the overall workflow

Fig. 3.1 introduces the overall workflow of the overall chain from data acquisition to material classification into system-independent material features, developed in this thesis.

## 3.2 Experimental setup and materials

All the experiments reported in this research work were conducted in the 3D Imaging Center at DTU, Denmark. Spectral X-ray acquisitions were performed using the custom-built experimental setup illustrated in Fig. 3.2. The X-ray beam was generated by an X-ray tube equipped with a tungsten anode, a micro focused Hamamatsu source, placed on a vertically translating motor. The operating parameters of the source like the acceleration tube voltage and the anode filament current were set to 150 kV and 0.5 mA, respectively. The focal spot is 75  $\mu\text{m}$ . The sample rotation stage and also the detector can move along the three orthogonal directions. The incident beam was collimated to a fan beam by using a JJ X-Ray IB-C80-AIR slit equipped with 5-mm-thick tungsten carbide blades, placed in front of the source. The frontal collimator also has a function in decreasing the background radiation of scattered and fluorescent photons by keeping the beam size to a minimum and irradiating mainly the full detector area. The instrumentation also incorporates a tungsten slit placed in front of the detector to remove the background radiation and environmental noise. A 2-mm-thick aluminum filter was attached to the collimator to remove photons with energies

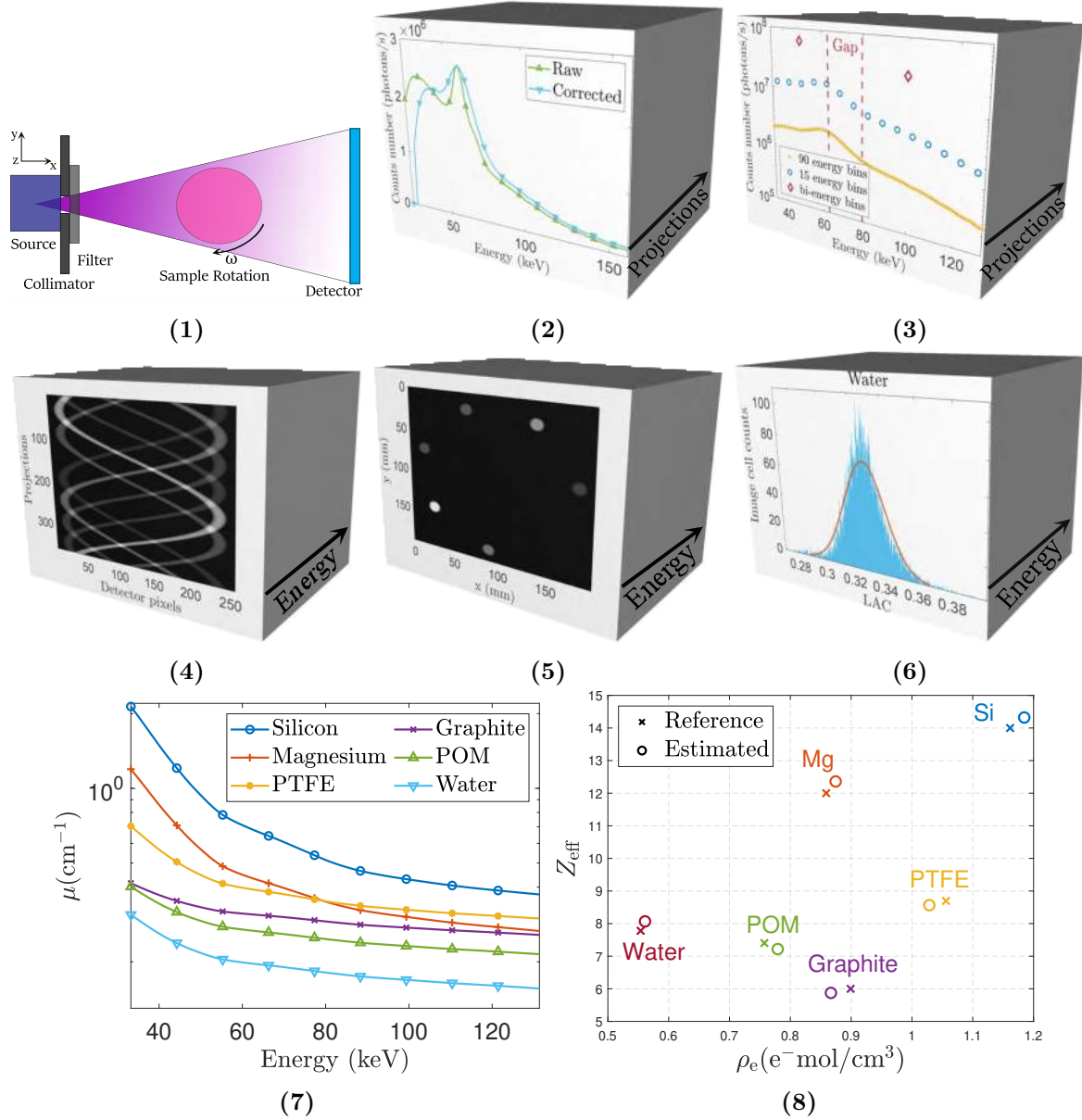
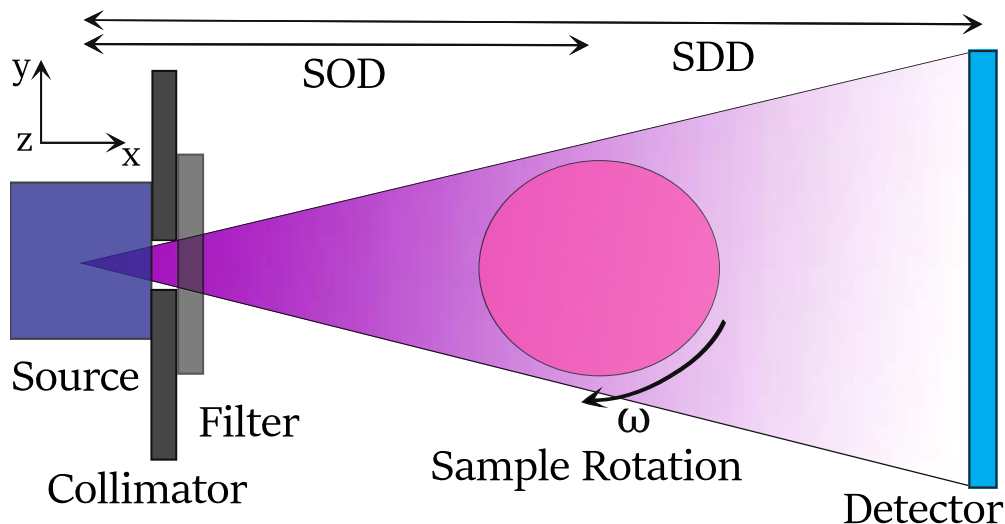


**Figure 3.1:** Illustration of the overall workflow of the individual data processing steps. (1) Data acquisition step described in the Section 3.2. (2) Spectral correction of detector’s spectral response applied to all projections, for which the correction algorithm is presented in the Section 3.4. The spectral distortions and photon starvation in X-ray spectra at the lower and higher energy bins still result in a distortion of the measured LACs, and cannot be corrected by the correction algorithm. These energy bins are excluded by setting low- and high-energy thresholds for further data processing, as described in the Section 3.5. (3) Energy channels rebinning applied to all projections, which is introduced in the Section 3.6. (4) The projection data or sinograms, generated for all energy bins. This step is described in the subsection 4.1.1. (5) Multi-energy image reconstruction step, described in the Section 4.2. (6) Technique for extraction of the energy-dependent LAC values, exemplified for water. How the LACs are extracted from the histogram based on Gaussian curve fits for each energy bin is described in the Section 3.5. (7) The energy-dependent LACs of the materials in the reconstruction sample. Note logarithmic scale in the  $y$ -axis. (8) Material classification step based on electron density ( $\rho_e$ ) and effective atomic number ( $Z_{\text{eff}}$ ) map, for which the methods are described in Chapter 5.

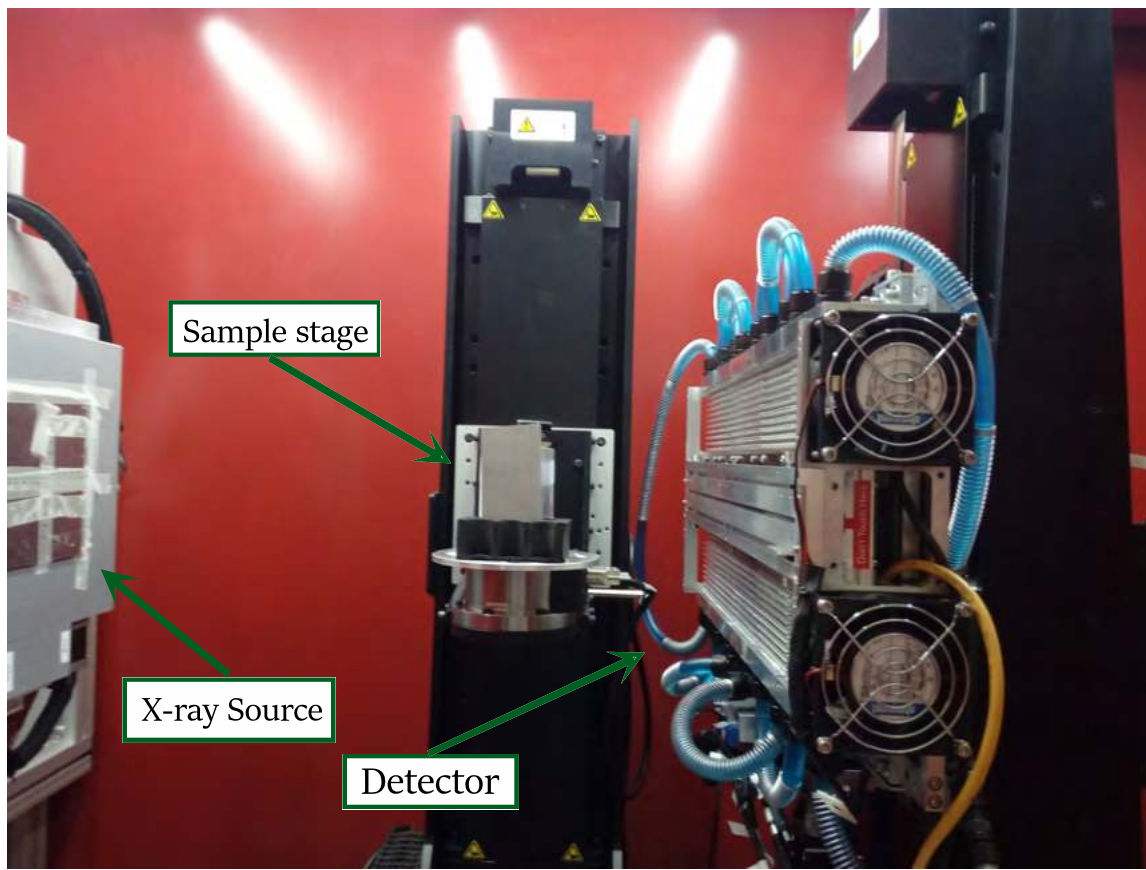
below the detector’s energy region from the source spectrum. A sample is placed on a holder which can be rotated to angles in the full range of 0–360 degrees, as illustrated in Fig. 3.2. The samples placed on the rotation stage are scanned between discrete rotations over a range of 360 degrees at certain increments. The amount of increments depend on the number of projections required for estimations of image reconstruction and material classification performances. The source to detector distance was 701 mm while the source to sample distance was set to 500 mm.

Fig. 3.3 shows picture of the experimental setup. Figures 3.4, 3.5 and 3.6 display the pictures of three different samples placed on a sample holder. The pictures in each figure are taken from the different angles by a camera. The pictures also show MultiX ME-100 v2 detector behind the phantoms, which is used for spectral CT data acquisitions as described in Section 3.3.

Tab. 3.1 lists all the materials scanned and processed through the reconstruction algorithms and the classification methods developed in this thesis. The material dimensions are presented through width×length and diameter for rectangular and circular samples, respectively. The materials corresponding to the indices 1–7 were scanned by placing them in groups in two different samples. The reconstructed images of both samples are shown in Figs. 3.7a and 3.7b. The materials corresponding to the indices 8–13, all being scanned in groups in one sample, were taken from the authors of Ref. [70] for estimations in this thesis. The reconstructed image of this sample is presented in Fig. 3.7c. The materials corresponding to the indices 14–35 were scanned individually. The reconstructed images of some of these materials such as acetone 2, water and aluminum are shown in Fig. 3.8, as an example.



**Figure 3.2:** The illustration of the instrumental setup. SDD and SOD denote the distance between the X-ray source and the detector, and the X-ray source and the sample stage, respectively. The figure is adapted from the Paper B in the appendix section.



**Figure 3.3:** Picture of the experimental setup for spectral CT measurements.



**Figure 3.4:** Pictures of the sample including seven different plastics, taken from the different angles. The image reconstruction of this sample is shown in Fig. 3.7b.

**Table 3.1:** The list of the materials used for classifications and their respective reference  $\rho_e$  and  $Z_{\text{eff}}$  values computed with Eq. 2.9 and Eq. 2.10, respectively. The size is represented through width $\times$ length for rectangular samples or diameter for circular samples. The unit of electron density is  $e^- \text{mol}/\text{cm}^3$ . The mass densities,  $\rho$  for the plastics corresponding to the indices 1–7 were estimated with uncertainties of  $\pm 0.15\%$ . The rest of mass density values are taken from PubChem database [74].

Index	Material	Chemical Formula	Size (mm)	$\rho$ (g/cm <sup>3</sup> )	$\rho_e$	$Z_{\text{eff}}$
1	PC	(CO <sub>3</sub> C <sub>13</sub> H <sub>8</sub> ) <sub>n</sub>	8.2 $\times$ 53.5	1.18	0.610	6.82
2	PMMA	(C <sub>5</sub> O <sub>2</sub> H <sub>8</sub> ) <sub>n</sub>	40 $\times$ 42	1.18	0.636	7.02
3	PET	(C <sub>10</sub> H <sub>8</sub> O <sub>4</sub> ) <sub>n</sub>	9 $\times$ 53.5	1.39	0.721	7.09
4	POM-C	(CH <sub>2</sub> O) <sub>n</sub>	9 $\times$ 53.5	1.41	0.753	7.40
5	POM-H	(CH <sub>2</sub> O) <sub>n</sub>	15.5 $\times$ 53.3	1.43	0.763	7.40
6	PVDF	(C <sub>2</sub> H <sub>2</sub> F <sub>2</sub> ) <sub>n</sub>	9 $\times$ 53.5	1.79	0.896	8.40
7	PTFE	(C <sub>2</sub> F <sub>4</sub> ) <sub>n</sub>	9 $\times$ 53.3	2.16	1.035	8.70
8	Graphite	C	12.7	1.8	0.899	6
9	POM	(CH <sub>2</sub> O) <sub>n</sub>	12.7	1.42	0.757	7.40
10	Water 3	H <sub>2</sub> O	12.7	0.997	0.554	7.78
11	PTFE 2	(C <sub>2</sub> F <sub>4</sub> ) <sub>n</sub>	12.7	2.2	1.056	8.70
12	Magnesium	Mg	12.7	1.74	0.859	12
13	Silicon 2	Si	12.7	2.33	1.161	14
14	N,N-Dimethylhydrazine	C <sub>2</sub> H <sub>8</sub> N <sub>2</sub>	67	0.791	0.447	6.44
15	Ethylenediamine	C <sub>2</sub> H <sub>8</sub> N <sub>2</sub>	67	0.90	0.509	6.44
16	2-Butanone	C <sub>4</sub> H <sub>8</sub> O	83	0.805	0.447	6.76
17	Acetone	C <sub>3</sub> H <sub>6</sub> O	20	0.785	0.432	6.90
18	Acetone 2	C <sub>3</sub> H <sub>6</sub> O	54	0.785	0.432	6.90
19	Nitrobenzene	C <sub>6</sub> H <sub>5</sub> NO <sub>2</sub>	49	1.20	0.624	7.00
20	Methanol	CH <sub>3</sub> OH	20	0.792	0.446	7.29
21	Methanol 2	CH <sub>3</sub> OH	81	0.792	0.446	7.29
22	Ethanol 96%	C <sub>2</sub> H <sub>6</sub> O (96%)	67 $\times$ 67	0.798	0.450	7.06
23	Ethanol 40%	C <sub>2</sub> H <sub>6</sub> O (40%)	67 $\times$ 67	0.947	0.532	7.63
24	Hydrazine solution	H <sub>4</sub> N <sub>2</sub> (35%)	54	1.0	0.561	7.43
25	Nitromethane	CH <sub>3</sub> NO <sub>2</sub>	20	1.14	0.597	7.50
26	Water	H <sub>2</sub> O	20	0.997	0.554	7.78
27	Water 2	H <sub>2</sub> O	51 $\times$ 51	0.997	0.554	7.78
28	Nitric acid	HNO <sub>3</sub> (65%)	83	1.39	0.714	7.80
29	Hyd. Peroxide	H <sub>2</sub> O <sub>2</sub> (50 %)	20	1.22	0.661	7.83
30	Hyd. Peroxide 2	H <sub>2</sub> O <sub>2</sub> (50%)	73 $\times$ 74	1.22	0.661	7.83
31	Magnesium 2	Mg	18	1.74	0.859	12
32	Aluminum	Al	25	2.70	1.3	13
33	Aluminum 2	Al	25	2.70	1.3	13
34	Aluminum 3	Al	20 $\times$ 20	2.70	1.3	13
35	Silicon	Si	25	2.33	1.161	14



**Figure 3.5:** Pictures of the sample including five different plastics and the different liquids in two bottles, taken from the different angles.



**Figure 3.6:** Pictures of the sample including five different plastics, taken from the different angles. The image reconstruction of this sample is shown in Fig. 3.7a.

### 3.3 Photon counting detectors

The development of energy separating, photon counting detectors (PCD) inspired the emergence of spectral CT. These detectors are usually made of semiconductor materials with higher dense and atomic number like CZT (CdZnTe), CdTe and GaAs, for which the photoelectric absorption is higher in photon and matter interactions. This type of semiconductor based detectors have higher rate of photon absorption than silicon based detectors for energies up to 160 keV, and therefore have better efficiency. However, high  $Z$  elements in the semiconductor sensor tend to have K-edges within detector's energy region, and may result in fluorescence noise signal for K-edge energies. This may lower the detector's performance at lower energies, where the contrast in the attenuation among organics is maximal.

The detector adopted for the experiments in this study is MultiX ME-100 v2 manufactured by Detection Technology S.A.S. in Moirans, France. We employ five

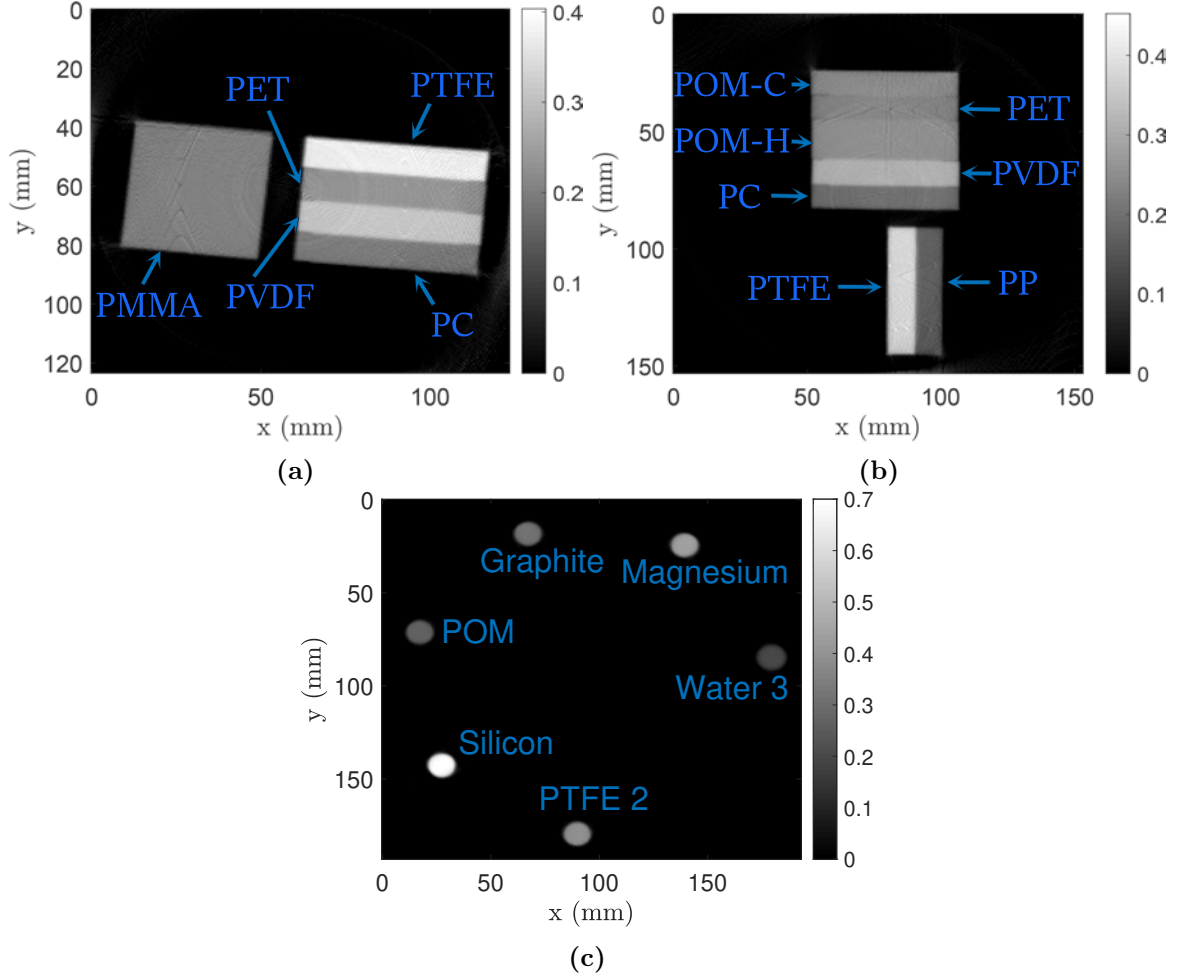


**Figure 3.7:** Samples scanned in groups and processed through the classification methods proposed in this thesis. The polypropylene (PP) material in the sample (b) is mixed with chemical colorants, which results in a higher  $Z_{\text{eff}}$  value compared to the pure PP, and therefore this material is excluded in classifications. 2D reconstructions were performed with the SIRT [75] from 360 projections at the energy of 61.9 keV. The gray scale bars denote the LACs with the unit of  $\text{cm}^{-1}$ .

daisy-chained detector modules. Single module has a  $1 \times 128$  linear array pixels of size  $0.8 \times 0.8 \text{ mm}^2$ , and operates with 128 energy bins, each with 1.1 keV width evenly allocated within 20 and 160 keV. The energy resolution of the detector operating under X-ray fluxes up to 7 Mphotons/s for single pixel is 6.5% (8 keV at 122 keV) [53]. The detector is composed of a 3-mm-thick CdTe sensor. A collective cathode made of a continuous metal film collects incident photons. The each sensor has small 128 pixelated anodes (pixels) placed on readout electronics, with a pitch of  $800 \mu\text{m}$  between anodes. A single MultiX detector is composed an array of 4 sensor crystals each with 32 pixels. The detector pixels between crystal edges are linearly interpolated to avoid the ring artifacts in reconstructions. The detector can work with integration time per projection from 2 ms to 100 ms (in  $10 \mu\text{s}$  increments). The lower integration

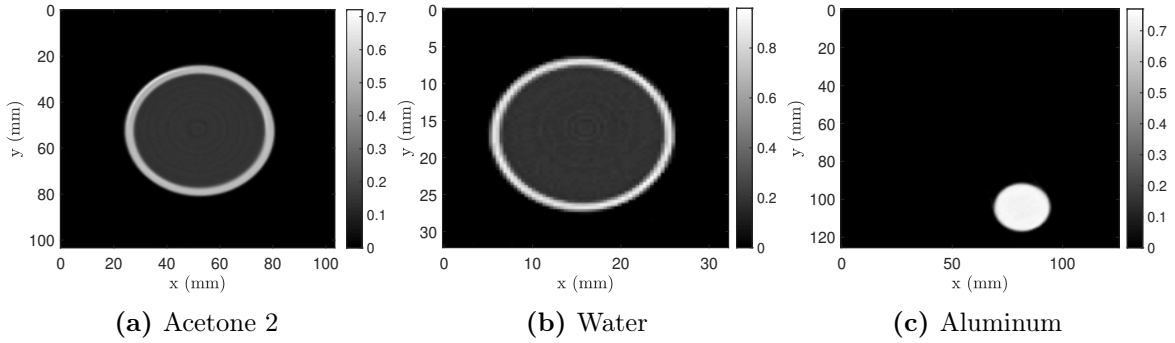


**Figure 3.8:** Samples scanned individually and processed through the classification methods proposed in this thesis, shown for acetone 2, water and aluminum as an example. 2D reconstructions were performed with the SIRT from 360 projections at the energy of 61.9 keV. The gray scale bars represent the LACs with the unit of  $\text{cm}^{-1}$ .

time, the lower photon counts or the higher noise levels in each energy channel. The total exposure time of the detector’s radiation per projection is specified in each Paper in the appendix section, varying between 2 ms and 8 seconds.

Based on Eq. 2.1, we can write the transmitted photon flux for energy bin  $E_k$ , captured by the detector, as follows

$$I(\vec{x}, E_k) = I_0(\vec{x}, E_k) \exp\left(-\int_0^d \mu(s, E_k) ds\right), \quad k = 1, 2, 3, \dots, K; \quad (3.1)$$

where  $\vec{x}$  represent the 1D linear detector pixel array,  $K$  is the total number of energy bins of the detector, and  $I_0$  is the initial photon flux  $I_0$  measured without the sample.

### 3.4 Correction of detector’s spectral response

PCDs suffer from severe distortions of the detector’s spectral response due to interactions between the photons and CdTe sensor crystal that leads to an error in energy detection and to activation of the neighboring pixels. Fig. 3.9 illustrates the spectral distortions in PCDs with the main photon interactions.

These interactions are energy and flux dependent, and lower the detector’s energy resolution and distort the extracted spectral LACs. X-ray photon absorbed nearby a pixel boundary produces electron charge cloud which may be divided between adjacent detector pixels. This leads to that the high-energy photon is incorrectly detected as two photons with lower energies, and this physical phenomenon is known as charge sharing.

Detector sensor layers Cd and Te have K-edges at 26.7 keV and 31.8 keV, respectively. Incident photons with an energy  $E$  larger than the K-shell binding energies can kick out K-electrons of CdTe crystal. The free K-shells are immediately refilled that causes emission of the fluorescence K-shell photons with energy  $E_{\text{fl}}$ , and



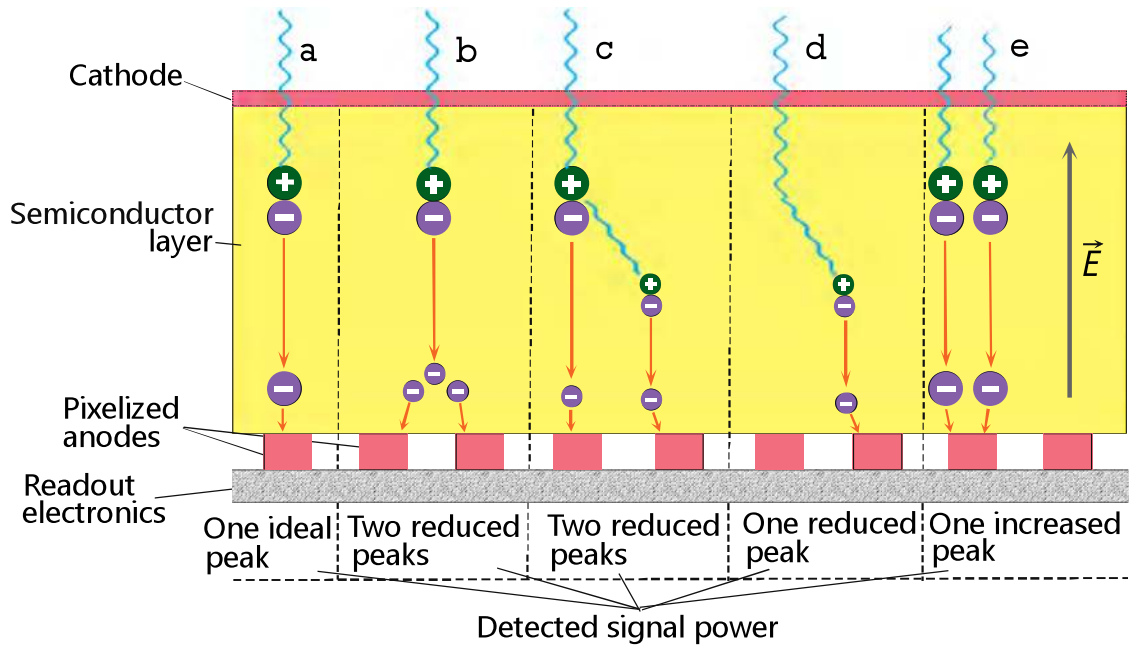


**Figure 3.9:** Schematic illustration of detector effects in the semiconductor sensor layer, which lead to spectral distortions in PCDs. The incoming X-ray photons absorbed in the sensor layer generate electron-hole pairs. Electrons move towards the readout electronics due to a strong electric field between cathode and pixelated anodes. a) All the electrons are ideally collected at single anode. b) The electrons can be collected at two neighboring anodes, especially if they travel towards the edge of the anode. This phenomenon is called charge sharing. c) X-ray fluorescence that is a part of energy of the incoming photons produces subsequent electrons that are collected in two neighboring anodes. This phenomenon is called escape peaks. d) The incoming photons experience a scattering phenomenon and are deflected producing electron-hole pairs. As a result, the electrons are collected in the neighboring anode. The incoherent scattering is more severe with the higher probability and energy loss. e) The detector sometimes cannot discriminate two incident photons that come very close in space and time. As a result, two photons are detected as one photon with increased signal strength, leading to a decrease in count rate. This phenomenon is known as pulse pile-up. Figure motivated by the works of Ehn [76], Busi [59] and Flohr et al. [77].

sometime re-absorption. Consequently, the incident photons may be recorded at an energy  $E - E_{\text{fl}}$  in the adjacent pixel (K-escape), and the consequent peak in the energy spectrum is therefore named K-escape (fluorescence) peak. Thus, high-energy photons are again registered at lower energies resulting in a decrease in energy separation and also spatial resolution.

Charge sharing and K-escape occur nearby the pixel boundary. Increasing pixel size can decrease the contribution of these phenomena to the total detector response, and thereby improve energy separation. However, this also increases the photon flux causing overlapping of signals of two photons and being counted as one photon with higher energy. This effect is called pulse pile-up, which leads to non-linear counting rate and thereafter detector saturation [77]. The deposition of this interaction to the overall detector response can be decreased with designing smaller detector pixels, but, this in turn may increase charge sharing and K-escape contributions. Therefore, one should consider a trade-off between the pixel size and the contribution of these interactions when producing a PCD.

Charge carriers recorded by the collecting pixel can generate a signal in the neighbouring pixel, and this phenomenon is called weighting potential (WP) cross talk, which results in growth of the source spectrum at energies below 30 keV [78]. PCDs are also subject to another interactions like electronic noise [79] and Compton scattering of the incident photons within the crystal layer. They have noticeably lower contributions to the total signal than other interactions.

Non-uniformly distributed defects or impurities of crystal lattice may trap some of charge carriers [80], this effect is named incomplete charge collection (ICC). The ICC gives rise to the spectrum at energies above 60 keV [81]. The electrons and holes flow at drift velocities  $v_e = \mu_e E_e$  and  $v_h = \mu_h E_e$  into the cathode and pixelated anodes, respectively.  $E_e$  is the external electric field, and  $\mu_e$  and  $\mu_h$  represent the electron and hole drift mobilities, respectively. The holes with 80 cm<sup>2</sup>/V have significantly smaller drift mobility compared to electrons that have 1000 cm<sup>2</sup>/V [82]. Therefore, the slow holes are more severely trapped than electrons. Designing significantly smaller size of pixelated anodes than the crystal thickness can reduce the hole trapping and thereby the contribution of hole transport to the overall pulse. Therefore, this can reduce ICC [83]. Moreover, positive charges are accumulated due to the trapped holes that causes nonlinear oscillation of the external electric field over time and distortion of the charge collection rate. This phenomenon is called polarization which may eventually result in ICC [80, 84]. Polarization can create ring artifacts in image reconstruction at higher photon fluxes [77], and may rapidly reduce signal pulses above a certain high flux [85].

Charge sharing, WP cross talk, X-ray fluorescence (escape peaks), Compton scattering and electronic noise are the flux-independent interactions, for which the raw data is first corrected by the correction algorithm using an inverse detector response matrix  $\mathbf{M}_C$  of size  $N \times N$ , where  $N$  is the number of energy bins. The matrix  $\mathbf{I}_C$  for

corrected data is defined per pixel as [78]

$$\mathbf{I}_C = \mathbf{M}_C \mathbf{I}_R, \quad (3.2)$$

where matrix  $\mathbf{I}_R$  of size  $N \times J$  represent the raw data, and  $J$  is the number of detector pixels. The inverse detector response matrix is separated into the individual detector response matrices as follows [78]

$$\mathbf{M}_C = \mathbf{D}_{WP} \mathbf{D}_E \mathbf{D}_C, \quad (3.3)$$

where  $\mathbf{D}_{WP}$ ,  $\mathbf{D}_E$  and  $\mathbf{D}_C$  denote the individual detector response matrices for WP cross talk, Compton scattering and electronic noise, and charge sharing interactions, respectively. The distortion at low energies due to WP cross talk is firstly calculated for correction, while the charge sharing is finally corrected.

A Monte Carlo simulation is used to compute the total detector response matrix for each pixel's response to X-ray irradiation, being dependent on the incident photon energy and location of the energy deposition. This location is related to depth in the sensor based on the probability distribution function, which is defined by the reference LACs and taken from NIST database [6]. In the simulation, the escape peaks are firstly calculated with assumption that the fluorescence photons move in random direction and are absorbed at definite distance.  $\mathbf{D}_{WP}$ ,  $\mathbf{D}_E$  and  $\mathbf{D}_C$  detector response matrices are then determined individually based on 2-D histograms of actual and recorded photon energy. To compute charge sharing contribution, the excited electron cloud is considered as it is shared between two neighboring pixels based on a 1-D normal distribution that has the alignment with the detector array. The excited charge cloud can generate current in the neighboring pixels, and the contribution of WP cross talk is proportional to the quantity of current. The correction algorithm employs a model proposed in Ref. [86] to compute WP cross talk, in which the detector is viewed as the detector surfaces consisting of two infinite aligned sheets. The approach of reflected dipole layers (i.e. mirror charges) is used in the model using the assumption that WP cross talk consists of an infinite sum of the WP elementary functions for each reflected dipole layer which is uniformly placed based on the depth of the crystal layer.

The corrections mentioned above are followed by the correction for flux dependent interactions such as the pulse pileup and incomplete charge collection. The model developed by Plagnard [87] is used to rectify the pile-up effect. The pile-up by photon with energy  $E_n$  on other total energies  $E_x$  of the raw data (measured spectrum)  $I_R(E)$  contributes to the corresponding pile-up spectrum  $I_P(E_{nx})$ , which can be described for all the  $x$  values as follows [78, 87]

$$E_{nx} = E_n + E_x, \quad (3.4)$$

$$I_P(E_{nx}) = \frac{I_R(E_n)}{I_R(E)_{\max}} C_P I_R(E_x), \quad (3.5)$$

where  $C_P$  denotes a coefficient determining pile-up probability. The model uses the assumption that two photons with energies  $E_n$  and  $E_x$  in the raw data are captured

as one photon with energy  $E_{nx}$  in the pile-up spectrum. Dreier et al. [78] employs an automatic fitting technique to find  $C_P$  coefficient through the LACs of aluminum. The corrected spectrum  $I_C(E_n)$  for the energy bin  $n$  is obtained by subtraction of the pile-up spectrum from the raw data, and adding  $\sum_x I_P(E_{nx})$  (integrated over the whole  $x$  range) to the result as follows [78]

$$I_C(E) = I_R(E) - I_P(E), \quad (3.6)$$

$$I_C(E_n) = I_C(E_n) + \sum_x I_P(E_{nx}). \quad (3.7)$$

The same modelling is used for each increment of  $n$  from the initial to final values to retrieve the entire corrected spectrum. To correct these data distortions in the PCD we employ the correction algorithm developed by Dreier et al. [78], in which more details on the correction algorithm can be found. Fig. 3.10 presents an example of water's source spectrum before (raw) and after (corrected) applying spectral correction algorithm.

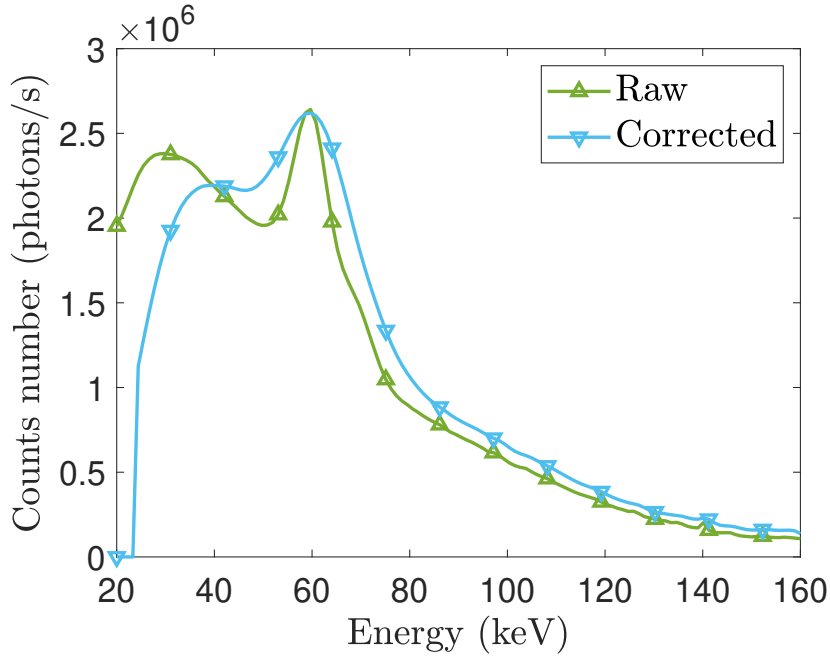


**Figure 3.10:** The raw and spectral corrected X-ray source spectra of water sample. The spectrum is corrected for spectral distortions in the PCD, using the correction algorithm. The number of counts per second is integrated over all detector pixels, captured by the MultiX ME100 PCD. The figure is adapted from the Paper A in the appendix section.

### 3.5 LAC extraction and setting low- and high-energy thresholds

Fig. 3.11 shows spectral LACs of water, obtained with the raw and corrected data, which are compared to the reference LACs. The correction algorithm significantly

corrects the LAC at the low energies, but cannot completely correct the distortions at lower and higher energies. This may be because of detector flux variation and photon starvation, i.e. complete attenuation of the radiation by the material, and pulse pile-up interaction at low and high energies [78]. Energy bins in which the LACs largely deviate from the expectation even after applying the correction algorithm are excluded in the later data processing by setting low- and high-energy thresholds,  $E_l$  and  $E_h$  that remain the same for all experimental samples.

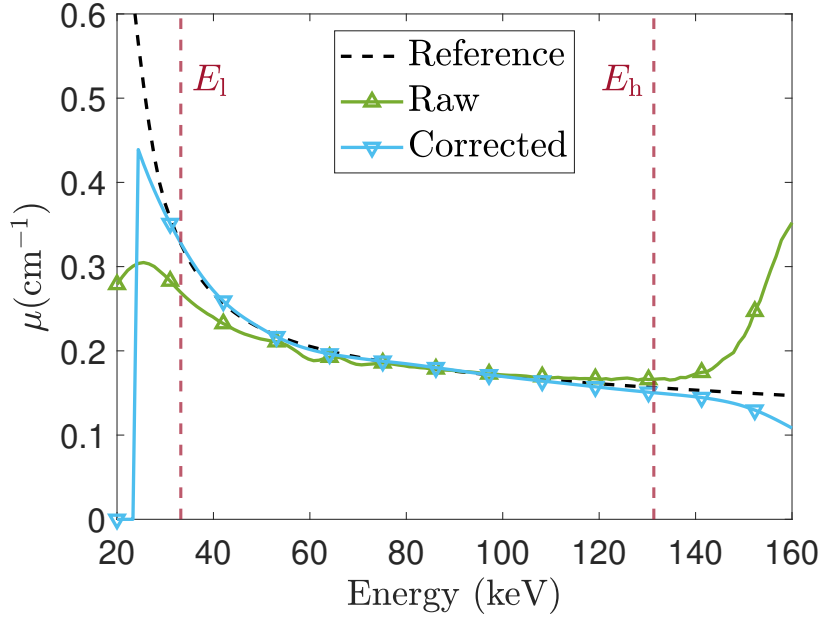


**Figure 3.11:** Energy resolved LACs calculated from the raw and corrected data, exemplified for water sample. The reference LACs are obtained from NIST database [6]. The vertical dash-dotted lines represent the low- and high-energy thresholds,  $E_l$  and  $E_h$ . The figure is adapted from the Paper D in the appendix section.

Fig. 3.12 shows how the mean LAC value of a segment in image reconstruction is extracted from the attenuation value histogram based on the normal distribution fitting, exemplified for water at the energy of 33.2 keV. A region of interest (ROI) in the reconstructed sample discretized into a certain number of image cells is manually segmented. This technique of the mean LAC extraction is used for all materials and energy bins.

### 3.6 Energy channels rebinning

After each projection data is corrected for the spectral distortions using the correction algorithm, the data is rebinned by merging photon counts between low- and high-energy thresholds. Spectral channelization, i.e. energy channels rebinning in spectral CT datasets plays an important role in achieving good accuracy in image reconstruction quality and material classification. The rebinning is performed to reduce the amount of

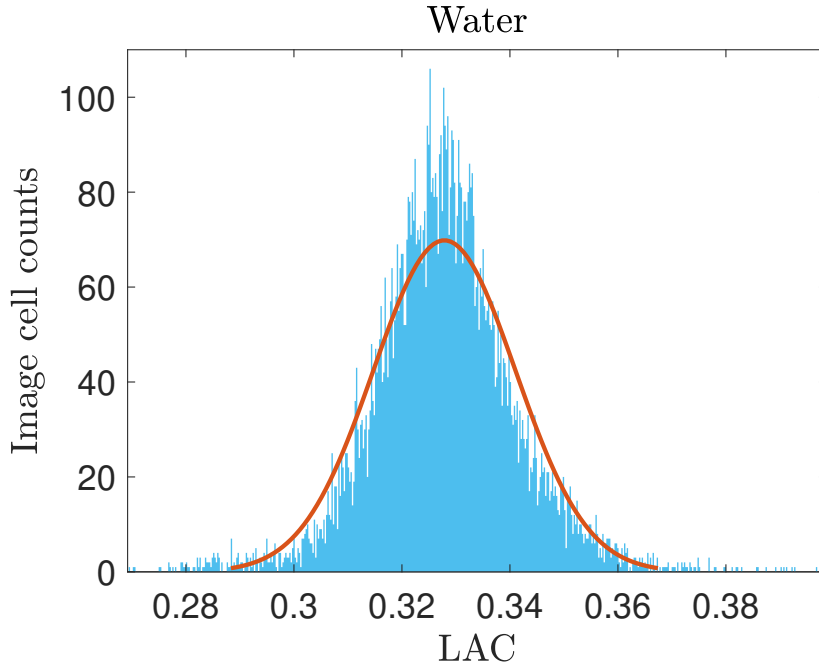


**Figure 3.12:** The LAC histogram of water shown with a Gaussian peak fit, obtained with the corrected data. The image cell counts indicate the number of cells within a region of interest (ROI) in the sample reconstruction, each having the respective LACs presented on the  $x$ -axis. The histogram corresponds to the X-ray energy of 33.2 keV. The reconstruction was performed with the simultaneous iterative reconstruction technique (SIRT) [75] from 360 projections. The figure is adapted from the Paper A in the appendix.

data and to accelerate the data processing. Hiring more energy bins results in longer computation time for individual reconstructions and thus for material classification. Furthermore, energy bins each with shorter width contain less photon counts, and thereby may increase noise artifacts because of low photon statistics and decrease the contrast to noise ratio [88]. On the other hand, the higher numbers of energy bins provide more spectral correlated information that can be useful for joint reconstruction algorithms, and therefore for classification methods. Spectral CT thus has a trade-off between using more energy bins and decreasing noise level. Therefore, we optimize the number of energy bins for a better classification performance in this thesis.

Dual-energy CT captures two various signals in the attenuation spectrum and can estimate both material features of electron density  $\rho_e$ , and effective atomic number  $Z_{\text{eff}}$ . However, the dual-energy detectors as illustrated in Fig. 3.13a possess overlapping low- and high-energy spectrums, and therefore the dual-energy CT systems have the limitation of poor energy separation. Dual-energy CT is done by a pair acquisitions using energy integrating detector, which captures two various source spectra based on different acceleration voltages or different filters in front of the source. Dual-energy CT is also performed by a simultaneous acquisition using dual-energy sandwich detector composed of two layers of scintillator-photodiode, which captures a single source spectrum. Fig. 3.13b and Fig. 3.13c illustrate the principles of the novel system-

independent materials classification methods based on spectral CT, which are presented in this thesis. To differ 2 energy bins from common overlapping dual-energies in dual-energy CT, we call them bi-energy bins in the remainder of the thesis. Non-overlapping bi-energy bins separated by a gap are optimized for the best classification performance in the Paper A in the appendix. This gap is illustrated with  $u$  and  $l$  boundaries in Fig. 3.13c. The optimization procedure is done by moving the gap from the lowest to the highest energy region of the source spectrum. Wang et al. [89, 90] showed that inserting a gap between low and high energy thresholds in energy discriminating PCDs improves material separability. Photons within this gap should either be excluded or counted independently to increase the separability accuracy. Therefore, the energy region corresponding to this gap was disregarded in the bi-energy bins approach in our work. In the Paper A, we also estimate classification performance with 6, 15, 30, 45 and 90 energy bins, which are uniformly distributed with same width between low- and high-energy thresholds.

There are a number of strategies of defining the width of rebinned energy bins. Based on simulation data acquired by a PCD with several energy bins, Wang et al. [91] investigated how to set the energy bin widths for obtaining optimal basis material decomposition. They tested five different strategies of energy bin rebinning to set energy bin thresholds for each; bins of equal width, bins of equal incoming photon counts, bins of equal incoming photon intensity, bins of equal photon counts and bins of equal photon intensity after transmitting through 3 cm of polymethyl methacrylate (PMMA). They demonstrated that employing energy bins with equal incoming photon counts gives the best performance in assessing the thickness of the two basis materials such as aluminum and PMMA.

Fig. 3.14 presents photon counts with respect to the energy values assigned to bi-, 15 and 90 energy bins for flat field spectra. The gap between low- and high-energies of bi-energy bins in which photon counts are discarded is important to avoid overlapping and achieve the improved classification performance. We uniformly allocate 15 and 90 energy bins with equal width within the detector's energy region. Usually, the energy thresholds can be manually set for most of the PCDs that have a large number of energy bins. In this work, using MultiX-ME100 PCD we acquire the data with the largest number of energy bins, and then merge them into fewer bins. Merging counts for all multiple energy bins approaches is performed by summing the incident photon counts  $I^{E_c}$  detected in energy channels  $E_c$  as follows

$$I^{E'_k} = \sum_{c=1}^C I^{E_c}, \quad k = 1, 2, \dots, K, \quad (3.8)$$

where  $C$  is the total number of energy channels that are rebinned between the two corresponding neighboring thresholds,  $K$  is the number of rebinned energy bins. We assign energy values to the new energy bins by taking the weighted mean between the

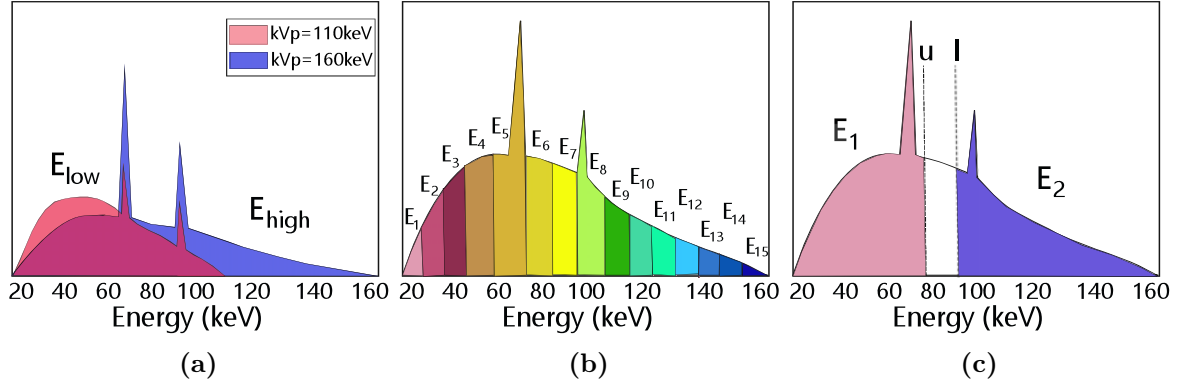


**Figure 3.13:** Illustration of the dual-energy CT, and spectral CT with 15 and bi-energy bins. (a) In dual-energy X-ray CT, the sample attenuation is extracted at overlapping low- and high energies with two various spectra, which results in a decrease in the classification performance [67, 69]. (b) In spectral X-ray CT, the sample attenuation is extracted at multiple energy bins with PCDs through a simultaneous data acquisition. (c) In the bi-energy bins approach to spectral X-ray CT, the sample attenuation is extracted at non-overlapping low- and high-energies with PCDs through a simultaneous acquisition. How the upper (u) and lower (l) thresholds of low- and high-energies separated by the gap is set is presented in each Paper in the appendix. The figures are adapted from the Paper A in the appendix section.

two corresponding neighboring thresholds as

$$E'_k = \frac{\sum_{c=1}^C I_0^{E_c} E_c}{\sum_{c=1}^C I_0^{E_c}}, \quad k = 1, 2, \dots, K, \quad (3.9)$$

where  $E'_k$  is the new assigned energy value, and  $I_0^{E_c}$  represents the flat-field measurement (i.e. the projection data without the sample being placed) corresponding to the energy value  $E_c$ . In our work, we do not employ the energy values in Eq. 3.9 assigned to the new energy bins for estimating classification performance, instead we use the calibration steps to register the energy-dependent components in the decomposed LACs. This allows us not to rely on how the energy values are accurately assigned to the rebinned energy bins, especially in cases of bi-energy bins with relatively wider energy width.



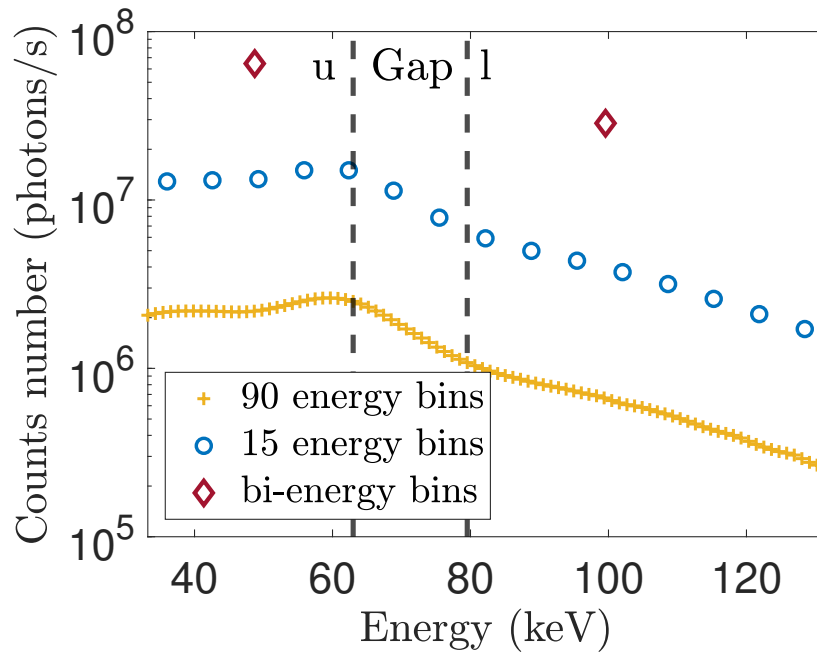


**Figure 3.14:** Photon counts in the flat field spectra for bi-, 15 and 90 energy bins approaches. The vertical black dash-dotted lines highlight the gap between low- and high-energies of bi-energy bins. In this work, the energy region falling into this gap is discarded in bi-energy bins approach for a better classification performance.  $u$  and  $l$  denote the upper and lower thresholds of low- and high-energies of bi-energy bins, respectively. The low and high boundaries of the gap are specified in each Paper in the appendix section. Note logarithmic scale on the  $y$ -axis. The figure is adapted from the Paper A in the appendix section.

# Joint reconstruction 4

---

This chapter describes the fundamentals of tomographic reconstruction, and the concepts of channel-by-channel and joint reconstruction algorithms, whose contributions to improving material classification performance and the robustness to noisy conditions are tested against each other in this thesis.

## 4.1 Fundamentals of tomographic reconstruction

### 4.1.1 Projection data

If we divide both sides of Eq. 2.1, i.e. the Beer Lambert law for multi-energy bins, by  $I_0$  and take the negative logarithm of the quantity, we obtain the projection integral or line integral of  $\mu(x, y)$  at projection angle,  $\theta$  from the measurements as

$$p(r, \theta) = -\ln \left( \frac{I(r, \theta)}{I_0} \right) = \int_0^d \mu(x, y) ds, \quad (4.1)$$

where  $r$  describes the axis parallel to detector, referred to scanning position,  $d$  is thickness of the sample along the ray at scanning position  $r$ . Tomographic measurement for 2D parallel beam is illustrated in Fig. 4.1. The collection of line integrals over all projection angles  $\theta$  is the Radon transform of  $\mu(x, y)$ . The Radon transform is also called the projection data or *sinogram*.

Radon transform maps  $\mu$  to  $p$  as the integral of  $\mu$  along the scanning position  $r$ , which can be defined as  $r = x \cos \theta + y \sin \theta$ . Here,  $x$  and  $y$  represent the spatial coordinates centered at the rotating axis.

In practice the data are collected as a discrete sampling of the continuous model, for which schematic is shown in Fig. 4.2. The projection data are represented as a vector  $\mathbf{p} \in \mathbb{R}^I$ , where  $I$  is the total number of rays for all projection angles, i.e. the number of detector pixels times the number of projection angles. Consider a cross section of the sample discretized into  $J$  image cells, for which the reconstruction unknowns are described as a vector  $\boldsymbol{\mu} \in \mathbb{R}^J$ . We can model the projection data  $p_i$  for each ray  $i$  as

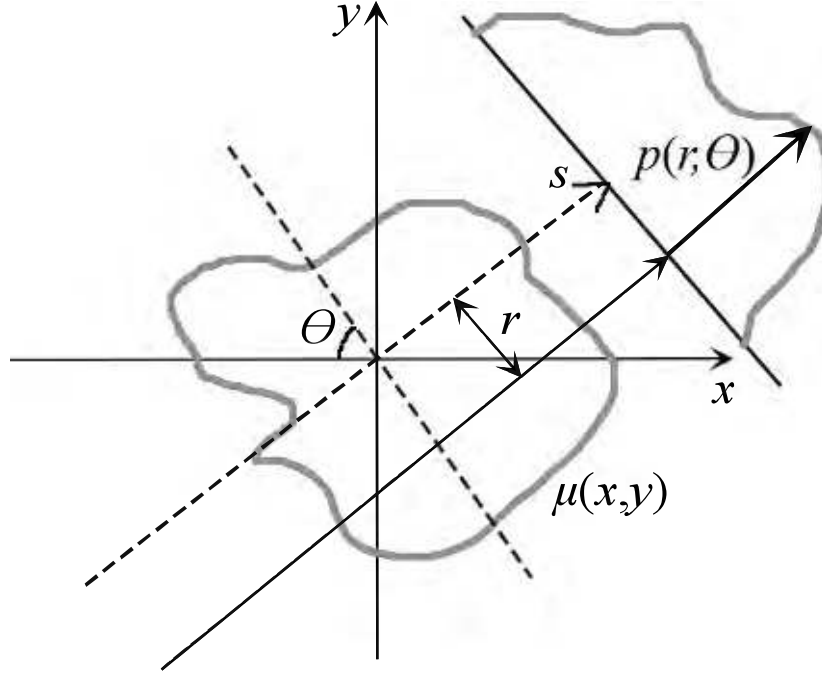


**Figure 4.1:** Schematic of tomographic measurements or the Radon transform in 2D. An X-ray beam travels in a path defined by scanning position  $r$  and rotation angle  $\theta$ . The measurement at the detector is described with the line integral  $p(r, \theta)$  of  $\mu(x, y)$  along  $r$ , which is referred to the projection data.

the weighted sum of the cell values  $\mu_j$  along the ray, which is determined as

$$p_i = \sum_{j=1}^J a_{ij} \mu_j, \quad (4.2)$$

where  $i = 1, 2, \dots, I$ , and  $j = 1, 2, \dots, J$ , and  $a_{ij}$  is the weight that describes how  $j_{\text{th}}$  cell contributes to the  $i_{\text{th}}$  measurement. For linear projection model, the weight can be set as the line segment length of the cell  $j$  intersected with the ray  $i$ , as illustrated in Fig. 4.2.

Expressing all projections as column vector

$$\mathbf{p} = (p_1, p_2, \dots, p_I)^T, \quad (4.3)$$

and also expressing the LACs that are to be reconstructed as a column vector

$$\boldsymbol{\mu} = (\mu_1, \mu_2, \dots, \mu_J)^T, \quad (4.4)$$

the weightings can thus be written as an  $I \times J$  matrix

$$\mathbf{A} = \begin{pmatrix} a_{11} & a_{12} & \dots & a_{1J} \\ a_{21} & \cdot & & a_{2J} \\ \vdots & & \cdot & \vdots \\ a_{I1} & & & a_{IJ} \end{pmatrix}, \quad (4.5)$$

such that we can construct the full set of equations for all the ray integrals in a vectorized form as

$$\mathbf{p} = \mathbf{A}\boldsymbol{\mu}, \quad (4.6)$$

where  $\mathbf{A} \in \mathbb{R}^{I \times J}$  represents a system matrix with elements  $a_{ij}$ , and  $\mathbf{p}$  is a vector denoting the projection data. The multiplication  $\mathbf{A}\boldsymbol{\mu}$  is known as the *forward projection* of  $\boldsymbol{\mu}$ . The aim of tomographic reconstruction is to compute the unknown LACs  $\boldsymbol{\mu}$  from the projection data  $\mathbf{p}$ .

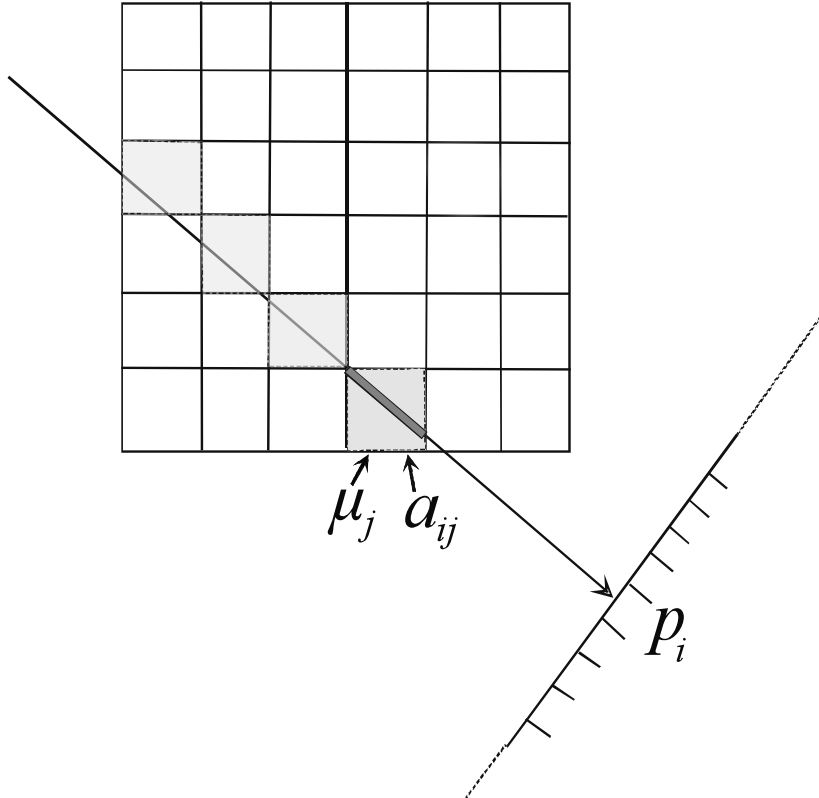


**Figure 4.2:** Illustration of the 2D discrete linear projection model.  $\mu_j$  denotes LAC corresponding to cell  $j$ , and  $p_i$  represents the measurement data corresponding to the  $i$ th ray. The contribution of  $\mu_j$  to  $p_i$  is described by  $a_{ij}\mu_j$ , where  $a_{ij}$  can be defined by the line segment length bounded by the intersection of the ray  $i$  and the pixel  $j$  (indicated in bold). The ray travels through the shaded cells where the weights are positive. Thus, the projection for the  $i$ th ray can be calculated by a weighted sum of cell values.

An example of a sinogram and the respective image reconstruction is presented in Fig. 4.3.

### 4.1.2 Conventional channel-by-channel reconstructions

One type of reconstruction algorithms rely on inverting the Radon transform Eq. 4.1 to analytically express  $\mu(x, y)$ , which is called the analytical reconstruction algorithms. A

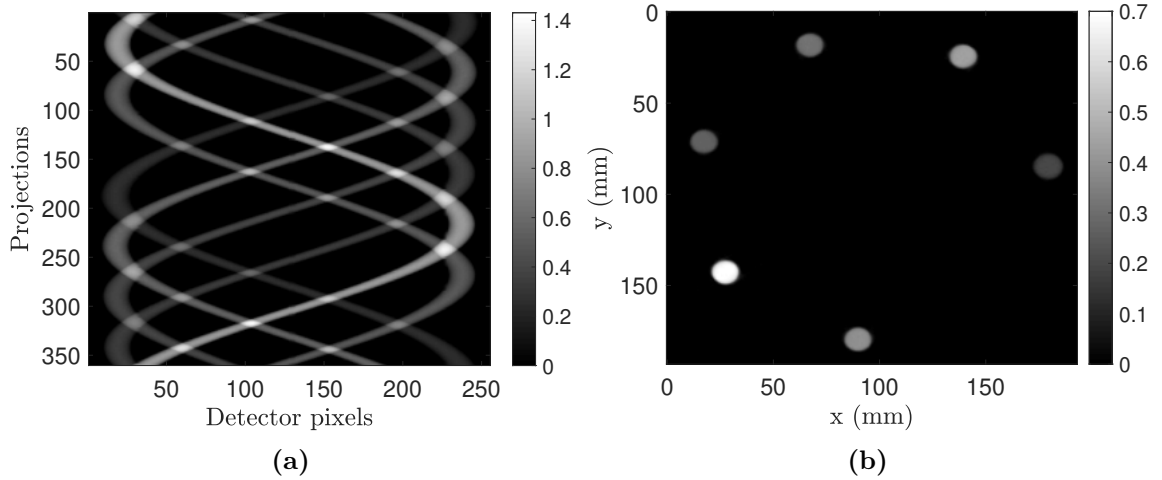


**Figure 4.3:** Sinogram (a) and the corresponding image reconstruction (b). 2D reconstruction was done with the SIRT from 360 projections at the energy of 61.9 keV. The gray scale bars denote the LACs with the unit of  $\text{cm}^{-1}$ . The figure (b) is adapted from the Paper D in the appendix section.

common analytical reconstruction algorithm is filtered backprojection (FBP) [92]. The advantage of the FBP algorithm is that it is computationally efficient and the fastest option, because it is only composed of a convolution operation and an integration operation. Another reason is the simplicity of the reconstruction approach, with fewer parameters to adjust. However, the analytical algorithms rely on the assumption that an infinite number of projections is available. When only a limited number of projections or noisy projections are measured, the reconstructed image will have different artifacts. Another type of reconstruction algorithm is named algebraic (or iterative) reconstruction, which relies on inverting the discrete model Eq. 4.6. Compared to the analytical algorithms, algebraic algorithms tend to handle better for cases where limited projection data such as few or noisy projections are available. This is because the algebraic reconstruction problem is discrete in nature being not based on the assumption of an infinite number of projections available. The unknown  $\boldsymbol{\mu}$  is often calculated by iteratively minimizing the data fidelity term  $\mathcal{D}(\mathbf{A}\boldsymbol{\mu}, \mathbf{p})$  that converges to the desired reconstruction as

$$\boldsymbol{\mu}^* = \arg \min_{\boldsymbol{\mu} \geq 0} \mathcal{D}(\mathbf{A}\boldsymbol{\mu}, \mathbf{p}). \quad (4.7)$$

The data fidelity term equals the square of reprojection error that is  $l_2$  norm of the difference between the acquired  $\mathbf{p}$  and the reprojected data  $\mathbf{A}\boldsymbol{\mu}$

$$\mathcal{D}(\mathbf{A}\boldsymbol{\mu}, \mathbf{p}) = \|\mathbf{A}\boldsymbol{\mu} - \mathbf{p}\|_2^2. \quad (4.8)$$

Algebraic reconstruction technique (ART) [93] and simultaneous iterative reconstruction technique (SIRT) [75] can be used to solve the minimization problem of Eq. 4.7.

More details on the fundamentals of conventional analytical and iterative reconstruction algorithms may be found in the books [94–96].

## 4.2 The state-of-the-art joint reconstruction

### 4.2.1 State-of-the-art literature review

Many investigations were carried out in improving the reconstruction results either in CT Systems or image processing domain. The total-variation (TV) regularization presented by Rudin, Osher, and Fatemi [97] has been widely employed to effectively suppress noise in different image processing tasks. TV appeared to preserve sharp discontinuities in the edge locations by encouraging sparse gradients of the images. Different TV regularization methods have been applied to CT reconstructions from few projections and limited angles [98, 99]. For CT systems, Sidky et al. (2006) [100] applied a TV algorithm to the reconstruction from few projections and limited angles, and presented that the TV can perform reconstructions more accurately than the conventional reconstruction algorithms from such sparse data.

Blomgren and Chan (1998) [101] first proposed vectorial total variation (VTV) for image processing tasks, which extends the conventional scalar TV to a multi-dimensional frame. VTV considers dependency both in the spatial (image cell) and spectral (energy or color) dimensions. The energy or color channel coupling can be formulated in several forms. For color image denoising problems, Holt (2014) [102] introduced channel coupling based on Total Nuclear Variation (TNV), which employs the nuclear norm defined as the sum of singular values of the Jacobian matrix [103]. Holt presented that TNV results in encouraging the image gradients along color channels dimension to be parallel at common edge positions, and found that the restoration of color images with TNV norm is more efficient than other VTV norms. Thus, TNV takes advantage of multi-channel images that share structural similarity between different channels. Based on synthesized simulation data in Spectral CT, Rigie et al. (2015) [104] implemented TNV in restoring tissue density maps, and found that TNV removes the edge blurring more efficiently than channel-by-channel TV regularization. They found that TNV is more robust to undesired noise transfer over energy channels, each with various noise levels.

Using experimental data, Rigie et al. (2017) [105] applied VTV regularizations such as the nuclear norm and the Frobenius norm, and TV norm to dual-energy CT. They showed that the TNV norm suppresses noise more efficiently than the other norms. Zhong et al. [106] joined two different imaging modalities to obtain improved tomographic reconstruction based on TNV norm, when the number of tilt angles is limited, and noise levels are high. These modalities were energy-dispersive X-ray spectroscopy (EDS), and high angle annular dark field scanning transmission microscopy (HAADF-STEM), which give multiple element-specific reconstructions and single-channel reconstruction with mixed properties of chemical elements, respectively. Compared to the SIRT and TV reconstruction, the TNV exhibited noticeably more enhancement in the element-specific reconstruction from EDS data by promoting the images to possess similar structure information with

the HAADF-STEM reconstruction.

Miyata et al. [107] proposed using a  $L_\infty$  norm for estimating the most differing color channels along the particular direction such that the maximum gradients are summed based on  $l_1$  norm over all the directions and over all the cell locations for minimization problem. For color image denoising tasks, they showed that the  $L_\infty$ -VTV norm can effectively penalize the detected outliers in the sense of gradient magnitudes, which are likely to be an artifact or a noise. Therefore,  $L_\infty$  norm can lead to strong coupling between color channels. For image denoising problems, Duran et al. [108] investigated the different VTV methods, which extend the conventional TV to multi-channel images. They applied different collaborative norms to a 3D matrix of the discrete gradients of the multi-channel images, whose dimensions correspond to the color channels, the spatial gradients in  $x$  and  $y$ -directions, and the image cells. They showed that the regularizations based on  $L_\infty$ -VTV and TNV norms remove color artifacts more strongly than the other VTV norms, and the effectiveness of particular norm depends on the experimental data collected from particular imaging modality.

Spectral CT can be considered as CT with multiple "color" channels, which we refer to as energy bins. For practical applications, with spectral CT we should consider two challenges. Firstly, rapid scanning requires few projections that may lead to reduced reconstruction quality and thereby to reduced classification performance. Secondly, spectral CT hires many energy bins each with reduced photon counts that decrease signal to noise ratio (SNR) in each bin. To address these challenges we aim to use the joint reconstruction algorithms with different VTV regularizations such as  $L_\infty$ -norm-based VTV and TNV.  $L_\infty$ -VTV is implemented and explored in spectral CT for the first time to our knowledge. To increase SNRs we consider energy bin rebinning described in the Section 3.6.

The joint reconstruction algorithms introduced in this work can be straightforwardly implemented in three-dimensional (3D) spectral CT imaging, which can be a valuable quantitative instrument for studying complex relations between the microstructure and features of materials in materials science [109, 110]. Therefore, the enhancement of material's  $(\rho_e, Z_{\text{eff}})$  estimation based on better image reconstruction can be valuable for exploring the complex microstructure of materials. The reconstruction algorithms developed can be adopted for the different spectral imaging modalities such as visible light, electron or neutron tomography.

### 4.2.2 TNV joint reconstruction

Consider a sample discretized into  $J$  cells in a 2D volume space. In spectral CT, we simultaneously measure the projection data for each energy bin, with the total number of energy bins, denoted  $N$ . Thus, the input data consisting of all projection data ( $N$  acquired sinograms) can be expressed as  $\mathbf{p}^1, \mathbf{p}^2, \dots, \mathbf{p}^N \in \mathbb{R}^I$ , where  $I$  is the total number of rays for all projection angles, i.e. the number of detector pixels times the number of projection angles. The reconstruction unknowns for the sample,

i.e. the LACs, reconstructed from  $N$  energy-resolved sinograms are expressed as  $\boldsymbol{\mu}^1, \boldsymbol{\mu}^2, \dots, \boldsymbol{\mu}^N \in \mathbb{R}^J$ , where  $J$  is the number of cells per each image.

The acquired X-ray counts are proportional to the linear projection of the reconstructed LACs for each image cell in each energy bin measurement. The projection data  $p_i^n$  for each ray  $i$  corresponding to each energy bin  $n$  can be modelled as the weighted sum of the cell values  $\mu_j^n$  along the ray, by the system of linear equations as

$$\begin{cases} p_i^1 = \sum_{j=1}^J a_{ij}^1 \mu_j^1 \\ p_i^2 = \sum_{j=1}^J a_{ij}^2 \mu_j^2 \\ \vdots \\ p_i^N = \sum_{j=1}^J a_{ij}^N \mu_j^N \end{cases}, \quad (4.9)$$

where  $i = 1, 2, \dots, I$ ,  $j = 1, 2, \dots, J$ , and  $n = 1, 2, \dots, N$ , and  $a_{ij}$  denotes the weight factor that describes how  $j_{\text{th}}$  cell contributes to the  $i_{\text{th}}$  ray integral. For linear integral model, the weight can be determined by the line segment length of the  $j_{\text{th}}$  cell intersected by the  $i_{\text{th}}$  ray integral, as illustrated in Fig. 4.2. We assume that the weights are similar for all energy bins because the sample is simultaneously scanned with a single source spectrum in spectral CT measurement,  $a_{ij}^1 = a_{ij}^2 = \dots = a_{ij}^N$ . Each detector pixel location  $i$  corresponding to a ray  $i$  is defined by the beam location ( $r$ ) and the projection angle ( $\theta$ ) of the sample, as illustrated in Fig. 4.1.

The full set of equations for all rays in each energy bin measurement can thus be written in a vector form as

$$\mathbf{p}^n = \mathbf{A}\boldsymbol{\mu}^n, \quad (4.10)$$

where  $\mathbf{p}^n = (p_1^n, p_2^n, \dots, p_I^n)^T$  and  $\boldsymbol{\mu}^n = (\mu_1^n, \mu_2^n, \dots, \mu_J^n)^T$  are the constructed column vectors of all projection data and all reconstruction unknowns corresponding to  $n_{\text{th}}$  energy bin. The matrix  $\mathbf{A} \in \mathbb{R}^{I \times J}$  is referred to a system matrix with elements  $a_{ij}$ , which are similar for each energy bin measurement, expressed as an  $I \times J$  matrix in Eq. 4.5.

In this thesis we concentrate on iterative reconstruction algorithms for their ability of applying regularization. The iterative algorithm minimizes the reprojection error (i.e. the difference between the synthesized and the measured projection data) for each energy bin to solve the inverse problems, based on the squared  $l_2$  norm of the reprojection error as

$$\begin{cases} \boldsymbol{\mu}^{1*} = \arg \min_{\boldsymbol{\mu}^1 \geq 0} \frac{1}{2} \|\mathbf{A}\boldsymbol{\mu}^1 - \mathbf{p}^1\|_2^2 \\ \boldsymbol{\mu}^{2*} = \arg \min_{\boldsymbol{\mu}^2 \geq 0} \frac{1}{2} \|\mathbf{A}\boldsymbol{\mu}^2 - \mathbf{p}^2\|_2^2 \\ \vdots \\ \boldsymbol{\mu}^{N*} = \arg \min_{\boldsymbol{\mu}^N \geq 0} \frac{1}{2} \|\mathbf{A}\boldsymbol{\mu}^N - \mathbf{p}^N\|_2^2 \end{cases}. \quad (4.11)$$



Here, we impose the non-negativity constraint on  $\boldsymbol{\mu}$ , as the LACs are expected to be non-negative.

If the projection data are highly noisy or obtained from a limited number of projection angles, adding a regularization term to the above data fidelity term can improve reconstruction results, leading to a new minimization problem. TV-regularized reconstruction is performed independently for each energy bin  $n = 1, 2, \dots, N$ , by solving the following minimization problem

$$\begin{cases} \boldsymbol{\mu}^{1*} = \arg \min_{\boldsymbol{\mu}^1 \geq 0} \frac{\lambda}{2} \|\mathbf{A}\boldsymbol{\mu}^1 - \mathbf{p}^1\|_2^2 + \mathcal{R}_{\text{TV}}(\boldsymbol{\mu}^1) \\ \boldsymbol{\mu}^{2*} = \arg \min_{\boldsymbol{\mu}^2 \geq 0} \frac{\lambda}{2} \|\mathbf{A}\boldsymbol{\mu}^2 - \mathbf{p}^2\|_2^2 + \mathcal{R}_{\text{TV}}(\boldsymbol{\mu}^2) \\ \vdots \\ \boldsymbol{\mu}^{N*} = \arg \min_{\boldsymbol{\mu}^N \geq 0} \frac{\lambda}{2} \|\mathbf{A}\boldsymbol{\mu}^N - \mathbf{p}^N\|_2^2 + \mathcal{R}_{\text{TV}}(\boldsymbol{\mu}^N) \end{cases}, \quad (4.12)$$

where  $\lambda$  is the weighting parameter between the data fidelity term and regularization term, defining the strength of the regularization. The regularization term,  $\text{TV}(\boldsymbol{\mu}^n)$  imposes a prior information on the solution like the smoothness on the reconstruction, which can be defined as

$$\mathcal{R}_{\text{TV}}(\boldsymbol{\mu}^n) = \sum_{j=1}^J \|\nabla(\mu_j^n)\|, \quad (4.13)$$

where

$$\nabla(\mu_j^n) = \begin{pmatrix} \frac{\partial \mu_j^n}{\partial x} \\ \frac{\partial \mu_j^n}{\partial y} \end{pmatrix}, \quad (4.14)$$

which discretely approximates the gradient for the  $j$ th cell corresponding to energy bin  $n$ .  $\frac{\partial \mu_j^n}{\partial x}$  and  $\frac{\partial \mu_j^n}{\partial y}$  are the gradients in the horizontal and vertical directions, respectively, computing the forward difference between cells.  $\|\cdot\|$  is typically selected as  $l_1$ -norm or  $l_2$ -norm. TV with  $l_1$ -norm is called an anisotropic variant of TV, which tends to preserve edges in horizontal and vertical directions, however the diagonal edges may be blurred. In contrast, using  $l_2$ -norm leads to an isotropic variant of TV, which is rotationally invariant. In our work we consider  $l_2$ -norm TV that is better suited for our experimental dataset. This can be expressed as

$$\mathcal{R}_{\text{TV}}(\boldsymbol{\mu}^n) = \sum_{j=1}^J \sqrt{\left(\frac{\partial \mu_j^n}{\partial x}\right)^2 + \left(\frac{\partial \mu_j^n}{\partial y}\right)^2}. \quad (4.15)$$

Thus, TV regularization does not take advantage of correlations between the images from different energy bins.

Now, we describe extending the TV to a vectorial TV (VTV), which couples the image gradients from different energy bins based on certain joint penalized model. The VTV can provide a more robust regularization. One technique to employ the inter-bin correlations of the image gradients is Total Nuclear Variation (TNV) [104, 108]

regularization that is common to all energy bins used. TNV couples the images from the different energy bins based on the sum of nuclear norm of the Jacobian matrix over all image cells

$$\mathcal{R}_{\text{TNV}}(\boldsymbol{\mu}^1, \boldsymbol{\mu}^2, \dots, \boldsymbol{\mu}^N) = \sum_{j=1}^J \|\mathbf{J}(\boldsymbol{\mu}^1, \boldsymbol{\mu}^2, \dots, \boldsymbol{\mu}^N)_j\|_*, \quad (4.16)$$

where  $\mathbf{J}(\boldsymbol{\mu}^1, \boldsymbol{\mu}^2, \dots, \boldsymbol{\mu}^N)_j$  denotes the Jacobian matrix at image cell  $j$ , which is composed of the gradient vectors of the different energy bins, defined as

$$\mathbf{J}(\boldsymbol{\mu}^1, \boldsymbol{\mu}^2, \dots, \boldsymbol{\mu}^N)_j = \begin{pmatrix} \frac{\partial \mu_j^1}{\partial x} & \frac{\partial \mu_j^1}{\partial y} \\ \frac{\partial \mu_j^2}{\partial x} & \frac{\partial \mu_j^2}{\partial y} \\ \vdots & \vdots \\ \frac{\partial \mu_j^N}{\partial x} & \frac{\partial \mu_j^N}{\partial y} \end{pmatrix}, \quad (4.17)$$

and the nuclear norm  $\|\cdot\|_*$  of the Jacobian matrix is determined by  $l_1$ -norm (i.e. the sum) of its singular values. For an image from single energy bin, the TNV transforms into the isotropic TV.

The nuclear norm promotes sparsity in the singular values of the Jacobian matrix [111, 112]. The gradient vectors of the different energy bins at common (coinciding) edge locations are typically supposed to be parallel or anti-parallel. A linear dependence between parallel or anti-parallel gradient orientations leads to rank one of the Jacobian, and therefore to just one non-zero singular value [104]. In contrast, the gradients with the different orientations result in all singular values being non-zero. Thus, promoting sparsity in the singular values of the Jacobian is equivalent to promoting gradient directions at common edges, during image reconstruction. Fig. 4.4 illustrates the concept of TNV for the images from three energy bins at certain image cell.

To jointly regularize spectral CT reconstructions we thus minimize the data fidelity terms of each energy bin together with a TNV regularization term as

$$\begin{aligned} \boldsymbol{\mu}^{1*}, \boldsymbol{\mu}^{2*}, \dots, \boldsymbol{\mu}^{N*} = \arg \min_{\boldsymbol{\mu}^1, \boldsymbol{\mu}^2, \dots, \boldsymbol{\mu}^N \geq 0} & \frac{\lambda}{2} \|\mathbf{A}\boldsymbol{\mu}^1 - \mathbf{p}^1\|_2^2 + \frac{\lambda}{2} \|\mathbf{A}\boldsymbol{\mu}^2 - \mathbf{p}^2\|_2^2 \\ & + \dots + \frac{\lambda}{2} \|\mathbf{A}\boldsymbol{\mu}^N - \mathbf{p}^N\|_2^2 + \mathcal{R}_{\text{TNV}}(\boldsymbol{\mu}^1, \boldsymbol{\mu}^2, \dots, \boldsymbol{\mu}^N), \end{aligned} \quad (4.18)$$

where  $\lambda$  is the weighting parameter defining the strength of the TNV regularization.

### 4.2.3 $L_\infty$ -VTV joint reconstruction

Considering inter channel dependency plays a significant role in obtaining effective VTV regularization. On the other hand, we can assume that the attenuation values at all the energy channels are likely to change simultaneously along particular direction at

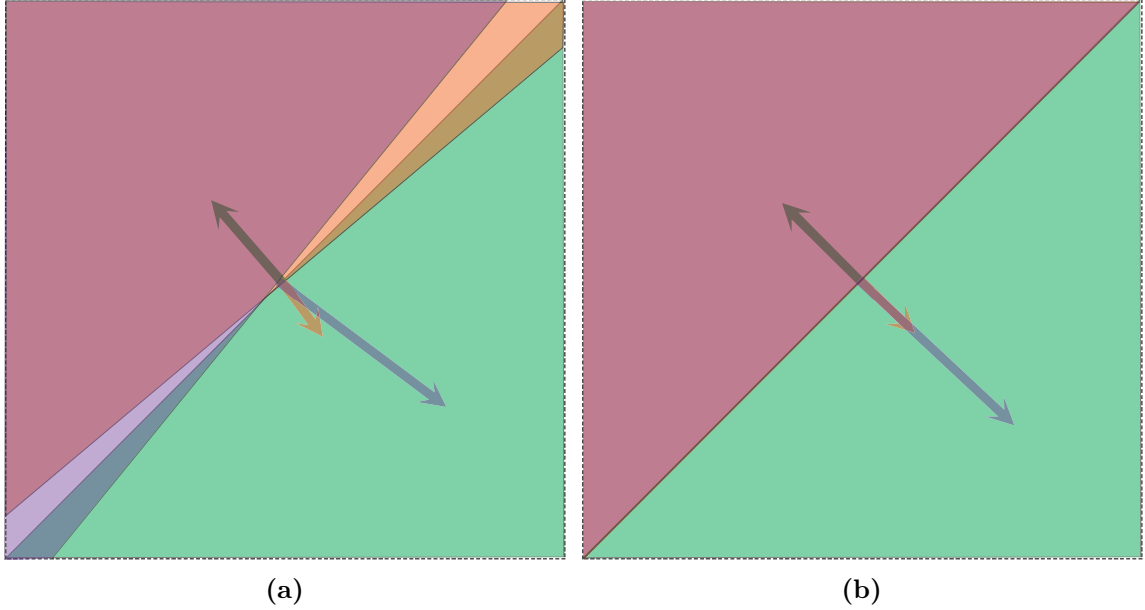


**Figure 4.4:** Illustration of TNV. (a) The gradients of the images from three energy bins at the particular image cell. (b) During image reconstruction, TNV promotes the gradients of all the energy bins to share a common orientation at common edge locations. Figures inspired by the works on TNV in Refs. [104, 106].

a particular edge location. If this assumption is violated, this distinction likely results from a noise or an artifact. Based on this assumption, we use  $L_\infty$  norm to estimate the maximum of gradients along the energy bins dimension at the same direction. The  $L_\infty$ -VTV regularization term is defined as the sum (based on  $l_1$  norm) of the maximum of gradients over all directions and all cell locations.

TNV approach forces the gradient vectors of all energy bins to be aligned parallel to each other. However, in practice some outliers in the gradient magnitudes may decrease the performance of TNV regularization. To overcome this drawback of TNV, we propose to employ  $L_\infty$ -VTV joint regularization, which can be defined based on collaborative norms [108] as

$$\mathcal{R}_{\text{VTV}}^{\text{L}_\infty}(\boldsymbol{\mu}^1, \boldsymbol{\mu}^2, \dots, \boldsymbol{\mu}^N) = \|\mathbf{D}\boldsymbol{\mu}^1, \mathbf{D}\boldsymbol{\mu}^2, \dots, \mathbf{D}\boldsymbol{\mu}^N\|_{\infty,1,1}, \quad (4.19)$$

where  $\mathbf{D}$  is a linear operator for the discrete gradient of the image such that  $\mathbf{D}\boldsymbol{\mu}^n \in \mathbb{R}^{N \times C \times J}$  forms a 3D matrix, with  $C$  being the number of spatial gradients. Usually,  $C = 2$  and it considers the gradients in  $x$ - and  $y$ -axis. We use the notation of collaborative norm  $\|\cdot\|_{\infty,1,1}$ , being applied to the discrete gradient of the multi-channel images. The collaborative norm consists of applying  $L_\infty$  (infinity) norm along the energy bins ( $N$ ) dimension, then  $l_1$ -norm along the spatial gradients ( $C$ ) dimension of the remaining 2D matrix, and, eventually,  $l_1$ -norm along the spatial cell locations ( $J$ ) dimension of the remaining vector [108].  $(\mathbf{D}\boldsymbol{\mu}^n)_{n,c,j}$  represents the gradient of the image  $\boldsymbol{\mu}^n$  at the pixel  $j$  with respect to  $x$ - axis when  $c = 1$  or  $y$  axis when  $c = 2$ , with corresponding norms being applied along each dimension. Thus,  $L_\infty$ -VTV can be

expressed based on the maximum of gradients along energy bins dimension, which are summed over image cells dimension as follows

$$\mathcal{R}_{\text{VTV}}^{\text{L}\infty}(\boldsymbol{\mu}^1, \boldsymbol{\mu}^2, \dots, \boldsymbol{\mu}^N) = \sum_{j=1}^J \left( \max_{1 \leq n \leq N} \left| \frac{\partial \mu_j^n}{\partial x} \right| + \max_{1 \leq n \leq N} \left| \frac{\partial \mu_j^n}{\partial y} \right| \right). \quad (4.20)$$

The  $\text{L}\infty$ -VTV norm correlates the image gradients strongly along the energy bins dimension, while disallowing some outliers in the gradient magnitudes. This property for each reconstruction algorithm presented above is investigated in the Paper B in the appendix.

We can thus write the minimization problem for  $\text{L}\infty$ -VTV joint regularization, consisting of the data fidelity terms of each energy bin and the regularization term, as follows

$$\begin{aligned} \boldsymbol{\mu}^{1*}, \boldsymbol{\mu}^{2*}, \dots, \boldsymbol{\mu}^{N*} = \arg \min_{\boldsymbol{\mu}^1, \boldsymbol{\mu}^2, \dots, \boldsymbol{\mu}^N \geq 0} & \frac{\lambda}{2} \|\mathbf{A}\boldsymbol{\mu}^1 - \mathbf{p}^1\|_2^2 + \frac{\lambda}{2} \|\mathbf{A}\boldsymbol{\mu}^2 - \mathbf{p}^2\|_2^2 \\ & + \dots + \frac{\lambda}{2} \|\mathbf{A}\boldsymbol{\mu}^N - \mathbf{p}^N\|_2^2 + \mathcal{R}_{\text{VTV}}^{\text{L}\infty}(\boldsymbol{\mu}^1, \boldsymbol{\mu}^2, \dots, \boldsymbol{\mu}^N). \end{aligned} \quad (4.21)$$

The regularization is always a trade-off between improvement in image visibility and edge blurring, which may lead to undesirable effects in the reconstruction. Therefore, the value of weighting parameter  $\lambda$  should be attentively set such that we can have an accurate reconstruction. A very small value may give an over-regularized image with blurred edges, whereas a very large value may give poor regularization effects. Smoothing with the optimal  $\lambda$  suppresses artifacts without significantly blurring a sharp edge, preserving the details of a border of an area, and has the capability to sharpen blurred edges caused by the limited number of projections and noise.

Fig. 4.5 illustrates the notion of  $\text{L}\infty$ -VTV for the images from three energy bins corresponding to a specific image cell.

In the Paper B in the appendix, we show that  $\text{L}\infty$ -VTV outperforms TNV of another state-of-the-art joint reconstruction, and TV of channel-by-channel reconstruction for classification performance and noise suppression in spectral CT. Therefore, we employ  $\text{L}\infty$ -VTV in the Paper C and D in the appendix. Tab. 4.1 compares computation times of the different reconstruction algorithms. TV, TNV and  $\text{L}\infty$ -VTV algorithms are written in Julia, while FBP and SIRT are based on MATLAB<sup>TM</sup> R2018b. The image reconstructions have a size of  $268 \times 268$  detector pixels, and are performed from 12 projections. The number of energy bins equals 15. A standard laptop equipped with an Intel i7-6600U quad-core CPUs at 2.60 GHz was used for the reconstructions. Thus, the novel  $\text{L}\infty$ -VTV algorithm requires 10.6% and 52.3% shorter computation time for image reconstruction than the classical TNV and TV algorithms, respectively. SIRT and FBP are much faster, but they give significantly lower reconstruction quality.

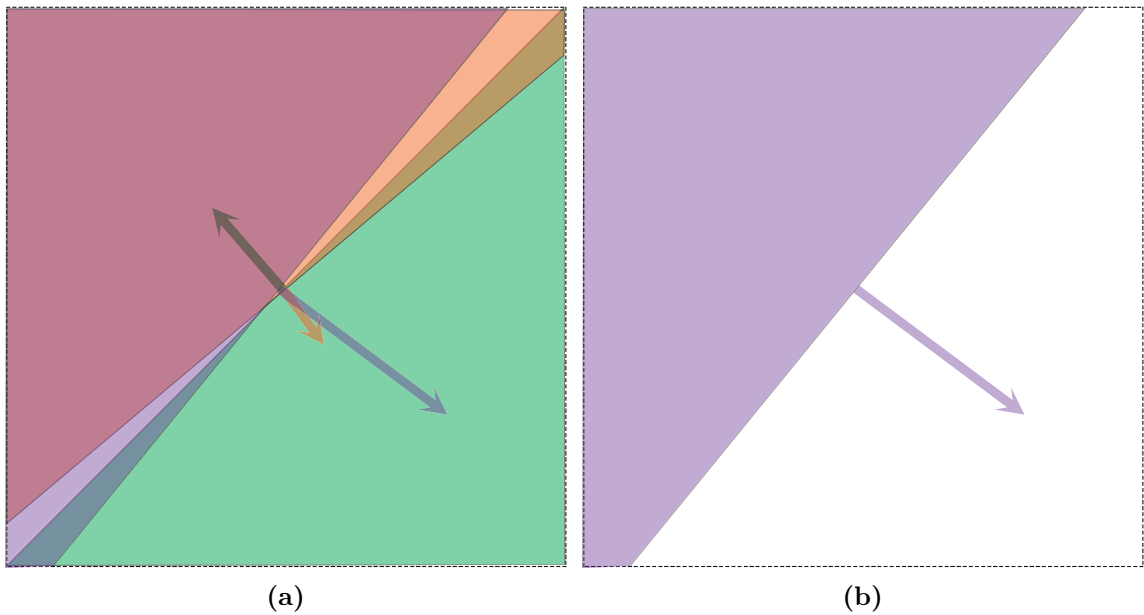


**Figure 4.5:** Illustration of  $L_\infty$ -VTV. (a) The gradients of the images from three energy bins at the specific image cell. (b) During image reconstruction, minimizing  $L_\infty$ -VTV gives preference to maximum of gradients among all the energy bins at all image cells. This results in restriction of some outliers in the gradient magnitudes, providing better suppression of reconstruction artifacts.

**Table 4.1:** Computation times of the different reconstruction algorithms.

Algorithm	Computation time (seconds)
TV	105.92
TNV	76.92
$L_\infty$ -VTV	69.54
FBP	0.25
SIRT	20.87

# Methods to material classification 5

---

In this chapter, I present the mathematical descriptions of two material classification methods developed with spectral CT techniques, both being based on a post-reconstruction data processing. In this thesis, we adopted a channel-by-channel and joint reconstruction algorithms. The system-independent material properties such as electron density  $\rho_e$  and effective atomic number  $Z_{\text{eff}}$ , being estimated are defined in the subsection 2.2.2. Both methods rely on data pre-corrections which mainly consist of correcting spectral distortions in the photon counting detector and setting low- and high-energy thresholds in the measured spectrum (see the Sections 3.4 and 3.5, respectively). For each method, the classification performance is explored with respect to the number of energy bins re-sampled in the spectrum, and optimized.

## 5.1 SIMCAD classification method

This is a system-independent material classification through attenuation decomposition (SIMCAD) method, which adopts the model of dual basis function decomposition described in the subsection 2.2.1. It estimates  $\rho_e$  and  $Z_{\text{eff}}$  using spectral CT measurements.

### 5.1.1 Calibration step

Adopting the dual basis function decomposition shown in Eq. 2.11, we can write the LACs of a reference material  $m$  for spectral CT with multiple energies  $E_k$  as follows

$$\mu_m(E_k) = \rho_{e,m} (Z_{\text{eff},m}^{n-1} p(E_k) + c(E_k)), \quad (5.1)$$

where  $m = 1, 2, \dots, M$ ,  $k = 1, 2, \dots, K$  with  $M$  and  $K$  being the number of reference materials and energy bins used, respectively.  $p(E_k)$  and  $c(E_k)$  are photoelectric absorption and Compton scattering basis functions, respectively. The basis functions are the same for all samples being scanned.

We optimize the basis functions as well as the parameter  $n$  for improved estimation of material properties, using a set of the reference materials. The presence of  $n$  in

Eq. 5.1 leads to non-linear equations. Imposing positivity constraints on the solution, we construct the objective function as

$$\min_{0 \leq p_1, c_1, \dots, p_K, c_K, n} \sum_{m=1}^M \sum_{k=1}^K (\mu_m(E_k) - \rho_{e,m}(Z_{\text{eff},m}^{n-1} p_k + c_k))^2, \quad (5.2)$$

where  $p_k = p(E_k)$  and  $c_k = c(E_k)$ . This problem is solved with a nonlinear least square solver defined with trust region method [113]. MATLAB<sup>®</sup>'s **lsqnonlin** function was employed for the minimization procedure based on initial constraints that we selected as  $p_k^0 = 0.5$ ,  $c_k^0 = 0.5$  and  $n^0 = 3.6$  for all energy bins,  $k$ . We observed that the calibration results did not depend on the initial values.  $n$  is optimized independently for each approach using certain number of energy bins for classification.

### 5.1.2 Calculation of material features

We extract LACs  $\mu(E_k)$  at all energy bins after scanning a unknown material, and then compute  $(\rho_e, Z_{\text{eff}})$  through the calibration parameters,  $p(E_k)$ ,  $c(E_k)$  and  $n$ . For  $M$ - and  $K$ - the total number of unknown materials and energy bins, respectively, we can rewrite Eq. 5.1 in the form of a linear equations as

$$\begin{pmatrix} \vec{p} & \vec{c} & & & \\ & & \ddots & & \\ & & & \vec{p} & \vec{c} \end{pmatrix} \begin{pmatrix} z_1 \\ \rho_{e,1} \\ \vdots \\ z_M \\ \rho_{e,M} \end{pmatrix} = \begin{pmatrix} \vec{\mu}_1 \\ \vdots \\ \vec{\mu}_M \end{pmatrix} \quad (5.3)$$

where  $z_m$  denotes a temporary variable that equals  $\rho_{e,m} Z_{\text{eff}}^{n-1}$ , and  $\vec{p} = (p_1, \dots, p_K)^T$ ,  $\vec{c} = (c_1, \dots, c_K)^T$  and  $\vec{\mu}_m = (\mu_m(E_1), \dots, \mu_m(E_K))^T$ . The size of the linear matrix in the latter equation is  $(M \times K)$ -by- $(2 \times M)$ , and the number of unknowns is equal to  $2 \times M$ . Employing a linear least square solver of MATLAB<sup>®</sup>'s **lsqnonneg** function with the positivity constraint on the solution, we obtain the vector  $(z_1, \rho_{e,1}, \dots, z_M, \rho_{e,M})$  that minimizes the norm. The effective atomic numbers are then calculated for all materials by

$$Z_{\text{eff},m} = \left( \frac{z_m}{\rho_{e,m}} \right)^{\frac{1}{n-1}}. \quad (5.4)$$

We use the percent relative deviation to estimate the method accuracy, determined by

$$\Delta Z_{\text{eff}}^{\text{rel}} = 100\% \cdot \frac{Z_{\text{eff}}^{\text{est}} - Z_{\text{eff}}^{\text{ref}}}{Z_{\text{eff}}^{\text{ref}}}, \quad (5.5)$$

$$\Delta \rho_e^{\text{rel}} = 100\% \cdot \frac{\rho_e^{\text{est}} - \rho_e^{\text{ref}}}{\rho_e^{\text{ref}}} \quad (5.6)$$

where superscripts *est* and *ref* designate the estimated and reference values, respectively.

## 5.2 BMD classification method

This is a basis material decomposition (BMD) method that estimates a material's  $Z_{\text{eff}}$  value from energy-resolved LACs corrected for spectral distortions.

### 5.2.1 Basis material decomposition

The basis material decomposition model can alternatively decompose material's LACs into a linear combination of basis materials' LACs with respective equivalent thicknesses [44, 71, 72, 114]. We adopt this model for spectral CT with multiple energies as follows

$$\mu(E_k) = h_1\mu_1(E_k) + h_2\mu_2(E_k) + \dots + h_N\mu_N(E_k), \quad (5.7)$$

where  $\mu_i(E_k)$  ( $i = 2, 3, \dots, N$ ;  $k = 2, 3, \dots, K$ ) and  $h_i$  are LAC at energy bin  $E_k$ , and the equivalent thickness of a basis material  $i$ , respectively.  $K$  and  $N$  denote the total number of energy bins and basis materials, respectively. The number of energy bins  $K$  should be larger than or equal to the number of basis materials  $N$ , otherwise the latter equation will become under-determined.

Fig. 5.1a presents the LAC decomposition with basis materials based on the experimental data from spectral CT, exemplified for water. To decompose we first computed equivalent thicknesses  $h_{\text{PE}}$  and  $h_{\text{PVC}}$  (for the basis materials of PE and PVC) through Eq. 5.10, and then approximated the LACs by linear combination of PE and PVC using Eq. 5.7. Fig. 5.1b shows the accuracy of this decomposition as percent relative deviation with regard to the reference (theoretical) LACs.

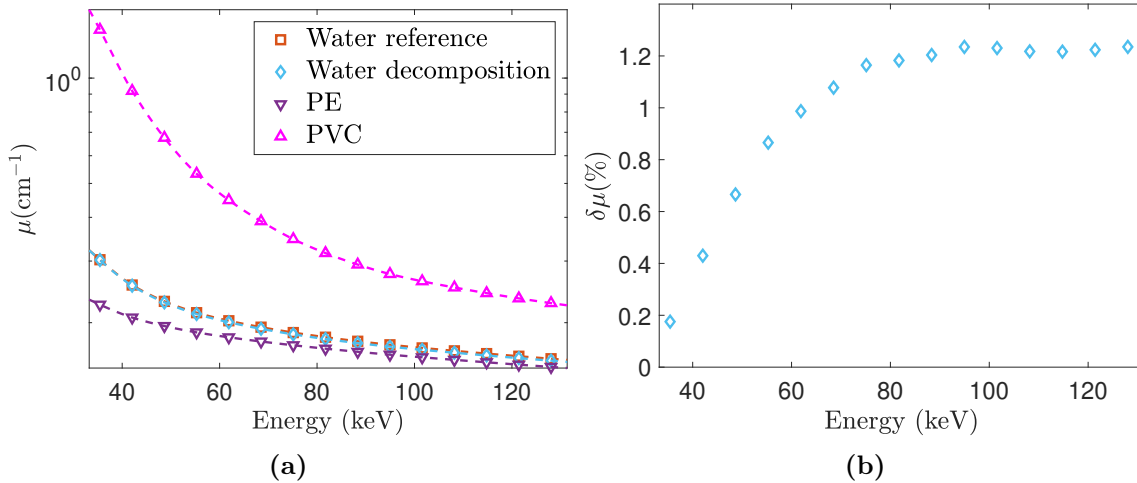


**Figure 5.1:** Energy resolved LAC decomposition, exemplified for water. (a) Basis material decomposition obtained with 15 energy bins. The reference LACs of water, PE and PVC are taken from NIST database [6]. Note logarithmic scale in the y-axis. (b) Percent relative deviations of the decomposition in regard to the reference LACs at each energy bin. The figure is adapted from the Paper D in the appendix.



The basis material decomposition model possesses superiority over the dual basis function decomposition presented in Eq. 2.3, based on the fact that the LAC of a material with a K-edge discontinuity can be correctly estimated by using a basis material with a K-edge within the identical energy range [33].

Material classification performance definitely depends on how the LAC is accurately decomposed, and thereby on the number of basis materials, i.e. the number of dimensions of attenuation vector space. The required number of basis materials for accurate decomposition is mostly related to the set of materials and the energy region used. In the Paper D in the appendix, we estimate the classification performance as a function of the number of basis materials, and we find that the decomposition with two basis materials provides the optimal performance for our study. Additionally, the SVD analysis in the Paper D also shows that the LACs of our materials can be approximated through two basis functions in the general decomposition model shown in Eq. 2.2.

### 5.2.2 Curve fitting and calculation of the material feature

Brambilla et al. [58] presented that  $Z_{\text{eff}}$  value of the estimated material can be related to quantity of equivalent thickness of PVC basis material that possesses the highest  $Z_{\text{eff}}$  among all the basis materials used. Particularly, the measurements showed that  $Z_{\text{eff}}$  of estimated materials monotonically increases as the PVC fraction value,  $f_{\text{PVC}}$  increases. This relation can thus be fitted by a polynomial interpolation and extrapolation of degree 3 as follows [58]

$$Z_{\text{eff}} = c_0 + c_1 \cdot f_{\text{PVC}} + c_2 \cdot f_{\text{PVC}}^2 + c_3 \cdot f_{\text{PVC}}^3, \quad (5.8)$$

where  $c$  represents a set of polynomial regression coefficients being determined. The PVC fraction can be computed by [58]

$$f_{\text{PVC}} = \frac{h_{\text{PVC}}}{\sum_{i=1}^N h_i}, \quad (5.9)$$

where  $N$  is the total number of basis materials, and  $h_i$  denotes equivalent thickness of basis material  $i$ , and  $i = 2, 3, \dots, N$ .

Fig. 5.2 demonstrates the relation between  $Z_{\text{eff}}$  and  $f_{\text{PVC}}$  fraction, fitted by Eq. 5.8. The different reference materials with the total number of 33 (listed in the Paper D) were employed to interpolate or extrapolate missing observations in the plot. The interpolated or extrapolated points refer to  $Z_{\text{eff}}$  values of unknown materials. Note that for estimations with the BMD method presented in the Paper D we employ only the theoretical LACs from NIST database [6] for all the basis materials.

Brambilla et al. [58] relied on the calibration phase to extract the equivalent thicknesses using maximum likelihood estimation. In this phase, they captured the detector's response for the basis materials, PE and PVC, with the different thicknesses of layers that are superposed on each other. In contrast to their method, we correct the

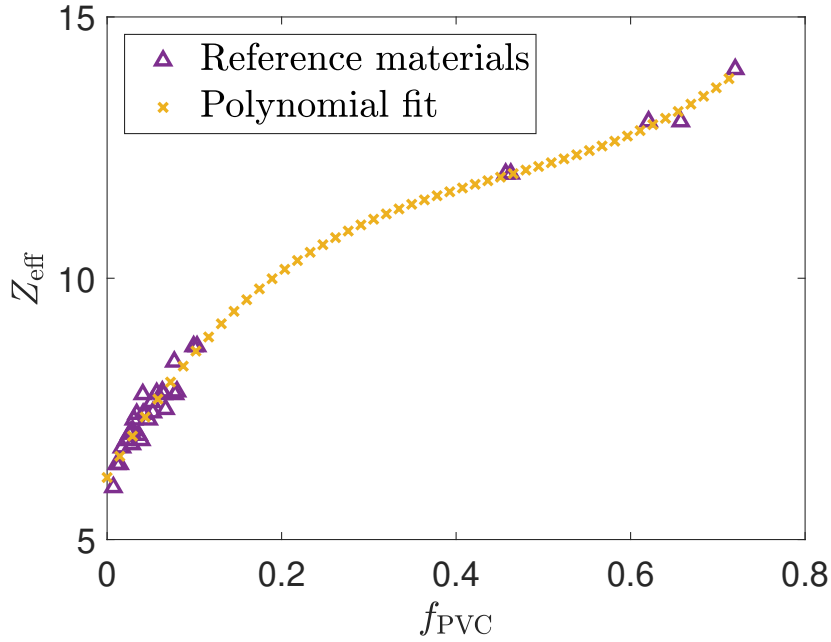


**Figure 5.2:** The dependence of materials'  $Z_{\text{eff}}$  values on respective PVC fraction values,  $f_{\text{PVC}}$  defined in Eq. 5.9.  $f_{\text{PVC}}$  values are found from Eq. 5.10 using a set of reference materials, while  $Z_{\text{eff}}$  values in the missing data points are interpolated or extrapolated with the polynomial fitting shown in Eq. 5.8.  $Z_{\text{eff}}$  values in the missing data points represent unknown materials. This plot is generated by using two basis materials of PE and PVC, and reconstructing the samples from 15 energy bins. The figure is adapted from the Paper D in the appendix section.

spectral distortion with the correction algorithm explained in the Section 3.4, which will lead to the significant deviations of LACs from the expected values without the correction. The equivalent thicknesses  $h_i$  are then retrieved using the following linear system of equations, which can be expressed by reformulating 5.7 as

$$\begin{pmatrix} \vec{\mu}_1 & \dots & \vec{\mu}_N \end{pmatrix} \begin{pmatrix} h_1 \\ \vdots \\ h_N \end{pmatrix} = \begin{pmatrix} \mu(E_1) \\ \vdots \\ \mu(E_K) \end{pmatrix} \quad (5.10)$$

where  $K$  designates the overall number of energy bins,  $\vec{\mu}_i = (\mu_i(E_1), \dots, \mu_i(E_K))^T$ , and  $k = 2, 3, \dots, K$ .  $\mu_i(E_k)$  represents the LAC of the basis material  $i$  at energy bin  $E_k$ , and  $\mu(E_k)$  the extracted LACs of the scanned unknown material. The number of unknowns in the above equation is equal to  $N$ , and the size of the linear matrix on the left hand side is  $K$ -by- $N$ . It is also noteworthy that in the Paper D we perform estimations with at least two basis materials and two energy bins. Employing a linear least square solver of **lsqnonneg** function in MATLAB<sup>®</sup>, we retrieve the vector  $(h_1, \dots, h_N)$  that minimizes the norm. The positivity constraint is imposed on the solution.

The PVC fraction value for the unknown material is calculated using the retrieved  $(h_1, \dots, h_N)$  equivalent thicknesses of the basis materials, and then we estimate its  $Z_{\text{eff}}$  feature using Eq. 5.8, as described in Fig. 5.2.

# Results 6

---

In this chapter, I briefly introduce all the Papers in the appendix section and present the main results. I leave the reader to find a more detailed description and more results in the Papers. As a reminder, we use a real experimental dataset with "real life" phantoms, as presented in the Section 3.2.

## 6.1 Results of the Paper A

### 6.1.1 A brief introduction

In the Paper A entitled "System-independent material classification through X-ray attenuation decomposition from spectral X-ray CT", we present a method for material classifications for Spectral CT using photon counting detectors, named system-independent material classification through attenuation decomposition (SIMCAD). The method is based on the dual basis function decomposition and estimates  $\rho_e$  and  $Z_{\text{eff}}$ . The decomposition model, the calibration step and calculation of material properties are described in the Section 5.1. The spectral distortions due to the detector artifacts and photon starvation at low- and high-energies result in a significant distortion of the measured LACs, which is described in Section 3.4. Therefore, the SIMCAD method employs a correction algorithm to correct the measured attenuation curve. Low- and high-energy bins in which LAC deviations from the expected values are still present even after correcting the detector response are truncated by setting low- and high-energy thresholds. LAC extraction technique and setting low- and high-energy thresholds were explained in the Section 3.5. In this work, the SIMCAD method is tested against another Spectral CT classification method called the Spectral  $\rho_e/Z_{\text{eff}}$  Estimation (SRZE), proposed by Busi et al. [70]. The SRZE estimates system-independent  $(\rho_e, Z_{\text{eff}})$  directly from the spectral LACs. The materials in the range of  $6 \leq Z_{\text{eff}} \leq 23$  are estimated in this work.

### 6.1.2 Main results

#### Classification performance as a function of the number of energy bins used

How a source spectrum is sampled for the different number of energy bins is described in the Section 3.6. Fig. 6.1 demonstrates the percent relative deviations for  $(\rho_e, Z_{\text{eff}})$  as a function of energy bins employed. For  $Z_{\text{eff}}$ , the mean deviation does not vary noticeably being 3.3% at 90 energy bins, with an exception for 6 energy bins where the deviation is equal to 7.2%. For  $\rho_e$ , the mean deviation goes up as the number of energy bins used becomes higher reaching 4.2% at 90 energy bins. Using 15, 30, 45 and 90 energy bins does not improve classification performance compared to optimized bi-energy bins, but rather worsens the performance. One reason may be that energy bin widths for 15, 30, 45 and 90 energy bins, which are uniformly shared across the source spectrum are under the detector's energy resolution (8 keV), with widths of 6.6 keV, 3.3 keV, 2.2 keV and 1.1 keV, respectively; Secondly the detector noise increases as the number of energy bins is larger. 15 energy bins approach gives better classification performance relative to 30, 45 and 90 energy bins, and can be used instead of employing a higher number of bins than 15.

The thresholds of non-overlapping bi-energy bins separated by a gap are optimized for the best classification performance. In other words, the position of the gap between non-overlapping bi-energy bins illustrated in Fig. 3.13c is optimized for the best classification. Note that the threshold optimization is not performed for other approaches with different energy bins used, which would make it challenging. Thus, our SIMCAD method optimizes the selection of widths of non-overlapping low- and high-energies, and appears to have the best classification performance with optimized bi-energy bins.

#### Results from optimized bi-energy bins

Fig. 6.2 presents a  $(\rho_e, Z_{\text{eff}})$  chart of estimated and reference values, obtained with optimized bi-energy bins. The relative deviations for all the estimated materials, for which the estimated and reference  $\rho_e$  and  $Z_{\text{eff}}$  values are shown in the map are listed in Tab. 6.1. The table compares the best accuracy results obtained by the SIMCAD and the SRZE, which use optimized bi- and 64 energy bins, respectively. The results on the table are comparable. The SIMCAD method gives up to 32 times reduction in computation time because of lower number of energy bins required, for which respective images are reconstructed. Thus, the SIMCAD requires only two information channels important for security applications where rapid scanning is required.

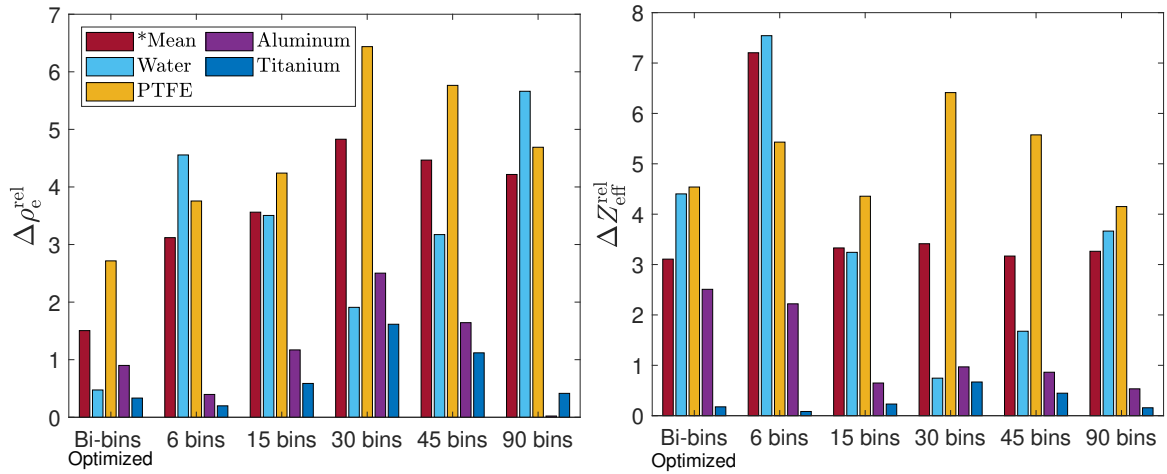


**Figure 6.1:** The percent relative deviations for  $\rho_e$  (left) and  $Z_{\text{eff}}$  (right) with respect to the number of energy bins used for classifications. The plots show that optimized bi-energy bins result in better classification performance. \*The mean deviation was calculated from absolute values of relative deviations for each material used in the Paper A in the appendix section. The figures are adapted from the Paper A.

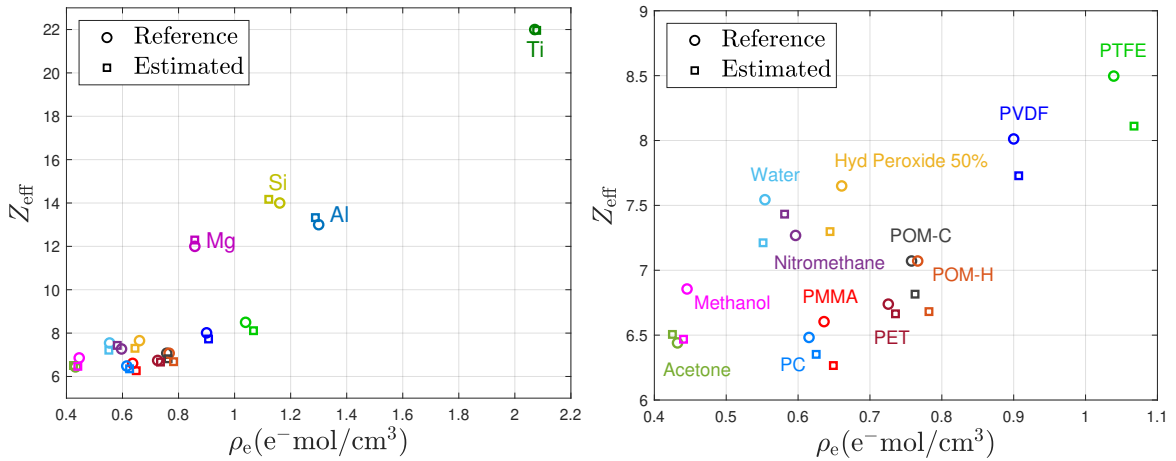


**Figure 6.2:** Electron density and effective atomic number ( $\rho_e, Z_{\text{eff}}$ ) map highlighting estimated and reference values, obtained with optimized bi-energy bins approach. Note that to avoid the overlap of the material labelled names, an enlarged version of the lower left region of the left frame is shown in the right frame. The figures are adapted from the Paper A.

**Table 6.1:** The percent relative deviations for  $(\rho_e, Z_{\text{eff}})$  for all the materials estimated. The SRZE uses 64 energy bins to reach these results taken from [59, 70], whereas the SIMCAD utilizes just optimized bi-energy bins. The reference  $\rho_e$  and  $Z_{\text{eff}}$  values are calculated from Eq. 2.9 and Eq. 2.10, respectively, and using the exponent value  $l = 3.8$ . The unit for  $\rho_e$  is  $\text{e}^- \text{mol}/\text{cm}^3$ . \*The mean values are calculated from absolute values of each column. The table is taken from the Paper A.

Material	$\rho_e^{\text{ref}}$	SIMCAD	SRZE	$Z_{\text{eff}}^{\text{ref}}$	SIMCAD	SRZE
		$\Delta\rho_e^{\text{rel}}(\%)$	$\Delta\rho_e^{\text{rel}}(\%)$		$\Delta Z_{\text{eff}}^{\text{rel}}(\%)$	$\Delta Z_{\text{eff}}^{\text{rel}}(\%)$
PMMA	0.636	-2.0	-2.3	6.60	5.1	-0.3
PTFE	1.039	-2.7	0.1	8.50	4.5	-2.5
PVDF	0.9	-0.8	-0.8	8.01	3.5	-1.4
PC	0.615	-1.6	1.4	6.48	2.0	-1.8
POM-C	0.758	-0.6	-1.4	7.07	3.6	-0.9
PET	0.726	-1.4	-3.1	6.74	1.1	-0.1
POM-H	0.766	-2.0	-2.4	7.07	5.5	-0.4
Acetone	0.432	1.6	-2.3	6.44	-1.0	5.0
H <sub>2</sub> O <sub>2</sub> (50%)	0.661	2.4	-0.2	7.65	4.6	5.4
Methanol	0.446	1.1	1.4	6.86	5.6	-4.7
Water	0.554	0.5	-6.9	7.54	4.4	-2.7
Nitromethane	0.597	2.6	1.7	7.27	-2.3	2.5
Aluminum	1.3	0.9	-3.2	13	-2.5	0.7
Silicon	1.161	3.4	-5.5	14	-1.2	-0.7
Magnesium	0.858	0.03	-5.4	12	-2.4	0.8
Titanium	2.071	-0.3	-0.7	22	0.2	-1.2
*Mean	-	1.5	2.4	-	3.1	1.9

## 6.2 Results of the Paper B

### 6.2.1 A brief introduction

In this paper, we present a joint image reconstruction algorithm for Spectral CT. In security screening material classification is found to benefit from spectrally resolved attenuation but the performance may decrease due to the poor image reconstruction quality caused by limited angle and few view projections, and an insufficient number of photons. We aim to improve Spectral CT reconstruction by employing correlations between multiple energy bins based on  $L_\infty$  norm-based vectorial total variation ( $L_\infty$ -VTV) regularization. To evaluate the joint reconstruction algorithm we use the SIMCAD classification method as a figure of merit. The mathematical foundations of the SIMCAD method were presented in the Section 5.1, and the main results of the method are shown in the previous section 6.1. In this work, we show that our joint reconstruction algorithm gives noticeably better reconstruction, and thereby better material classification accuracy than other iterative algorithms. We compare  $L_\infty$ -VTV against total nuclear variation (TNV) of another state-of-the-art joint reconstruction in

spectral CT, and against bin-by-bin reconstructions such as the classic total variation (TV) regularization and the non-regularized SIRT. Mathematical descriptions of the novel  $L_\infty$ -VTV and TNV algorithm are provided in the Section 4.2.

To test the performance of the reconstruction algorithms we employ the correlation coefficient  $r$  as another figure of merit, which indicates how the reconstructed image value  $\boldsymbol{\mu}$  is linearly related to the ground-truth image value  $\mathbf{v}$ , defined as

$$r = \frac{\sum_i (\mu_i - \bar{\mu})(v_i - \bar{v})}{\sqrt{\sum_i (\mu_i - \bar{\mu})^2 \sum_i (v_i - \bar{v})^2}}, \quad (6.1)$$

where  $\bar{\mu}$  and  $\bar{v}$  are the mean attenuation values of image cells, and  $\mu_i$  and  $v_i$  are the  $i^{\text{th}}$  cell attenuation values of  $\boldsymbol{\mu}$  and  $\mathbf{v}$ , respectively. 2D ground truth images of the sample at multiple energy bins is synthetically generated by assigning the respective mean LAC to each energy bin for each material in the sample. The mean LAC for each energy bin is extracted from the attenuation value histogram of a material's region of interest (ROI) based on the normal distribution, described in the Section 3.5. For the attenuation extraction to generate ground truth images, the sample reconstructions are performed with SIRT from 360 projections.

### 6.2.2 Main results

All the results of the Paper B presented below are obtained with the data rebinned into 15 energy bins. This is because we find in the Paper A that 15 energy bins can provide better classification performance than 30, 45 and 90 energy bins. We analyze performance of TV, TNV and  $L_\infty$ -VTV for a set of weighting parameter  $\lambda$ , based on the following figure-of-merits: correlation coefficient, L-curve, the dataset of which certain energy bins possess very high noise levels, and the SIMCAD method.

#### Correlation coefficient when decreasing the number of projections

For each reconstruction algorithm, we performed reconstructions from 7, 12 and 36 projections using different weighting parameters  $\lambda$  and computed the correlation coefficients with respect to the ground-truth images, which are plotted in Fig. 6.3b. The sample shown in Fig. 6.3a was used to produce the correlation coefficients by scanning it and reconstructing the images at 15 energy bins. For 36 projections, in which the data quality is relatively better, the differences between the maximal correlation coefficients of each algorithm are clearly smaller than the sparse-view cases of 7 and 12 projections. For 7 and 12 projections, the maximal correlation coefficient (at the optimal  $\lambda$  values) for the  $L_\infty$ -VTV is clearly larger than the coefficients for TNV and TV reconstructions, which are in turn significantly larger compared to the coefficient for SIRT reconstruction. The maximal correlation coefficient for the joint TNV reconstruction is in turn larger than the coefficient for channel-by-channel TV reconstruction. Thus, the  $L_\infty$ -VTV reconstruction outperforms the TNV, TV and

SIRT algorithms when the number of projections is decreased or the data SNR is decreased.

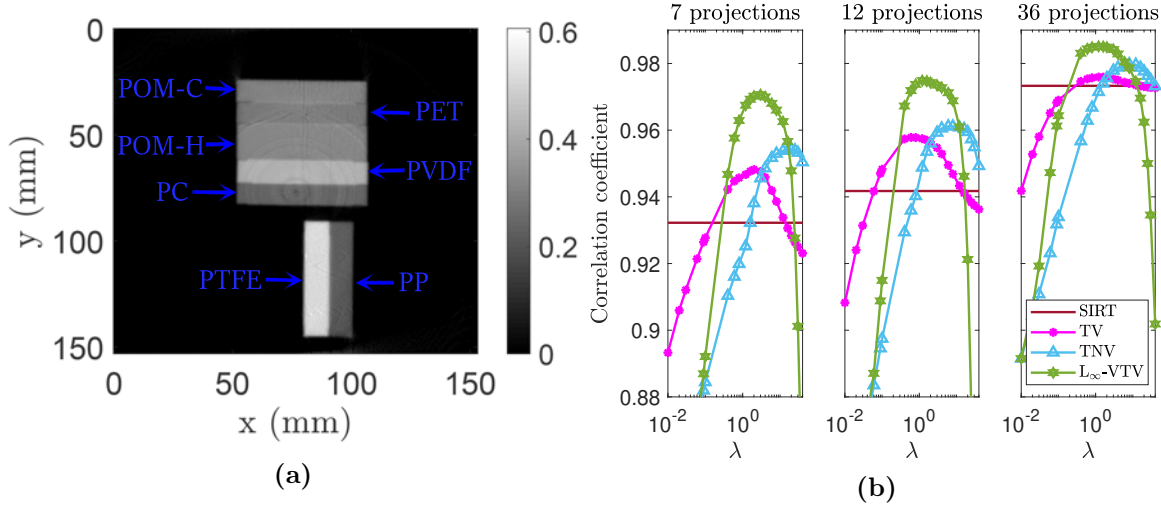


**Figure 6.3:** Comparing the performances of the reconstruction algorithms based on the correlation coefficient. (a) The sample including the plastics indicated by blue arrows, reconstructed with SIRT from 360 projections (at 42 keV) for sample presentation. The gray scale bar represents the LACs with the unit of  $\text{cm}^{-1}$ . This sample is scanned with the different numbers of projections to produce the correlation coefficients shown in the right frame. (b) The correlation coefficients as a function of weighting parameter  $\lambda$  for 7, 12 and 36 projections, computed with different algorithms. The correlation coefficients represent the mean values calculated from the coefficients for 15 energy bins. Note the logarithmic scale in the x-axis. The figures are adapted from the Paper B in the appendix.

### Adding high noise levels to specific energy bins

Certain energy bins may be subject to high noise levels during scanning, being local to certain energy bins. For example, metals in the sample may induce high noise in specific energy bins resulting in the reduced photon statistics, and thereby in photon starvation. This in turn causes the appearance of metal artifacts in reconstructed images, which leads to a significantly low signal-to-noise ratio (SNR) in the metal shadow and mainly affects the lower energy bins. As a result, metal artifacts can significantly decrease classification performance. Another example can be that the transmitted spectrum may have a significantly lower SNR, especially at low- and high-energies, depending on the density or effective atomic number of materials. This study will also show how the spectral information is sharing between different energy bins when using joint reconstruction. To evaluate the robustness of the reconstruction algorithms to such artifacts, we introduced Gaussian noise to two sinograms at specific energies such as 48.7 keV and 101.6 keV, with a standard deviation ( $\sigma$ ) of 0.5, 1.0 and 1.5.

Fig. 6.5 highlights the correlation coefficients depending on photon energy for each  $\sigma$  value, produced by different algorithms. The correlation coefficients represent the



mean values calculated from the coefficients for 15 energy bins. We first found the optimal  $\lambda$  resulting in the highest coefficient for  $\sigma = 1.5$ . For each algorithm, we then employed this optimal  $\lambda$  value to compute the correlation coefficients for other  $\sigma$  values. As expected, the TV shows no interactions between different energy bins, while the correlation coefficients for the unaffected bins of the TNV and  $L_\infty$ -VTV decrease when increasing the noise level, caused by inter-bin correlations. Compared to TV, they have noticeably higher coefficients for the affected bins, achieved by efficiently utilizing the 'healthy' energy bins for which the reconstruction quality is slightly reduced due to noise transfer. The  $L_\infty$ -VTV in turn shows potential to perform better than TNV in terms of overcoming such high noise levels, based on using strong inter-bin correlations more effectively. The superiority of the  $L_\infty$ -VTV with the improved SNR is significant, especially in the low energy domain. This property of the  $L_\infty$ -VTV can be useful to reduce metal artifacts that mostly impact low energies, and to overcome the problems with low SNRs at low energies in the spectrum.

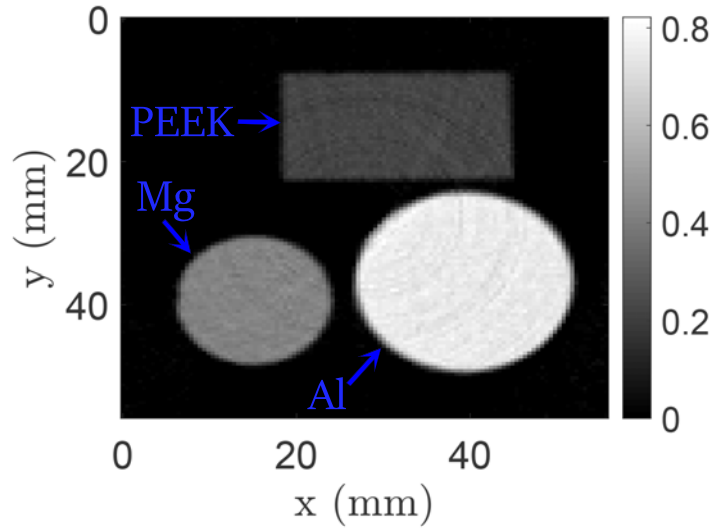


**Figure 6.4:** The sample including aluminum, magnesium and polyetheretherketone (PEEK) indicated by blue arrows, reconstructed with SIRT from 360 projections (at 61.9 keV) for sample presentation. The gray scale bar represents the LACs with the unit of  $\text{cm}^{-1}$ . This sample is used to produce the results shown in Figs. 6.5 and 6.6, for which it is scanned with the integration time of 100 ms and reconstructed from 12 projections. The figure is adapted from the Paper B.

### L-curve criterion

L-curve is a plot presenting the trade-off between the regularization term and the corresponding reprojection error that both quantities should be regulated, while the weighting parameter alters [115]. The reprojection error  $\| \mathbf{A}\boldsymbol{\mu}_\lambda - \mathbf{p} \|_2$  represents the square root of the data fidelity term described in Eq. 4.8, and summed over all energy bins. The regularization term  $\mathcal{R}_{\text{TV}}(\boldsymbol{\mu})$  for TV expressed in Eq. 4.15 is calculated separately for each energy bin, and summed over all energy bins to produce

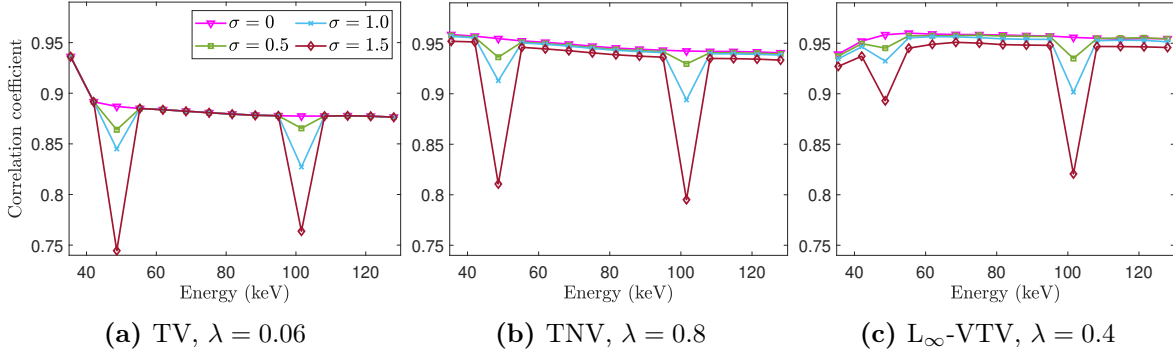


**Figure 6.5:** Correlation coefficients with respect to photon energy when different high Gaussian noise levels with standard deviation ( $\sigma$ ) of 0.5, 1.0 and 1.5 are introduced to specific energies such as 48.7 keV and 101.6 keV. These results are produced with the sample presented in Fig. 6.4, that is scanned with the integration time of 100 ms and reconstructed from 12 projections. The figures are adapted from the Paper B.

L-curve. The regularization terms  $\mathcal{R}_{\text{TNV}}(\boldsymbol{\mu})$  and  $\mathcal{R}_{\text{L}_\infty\text{-VTV}}(\boldsymbol{\mu})$  for TNV and  $\text{L}_\infty\text{-VTV}$  are common to all energy bins, and defined in Eq. 4.16 and Eq. 4.20, respectively. If the L-curve criterion for a reconstruction algorithm yields a good assessment of the optimal  $\lambda$ , L-curve can be alternatively employed to evaluate suitable range of  $\lambda$  values, instead of correlation coefficient that requires the ground truth image.

Fig. 6.6 presents the correlation coefficient as a function of  $\lambda$ , and L-curve indicated by  $\lambda$  values. Due to L-curve criterion,  $\lambda$  value located on the corner of the L-curve can be ideally considered as the optimal value, and the values on the horizontal and vertical parts result in the over-regularized and under-regularized reconstruction, respectively, that can be noted from Eqs. 4.18 and 4.21. A log-log scale representation of L-curve is more suitable for the Tikhonov regularization [115], while TV reconstruction requires a linear-linear representation [116]. Similarly, we saw that our reconstruction algorithms are more accurate with the linear-linear representation. We scanned the sample shown in Fig. 6.4 with 12 projections, and reconstructed with a set of  $\lambda$  values to plot L-curves presented. Using experimental data and few projections may cause some limitations of L-curve whose criterion may ideally be suitable for synthetic data. Hanke [117] presented based on the Tikhonov regularization that the smoother the reconstruction is, the lower accuracy the measured  $\lambda$  gives, in the sense of the optimal value.

Fig. 6.6a shows TV reconstruction with some limitation of L-curve consisting of that  $\lambda$  on the corner of the plot clearly results in over-regularization. This may be due to that TV gets over-regularized to overcome the problem of few projections. The TNV tends to produce  $\lambda$  that slightly over-smooths, as shown in Fig. 6.6b. Fig. 6.6c highlights that the  $\text{L}_\infty\text{-VTV}$  has the most accurate correspondence between two  $\lambda$  values found through the maximal correlation coefficient and L-curve criterion. The  $\text{L}_\infty\text{-VTV}$  has the sharpest corner on the L-curve, being clearly visible. Thus, the experiment shows that the L-curve criterion for the  $\text{L}_\infty\text{-VTV}$  regularization can provide

a robust evaluation of  $\lambda$ .

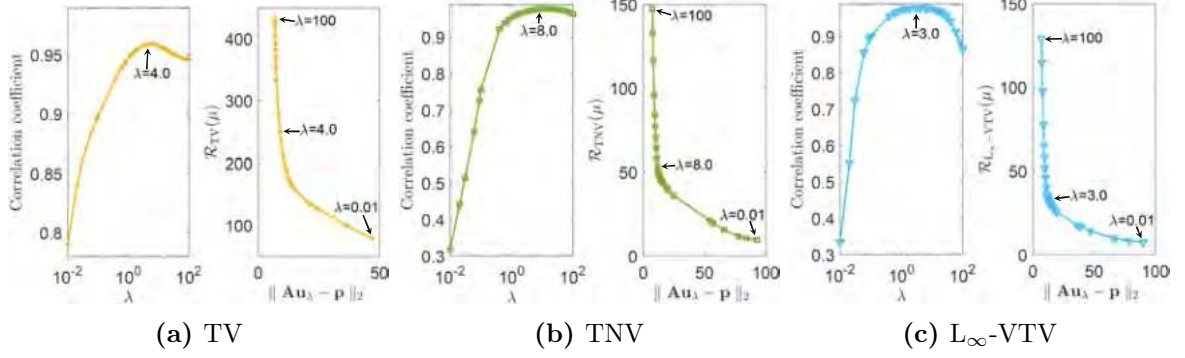


**Figure 6.6:** The correlation coefficient with respect to weighting parameter  $\lambda$  and L-curve, obtained by different algorithms. The signs in L-curve plot indicate weighting parameters, for which the corresponding correlation coefficients are shown in the left frame in each figure. The sample displayed in Fig. 6.4 was used to reproduce these results, scanned with the integration time of 100 ms and reconstructed from 12 projections. Note the logarithmic scale in the x-axis for the correlation coefficient. The figures are adapted from the Paper B.

### Classification performance as a function of $\lambda$

Next, we classified the materials with the SIMCAD method estimating  $(\rho_e, Z_{\text{eff}})$ , for which the relative deviations are plotted in Fig. 6.7a. All the samples used in this work are reconstructed for the set of weighting parameters to examine the impact of this factor on the classification performance. The results in the figure correspond to sparse-view 7 projections. The deviations represent the mean values calculated from absolute values of relative deviations for each material estimated. For the maximal classification performance (at the optimal  $\lambda$  value), the TV gives the deviations of 3.8% for  $\rho_e$  and 4.2% for  $Z_{\text{eff}}$  (at  $\lambda = 16.0$ ), while the TNV and  $L_\infty$ -VTV have the deviations of 3.4% and 3.1% (at  $\lambda = 150.0$ ), and 3.5% and 2.4% (at  $\lambda = 30.0$ ), respectively. Thus, for such sparse-view projections both joint reconstruction algorithms significantly outperform TV reconstruction in terms of classification performance.  $L_\infty$ -VTV gives in turn noticeably more accurate results than TNV.

Fig. 6.7b compares the relative deviations in  $(\rho_e, Z_{\text{eff}})$  for the different materials, corresponding to the maximal classification performance for each algorithm as presented in Fig. 6.7a. The  $L_\infty$ -VTV yields the highest classification accuracy for POM-H plastic, which can imitate a common explosive simulant with almost identical chemical compositions [67].

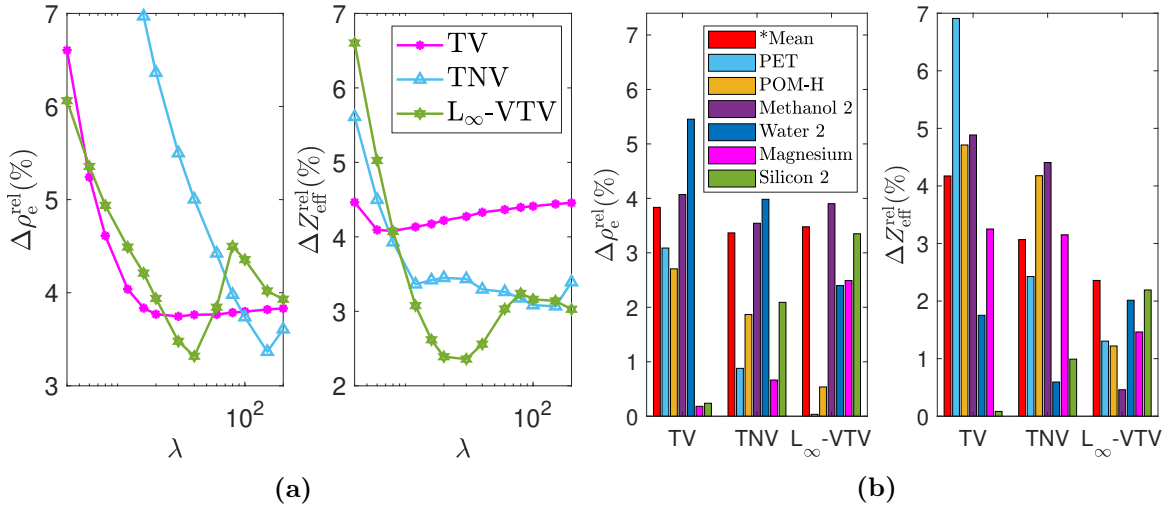


**Figure 6.7:** Comparison of the performances of different algorithms based on the SIMCAD classification method. (a) The relative deviations for  $(\rho_e, Z_{\text{eff}})$  as a function of weighting parameter  $\lambda$ , for which the reconstructions are performed from sparse-view 7 projections. The deviations represent the mean values computed from the absolute values of relative deviations for each material estimated. Note the logarithmic scale in the x-axis. (b) The relative deviations for  $(\rho_e, Z_{\text{eff}})$  corresponding to the optimal  $\lambda$  values providing the maximal classification performances, as shown in the left frame. The deviations for the different materials represent the absolute values. The figures are adapted from the Paper B.

## 6.3 Results of the Paper C

### 6.3.1 A brief introduction

In this paper, for spectral CT measurements we investigate the significance of the spectral correction of the detector response in material classification. As explained in the Section 3.4, high flux PCDs tend to suffer from severe spectral distortions of raw signal caused by detector artifacts such as charge sharing and weighting potential cross-talk, fluorescence radiation, Compton scattering, pulse pile up and incomplete charge collection. The spectral distortions lead to strong deviations of the measured spectral LACs from the actual attenuation curve, and therefore to a significant decrease in classification performance. PCDs thus require the correction algorithm to reduce the spectral distortions. In this study, we perform reconstructions from only 12 projections, because few projections can enable rapid scanning important for security applications. To improve reconstruction quality in such sparse projection data condition, we use the joint reconstruction algorithm,  $L_\infty$  norm based vectorial total variation ( $L_\infty$ -VTV), for which a mathematical description was given in the Section 4.2. In the previous section 6.2, we showed that in terms of reconstruction quality and classification performance  $L_\infty$ -VTV outperforms another joint reconstruction, TNV, and channel-by-channel reconstructions such as TV and SIRT. In this work, to test classification performance with and without the correction we employ the SIMCAD method that

estimates  $\rho_e$  and  $Z_{\text{eff}}$ . We use the broad range of materials including low contrast materials and organic compounds. We show that using the correction algorithm significantly improves classification performance. The paper can be useful for readers in the fields of energy resolved tomography especially where the accurate separation of tissues and materials with low contrast is important.

### 6.3.2 Main results

In the Section 3.1 we described the overall workflow of the main data processing steps from data acquisition to material classification. The data rebinning is performed after the data is corrected for the spectral distortions with the correction algorithm. 15 energy bins rebinned are used to produce the results presented in Fig. 6.8, which plots the classification accuracy as a function of weighting parameter  $\lambda$  for the raw and corrected data. As explained in the Section 4.2, the weighting parameter is the factor defining the strength of the  $L_\infty$ -VTV regularization. The corrected data yields the relative deviations of 3.4% for  $\rho_e$  and 2.7% for  $Z_{\text{eff}}$  (at  $\lambda = 16.0$ ), while the raw data leads to the deviations of 5.6% and 10.3% (at  $\lambda = 4.0$ ), respectively. Thus, the correction algorithm that requires additional computation time is very important to have desired classification performance.

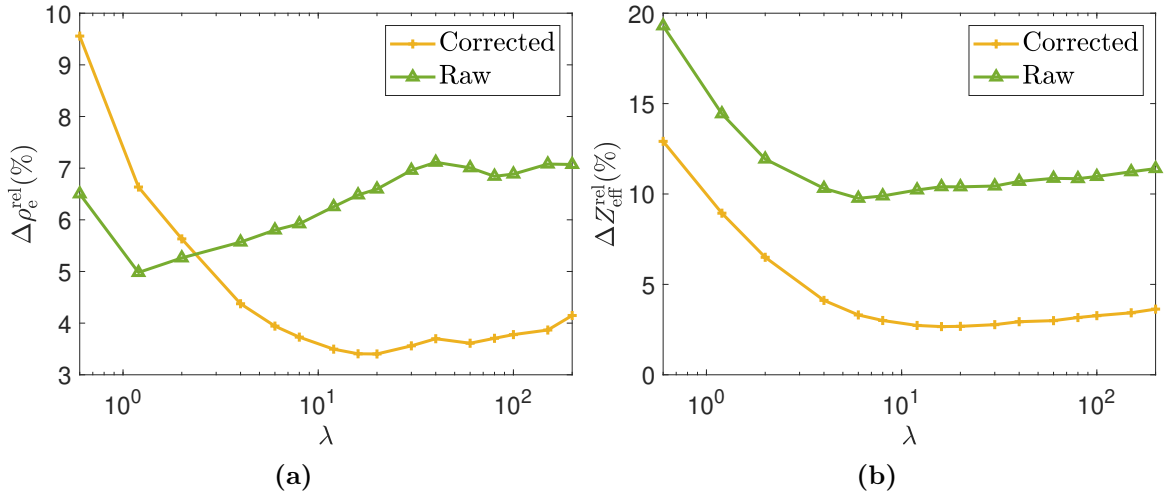


**Figure 6.8:** The percent relative deviations with respect to weighting parameter  $\lambda$  for  $\rho_e$  (a) and  $Z_{\text{eff}}$  (b), obtained with the raw data and the data corrected using the correction algorithm. The projection data rebinned into 15 energy bins is used to reproduce these results. The deviations represent the mean values computed from the absolute values of relative deviations for each material estimated. Note the logarithmic scale in the x-axis. The figures are adapted from the Paper C.

## 6.4 Results of the Paper D

### 6.4.1 A brief introduction

In this paper, we present another method for material characterization using spectral CT. The method estimates effective atomic numbers  $Z_{\text{eff}}$  of materials directly from the energy-dependent LACs. The method uses the basis material decomposition (BMD) model that can accurately define the LAC of any material by a linear combination of multiple basis materials with respective equivalent thicknesses, as introduced in the Section 5.2. As mentioned in the previous section, the imperfections of the detector's spectral response due to a range of detector effects severely distort the measured spectrum, and thereby the measured LACs. To overcome the spectral distortions, Brambilla et al. [58] used a calibration step to record the detector's response to x-ray irradiation for different combinations of the basis materials with different thicknesses. After the calibration step, the thicknesses of the basis materials that match the measured spectra are computed based on a maximum likelihood approach assuming Poisson-distributed photon counts for each energy bin. The computed equivalent thicknesses of scanned samples are employed to estimate  $Z_{\text{eff}}$  values. However, using the calibration step gives a system-dependent solution due to the dependence on the source spectrum. In this work, instead of using this calibration phase we propose the correction algorithm to correct the imperfections of the detector response. The corrected LACs allow for directly using the formulation of the BMD, defined in Eq. 5.7, without any calibration of detector response in order to estimate  $Z_{\text{eff}}$ . The BMD method offers system-independent solution, independent from the scanner or system specification like the source spectrum or filtration.

We use just 12 projections to address scanning requirements for high throughput of scanned objects in the security domain. To reduce the resulting few-views artifacts, we use the  $L_{\infty}$ -VTV joint reconstruction taking advantage of strong correlations between multiple energy bins through the  $L_{\infty}$  norm. We estimate the method's performance with respect to the set of weighting parameters  $\lambda$ . The materials in the range of  $6 \leq Z_{\text{eff}} \leq 15$  are inspected. We find that the BMD can provide better classification accuracy with 17.4% improvement in estimating  $Z_{\text{eff}}$ , compared to the SIMCAD method. However, the BMD has one disadvantage that it can estimate only  $Z_{\text{eff}}$ , as a reminder.

### 6.4.2 Main results

We perform classifications with the different number of basis materials in the basis material decomposition, denoted as  $N$  in Eq. 5.7, which defines the dimensionality of attenuation space. Tab. 6.2 gives information about all the basis materials with chemical formula, reference density and  $Z_{\text{eff}}$ , which are used for estimating classification performance as a function of the number of basis materials. Tab. 6.3 presents the basis materials used for classifications with the different number of basis materials  $N$ . The

LACs of the basis materials are theoretical, and obtained from NIST database [6]. For all the different numbers of basis materials, we employ PVC with the highest  $Z_{\text{eff}}$  value among all the basis materials, whose  $f_{\text{PVC}}$  fraction is used to estimate  $Z_{\text{eff}}$  of materials based on Eq. 5.8.

**Table 6.2:** The list of all the basis materials used for classifications with different number of basis materials. The reference  $Z_{\text{eff}}$  values are calculated with Eq. 2.10. The mass densities are obtained from in PubChem data [74].

Basis material	Chemical Formula	$\rho$ (g/cm <sup>3</sup> )	$Z_{\text{eff}}$
Polyethylene (PE)	(C <sub>2</sub> H <sub>4</sub> ) <sub>n</sub>	0.93	5.79
Polyacetylene (PAC)	(C <sub>2</sub> H <sub>2</sub> ) <sub>n</sub>	0.4	5.89
Polypyrrole (PPy)	(C <sub>4</sub> H <sub>5</sub> N) <sub>n</sub>	0.97	6.22
Polymethyl methacrylate (PMMA)	(C <sub>5</sub> O <sub>2</sub> H <sub>8</sub> ) <sub>n</sub>	0.94	7.02
Polyoxymethylene (POM)	(CH <sub>2</sub> O) <sub>n</sub>	1.42	7.40
Polyvinyl Chloride (PVC)	(C <sub>2</sub> H <sub>3</sub> Cl) <sub>n</sub>	1.406	15.71

**Table 6.3:** The basis materials used for classifications with the different number of basis materials  $N$  in the basis material decomposition, as defined in Eq. 5.7.

Number of basis materials $N$	Basis materials
2	PE, PVC
3	PE, PPy, PVC
4	PE, PPy, POM, PVC
5	PE, PAC, PPy, POM, PVC
6	PE, PAC, PPy, PMMA, POM, PVC

### Classification performance as a function of the number of basis materials used

We assess the dimensionality of decomposed LAC space, for the set of our materials, source spectrum, detector's energy region and system features, based on classification performance obtained with the different numbers of basis materials  $N$ . Fig. 6.9 shows the relative deviations in  $Z_{\text{eff}}$  as a function of weighting parameter  $\lambda$  for each  $N$ . The deviation clearly increases as the number of basis materials increases. 2 basis materials give the optimal performance with the deviation of 2.4% (at  $\lambda = 60$ ), while 5 basis materials provide this with the deviation of 4.4% (at  $\lambda = 30$ ). This deviation equals 4.1% (at  $\lambda = 30$ ) for 6 basis materials. Moreover, the classification performance with 2 basis materials appears to be more stable with respect to  $\lambda$ , showing better robustness against changes of  $\lambda$ . Thus, the BMD is the most accurate with just two basis materials, for which PE and PVC are used. In the Paper D we also find that the

Singular Value Decomposition (SVD) [33] analysis, a tool from matrix algebra, shows the dimensionality of LAC vector space being equal to two.

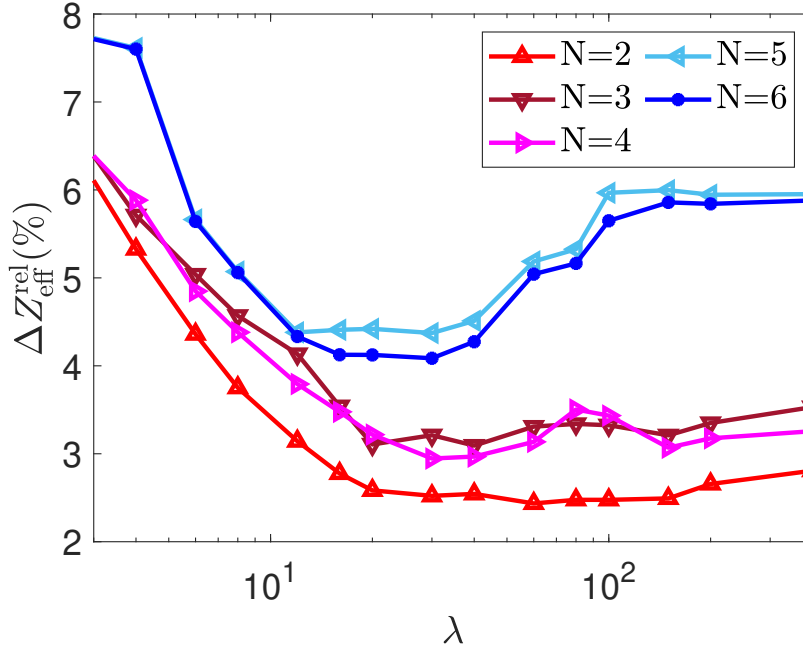


**Figure 6.9:** The percent relative deviations in  $Z_{\text{eff}}$  with respect to weighting parameter  $\lambda$ , obtained with the different numbers of basis materials  $N$  in the basis material decomposition. The deviations represent the mean values of the absolute deviations for each material estimated. Note the logarithmic scale in the x-axis. The figure is adapted from the Paper D.

### Comparing the BMD and SIMCAD

Fig. 6.10 shows the relative deviations in  $Z_{\text{eff}}$  as a function of weighting parameter  $\lambda$  for the BMD and SIMCAD. The BMD shows the maximal performance with the deviation of 2.3% (at  $\lambda = 60.0$ ), while the SIMCAD shows 2.7% (at  $\lambda = 16.0$ ). For the maximal classification performance, the SIMCAD gives the deviation of 2.5% in estimating  $\rho_e$  (at  $\lambda = 16.0$ ). The deviations represent the mean values calculated from the absolute deviations for each material listed in Tab. 6.4. This table reports the deviations for different estimated materials, corresponding to the maximal classification performance for both methods. All the absolute relative deviations are below 5.6% and 6.6% for the BMD and SIMCAD, respectively. Thus, the BMD achieves 17.4% increase in classification accuracy than the SIMCAD.



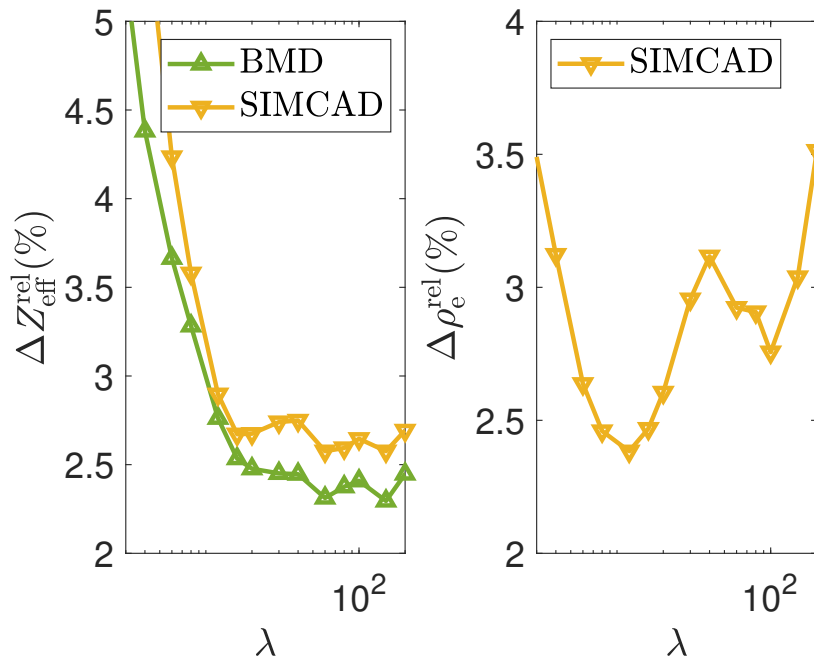


**Figure 6.10:** The percent relative deviations in  $Z_{\text{eff}}$  with respect to weighting parameter  $\lambda$ , obtained with the BMD and SIMCAD. The deviations represent the mean values of the absolute deviations for each material listed in Tab. 6.4. Note the logarithmic scale in the x-axis. The figure is adapted from the Paper D.

**Table 6.4:** The percent relative deviations in  $Z_{\text{eff}}$  and  $\rho_e$  for the BMD and SIMCAD classification method, corresponding to the maximal classification performance shown in Fig. 6.10. The reference  $Z_{\text{eff}}$  and  $\rho_e$  values are calculated from Eq. 2.10 and Eq. 2.9, respectively. The unit of  $\rho_e$  is  $\text{e}^- \text{mol}/\text{cm}^3$ . \*The mean values are calculated from absolute values of each column. As a reminder, the BMD does not estimate  $\rho_e$ . The table is adapted from the Paper D.

<b>Material</b>	$Z_{\text{eff}}^{\text{ref}}$	<b>BMD</b> $\Delta Z_{\text{eff}}^{\text{rel}}(\%)$	<b>SIMCAD</b> $\Delta Z_{\text{eff}}^{\text{rel}}(\%)$	$\rho_e^{\text{ref}}$	<b>BMD</b> $\Delta \rho_e^{\text{rel}}(\%)$	<b>SIMCAD</b> $\Delta \rho_e^{\text{rel}}(\%)$
PMMA	7.02	1.3	-0.4	0.636		1.8
PTFE	8.70	3.0	4.0	1.035		3.2
PVDF	8.40	4.3	3.9	0.896		-3.1
PC	6.82	0.2	-2.0	0.610		-1.9
POM-C	7.40	0.9	0.4	0.753		3.9
PET	7.09	0.1	-1.3	0.721		2.8
POM-H	7.40	1.7	0.3	0.763		2.4
Acetone	6.90	-4.1	-2.6	0.432		0.9
Hyd. Peroxide	7.83	-4.7	-4.9	0.661		2.5
Methanol	7.29	-1.8	-2.6	0.446		1.5
Water	7.78	-4.5	-4.7	0.554		0.5
Nitromethane	7.50	-5.6	-6.6	0.597		1.1
Aluminum	13	-1.8	-2.9	1.3		1.8
Silicon	14	0.7	3.5	1.161		-4.8
Magnesium	12	0.2	-0.1	0.859		-4.8
*Mean	-	2.3	2.7	-	-	2.5

# Discussion and Outlook 7

---

## Material identification method

I have shown the SIMCAD method for material classification into system-independent physical features  $(\rho_e, Z_{\text{eff}})$  with Spectral CT. The method was evaluated for the materials in the wide range of  $6 \leq Z_{\text{eff}} \leq 23$ . We observed that the use of a correction algorithm for spectral distortions suppresses the major detector response artifacts from the LACs. The low- and high-energy thresholds truncates the spectral LACs where they have the highest deviations from expected values. SIMCAD uses a calibration step with a set of reference materials to register photoelectric absorption and Compton scattering basis functions and  $n$  from the decomposed LAC expression as explained in the subsection 5.1.1. The impact of the number of rebinned energy bins on the method's performance has been investigated. Using a low number of energy bins without energy threshold optimization such as 6 energy bins approach results in a significant decrease in the performance. It was observed that classification is not improved further by high number of energy bins with widths below the detector's energy resolution. Optimized bi-energy bins that are not overlapping and are thus not affected by system features like X-ray source or sample parameters can provide the most accurate results. With optimized bi-energy bins, all the absolute relative deviations for estimated materials for  $\rho_e$  and  $Z_{\text{eff}}$  are below 3.4% and 5.6%, with the mean deviations of 1.5% and 3.1%, respectively. The SRZE method requires 64 energy bins for the best performance [70], and all the absolute relative deviations with this method are below 6.9% and 5.4% for  $\rho_e$  and  $Z_{\text{eff}}$ , with the mean deviations of 2.4% and 1.9%, respectively. Compared to the SRZE, the SIMCAD uses just optimized bi-energy bins and achieves comparable results, which results in 32 times reduction in computation time because of a lower number of image reconstructions required. This makes the method suitable for the requirements of high speed security scanners. Moreover, our method with a single scan achieves the classification accuracy comparable to traditional dual-energy CT techniques, which are usually performed through consecutive scans, and the accuracy for highly attenuating materials is even higher [50, 51].

### **Improving material identification for few projections**

We focus on improving the classification performance in case of few projections and the low signal-to-noise ratios that may hinder the application of the classification method due to the poor reconstruction quality. The separation of photon counts into multiple energy bins in spectral CT results in the increased noise levels, which can be another factor for a decrease in the reconstruction quality. To improve the reconstruction quality under such conditions, we propose to use correlations between multiple energy bins with  $L_\infty$ -norm-based VTV joint reconstruction. We tested the  $L_\infty$ -VTV against another joint reconstruction with TNV, and against bin-by-bin TV and SIRT algorithms. The following figure-of-merits for quantifying the performance of the reconstruction algorithms are used: the correlation coefficient, the dataset of which the specific energy bins have significantly high noise levels, the L-curve criterion and the SIMCAD classification method. The  $L_\infty$ -VTV showed the highest values of the correlation coefficient as a function of weighting parameter. The results from studying the robustness of each algorithm for high noise levels in specific energy bins showed that both joint reconstructions efficiently reduce such noise using spectral information from 'healthy' energy bins, and reach better reconstructions for all the energy bins than the TV. The  $L_\infty$ -VTV appears in turn to compensate more efficiently for excess noise in certain energy bins. Thus, the  $L_\infty$ -VTV more effectively utilizes the strong correlations between multiple energy bins, decreasing the effect of outliers in image gradient magnitudes. Outliers usually violate the attenuation variations over the different image cells and over the different energy bins. This feature can be significantly helpful for reducing metal artifacts, which mostly influence the low energies, and not only worsen the reconstruction quality, but also degrade the classification performance.

The study of the L-curve that helps to find the optimal weighting parameter  $\lambda$  for reconstruction shows that the  $L_\infty$ -VTV has a clear agreement between two  $\lambda$  values found as the optimal values by the correlation coefficient and the L-curve criterion. The TNV shows less efficiency to evaluate the optimal  $\lambda$  based on the L-curve criterion than the  $L_\infty$ -VTV, whereas the TV presented a clear disagreement between the correlation coefficient and the L-curve criterion. The classification performance of each algorithm has been evaluated based on the SIMCAD method, with the materials in the range of  $6 \leq Z_{\text{eff}} \leq 15$ . The  $L_\infty$ -VTV reaches explicitly up to 1.29 and 1.75 times better classification accuracy for estimating  $Z_{\text{eff}}$  compared to the TNV and TV, respectively. Thus, improving the reconstruction quality with better preservation of the real features can consequently improve the classification performance.

### **The significance of the spectral correction in material identification**

We are interested in the significance of the correction algorithm in material identification, which corrects spectral distortions in PCDs. We use the following figure-of-merits for quantifying the performance of the correction algorithm: the correlation coefficient, the L-curve criterion, the raw dataset of which the specific energy bins

---

have significantly high noise levels, and the SIMCAD classification method. The raw data and corrected data are assessed based on the above figure-of-merits. Because few projections for estimations suitable for fast scanning requirements are used, we aim to improve the reconstruction results with the  $L_\infty$ -VTV joint reconstruction. Even at 2 ms that is the lowest integration time of the detector and gives the lowest signal-to-noise ratios in all the energy bins, the raw and corrected data produce the similar results from the correlation coefficients and the L-curves. Applying the correction algorithm to the raw dataset of which the specific energy bins have significantly high noise levels, we saw that the correction algorithm effectively improves the quality of reconstruction measured by the correlation coefficient. This also indicates the good robustness of the algorithm to such noise levels. Finally, the significance of the correction algorithm has been estimated based on the SIMCAD, with the materials in the range of  $6 \leq Z_{\text{eff}} \leq 15$ . As a result, applying the correction algorithm to the raw data appears to play a significant role in improving the classification performance, resulting in up to 1.65 and 3.81 times better accuracy for estimating  $\rho_e$  and  $Z_{\text{eff}}$ , respectively.

### **Another material identification method**

I have presented another classification method called the BMD, which estimates system-independent physical parameter  $Z_{\text{eff}}$  based on basis material decomposition model for spectral LACs. I explore the impact of the number of basis materials on the method's performance, testing the method on the wide range of different materials. Consequently, using just two basis materials such as PE and PVC appears to provide the best results. The BMD is tested against the SIMCAD method for classifying materials in the range of  $6 \leq Z_{\text{eff}} \leq 15$ . We find that with the BMD the accuracy was improved up to 17.4% for  $Z_{\text{eff}}$  estimation. In addition, the BMD can use a basis material with a K-edge in LACs and thereby estimate materials presenting K-edges within detector's energy range. In comparison, for the SIMCAD the energy bins below the edge should be truncated making the energy range compatible with this method, which would decrease the classification performance. However, none of the materials presented in this thesis have a K-edge within the detector's energy range. As a reminder, the SIMCAD possesses the main advantage of characterizing both  $Z_{\text{eff}}$  and  $\rho_e$  features, providing a complete way of material characterization.

### **Outlook**

Some suggestions for future work are listed below.

- The Section 3.5 describes how the mean LAC is calculated from the attenuation histogram based on Gaussian distribution fitting for each energy bin. The individual materials are segmented manually from the energy-resolved reconstructions within their corresponding region of interest (ROI) surfaces or volumes. Multi-energy information provided by spectral CT is not employed

in the manual segmentation process. Moreover, in the security domain there is a need for rapid and automatic object segmentation to decrease possible human involvement and the manual workload. Therefore, I would incorporate automatic material segmentation to extract the mean LAC for each energy bin by taking advantage of additional multi-energy information. This could be done by exploiting the joint distribution of the image cell values (LACs) and their gradient magnitudes over multiple energy bins.

- Exploring mechanisms on how to automatically set the optimal weighting parameter  $\lambda$  of the reconstruction algorithms developed, in order to reduce the computation time valuable in the security screening. For this, based on spectral CT scans I will analyze and define the correlation between different reconstruction volume sizes and the respective optimal  $\lambda$  values, and also between different material sizes and the respective optimal  $\lambda$  values. The optimal  $\lambda$  may be dependent on reconstruction data amount in terms of different sample sizes and reconstruction volume sizes. Based on this correlation the optimal  $\lambda$  could be set depending on the amount of reconstruction data, but this may be the challenge for security where *a-priori* knowledge of the sample is not available.
- Elements and compounds with effective atomic number higher than 30 can have a K-edge absorption within the energy spectrum employed in CT. The BMD method can approximate the LACs of estimated materials with the K-edge, which is done by including a K-edge basis material in order to avoid a typical smooth attenuation function of energy. Therefore, I will test the performance of this method for the K-edge materials, which would attract interest in medical applications to differentiate contrast agents from body tissues and other materials based on spectral CT measurements [37].
- Adapting the developed joint reconstruction algorithms for other multi-energy imaging modalities such as visible light, electron or neutron tomography, and testing the performance of the algorithms on other tomographic data that may consist of a sufficient or limited number of projections.
- Exploring the possibility of classifying materials into three material parameters such as  $\rho_e$ ,  $Z_{\text{eff}}$  and exponent  $n$  in the dual basis function decomposition model of spectral LACs as defined in Eq. 5.1. This could be done using energy-resolved LACs at multiple energy bins.

# Conclusion 8

---

This PhD thesis has explored how all steps of the spectral CT workflow influence the resulting classification performance that is the main objective, from the data acquisition to reconstruction and post-processing. I believe that the objectives set for the thesis as stated in the introduction have been met. In this thesis we propose several approaches to pave the way for enhanced material classification with spectral CT that are listed below.

- We propose the SIMCAD method classifying materials into electron density and effective atomic number, which is based on the dual basis function decomposition into material- and energy-dependent components. With this method, we can accurately estimate materials in the range of  $6 \leq Z_{\text{eff}} \leq 23$  that include most of the materials commonly found in a passenger luggage [17], and most of human organs and tissues [118–121]. We tested the method against another state-of-the-art competitor that is the SRZE method using spectral CT scans. Our method has achieved significant reduction in computation time for classifications.
- We focus on improving the performance of the classification method for few CT projections, taking into account the requirements of high speed security applications. To realize this, we developed the joint reconstruction algorithm,  $L_{\infty}$ -VTV, and tested it based on several figure-of-merits under conditions of few projections and low signal-to-noise ratios. As a result, we found that novel  $L_{\infty}$ -VTV gives the most accurate results in comparison to other algorithms.
- We show the significance of the correction algorithm for detector’s spectral imperfections in material classification, with respect to the different number of energy bins rebinned in the source spectrum.
- We present the BMD method classifying materials into just effective atomic number, which is based on decomposing attenuation coefficients into basis materials with corresponding equivalent thicknesses. Testing a broad range of

materials, we show that the BMD can accurately separate materials with better accuracy than the SIMCAD for estimating  $Z_{\text{eff}}$ .

- The developed methods and algorithms can be used in other spectral CT based applications such as low-dose imaging that requires few projections and therefore suffers from poor photon statistics.

Both the SIMCAD and BMD methods can produce system-independent results, independent of the scanner or the system features such as source spectrum and filtration. Both methods are post reconstruction types. In the security domain, this is justified by the fact that the content in the luggage can change for each sample during the scans, with a larger range of materials appearing in high clutter. Pre-reconstruction techniques are more suitable for special applications, where it is possible to define *a-priori* knowledge of the samples. The classification results presented are also comparable with those by conventional dual-energy CT that also offers system-independent classification, which is usually realized through successive data acquisitions. However, the performance of these techniques are dependent on the selection of the pair of spectra employed for dual-energy CT acquisitions, and the assessment of their corresponding detector spectral responses.

The novel system-independent methods developed in this thesis are compatible with any multi-energy detector, and aim to help to reduce false alarms in threat detection, and enhance system reliability. Using the methods, potential threats can be found by accurately classifying the segmented regions and labeling the objects in the sample.

Implementations of the presented iterative joint reconstruction algorithms in Julia are publicly available at <https://github.com/JuliaTomo/XfromProjections.jl>. All experimental data without and with the correction algorithm applied are available to download from [122], and ready to use. With this, I believe that our classification methods and iterative joint reconstruction algorithms developed are ready enough for a practical use in security applications. I hope that the contributions of this thesis will inspire researchers working within the spectral CT field, material science or other industrial applications to future work and development.



# Bibliography

---

- [1] Robert E. Alvarez and Albert Macovski. Energy-selective reconstructions in X-ray computerised tomography. *Physics in Medicine and Biology*, 21(5):733–744, 1976.
- [2] Laszlo Tabar, Gunnar Fagerberg, Hsiu-Hsi Chen, Stephen W Duffy, Charles R Smart, Adel Gad, and Robert A Smith. Efficacy of breast cancer screening by age. new results swedish two-county trial. *Cancer*, 75(10):2507–2517, 1995.
- [3] Robert D Rosenberg, James F Lando, William C Hunt, Ronald R Darling, Michael R Williamson, Michael N Linver, Frank D Gilliland, and Charles R Key. The new mexico mammography project: screening mammography performance in albuquerque, new mexico, 1991 to 1993. *Cancer: Interdisciplinary International Journal of the American Cancer Society*, 78(8):1731–1739, 1996.
- [4] Albert Macovski. *Medical imaging systems*. Prentice Hall, 1983.
- [5] Albert C Thompson, Douglas Vaughan, et al. *X-ray data booklet*, volume 8. Lawrence Berkeley National Laboratory, University of California Berkeley, CA, 2001.
- [6] K. Berger, M.J., Hubbell, J.H., Seltzer, S.M., Chang, J., Coursey, J.S., Sukumar, R., Zucker, D.S., and Olsen. XCOM: Photon Cross Section Database, 2010.
- [7] SE Bragg, WH and Peirce. LXIV. The absorption coefficients of X rays. *The London, Edinburgh, and Dublin Philosophical Magazine and Journal of Science*, 28(166):626–630, 1914.
- [8] EA Owen. The absorption of x-rays. *Proceedings of the Royal Society of London. Series A, Containing Papers of a Mathematical and Physical Character*, 94(664):510–524, 1918.
- [9] F. K. Richtmyer and F. W. Warburton. The absorption of X-rays by iron, cobalt, nickel and copper. *Physical Review*, 22(6):539–545, 1923.
- [10] DR White. An analysis of the Z-dependence of photon and electron interactions. *Physics in Medicine & Biology*, 22(2):219, 1977.

- [11] Alvin C Silva, Brian G Morse, Amy K Hara, Robert G Paden, Norio Hongo, and William Pavlicek. Dual-energy (spectral) ct: applications in abdominal imaging. *Radiographics*, 31(4):1031–1046, 2011.
- [12] Zhengrong Ying, Ram Naidu, and Carl R Crawford. Dual energy computed tomography for explosive detection. *Journal of X-Ray Science and Technology*, 14(4):235–256, 2006.
- [13] Kristoph D Krug, William F Aitkenhead, Richard F Eilbert, Jeffrey H Stillson, and Jay A Stein. Identifying explosives or other contraband by employing transmitted or scattered x-rays, October 26 1999. US Patent 5,974,111.
- [14] Richard F Eilbert and Kristoph D Krug. Aspects of image recognition in vivid technologies’ dual-energy x-ray system for explosives detection. In *Applications of Signal and Image Processing in Explosives Detection Systems*, volume 1824, pages 127–143. International Society for Optics and Photonics, 1993.
- [15] Xinhua Shi. *Improving object classification in X-ray luggage inspection*. PhD thesis, Virginia Polytechnic Institute and State University, 2000.
- [16] Ernst Kalender, Willi A and Perman, WH and Vetter, JR and Klotz. Evaluation of a prototype dual-energy computed tomographic apparatus. I. Phantom studies. *Medical physics*, 13(3):334—339, 1986.
- [17] Michael Ellenbogen and Richard Bijjani. Liquids and homemade explosive detection. In *Optics and Photonics in Global Homeland Security V and Biometric Technology for Human Identification VI*, volume 7306, page 73060Y. International Society for Optics and Photonics, 2009.
- [18] B. J. Heismann, J. Leppert, and K. Stierstorfer. Density and atomic number measurements with spectral x-ray attenuation method. *Journal of Applied Physics*, 94(3):2073–2079, 2003.
- [19] Ji Sung Park and Jong Kyung Kim. Calculation of effective atomic number and normal density using a source weighting method in a dual Energy X-ray inspection system. *Journal of the Korean Physical Society*, 59(4):2709–2713, 2011.
- [20] Timothy P. Szczykutowicz, Zhihua Qi, and Guang-Hong Chen. A simple image based method for obtaining electron density and atomic number in dual energy CT. In *Medical Imaging 2011: Physics of Medical Imaging*, volume 7961, page 79613A. International Society for Optics and Photonics, 2011.
- [21] Oguz Semerci and Eric L. Miller. A parametric level-set approach to simultaneous object identification and background reconstruction for dual-energy computed tomography. *IEEE Transactions on Image Processing*, 21(5):2719–2734, 2012.

- 
- [22] Guillaume Landry, Joao Seco, Mathieu Gaudreault, and Frank Verhaegen. Deriving effective atomic numbers from DECT based on a parameterization of the ratio of high and low linear attenuation coefficients. *Physics in Medicine and Biology*, 58(19):6851–6866, 2013.
- [23] Hyun Woo Goo and Jin Mo Goo. Dual-energy CT: New horizon in medical imaging. *Korean Journal of Radiology*, 18(4):555–569, 2017.
- [24] Harry E Martz, Clint M Logan, Daniel J Schneberk, and Peter J Shull. *X-ray Imaging: fundamentals, industrial techniques and applications*. CRC Press, 2016.
- [25] Shingo Ohira, Hayate Washio, Masashi Yagi, Tsukasa Karino, Kenji Nakamura, Yoshihiro Ueda, Masayoshi Miyazaki, Masahiko Koizumi, and Teruki Teshima. Estimation of electron density, effective atomic number and stopping power ratio using dual-layer computed tomography for radiotherapy treatment planning. *Physica Medica*, 56(September):34–40, 2018.
- [26] M. Antoniassi, A. L.C. Conceição, and M. E. Poletti. Study of effective atomic number of breast tissues determined using the elastic to inelastic scattering ratio. *Nuclear Instruments and Methods in Physics Research, Section A: Accelerators, Spectrometers, Detectors and Associated Equipment*, 652(1):739–743, 2011.
- [27] Magdalena Bazalova and Edward E. Graves. The importance of tissue segmentation for dose calculations for kilovoltage radiation therapy. *Medical Physics*, 38(6):3039–3049, 2011.
- [28] Murat Kurudirek. Effective atomic numbers and electron densities of some human tissues and dosimetric materials for mean energies of various radiation sources relevant to radiotherapy and medical applications. *Radiation Physics and Chemistry*, 102:139–146, 2014.
- [29] HC Manjunatha. Comparison of effective atomic numbers of the cancerous and normal kidney tissue. *Radiation Protection and Environment*, 38(3):83, 2015.
- [30] H. C. Manjunatha and L. Seenappa. Pocket formula for mass attenuation coefficient, effective atomic number, and electron density of human tissues. *Nuclear Science and Techniques*, 30(3), 2019.
- [31] Zhihua Qi, Joseph Zambelli, Nicholas Bevins, and Guang Hong Chen. Quantitative imaging of electron density and effective atomic number using phase contrast CT. *Physics in Medicine and Biology*, 55(9):2669–2677, 2010.
- [32] Mukta D. Agrawal, Daniella F. Pinho, Naveen M. Kulkarni, Peter F. Hahn, Alexander R. Guimaraes, and Dushyant V. Sahani. Oncologic applications of dual- energy CT in the abdomen. *Radiographics*, 34(3):589–612, 2014.

- [33] Robert E. Alvarez. Energy Dependent Information in X-Ray Imaging : Part 1 . The Vector Space Description. *unpublished, year*, unpublished(January 1982), 1982.
- [34] L. A. Lehmann and R. E. Alvarez. Energy selective radiography: a review. *Digital Radiography: Selected Topics*, New York: Plenum(1):145–188, 1986.
- [35] Jeffrey A Fessler, Idris Elbakri, Predrag Sukovic, and Neal H Clinthorne. Maximum-likelihood dual-energy tomographic reconstruction. *Energy [keV]*, 20(72):105, 2002.
- [36] David Skillicorn. Singular Value Decomposition (SVD). *Understanding Complex Datasets*, pages 71–112, 2021.
- [37] Thorsten RC Johnson, Bernhard Krauss, Martin Sedlmair, Michael Grasruck, Herbert Bruder, Dominik Morhard, Christian Fink, Sabine Weckbach, Miriam Lenhard, Bernhard Schmidt, et al. Material differentiation by dual energy CT: Initial experience. *European Radiology*, 17(6):1510–1517, 2007.
- [38] Arthur Holly Compton, Samuel King Allison, et al. X-rays in theory and experiment. *New York, NY, USA: Van Nostrand*, 1935.
- [39] Mayneord, WV. The significance of the roentgen. *Acta of the International Union Against Cancer*, 2:271, 1937.
- [40] F. W. SPIERS. Effective atomic number and energy absorption in tissues. *The British journal of radiology*, 19(218):52–63, 1946.
- [41] Edwin C McCullough. Photon attenuation in computed tomography. *Medical Physics*, 2(6):307–320, 1975.
- [42] J. Weber and D. J. van den Berge. The effective atomic number and the calculation of the composition of phantom materials. *The British journal of radiology*, 42(497):378–383, 1969.
- [43] Z. H. Cho, C. M. Tsai, and G. Wilson. Study of contrast and modulation mechanisms in X-ray/photon transverse axial transmission tomography. *Physics in Medicine and Biology*, 20(6):879–889, 1975.
- [44] LA Lehmann, RE Alvarez, Aetal Macovski, WR Brody, NJ Pelc, Stephen J Riederer, and AL Hall. Generalized image combinations in dual kvp digital radiography. *Medical physics*, 8(5):659–667, 1981.
- [45] Jeffrey F. Williamson, Sicong Li, Slobodan Devic, Bruce R. Whiting, and Fritz A. Lerma. On two-parameter models of photon cross sections: Application to dual-energy CT imaging. *Medical Physics*, 33(11):4115–4129, 2006.

- 
- [46] Deborah J. Walter, Eric J. Tkaczyk, and Xiaoye Wu. Accuracy and precision of dual energy CT imaging for the quantification of tissue fat content. In *Medical Imaging 2006: Physics of Medical Imaging*, volume 6142, page 61421G. International Society for Optics and Photonics, 2006.
- [47] Willem G.J. Langeveld. Effective Atomic Number, Mass Attenuation Coefficient Parameterization, and Implications for High-Energy X-Ray Cargo Inspection Systems. *Physics Procedia*, 90(November 2016):291–304, 2017.
- [48] Doniyor Jumanazarov, Jakeoung Koo, Matteo Busi, Henning F. Poulsen, Ulrik L. Olsen, and Mihai Iovea. System-independent material classification through X-ray attenuation decomposition from spectral X-ray CT. *NDT and E International*, 116(July):102336, 2020.
- [49] K Wells and D A Bradley. A Review of X-ray Explosives Detection Techniques for Checked Baggage. *Applied Radiation and Isotopes*, 70(8):1729–1746, 2012.
- [50] Stephen G. Azevedo, Harry E. Martz, Maurice B. Aufderheide, William D. Brown, Kyle M. Champley, Jeffrey S. Kallman, G. Patrick Roberson, Daniel Schneberk, Isaac M. Seetho, and Jerel A. Smith. System-Independent Characterization of Materials Using Dual-Energy Computed Tomography. *IEEE Transactions on Nuclear Science*, 63(1):341–350, 2016.
- [51] Kyle M Champley, Stephen G Azevedo, Senior Member, Isaac M Seetho, Steven M Glenn, Larry D Mcmichael, Jerel A Smith, Jeffrey S Kallman, William D Brown, and Harry E Martz. Method to Extract System-Independent Material Properties From Dual-Energy X-Ray CT. *IEEE Transactions on Nuclear Science*, 66(3):674–686, 2019.
- [52] Polad M. Shikhaliev. Energy-resolved computed tomography: First experimental results. *Physics in Medicine and Biology*, 53(20):5595–5613, 2008.
- [53] A. Brambilla, P. Ouvrier-Buffet, J. Rinkel, G. Gonon, C. Boudou, and L. Verger. CdTe linear pixel X-ray detector with enhanced spectrometric performance for high flux X-ray imaging. *IEEE Transactions on Nuclear Science*, 59(4 PART 3):1552–1558, 2012.
- [54] Diana Shvydka, Xiance Jin, and E. Ishmael Parsai. Performance of Large Area Thin-Film CdTe Detector in Diagnostic X-Ray Imaging. *International Journal of Medical Physics, Clinical Engineering and Radiation Oncology*, 02(03):98–109, 2013.
- [55] E. Ishmael Parsai, Diana Shvydka, and Jun Kang. Design and optimization of large area thin-film CdTe detector for radiation therapy imaging applications. *Medical Physics*, 37(8):3980–3994, 2010.

- [56] Xiaolan Wang, Dirk Meier, Katsuyuki Taguchi, Douglas J. Wagenaar, Bradley E. Patt, and Eric C. Frey. Material separation in x-ray CT with energy resolved photon-counting detectors. *Medical Physics*, 38(3):1534–1546, 2011.
- [57] Limor Martin. *Enhanced information extraction in multi-energy X-ray tomography for security*. Phd thesis, Boston University, 2014.
- [58] A Brambilla, A Gorecki, A Potop, C Paulus, and L Verger. Basis material decomposition method for material discrimination with a new spectrometric X-ray imaging detector. *Journal of Instrumentation*, 12(8):P08014, 2017.
- [59] Busi, Matteo. *Enhanced Security Screening Using Spectral X-ray Imaging*. Phd thesis, Technical University of Denmark, 2019.
- [60] M. Joshi, D. A. Langan, D. S. Sahani, A. Kambadakone, S. Aluri, K. Procknow, X. Wu, R. Bhotika, D. Okerlund, N. Kulkarni, and D. Xu. Effective atomic number accuracy for kidney stone characterization using spectral CT. *Medical Imaging 2010: Physics of Medical Imaging*, 7622(March 2010):76223K, 2010.
- [61] Katsuyuki Taguchi and Jan S. Iwanczyk. Vision 20/20: Single photon counting x-ray detectors in medical imaging. *Medical physics*, 40(10):100901, 2013.
- [62] Nigel G. Anderson and Anthony P. Butler. Clinical applications of spectral molecular imaging: Potential and challenges. *Contrast Media and Molecular Imaging*, 9(1):3–12, 2014.
- [63] A. Potop, V. Rebuffel, J. Rinkel, A. Brambilla, F. Peyrin, and L. Verger. Investigation of the polynomial approach for material decomposition in spectral X-ray tomography using an energy-resolved detector. *Medical Imaging 2014: Physics of Medical Imaging*, 9033(March 2014):90333I, 2014.
- [64] Carsten O. Schirra, Bernhard Brendel, Mark A. Anastasio, and Ewald Roessl. Spectral CT: A technology primer for contrast agent development. *Contrast Media and Molecular Imaging*, 9(1):62–70, 2014.
- [65] Polad M. Shikhaliev. Soft tissue imaging with photon counting spectroscopic CT. *Physics in Medicine and Biology*, 60(6):2453–2474, 2015.
- [66] Veronique Rebuffel, Jean Rinkel, Joachim Tabary, and Loick Verger. New perspectives of X-ray techniques for explosive detection based on CdTe/CdZnTe spectrometric detectors. In *Proc. of the Int. Symp. on Digital Industrial Radiology and Computed Tomography*, volume 2, pages 1–8, 2011.
- [67] Jean Rinkel, Guillaume Beldjoudi, Véronique Rebuffel, Caroline Boudou, Patrice Ouvrier-buffet, Georges Gonon, Loïck Verger, and Andrea Brambilla. Experimental Evaluation of Material Identification Methods With CdTe X-ray Spectrometric Detector. *IEEE Transactions on Nuclear Science*, 58(5):2371–2377, 2011.

- 
- [68] G. Beldjoudi, V. Rebuffel, L. Verger, V. Kaftandjian, and J. Rinkel. Multidimensional data processing methods for material discrimination using an ideal X-ray spectrometric photon counting detector. *IEEE Transactions on Nuclear Science*, 58(6 PART 2):3190–3203, 2011.
- [69] Guillaume Beldjoudi, Véronique Rebuffel, Loïck Verger, Valérie Kaftandjian, and Jean Rinkel. An optimised method for material identification using a photon counting detector. *Nuclear Instruments and Methods in Physics Research, Section A: Accelerators, Spectrometers, Detectors and Associated Equipment*, 663(1):26–36, 2012.
- [70] Matteo Busi, K. Aditya Mohan, Alex A. Dooraghi, Kyle M. Champley, Harry E. Martz, and Ulrik L. Olsen. Method for system-independent material characterization from spectral X-ray CT. *NDT & E International*, 107(August):102136, 2019.
- [71] Robert Alvarez and Edward Seppi. A comparison of noise and dose in conventional and energy selective computed tomography. *IEEE Transactions on Nuclear Science*, 26(2):2853–2856, 1979.
- [72] Stephen J Riederer and CA Mistretta. Selective iodine imaging using K-edge energies in computerized x-ray tomography. *Medical Physics*, 4(6):474–481, 1977.
- [73] R. C. Smith and J. M. Connelly. CT Technologies. *Aspects of Explosives Detection*, pages 131–145, 2009.
- [74] Sunghwan Kim, Jie Chen, Tiejun Cheng, Asta Gindulyte, Jia He, Siqian He, Qingliang Li, Benjamin A. Shoemaker, Paul A. Thiessen, Bo Yu, Leonid Zaslavsky, Jian Zhang, and Evan E. Bolton. PubChem 2019 update: Improved access to chemical data, 2019.
- [75] Jens Gregor and Thomas Benson. Computational analysis and improvement of SIRT. *IEEE Transactions on Medical Imaging*, 27(7):918–924, 2008.
- [76] Sebastian Siegfried Lukas Ehn. *Photon-counting hybrid-pixel detectors for spectral x-ray imaging applications*. PhD thesis, Technische Universität München, 2017.
- [77] Thomas Flohr, Martin Petersilka, Andre Henning, Stefan Ulzheimer, Jiri Ferda, and Bernhard Schmidt. Photon-counting CT review. *Physica Medica*, 79(October):126–136, 2020.
- [78] Erik Schou Dreier, Jan Kehres, Mohamad Khalil, Matteo Busi, Yun Gu, Robert Feidenhans, and Ulrik Lund Olsen. Spectral correction algorithm for multispectral CdTe x-ray detectors. *Optical Engineering*, 57(5):16, 2018.

- [79] Andrea Brambilla, P. Ouvrier-Buffet, G. Gonon, J. Rinkel, V. Moulin, C. Boudou, and L. Verger. Fast CdTe and CdZnTe semiconductor detector arrays for spectroscopic X-ray imaging. *IEEE Transactions on Nuclear Science*, 60(1):408–415, 2013.
- [80] Mats Persson, Ben Huber, Staffan Karlsson, Xuejin Liu, Han Chen, Cheng Xu, Moa Yveborg, Hans Bornefalk, and Mats Danielsson. Energy-resolved CT imaging with a photon-counting silicon-strip detector. *Physics in Medicine and Biology*, 59(22):6709–6727, 2014.
- [81] Y. Eisen and Y. Horovitz. Correction of incomplete charge collection in CdTe detectors. *Nuclear Inst. and Methods in Physics Research, A*, 353(1-3):60–66, 1994.
- [82] D. S. McGregor and H. Hermon. Room-temperature compound semiconductor radiation detectors. *Nuclear Instruments and Methods in Physics Research, Section A: Accelerators, Spectrometers, Detectors and Associated Equipment*, 395(1):101–124, 1997.
- [83] Harrison H Barrett, JD Eskin, and HB Barber. Charge transport in arrays of semiconductor gamma-ray detectors. *Physical Review Letters*, 75(1):156, 1995.
- [84] Hiroyuki Toyama, Akira Higa, Masaaki Yamazato, Takehiro Maehama, Ryoichi Ohno, and Minoru Toguchi. Quantitative analysis of polarization phenomena in CdTe radiation detectors. *Japanese Journal of Applied Physics, Part 1: Regular Papers and Short Notes and Review Papers*, 45(11):8842–8847, 2006.
- [85] Derek S. Bale and Csaba Szeles. Nature of polarization in wide-bandgap semiconductor detectors under high-flux irradiation: Application to semi-insulating Cd<sub>1-x</sub>Zn<sub>x</sub>Te. *Physical Review B - Condensed Matter and Materials Physics*, 77(3):1–16, 2008.
- [86] P. Guerra, A. Santos, and D. G. Darambara. Development of a simplified simulation model for performance characterization of a pixellated CdZnTe multimodality imaging system. *Physics in Medicine and Biology*, 53(4):1099–1113, 2008.
- [87] Johann Plagnard. Comparison of measured and calculated spectra emitted by the X-ray tube used at the Gustave Roussy radiobiological service. *X-Ray Spectrometry*, 43(5):298–304, 2014.
- [88] Daniel J Schroeder. *Astronomical optics*. Elsevier, 1999.
- [89] Adam S. Wang and Norbert J. Pelc. Optimal energy thresholds and weights for separating materials using photon counting x-ray detectors with energy discriminating capabilities. In *Medical Imaging 2009: Physics of Medical*



- Imaging*, volume 7258, page 725821. International Society for Optics and Photonics, 2009.
- [90] Adam S. Wang and Norbert J. Pelc. Sufficient statistics as a generalization of binning in spectral X-ray imaging. *IEEE Transactions on Medical Imaging*, 30(1):84–93, 2011.
- [91] Xiaolan Wang, Jingyan Xu, and Eric C. Frey. Optimization of energy window widths in basis material decomposition using a multi-window photon counting X-ray detector. In *2007 IEEE Nuclear Science Symposium Conference Record*, volume 5, pages 3826–3829. IEEE, 2007.
- [92] Slaney M Kak, A.C. *Principles of computerized tomographic imaging*. IEEE press, 1988.
- [93] Richard Gordon, Robert Bender, and Gabor T Herman. Algebraic reconstruction techniques (art) for three-dimensional electron microscopy and x-ray photography. *Journal of theoretical Biology*, 29(3):471–481, 1970.
- [94] Thorsten M. Buzug. *Computed Tomography: From Photon Statistics to Modern Cone-Beam CT*. Springer-Verlag Berlin Heidelberg, 2008.
- [95] Gengsheng Lawrence Zeng. *Medical image reconstruction: a conceptual tutorial*. Springer, 2010.
- [96] Jiang Hsieh. *Computed tomography : principles, design, artifacts, and recent advances*, volume 114. SPIE press, 2003.
- [97] Leonid I. Rudin, Stanley Osher, and Emad Fatemi. Nonlinear total variation based noise removal algorithms. *Physica D: nonlinear phenomena*, 60(1-4):259–268, 1992.
- [98] Jiayu Song, Qing H. Liu, G. Allan Johnson, and Cristian T. Badea. Sparseness prior based iterative image reconstruction for retrospectively gated cardiac micro-CT. *Medical Physics*, 34(11):4476–4483, 2007.
- [99] Junguo Bian, Jiong Wang, Xiao Han, Emil Y. Sidky, Lingxiong Shao, and Xiaochuan Pan. Optimization-based image reconstruction from sparse-view data in offset-detector CBCT. *Physics in Medicine and Biology*, 58(2):205–230, 2013.
- [100] Emil Y. Sidky, Chien Min Kao, and Xiaochuan Pan. Accurate image reconstruction from few-views and limited-angle data in divergent-beam CT. *Journal of X-Ray Science and Technology*, 14(2):119–139, 2006.
- [101] Peter Blomgren and Tony F. Chan. Color TV: Total variation methods for restoration of vector-valued images. *IEEE Transactions on Image Processing*, 7(3):304–309, 1998.

- [102] Kevin M. Holt. Total Nuclear Variation and Jacobian Extensions of Total Variation for Vector Fields. *IEEE Transactions on Image Processing*, 23(9):3975–3989, 2014.
- [103] Benjamin Recht, Maryam Fazel, and Pablo A Parrilo. Guaranteed minimum-rank solutions of linear matrix equations via nuclear norm minimization. *SIAM review*, 52(3):471–501, 2010.
- [104] David S. Rigie and Patrick J. La Rivière. Joint reconstruction of multi-channel, spectral CT data via constrained total nuclear variation minimization. *Physics in Medicine and Biology*, 60(5):1741–1762, 2015.
- [105] David S. Rigie, Adrian A. Sanchez, and Patrick J. La Rivière. Assessment of vectorial total variation penalties on realistic dual-energy CT data. *Physics in Medicine and Biology*, 62(8):3284–3298, 2017.
- [106] Zhichao Zhong, Willem Jan Palenstijn, Jonas Adler, and K. Joost Batenburg. EDS tomographic reconstruction regularized by total nuclear variation joined with HAADF-STEM tomography. *Ultramicroscopy*, 191:34–43, 2018.
- [107] Takamichi Miyata and Yoshinori Sakai. Vectorized total variation defined by weighted L infinity norm for utilizing inter channel dependency. In *2012 19th IEEE International Conference on Image Processing*, pages 3057–3060. IEEE, 2012.
- [108] Joan Duran, Michael Moeller, Catalina Sbert, and Daniel Cremers. On the Implementation of Collaborative TV Regularization: Application to Cartoon+Texture Decomposition. *Image Processing On Line*, 5:27–74, 2016.
- [109] Luc Salvo, Michel Suéry, Ariane Marmottant, Nathalie Limodin, and Dominique Bernard. 3D imaging in material science: Application of X-ray tomography. *Comptes Rendus Physique*, 11(9-10):641–649, 2010.
- [110] E. Maire and P. J. Withers. Quantitative X-ray tomography. *International Materials Reviews*, 59(1):1–43, 2014.
- [111] Jian-Feng Cai, Emmanuel J Candès, and Zuowei Shen. A singular value thresholding algorithm for matrix completion. *SIAM Journal on optimization*, 20(4):1956–1982, 2010.
- [112] Emmanuel J Candès, Xiaodong Li, Yi Ma, and John Wright. Robust principal component analysis? *Journal of the ACM (JACM)*, 58(3):1–37, 2011.
- [113] Jorge Nocedal and Stephen J Wright. *Numerical Optimization*. Springer, New York, 1999.

- 
- [114] Predrag Sukovic and Neal H. Clinthorne. Penalized weighted least-squares image reconstruction for dual energy X-ray transmission tomography. *IEEE Transactions on Medical Imaging*, 19(11):1075–1081, 2000.
- [115] P C Hansen. The L-Curve and its Use in the Numerical Treatment of Inverse Problems. *in Computational Inverse Problems in Electrocardiology*, ed. P. Johnston, *Advances in Computational Bioengineering*, 4:119–142, 2000.
- [116] Xiaoli Yang, Ralf Hofmann, Robin Dapp, Thomas van de Kamp, Tomy dos Santos Rolo, Xianghui Xiao, Julian Moosmann, Jubin Kashef, and Rainer Stotzka. TV-based conjugate gradient method and discrete L-curve for few-view CT reconstruction of X-ray in vivo data. *Optics Express*, 23(5):5368, 2015.
- [117] Martin Hanke. Limitations of the L-curve method in ill-posed problems. *BIT Numerical Mathematics*, 36(2):287–301, 1996.
- [118] Shivaramu. Effective atomic numbers for photon energy absorption and photon attenuation of tissues from human organs. *Medical Dosimetry*, 27(1):1–9, 2002.
- [119] Madelon AF Zenobio, Teogenes A Silva, Maria SN Tavares, and Elton G Zenobio. Effective atomic number of human enamel and dentin within a photo energy range from 10 to 200 keV. ', 2011.
- [120] Mitchell M. Goodsitt, Emmanuel G. Christodoulou, and Sandra C. Larson. Accuracies of the synthesized monochromatic CT numbers and effective atomic numbers obtained with a rapid kVp switching dual energy CT scanner. *Medical Physics*, 38(4):2222–2232, 2011.
- [121] H. C. Manjunatha and B. Rudraswamy. Study of effective atomic number and electron density for tissues from human organs in the energy range of 1 keV-100 GeV. *Health Physics*, 104(2):158–162, 2013.
- [122] Doniyor Jumanazarov, Jakeoung Koo, Jan Kehres, Henning F. Poulsen, Ulrik L. Olsen, and Mihai Iovea. Material classification from sparse spectral X-ray CT using vectorial total variation based on L infinity norm [Data set]. Zenodo, May 2021.

# APPENDIX

---

## Paper A

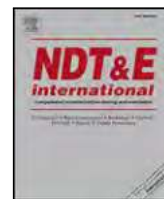
**System-independent material classification through X-ray attenuation decomposition from spectral X-ray CT.**

Doniyor Jumanazarov, Jakeoung Koo, Matteo Busi, Henning. F. Poulsen, Ulrik L. Olsen and Mihai Iovea



Contents lists available at ScienceDirect

NDT and E International

journal homepage: [www.elsevier.com/locate/ndteint](http://www.elsevier.com/locate/ndteint)

## System-independent material classification through X-ray attenuation decomposition from spectral X-ray CT

Doniyor Jumanazarov<sup>a,d</sup>, Jakeoung Koo<sup>b</sup>, Matteo Busi<sup>c,a</sup>, Henning F. Poulsen<sup>a</sup>, Ulrik L. Olsen<sup>a</sup>, Mihai Iovea<sup>d,\*</sup>

<sup>a</sup> Technical University of Denmark, DTU Physics, 2800 Kgs. Lyngby, Denmark

<sup>b</sup> Technical University of Denmark, DTU Compute, 2800 Kgs. Lyngby, Denmark

<sup>c</sup> Paul Scherrer Institute, Forschungsstrasse 111, 5232 Villigen, Switzerland

<sup>d</sup> ACCENT PRO 2000 s.r.l. (AP2K), Nerva Traian 1, K6, Ap. 26, Bucharest, S3, 031041, Romania

### ARTICLE INFO

#### Keywords:

Spectral X-ray CT  
Electron density  
Effective atomic number  
Photon counting detectors  
Security screening

### ABSTRACT

We present a method for material classifications in spectral X-ray Computed Tomography (SCT) taking advantage of energy-resolving 2D detectors to simultaneously extract the energy dependence of a material's linear attenuation coefficient (LAC). The method employs an attenuation decomposition presented by Alvarez et al., and estimates system-independent material properties of electron density ( $\rho_e$ ) and effective atomic number ( $Z_{\text{eff}}$ ), independent of the scanner, from the energy-dependent LAC measurements. The method uses a spectral correction algorithm and the energy range is truncated to exclude bins with photon starvation and spectral distortion present even after correction of detector response. A novel technique of energy bin selection is used for optimized classification performance. The method is tested against another SCT classification method called SRZE for inspecting materials in the range of  $6 \leq Z_{\text{eff}} \leq 23$ . Our method aims at an increase in the speed of post processing workflow after the data acquisition, and it achieves explicitly up to 32 times better time efficiency for the reconstruction with comparable accuracy for a range of materials important in threat detection.

### 1. Introduction

The discrimination between innocuous liquids and precursors for homemade explosives is a difficult challenge for civil aviation safety screenings, since both types of materials are organic liquids with similar X-ray attenuation. The detection of these threats and other traditional explosives requires a technology that can provide accurate material features [1]. Over the years, X-ray Computed Tomography (CT) has been widely used for Non-Destructive Testing (NDT), as well as in the field of illegal material detection [2]. Conventional CT measures the effective linear attenuation coefficient (LAC) across a broad energy range since the typical X-ray sources generate a polychromatic beam. The Hounsfield unit is often used with conventional CT. It represents the attenuation spectra with a single value, with an uncertainty that is larger than the inter-material variation for some materials [1]. In 1976, Alvarez et al. [3] showed a method for CT that decomposes LAC into photoelectric absorption and Compton scattering basis functions and they demonstrated that an alternative material characterization with just two parameters density,  $\rho$ , and effective atom number,  $Z_{\text{eff}}$  can define the whole spectral range of the LAC. Dual-energy CT (DECT)

measures two different signals in the attenuation spectrum and can be used to reconstruct both parameters [4–14]. The Dual-Energy detector as shown in Fig. 1 have overlapping low- and high-energy spectrums and the Dual-Energy Systems suffer from poor energy separation.

The material classification through the effective LAC with dual-energy sandwich detectors, detectors currently in use in security screening systems is a system-dependent solution [4,15] since it depends on source spectrum, filtration, and detector's efficiency. Recently, Azevedo et al. [4] proposed a method that estimates ( $\rho_e$ ,  $Z_{\text{eff}}$ ) from dual-energy CT known as the System-Independent  $\rho_e/Z_{\text{eff}}$  (SIRZ), independent of the scanner, presented in Fig. 1 and Champléy et al. [16] have developed the method further (SIRZ-2). Like all DECT this method requires two successive scans with different source kilovoltage peaks and filtration, and additionally the calibration of the detector's spectral response by using a group of reference materials. In the range of  $Z_{\text{eff}}$  between 6 and 20, and energies up to 200 keV, the accuracy error and precision errors for estimating both ( $\rho_e$ ,  $Z_{\text{eff}}$ ) features in SIRZ were less than 3% and 2% respectively, while the SIRZ-2 accuracy errors were 0.7% for  $\rho_e$  and < 1.5% for  $Z_{\text{eff}}$ , and the SIRZ-2 precision errors for both were up to 2.3%.

\* Corresponding author.

E-mail addresses: [doniyor.jumanazarov@fysik.dtu.dk](mailto:doniyor.jumanazarov@fysik.dtu.dk) (D. Jumanazarov), [jakoo@dtu.dk](mailto:jakoo@dtu.dk) (J. Koo), [matteo.busi@psi.ch](mailto:matteo.busi@psi.ch) (M. Busi), [hفو@fysik.dtu.dk](mailto:hفو@fysik.dtu.dk) (H.F. Poulsen), [ullu@dtu.dk](mailto:ullu@dtu.dk) (U.L. Olsen), [office@accent.ro](mailto:office@accent.ro) (M. Iovea).

<https://doi.org/10.1016/j.ndteint.2020.102336>

Received 21 June 2020; Accepted 22 July 2020

Available online 28 July 2020

0963-8695/© 2020 Elsevier Ltd. All rights reserved.

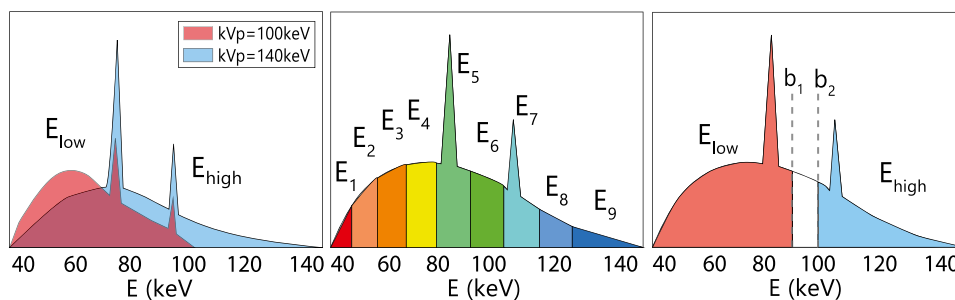


Fig. 1. Illustration of the dual-energy CT, SRZE and SIMCAD methods. Left: in dual-energy X-ray CT, the sample attenuation is measured at low- and high energies with two different spectra that are overlapping and thus reduces the estimation performance [17,18]. Center: in classical spectral X-ray CT, the sample attenuation is measured at multiple energy bins using PCDs [19,20]. Right: in the optimized bi-energy bins approach to spectral X-ray CT, the sample attenuation is measured without overlap at low- and high energies with PCDs in a single acquisition. The selection of the upper and lower thresholds of low- and high-energies, respectively  $b_1$  and  $b_2$  is discussed in the Section 3.2.

The development of cadmium telluride (CdTe) energy-discriminating imaging detectors has paved the way for Spectral CT [21–23]. Spectral CT with an energy resolved photon counting detector (PCD) is proved to have a number of advantages over dual-energy CT for improving material identification [24,25]. This has resulted in a large interest in PCDs within security applications [19,26]. In material identification by radiography, Rinkel et al. [17] presented through experimental data that the false detection rate when using 90 energy bins with a PCD was reduced by a factor of up to 2 and more than 3 (for thin objects) compared to an optimized dual-energy bins approach applied both on the same PCD data and to a dual-layer sandwich detector, respectively. Beldjoudi et al. [18,24] showed through simulations in Radiography that PCDs with data condensed into two energy bins enhanced recognition of single materials by over 50% relative to dual-layer sandwich detectors. Increasing the number of energy bins resulted in a further rise of 80% in material identification with 90 energy bins compared to dual-layer sandwich detectors. They found that the poor spectral separation in the dual-layer sandwich detectors appears to be the main reason for the inferior performance. In contrast PCDs exhibit a significantly better spectral resolution. As expected, using energy bins with a width below the energy resolution of the detector did not lead to great improvement in identification performances. However, using a higher number of energy bins or narrow bin widths provided a more robust configuration, regardless of the thickness and nature of the material. A simulation study by Wang et al. [27] showed how to select the energy bin widths to optimize the performance of basis material decomposition in material recognition. To check the accuracy and precision of the method in estimating the thickness of the two basis materials, they investigated five different energy bin combinations to define energy bins setting energy bin thresholds for each; bins of equal width, bins of equal incident photon counts, bins of equal incident photon intensity, bins of equal photon count and bins with equal photon intensity after passing through 3 cm of PMMA. They found the best results when using energy bins with similar incident photon counts. Martin et al. [19] introduced a learning and adaptive model-based method to optimally select the bins for material characterization from multi-energy data.

The MultiX ME100 (MultiX, Neuilly-sur-Seine, France) PCD is a good candidate for high flux measurements to extract a spectrally resolved LAC. Brambilla et al. [28] implemented a basis material decomposition method for material characterization using this detector. This method requires a calibration of the detector's spectral response for a group of reference materials, and only estimates  $Z_{\text{eff}}$  accurately in 3D measurements. Based on the MultiX detector the SIRZ method was further extended into the Spectral  $\rho_e/Z_{\text{eff}}$  Estimation (SRZE) method presented by Busi et al. [20], which estimates system-independent ( $\rho_e$ ,  $Z_{\text{eff}}$ ) directly from the spectral LACs in Spectral CT (in Fig. 1). The accuracy of the SRZE method relies on the accurate measurement of spectral LACs, and it decreased for materials with smaller  $Z_{\text{eff}}$  due to

detector response artifacts at lower energies, where the contrast of low  $Z_{\text{eff}}$  material is also highest [20].

The method presented in this work aims to estimate the system-independent material features ( $\rho_e Z_{\text{eff}}$ ), independent of the system or specifics of the scanner, such as the X-ray spectrum. It uses the attenuation decomposition presented by Alvarez et al. [3] for Spectral CT. Fig. 1 illustrates the principles of the novel method, named system-independent material classification through attenuation decomposition (SIMCAD). As illustrated, this approach is based on non-overlapping optimized bi-energy bins separated by a gap. Wang et al. [29,30] presented that for PCDs that discriminate between low and high energy photons, having a gap between energy thresholds is useful for material separability. Photons with energies that lie in this gap should either be discarded or counted separately to enhance performance. Therefore, the energy range falling into this gap was discarded in the optimized bi-energy bins approach in our work. The method requires a calibration step to find the energy-dependent basis functions of the decomposed attenuation by using a set of reference materials. Materials are then classified through the two parameters ( $\rho_e$  and  $Z_{\text{eff}}$ ) that can fully describe the wide range of materials that may appear in baggage scanners [31].

In this work, we compare the performance of the SRZE and SIMCAD methods over a common set of materials using experimental data. The SRZE method reaches the optimal performance at 64 energy bins and provides noticeably lower classification performance with two energy bins [32]. The SIMCAD method utilizes optimized bi-energy bins for comparable classification performance, and uses at least 32x shorter time for the tomographic reconstruction after the data acquisition directly due to a lower number of energy bins. The speed makes the method compatible with the requirements for applications where rapid scanning is required. Check-in baggage inspection at airports is such an application where the time and computational resources required for spectral reconstruction represents a major issue [33].

## 2. Theory and methods

The aim of this section is firstly to define the system-independent material features used to classify materials from experimental data, and secondly to present instrumentation and methods with the detection algorithm.

### 2.1. Photoelectric-Compton decomposition

Bragg and Peirce (1914) [34], Owen (1919) [35] and Richtmyer and Warburton (1923) [36] established the original concept of the dependence of photon interactions upon atomic number ( $Z$ ), and this concept has been implemented in many radiation studies [37]. For a computerized tomography system, Alvarez et al. [3] showed empirically over the range of 30–200 keV that the LAC could be decomposed in the form:

$$\mu(E) = a_1 \frac{1}{E^3} + a_2 f_{\text{KN}}(E), \quad (1)$$

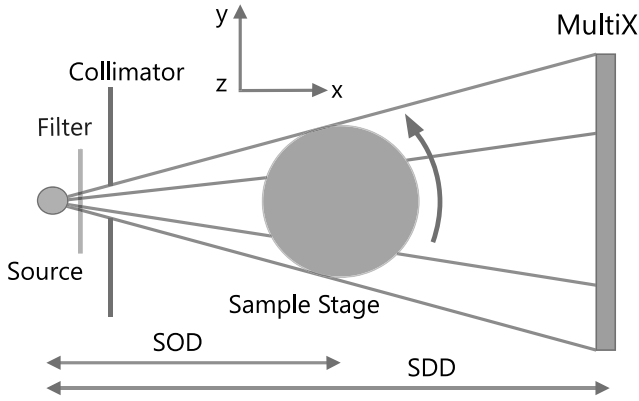


Fig. 2. The illustration of the instrumental setup.

where  $f_{\text{KN}}(E)$  is the Klein–Nishina function

$$f_{\text{KN}}(\epsilon) = \frac{1 + \epsilon}{\epsilon^2} \left( 2 \frac{1 + \epsilon}{1 + 2\epsilon} - \frac{\ln(1 + 2\epsilon)}{\epsilon} \right) + \frac{\ln(1 + 2\epsilon)}{2\epsilon} - \frac{1 + 3\epsilon}{(1 + 2\epsilon)^2}, \quad (2)$$

and  $\epsilon = E/511 \text{ keV}$  ( $\epsilon = E/m_e c^2$ ) is the reduced energy of the incident photon. The functions  $1/E^3$  and  $f_{\text{KN}}(E)$  approximate the energy dependence of the photoelectric absorption and Compton scattering, respectively. Excluding the effect of absorption edges, they further showed that the photoelectric coefficient,  $a_1$  and the Compton scattering coefficient,  $a_2$  could be expressed in terms of physical parameters as:

$$a_1 \approx K_1 \frac{\rho}{A} Z^n, \quad a_2 \approx K_2 \frac{\rho}{A} Z \quad (3)$$

where  $K_1$  and  $K_2$  are constants,  $\rho$  is mass density ( $\text{g}/\text{cm}^3$ ),  $A$  is atomic mass and  $Z$  is atomic number.  $n$  is the exponent for photoelectric attenuation (per atom). We optimize  $n$  for each of the classification approaches depending on how many energy bins are used.  $a_1$  and  $a_2$  represent only approximate expressions. The insertion of  $a_1$  and  $a_2$  from Eq. (3) into Eq. (1) yields the LAC:

$$\mu(E) = \frac{Z}{A} \rho (Z^{n-1} p(E) + c(E)), \quad (4)$$

where

$$p(E) = K_1 \frac{1}{E^3}, \quad c(E) = K_2 f_{\text{KN}}(E). \quad (5)$$

$p(E)$  and  $c(E)$  are photoelectric absorption and Compton scattering basis functions, respectively. The basis functions are empirical defined through experimental fit to data. In our calculations, we optimize the basis functions and parameter  $n$  for the best classification performance and the resulting optimized values for all the multiple energy bins approaches are presented in the Section 2.5.

## 2.2. Electron density and effective atomic number

X-ray attenuation is proportional to a material's electron density [38]. The electron density is the number of electrons per unit volume (electron – mole/ $\text{cm}^3$ ) and related to mass density, atomic number and atomic mass of an element as:

$$\rho_e = \frac{Z}{A(Z)} \rho, \quad (6)$$

For a compound or mixture that has the composition of  $N$  total different elements  $i$  each with a number of atoms,  $\alpha_i$ , the electron density can be derived as

$$\rho_e = \frac{\sum_{i=1}^N \alpha_i Z_i}{\sum_{i=1}^N \alpha_i A_i} \rho. \quad (7)$$

For compounds, the atomic number is referred to as effective atomic number,  $Z_{\text{eff}}$  and a now classical parameterization was proposed by Mayneord (1937) [39] and Spiers (1946) [40] as

$$Z_{\text{eff}} = \sqrt{\sum_{i=1}^N r_i Z_i^l}, \quad (8)$$

where  $N$  is the number of elements in the material,  $Z_i$  is the atomic number for each element,  $i$ ,  $r_i$  is “relative electron fraction” contribution. The relative electron fraction of an element,  $i$  is expressed as

$$r_i = \frac{\alpha_i Z_i}{\sum_{j=1}^N \alpha_j Z_j},$$

where  $\alpha_i$  is the number of atoms that have atomic number  $Z_i$ .

No single formula of  $Z_{\text{eff}}$  can characterize the alteration of photoelectric absorption cross section over the particular range of the photon energies and materials with the acceptable accuracy of interest in CT [37,40–47]. The Compton interaction takes place with relatively unbound electrons for the photon energy range and materials relevant to CT Systems, and consequently the Compton scattering cross section is independent of chemical makeup of materials and only is a function of photon energy [41], as discussed in the Sections 2.1 and 2.5. Therefore, the exponent  $l$  is optimized depending on the material, source spectrum and system features. Usually, this parameter,  $l$  changes between 2.94 and 3.8 based on experimental fits for different CT systems. In our calculations,  $l$  is set to the value of the original Lehmann parameterization, which is 3.8 [44]. Even though Eq. (8) neglects the coherent scatter part, this definition of  $Z_{\text{eff}}$  based on the Lehmann parameterization operates quite well because the total cross section is mostly governed by the Compton cross section for the set of our materials and photon energy range [44,47]. Thus, we use two separate sets of parameters,  $n$  and  $l$  to define the photoelectric absorption cross section term, being optimized depending on the approach of multiple energy bins and single value for all the materials, respectively. In the Section 3.1, the dependence of the classification performance on exponent  $l$  is presented and it is discussed how this exponent is selected in this work.

Substituting Eq. (6) into Eq. (4) we obtain a parameterized LAC for a compound material as

$$\mu(E) = \rho_e (Z_{\text{eff}}^{n-1} p(E) + c(E)). \quad (9)$$

## 2.3. Experimental setup and data correction

Fig. 2 illustrates the instrumentation. The experiments were performed in the 3D Imaging Center at DTU, Denmark. A Hamamatsu X-ray source was used operating at the acceleration voltage and the filament current set to 160 kV and 0.5 mA, respectively. The focal spot for these parameters is 75  $\mu\text{m}$ . An aluminum filter of 2 mm thickness was used to remove photons with energies lower than the detector energy range. The beam was collimated into a fan beam geometry. The samples were placed on the rotation stage and scanned during the acquisition over a range of 360 degrees in discrete steps of 1° increments. The source to detector distance (SDD) was set to 701 mm while the source to sample distance (SOD) was 500 mm.

The detector system comprises five MultiX ME100 modules, each consisting of  $1 \times 128$  pixels of size  $0.8 \times 0.8 \text{ mm}^2$ . The number of energy bins is flexible and could be configured for the purpose of the experiment between 2 and 128. In this work it was set to 128 with a width of 1.1 keV each, evenly distributed in the energy range between 20 and 160 keV. The energy resolution of the detector, defined by the Full Width at Half Maximum (FWHM) is 6.5% (8 keV at 122 keV) by high X-ray fluxes [23]. In this work, the total integration time per projection is 8 s.

Charge sharing, weighting potential, escape peaks, pulse pile-up and incomplete charge collection in PCDs lead to data distortion [48]. These

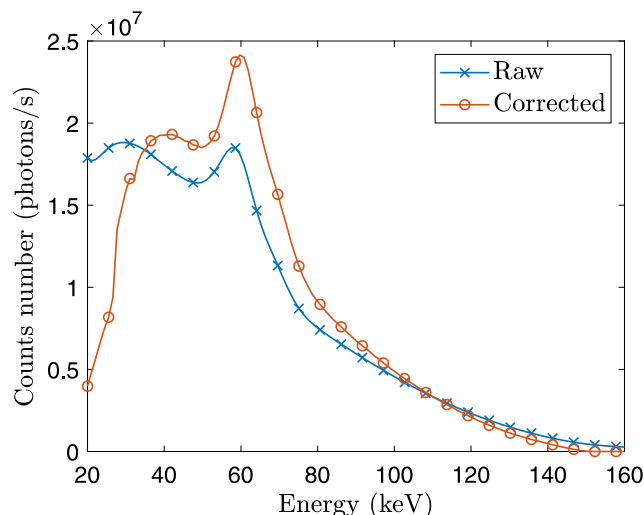


Fig. 3. X-ray source spectra before and after applying spectral correction algorithm. The number of counts per second summed over all detector pixels is shown, measured through the MultiX ME100 PCD.

effects are related to energy and flux, and therefore, the data distortion affects the material's attenuation property. To correct for these spectral effects we used the correction algorithm presented by Dreier et al. [48]. Fig. 3 shows the raw and corrected source spectrum. The average counts integrated for the spectra was approximately  $1.6 \times 10^6$  counts/pixel per second.

Table 1 lists the materials studied in this work as well as their reference  $\rho_e$  and  $Z_{\text{eff}}$  values that were calculated by using Eq. (7) and Eq. (8) and the exponent  $l = 3.8$ , respectively. The material features presented in the table will be used as the reference values in the following sections. The distribution of  $Z_{\text{eff}}$  for materials commonly found in a passenger bag peaks between 7–8. Most organic materials belong to this range [1]. The plastics used for the experiment were polymethyl methacrylate (PMMA), polytetrafluoroethylene (PTFE), polyvinylidene fluoride (PVDF), polycarbonate (PC), polyoxymethylene-C (POM-C), polyethylene terephthalate (PET) and polyoxymethylene-H (POM-H). These plastics were chosen since several explosives have similar chemical compositions, e.g. POM has been considered an explosive simulant [17]. The classification of plastics is thus an efficient gauge for a system's ability to identify explosive materials in luggage. The materials used in the work represents the same  $Z_{\text{eff}}$  variation as various organic tissues [49] and none have K-edge absorption within the detector's energy range. Sample dimension are found in Table 1 through width $\times$ length or diameter for rectangular and circular samples respectively.

#### 2.4. Setting low- and high-energy thresholds and LAC extraction

For each projection the photon counts  $I_k$  of energy bin  $k$  is converted to line integrals  $L_k$  based on Lambert–Beer's law as:

$$L_k(\vec{x}) = -\log \frac{I_k(\vec{x})}{I_{0,k}(\vec{x})}, \quad k = 1, 2, 3, \dots, 128; \quad (10)$$

where  $I_{0,k}$  is the flat-field photon flux for energy bin  $k$ , i.e. the projection measured by the detector without inserting the sample. This is also referred as the source spectrum or the system's spectral response.  $\vec{x}$  represents the 1D detector pixel array, the detector has total 128 energy bins.

The intensity in the gap spaces between two adjacent modules, with the width approximately equal to two pixels, were filled by neighbor interpolation. Slice reconstructions were performed individually for each energy bin from each line integral (or sinogram) by using the

SIRT implementation in the ASTRA Toolbox [51] to extract LACs of materials. Fig. 4 presents how the LAC values are extracted from the histogram based on Gaussian curve fits after sample reconstruction. MATLAB<sup>®</sup>'s `fitdist` function with normal distribution was used to extract the LACs for all materials and for all approaches of the number of used energy bins. The ring artifacts in the reconstruction may be due to the difference in detector response for the pixels at crystal edges in the detector since the correction algorithm is optimized for the central pixels.

Fig. 5 shows measured and reference spectral LAC of PTFE plastic and aluminum with and without spectral correction. Additional spectral distortions appear at low- and high-energies, which cannot be totally corrected by the spectral correction algorithm. LAC deviations from the reference values at low- and high-energies could be due to detector flux variation and photon starvation, i.e. complete attenuation of photons [48]. Energy bins with those deviations are excluded by setting low- and high-energy thresholds,  $E_l$  and  $E_f$  that are kept constant for all materials. We note that there is a slight deviation between the measured LAC and the reference values between 55 keV and 65 keV. We suspect that the detector resolution is lower for the higher flux flat field and at places in the spectrum of higher discontinuities the LAC is affected.

The data is rebinned in low- and high energy. The formulation presented here for the thresholds is compatible with an arbitrary number of bins. As an example, merging energy-resolved data in the optimized bi-energy bins approach defined in the Section 3.2 is performed by summing the corrected incident photon flux  $I_k$  for selected  $k$  energy bins before converting to line integrals as:

$$I_L = \sum_{k=i}^{k=b_1} I_k, \quad I_H = \sum_{k=b_2}^{k=f} I_k \quad (11)$$

where  $I_L$  and  $I_H$  are merged photon flux for low- and high-energies, and  $i$  and  $f$  denote low- and high-energy threshold bins, respectively.  $b_1$  and  $b_2$  are the upper and lower thresholds of low- and high-energies, respectively (in Fig. 1).

The classification performance has been tested for optimized bi-, 6, 15, 30, 45 and 90 energy bins and the results are presented in the Section 3.4. Titanium showed the LAC noticeably deviated from the reference values at lower energies that is due to complete attenuation of radiation at this energy range. Fig. 6 presents the measured, fitted and reference LAC of titanium. The deviated LAC of titanium has been fitted by using polynomial extrapolation with MATLAB<sup>®</sup>'s `polyfit` function between 32.1 keV and 131.3 keV, which became low- and high-energy thresholds, respectively for 15, 30, 45 and 90 energy bins approaches and for all materials. The energy bins in these approaches were spaced uniformly between low- and high-energy thresholds with equal width bins. For optimized bi- and 6 energy bins approaches the number of bins was insufficient for the extrapolation, instead the deviated LAC of titanium from 32.1 keV was truncated and the energy bins were spaced over 57.5 keV and 131.3 keV that were set as low- and high-energy thresholds, respectively for all materials. Without LAC extrapolation, the number of bins in this PCD is insufficient to employ 90 bins for classifications between 57.5 keV and 131.3 keV thresholds as shown in Fig. 5.

Fig. 6 also shows counts for flat field spectra and low- and high-energy thresholds for all variations of energy bins used and the gap between low- and high-energies in the optimized bi-energy bins approach.

#### 2.5. Calibration of basis functions and $n$

From Eq. (9), LAC for each energy bin can be expressed as

$$\mu_m(E_k) = \rho_{e,m} \left( Z_{\text{eff},m}^{n-1} p(E_k) + c(E_k) \right), \quad (12)$$

where  $m = 1, 2, \dots, M$ ,  $k = 1, 2, \dots, K$  with  $M$  being the total number of reference materials listed in Table 1 and  $K$  being the number of energy



**Table 1**

The list of all the materials scanned and processed through the method, and their physical properties  $\rho_e$  and  $Z_{\text{eff}}$ . The mass density,  $\rho$  for the plastic materials was measured with uncertainties of  $\pm 0.15\%$ . The mass densities for the rest of materials represent the theoretical values found in PubChem data, [50].

Material	Chemical formula	Width×length/ Diameter (mm)	$\rho$ (g/cm <sup>3</sup> )	$\rho_e$ (e <sup>-</sup> mol/cm <sup>3</sup> )	$Z_{\text{eff}}$
PMMA	(C <sub>5</sub> O <sub>2</sub> H <sub>8</sub> ) <sub>n</sub>	40 × 42	1.18	0.636	6.60
PTFE	(C <sub>2</sub> F <sub>4</sub> ) <sub>n</sub>	9 × 53.3	2.16	1.039	8.50
PVDF	(C <sub>2</sub> H <sub>2</sub> F <sub>2</sub> ) <sub>n</sub>	9 × 53.5	1.8	0.9	8.01
PC	(CO <sub>3</sub> C <sub>13</sub> H <sub>8</sub> ) <sub>n</sub>	8.2 × 53.5	1.19	0.615	6.48
POM-C	(CH <sub>2</sub> O) <sub>n</sub>	9 × 53.5	1.42	0.758	7.07
PET	(C <sub>10</sub> H <sub>8</sub> O <sub>4</sub> ) <sub>n</sub>	9 × 53.5	1.39	0.726	6.74
POM-H	(CH <sub>2</sub> O) <sub>n</sub>	15.5 × 53.3	1.44	0.766	7.07
Acetone	C <sub>3</sub> H <sub>6</sub> O	20	0.785	0.432	6.44
Hyd. Peroxide	H <sub>2</sub> O <sub>2</sub> (50%)	20	1.22	0.661	7.65
Methanol	CH <sub>3</sub> OH	20	0.792	0.446	6.86
Water	H <sub>2</sub> O	20	0.997	0.554	7.54
Nitromethane	CH <sub>3</sub> NO <sub>2</sub>	20	1.14	0.597	7.27
Aluminum	Al	25	2.70	1.3	13
Silicon	Si	25	2.33	1.161	14
Magnesium	Mg	12.7	1.74	0.858	12
Titanium	Ti	12.7	4.51	2.071	22

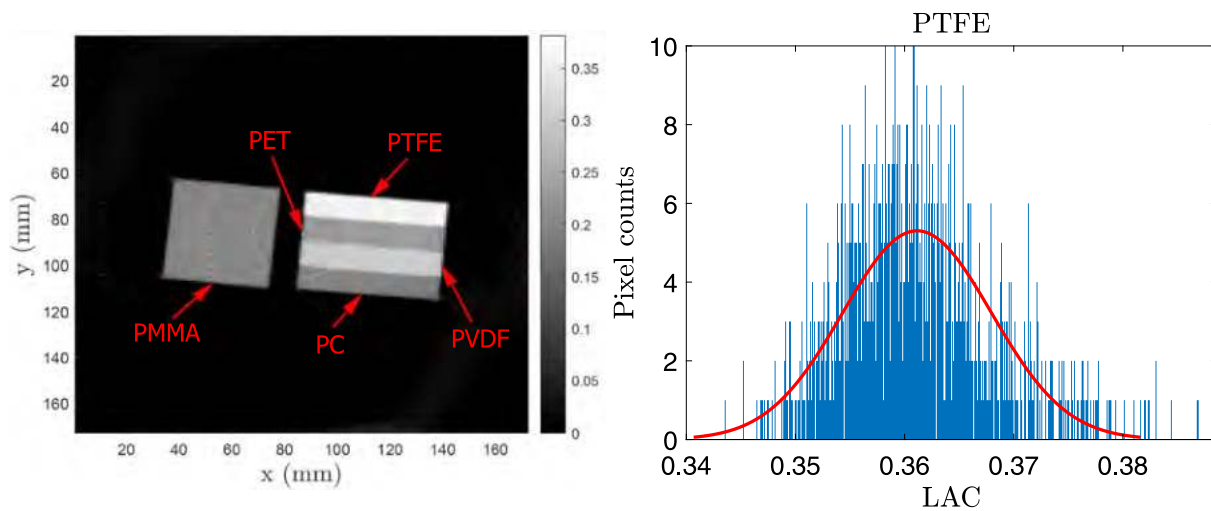


**Fig. 4.** The mean LAC extraction based on the normal distribution. Left: 2D reconstruction of a sample including the five plastic materials indicated by red arrows. The color bar shows linear attenuation coefficients (LACs) for the low energy bin of the optimized bi-energy approach defined in the Section 3.2. Right: the histogram of PTFE plastic (blue bars) shown with a Gaussian peak fit (red line). The pixel counts represent the number of pixels in the PTFE plastic area marked by the arrow to the left, each having the corresponding LACs presented on the x-axis.

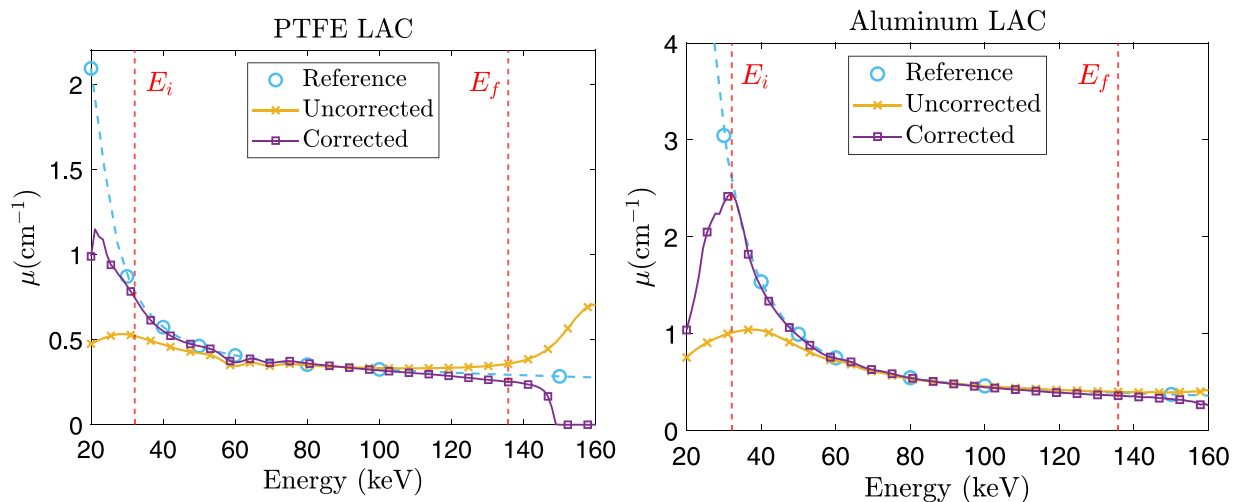


**Fig. 5.** Energy resolved LAC for PTFE (left) and aluminum (right) obtained with and without spectral correction. The reference LACs were defined by using NIST cross-sections, [52]. Where the LAC deviates at low- and high-energies the spectra are truncated, and low- and high-energy thresholds,  $E_i$  and  $E_f$  are constant for all materials as shown with the vertical red dash-dotted lines.

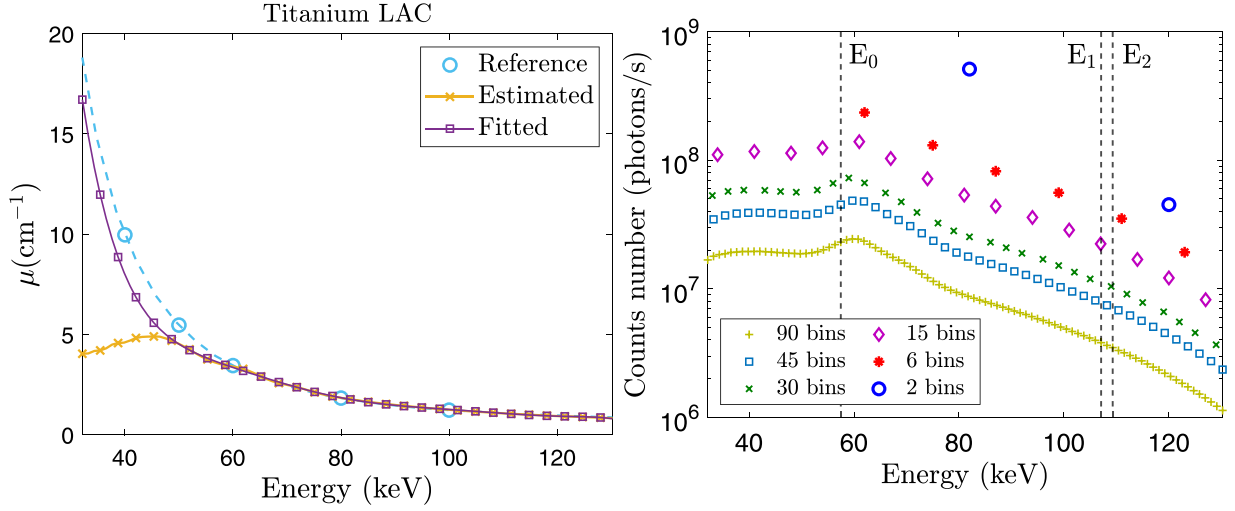


**Fig. 6.** Fitting LAC by extrapolation and photon counts for all the approaches for variations of energy bins used. Left: the measured and fitted LAC obtained by using polynomial extrapolation and the reference LAC of titanium. Right: counts in the flat field spectra for optimized bi-, 6, 15, 30, 45 and 90 energy bins approaches. A vertical lines at  $E_0$  (57.5 keV) is the low-energy threshold for optimized bi- and 6 energy bins, and the lines at  $E_1$  (107 keV) and  $E_2$  (109.3 keV) show the gap between low- and high-energies of optimized bi-energy bins. Note logarithmic scale on the y-axis.

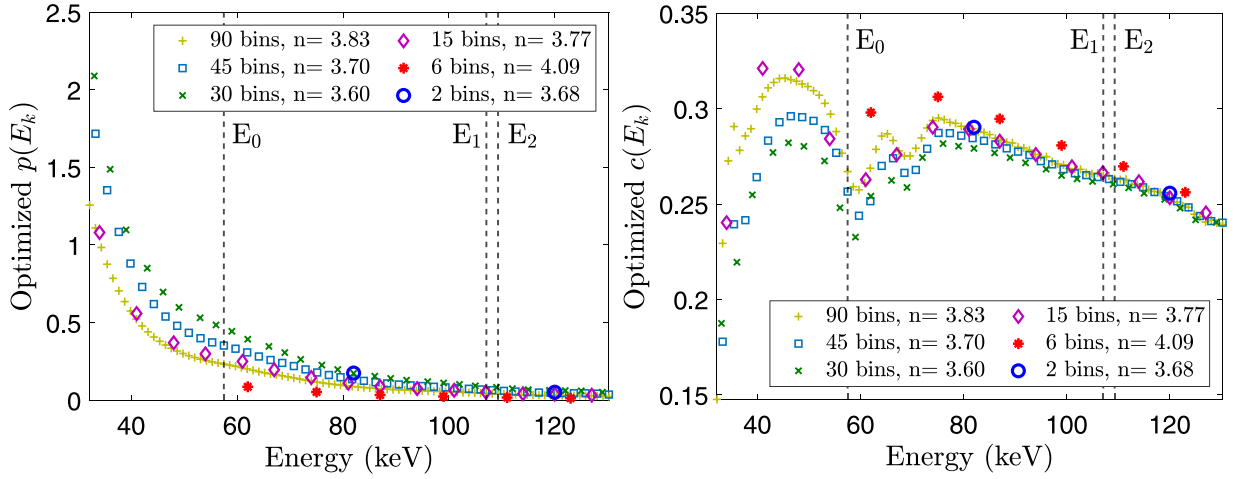


**Fig. 7.** Optimized photoelectric absorption  $p(E_k)$  (left) and Compton scattering  $c(E_k)$  (right) basis functions for optimized bi-, 6, 15, 30, 45 and 90 energy bins approaches. The optimized values of exponent  $n$  are also presented for each multiple energy bins approach. A vertical lines at  $E_0$  (57.5 keV) is the low-energy threshold for optimized bi- and 6 energy bins, and the lines at  $E_1$  (107 keV) and  $E_2$  (109.3 keV) shows the gap between low- and high-energies of optimized bi-energy bins.

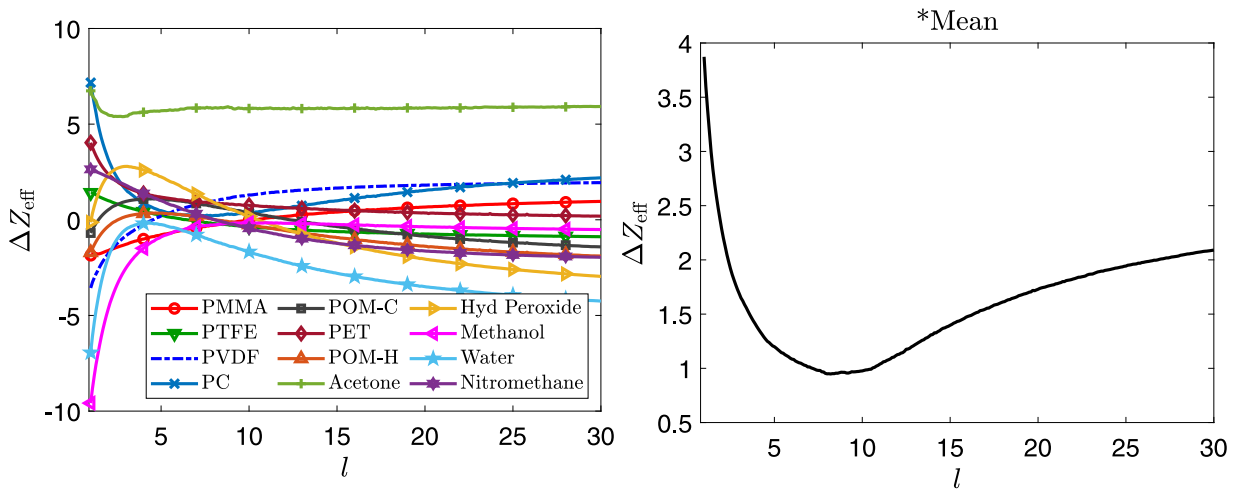


**Fig. 8.** The variation of accuracy with exponent  $l$ . Left: the percent relative deviations for  $Z_{\text{eff}}$  defined in Eq. (8), as a function of exponent  $l$  for the materials presented. Right: the mean percent relative deviation for  $Z_{\text{eff}}$  calculated from absolute values of relative deviations for each material shown in the left frame. As expected, the relative deviations for the electron density for all the materials did not show noticeable dependence on  $l$ .

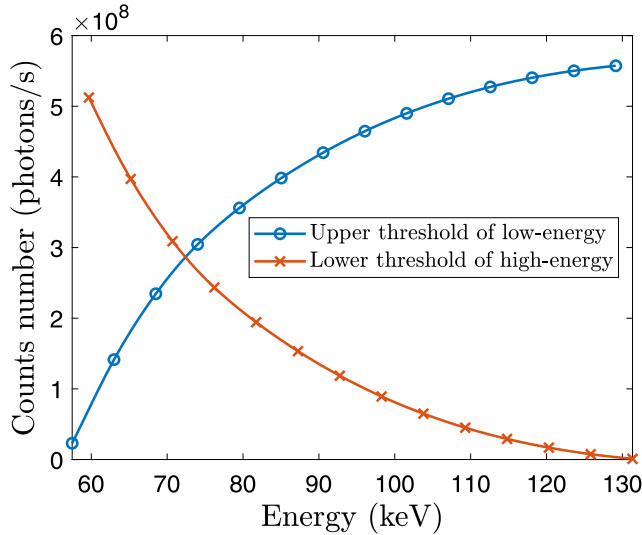


Fig. 9. Photon counts of low- and high-energies of all detector pixels in the flat field spectrum as a function of the gap position being shifted from low- to high-energy threshold. The gap corresponds to the upper and lower thresholds of low- and high-energies in the bi-energy bins approach, respectively.

bins used for a particular classification approach.  $p(E_k)$  and  $c(E_k)$  are photoelectric absorption and Compton scattering basis functions for energy bin  $E_k$ , respectively. These are calibrated and the same for all materials.

We optimize not only the basis functions, but also the parameter  $n$  for better estimation. Due to the non-linearity with respect to  $n$ , solving Eq. (12) is not straightforward. We impose positivity constraints for all basis functions and  $n$  on the solution. With this constraint, we formulate the objective function as follows:

$$\min_{0 \leq p_1, c_1, \dots, p_K, c_K, n} \sum_{m=1}^M \sum_{k=1}^K \left( \mu_m(E_k) - \rho_{e,m} (Z_{\text{eff},m}^{n-1} p_k + c_k) \right)^2, \quad (13)$$

where  $p_k = p(E_k)$  and  $c_k = c(E_k)$ . To optimize Eq. (13), we employ a nonlinear least square solver based on trust region method [53]. The minimization was performed with MATLAB<sup>®</sup>'s **lsqnonlin** function with initial constraints that we chose as  $p_k^0 = 0.5$ ,  $c_k^0 = 0.5$  and  $n^0 = 3.6$  for all  $k$ . The calibration results showed no particular dependency on the starting values.

At low energies, the photoelectric cross section is a strong function of atomic number, as seen in Eq. (1) and Eq. (3). This effect can be used to achieve strong contrast even for materials with small differences in electron densities and effective atomic numbers. For most biological materials, as the photon energy increases over 60 keV, the dependence of the LACs on atomic number rapidly decreases and the photon attenuation occur mostly due to Compton interaction where mass density and electron density dominate the LACs [43]. Fig. 7 shows the resulting optimized values of the  $p(E_k)$ ,  $c(E_k)$  basis functions and of  $n$  for all the multiple energy bins approaches analyzed in our work. As expected, over roughly 60 keV, photoelectric absorption basis functions that decrease over the whole energy range become lower than those for Compton scattering part. As a result, the  $p(E_k)$  basis functions values in optimized bi- and 6 energy bins approaches are 1.7 to 5 and 3.5 to 19.7 times lower than  $c(E_k)$ , respectively.

The reported values of exponent  $n$  defined in photoelectric cross section term in the literature changes between nearly 3.94 and 5, as a function of the photon energy and also materials [37,42–45,47,54]. Weber et al. (1969) [42] proposed the value of 4.4 for  $n$ . For CT systems, the suggested exponents were 3.94 by Phelps et al. (1975) [55], 4.4 by Cho et al. (1975) [43], 4.62 by Rutherford et al. (1976) [54] and 4.8 by McCullough (1975) [41]. For idealized dual-energy CT imaging in the

energies between 20 keV and 1000 keV, Williamson et al. (2006) [45] separated parameterization into two sets of exponents depending on atomic number range and found 5.05 and 4.69 for  $2 \leq Z \leq 8$  and  $8 < Z \leq 20$ , respectively. They estimated theoretically linear attenuation coefficients with absolute mean and maximum accuracy errors of up to 2.2% and 6%, respectively, however there were relatively higher errors at low energies and at higher  $Z$ . For high-energy X-ray cargo inspection, Langeveld (2017) [47] gave an improved Lehmann-type parameterization of LACs at energies of 20 – 1000 keV, which resulted in a better definition of photoelectric absorption cross section term and in turn  $Z_{\text{eff}}$ . X-ray attenuation coefficients were fitted quite well over a broad range of  $Z$ . The value of  $n$  in their fits was 4.14. In our work, the optimized values of exponent  $n$  were found to be between 3.60 and 4.09 depending on the number of energy bins, as shown in Fig. 7. The higher the  $n$  value is, the lower  $p(E_k)$  and the higher  $c(E_k)$  basis functions are for all energies. The highest value of  $n = 4.09$  found for the approach using 6 energy bins presents the lowest classification performance, as discussed in the Section 3.4. The reason for relatively lower values of  $n$  found in our work may be due to our parameterization and the multi-spectral dimensionality of LACs defined in Eq. (12).

## 2.6. $(\rho_e, Z_{\text{eff}})$ calculation

The calibration parameters ( $p(E_k)$ ,  $c(E_k)$  and  $n$ ) and the measured LAC  $\mu(E_k)$  are used to retrieve  $(\rho_e, Z_{\text{eff}})$ . For  $M$ - and  $K$ - total number of unknown materials and energy bins, respectively, we reformulate Eq. (12) as a linear system equation as follows:

$$\begin{pmatrix} \bar{p} & \bar{c} & & & \\ & & \ddots & & \\ & & & \bar{p} & \bar{c} \end{pmatrix} \begin{pmatrix} z_1 \\ \rho_{e,1} \\ \vdots \\ z_M \\ \rho_{e,M} \end{pmatrix} = \begin{pmatrix} \bar{\mu}_1 \\ \vdots \\ \bar{\mu}_M \end{pmatrix} \quad (14)$$

where  $z_m$  is a temporary variable introduced instead of  $\rho_{e,m} Z_{\text{eff}}^{n-1}$  and  $\bar{p} = (p_1, \dots, p_K)^T$ ,  $\bar{c} = (c_1, \dots, c_K)^T$  and  $\bar{\mu}_m = (\mu_m(E_1), \dots, \mu_m(E_K))^T$ . In the latter equation, the size of the linear matrix is  $(M \times K)$ -by- $(2 \times M)$  and the number of unknowns is  $2 \times M$ . We use a linear least square solver called **lsqnonneg** function in MATLAB<sup>®</sup> with the positivity constraint on the solution returning the vector  $(z_1, \rho_{e,1}, \dots, z_M, \rho_{e,M})$  that minimizes the norm. After solving it, the effective atomic numbers are retrieved for all materials by

$$Z_m = \left( \frac{z_m}{\rho_{e,m}} \right)^{\frac{1}{n-1}}. \quad (15)$$

The method accuracy was estimated as the percent relative deviation from the reference values for  $\rho_e$  and  $Z_{\text{eff}}$  as:

$$\Delta Z_{\text{eff}}^{\text{rel}} = 100\% \cdot \frac{Z_{\text{eff}}^{\text{est}} - Z_{\text{eff}}^{\text{ref}}}{Z_{\text{eff}}^{\text{ref}}}, \quad (16)$$

$$\Delta \rho_e^{\text{rel}} = 100\% \cdot \frac{\rho_e^{\text{est}} - \rho_e^{\text{ref}}}{\rho_e^{\text{ref}}} \quad (17)$$

where superscripts est and ref refer to the estimated and reference values, respectively.

## 3. Results and discussions

### 3.1. Investigating classification performance as a function of exponent $l$

We studied how the classification performance changes with the selection of the exponent  $l$  defined in  $Z_{\text{eff}}$  formula (Eq. (8)) for the materials such as plastics and liquids listed in Table 1, to tune this value on the best match for our experimental data. The classifications were performed using plastic materials as references in the calibration step and optimized bi-energy bins for the calculations. Fig. 8 presents the dependence of relative errors for  $Z_{\text{eff}}$  on exponent  $l$  for the materials

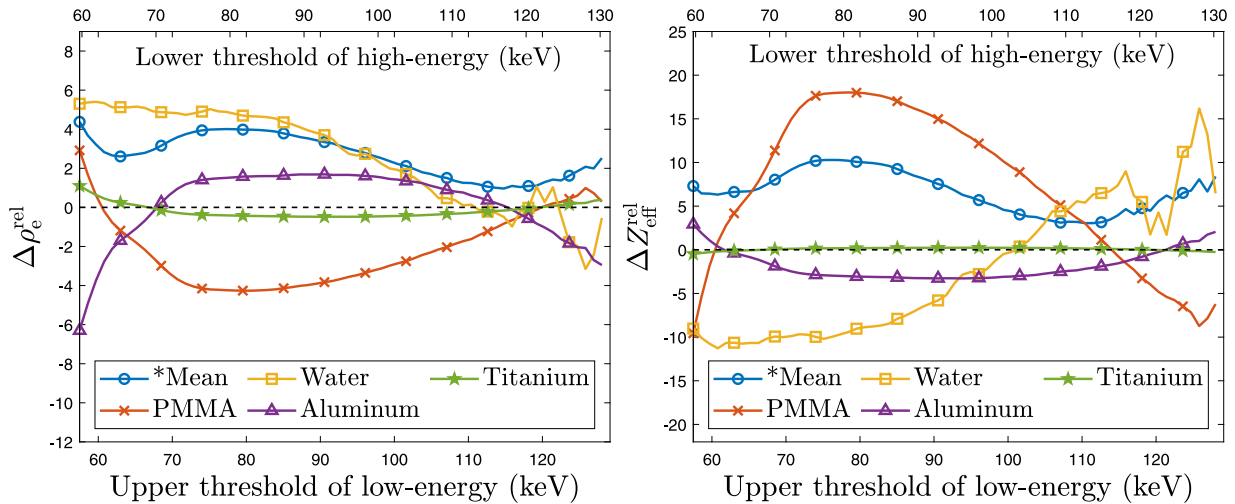


Fig. 10. Optimization of the bi-energy-bin method based on relative deviations for  $\rho_e$  (left) and  $Z_{eff}$  (right). \*The mean deviation was calculated from the absolute values of relative deviations for each material listed in Table 1.

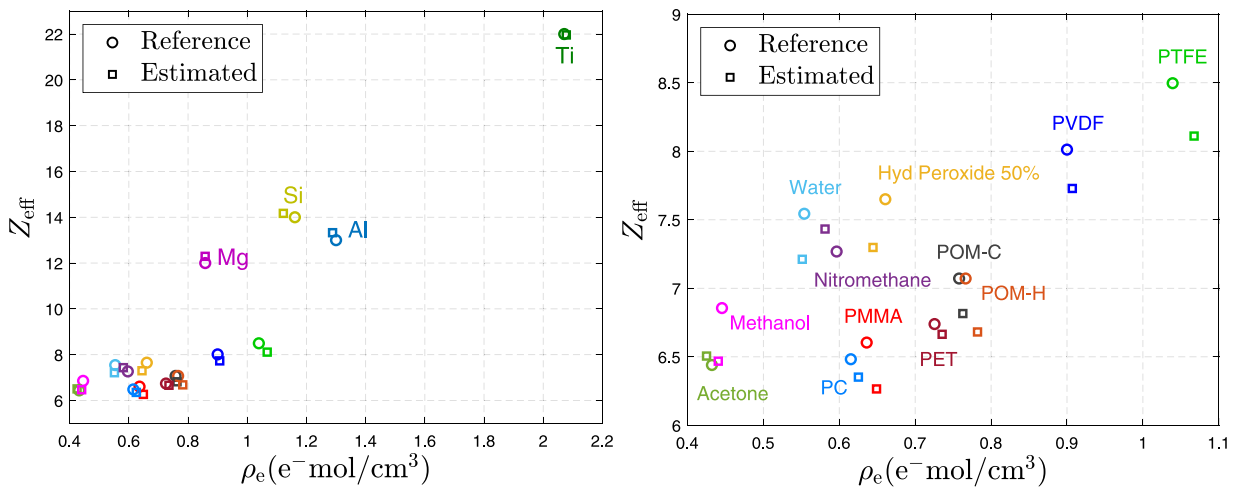


Fig. 11. Estimated and reference ( $\rho_e, Z_{eff}$ ) obtained with the SIMCAD method using optimized bi-energy bins. A magnified version of the lower left part of the left frame is presented in the right frame to avoid overlap of the material labeled names.

shown. Based on the mean relative deviations, we find that the optimal range of exponent  $l$  is between 7.2 and 10.5 with lower than 1% deviations and the minimum deviation is approximately 0.9% at  $l = 8.0$  whereas the deviation is 1.4% at the reference value of  $l = 3.8$ . Thus, the exponent  $l$  given in the references is not optimal with this set of materials, source spectrum and detector response. To preserve consistence with the previously published works in comparing the performance, we keep the reference value of  $l = 3.8$  for our calculations of reference  $Z_{eff}$  values.

### 3.2. Optimizing the method for bi-energy bins

Fig. 1 illustrates the gap between low- and high-energies when using optimized bi-energy bins. How low and high energy photons are binned together is important for classification performance. Therefore, to optimize the method the gap is shifted from low- to high-energy threshold in increments of one energy bin and the gap width is selected as two energy bins equal to 2.3 keV and kept constant over the whole energy range. Fig. 9 presents how the photon counts for low- and high-energies change with respect to position of the gap corresponding to the upper and lower thresholds of low- and high-energies, respectively.

Fig. 10 shows the changes in the percent relative deviations for  $\rho_e$  and  $Z_{eff}$  of the mean values (for all materials), PMMA, water,

aluminum and titanium between the low- and high-energy thresholds when using bi-energy bins. The chart shows that the relative deviations for the materials with higher  $Z_{eff}$  values such as aluminum and titanium remain lower and more stable over the whole energy range compared to liquids and plastics for both  $\rho_e$  and  $Z_{eff}$ . The optimal classification performance is reached when low-energy is between 57.5 keV and 107 keV while high-energy is 109.3 keV to 131.3 keV with mean relative deviations of 1.5% and 3.1% for  $\rho_e$  and  $Z_{eff}$ , respectively. The results for all the materials obtained with optimized bi-energy bins are presented in the next subsection. In contrast to a simulation study presented by Wang et al. [27] estimating the thickness of the two basis materials, we find that similar incident photon flux in low- and high-energies when using bi-energy bins do not provide the optimal classification performance, this result is seen in Fig. 9. The reason may be because our results are based on experimental data with realistic noise level and spectral artifact.

### 3.3. ( $\rho_e, Z_{eff}$ ) map

Fig. 11 shows a ( $\rho_e, Z_{eff}$ ) chart of estimated and reference values. Table 2 lists the percent relative deviations for both of estimated material features for SIMCAD and SRZE methods. The SIMCAD method gives promising results with mean relative deviations of 1.5% for  $\rho_e$ ,

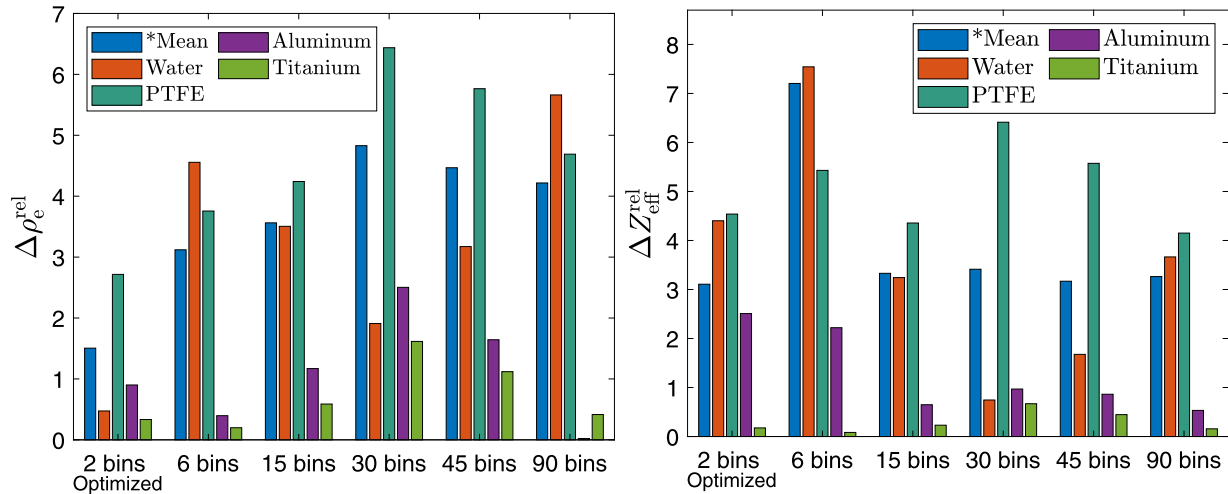


Fig. 12. The percent relative deviations for  $\rho_e$  (left) and  $Z_{\text{eff}}$  (right) as a function of the number of energy bins used for classifications. Optimized bi-energy bins gives better classification performance. \*The mean deviation was calculated from absolute values of relative deviations for each material listed in Table 1.

Table 2

The percent relative deviations for  $(\rho_e, Z_{\text{eff}})$  with the reference values. To compare, SRZE estimations are taken from [20,32].

Material	$\rho_e^{\text{ref}} (\text{e}^- \text{mol}/\text{cm}^3)$	SIMCAD $\Delta\rho_e^{\text{rel}} (\%)$	SRZE $\Delta\rho_e^{\text{rel}} (\%)$	$Z_{\text{eff}}^{\text{ref}}$	SIMCAD $\Delta Z_{\text{eff}}^{\text{rel}} (\%)$	SRZE $\Delta Z_{\text{eff}}^{\text{rel}} (\%)$
PMMA	0.636	-2.0	-2.3	6.60	5.1	-0.3
PTFE	1.039	-2.7	0.1	8.50	4.5	-2.5
PVDF	0.9	-0.8	-0.8	8.01	3.5	-1.4
PC	0.615	-1.6	1.4	6.48	2.0	-1.8
POM-C	0.758	-0.6	-1.4	7.07	3.6	-0.9
PET	0.726	-1.4	-3.1	6.74	1.1	-0.1
POM-H	0.766	-2.0	-2.4	7.07	5.5	-0.4
Acetone	0.432	1.6	-2.3	6.44	-1.0	5.0
H <sub>2</sub> O <sub>2</sub> (50%)	0.661	2.4	-0.2	7.65	4.6	5.4
Methanol	0.446	1.1	1.4	6.86	5.6	-4.7
Water	0.554	0.5	-6.9	7.54	4.4	-2.7
Nitromethane	0.597	2.6	1.7	7.27	-2.3	2.5
Aluminum	1.3	0.9	-3.2	13	-2.5	0.7
Silicon	1.161	3.4	-5.5	14	-1.2	-0.7
Magnesium	0.858	0.03	-5.4	12	-2.4	0.8
Titanium	2.071	-0.3	-0.7	22	0.2	-1.2
Mean <sup>a</sup>	-	1.5	2.4	-	3.1	1.9

<sup>a</sup>The mean values were calculated from absolute values of each column.

and 3.1% for  $Z_{\text{eff}}$  using optimized bi-energy bins, whereas the SRZE method yields deviations of 2.4% and 1.9% respectively with 64 energy bins [20]. With only two energy bins, the SRZE method has a noticeably higher deviation of 9.4% for  $\rho_e$ , and 13.4% for  $Z_{\text{eff}}$  for single material samples [32]. Thus, our method using much fewer energy bins can provide a significant reduction in computing time, which is important for security screening scanners. It can be noted from the table that as the effective atomic number increases, the classification accuracy also increases. Thus the method may be robust also for materials with higher  $Z_{\text{eff}}$  values.

### 3.4. Classification performance as a function of the number of energy bins used

How a source spectrum is sampled for all the multiple energy bins approaches is described in the Section 2.4. Fig. 12 highlights the relative errors for  $(\rho_e, Z_{\text{eff}})$  depending on the number of energy bins used. For  $\rho_e$ , the mean relative error values increase as the number of energy bins used increases reaching 4.2% at 90 energy bins. For  $Z_{\text{eff}}$ , the error remains almost unchanged being equal to 3.3% at 90 energy bins, with an exception for 6 energy bins where the error is 7.2%. Materials with higher  $Z_{\text{eff}}$  values such as aluminum and titanium show noticeably lower relative error for all numbers of energy bins used compared to plastics and liquids.

The classification performance is worse for the 6 energy bins approach compared to optimized-bi-energy bins. The reason may be that the thresholds of 6 energy bins approach are not optimized whereas those for optimized-bi-energy bins are. Thus, optimizing the energy bin thresholds is desired for better performance when the number of energy bins used is low. A similar phenomenon was previously observed in radiography studies by Beldjoudi et al. [18,24]. However, contrary to their findings, employing 15, 30, 45 and 90 energy bins does not enhance but rather deteriorates classification performance relative to optimized-bi-energy bins approach. This may be because energy bin widths for 15, 30, 45 and 90 energy bins, which are equally distributed throughout the spectrum are below the energy resolution of the detector (8 keV) corresponding, respectively, to energy bin widths of 6.6 keV, 3.3 keV, 2.2 keV and 1.1 keV; Secondly the detector noise becomes greater as the number of energy bins increases. Since the bin width for approaches using 30 and 45 energy bins are smaller compared to the approach of 15 energy bins, they are less dependent on energy threshold optimization. The approach of 90 energy bins does not require any threshold optimization. Despite this fact, 15 energy bins approach without the energy bin threshold optimization appears to have better classification performance compared to 30, 45 and 90 energy bins. Overall optimized bi-energy bins achieve the best classification performance, and shows the best robustness for all the materials we classified in this work.

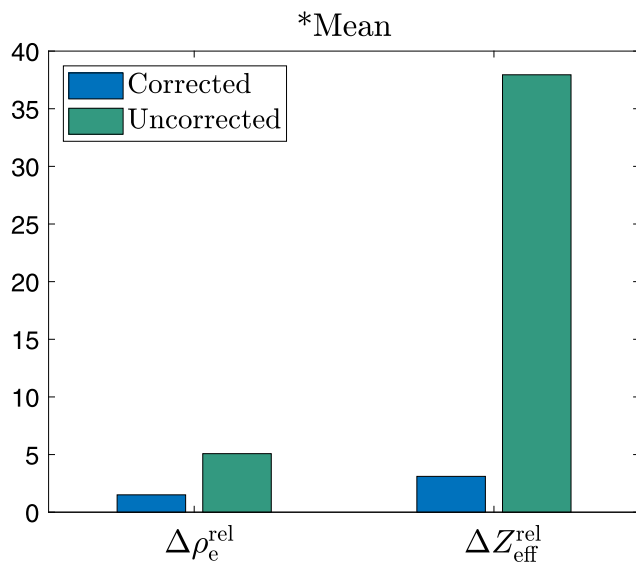


Fig. 13. \*The mean deviation for  $(\rho_e, Z_{\text{eff}})$  obtained by corrected and uncorrected LACs in the optimized bi-energy approach, calculated from absolute values of relative deviations for each material used.

Fig. 13 shows the mean relative deviations obtained by corrected and uncorrected LACs from optimized bi-energy bins, which equals 5.0% and 37.9% for  $\rho_e$  and  $Z_{\text{eff}}$ , respectively without the correction. Therefore the method requires the use of a spectral correction algorithm.

#### 4. Conclusion

We have presented the SIMCAD method for material characterization from system-independent physical parameters  $(\rho_e, Z_{\text{eff}})$  using Spectral CT systems. We explored the influence of the number of used energy bins on the performance of the method by applying different energy thresholds to define the energy bins. Employing a non-optimized energy bins approaches with a low number of energy bins used leads to a noticeable decrease in classification performance. It was presented that the approaches with energy bin widths below the detector energy resolution does not provide noticeable enhancement in classifications further, and we found the method to be most accurate employing just optimized bi-energy bins. The formulation of method however, is compatible with an arbitrary number of energy bins. We saw the use of a correction algorithm remove most detector response artifacts from the LAC, and classification even with optimized bi-energy bins is shown to require the correction. SIMCAD requires a calibration step using a set of reference materials to calibrate photoelectric absorption and Compton scattering basis functions and  $n$  from the LAC expression.

In contrast to the SRZE method, which reaches the best accuracy with 64 energy bins [20], the SIMCAD method gives comparable accuracy with only optimized bi-energy bins, which gives up to 32 times reduction in computing time due to the reduced number of CT reconstructions required. This makes the method compatible with the requirements of high speed security scanners. Our method employing a single scan is also comparable to the state-of-the-art techniques using dual-energy CT scans in terms of reconstruction time and material classifications, and it provides a better classification performance for highly attenuating materials [4,16]. The method is shown to be applicable in the range of  $6 \leq Z_{\text{eff}} \leq 23$  however, since higher  $Z_{\text{eff}}$  materials showed noticeably better accuracy compared to plastics and liquids, the method may be expected to be suitable for a larger range of  $Z_{\text{eff}}$  materials. Contrary to the results obtained in the studies by Rinkel et al. [17] and Beldjoudi et al. [18], the method gives better accuracy with optimized bi-energy bins, compared to the same technique with 90 energy

bins. This may be because the high and low energy thresholds of our technique truncates the LAC's where they have the highest amount of experimental artifacts; Secondly compared to dual energy detectors our energy bins are not overlapping and are thus not influenced by system or sample parameters. The optimized bi-energy approach truncated the low-energy bin below 57.5 keV and therefore the method is expected also to work for the materials with  $Z_{\text{eff}} \leq 68$ , which do not exhibit absorption edges above this low-energy threshold. This range of atomic numbers include most of the materials scanned by security screening instruments. For further experiments, we will investigate robustness of the technique for a broader range of  $Z_{\text{eff}}$ , and in the presence of K-edges.

#### CRedit authorship contribution statement

**Doniyor Jumanazarov:** Conceptualization, Methodology, Software, Formal analysis, Investigation, Data curation, Writing - original draft, Visualization. **Jakeoung Koo:** Software, Validation, Formal analysis. **Matteo Busi:** Validation, Resources, Writing - review & editing. **Henning F. Poulsen:** Writing - review & editing, Supervision. **Ulrik L. Olsen:** Validation, Resources, Data curation, Writing - review & editing, Supervision. **Mihai Iovea:** Conceptualization, Methodology, Validation, Writing - review & editing, Supervision, Funding acquisition.

#### Declaration of competing interest

The authors declare that they have no known competing financial interests or personal relationships that could have appeared to influence the work reported in this paper.

#### Acknowledgments

This project has received funding from the European Union Horizon 2020 research and innovation programme under the Marie Skłodowska-Curie grant agreement No. 765604 as part of the MULTISCALE, Multimodal and Multidimensional imaging for EngineerRING project (MUMMERING Innovative Training Network, [www.mummering.eu](http://www.mummering.eu)).

The authors want to acknowledge also the 3D Imaging Center at DTU, where the experiments have been conducted.

#### References

- [1] Ellenbogen M, Bijjani R. Liquids and homemade explosive detection. In: Optics and photonics in global homeland security V and biometric technology for human identification VI, vol. 7306. International Society for Optics and Photonics; 2009, p. 73060Y. <http://dx.doi.org/10.1117/12.821806>.
- [2] Martz HE, Logan CM, Schneberk DJ, Shull PJ. X-ray Imaging: fundamentals, industrial techniques and applications. CRC Press; 2016.
- [3] Alvarez RE, Macovski A. Energy-selective reconstructions in X-ray computerized tomography. Phys Med Biol 1976;21(5):733–44. <http://dx.doi.org/10.1088/0031-9155/21/5/002>.
- [4] Azevedo SG, Martz HE, Auferheide MB, Brown WD, Champley KM, Kallman JS, et al. System-independent characterization of materials using dual-energy computed tomography. IEEE Trans Nucl Sci 2016;63(1):341–50. <http://dx.doi.org/10.1109/TNS.2016.2514364>.
- [5] Ying Z, Naidu R, Crawford CR. Dual energy computed tomography for explosive detection. J X-Ray Sci Technol 2006;14(4):235–56.
- [6] Kalender, Willi A and Perman, WH and Vetter, JR and Klotz E. Evaluation of a prototype dual-energy computed tomographic apparatus. I. Phantom studies. Med Phys 1986;13(3):334–9.
- [7] Robert-Coutant C, Moulin V, Sauze R, Rizo P, Casagrande JM. Estimation of the matrix attenuation in heterogeneous radioactive waste drums using dual-energy computed tomography. Nucl Instrum Methods Phys Res A 1999;422(1–3):949–56. [http://dx.doi.org/10.1016/S0168-9002\(98\)01053-5](http://dx.doi.org/10.1016/S0168-9002(98)01053-5).
- [8] Braz D, Lopes RT, Motta LM. Dual-energy computerized tomography in compacted soil. Geotech Geol Eng 2000;18(3):221–38. <http://dx.doi.org/10.1023/A:1026552720419>.

- [9] Heismann BJ, Leppert J, Stierstorfer K. Density and atomic number measurements with spectral x-ray attenuation method. *J Appl Phys* 2003;94(3):2073–9. <http://dx.doi.org/10.1063/1.1586963>.
- [10] Iovea M, Neagu M, Duliu OG, Mateiasi G. High accuracy x-ray dual-energy experiments and non-rotational tomography algorithm for explosives detection technique in luggage control. In *Int. symp. digital industrial radiology and computed tomography*; 2007. p. 8.
- [11] Park JS, Kim JK. Calculation of effective atomic number and normal density using a source weighting method in a dual Energy X-ray inspection system. *J Korean Phys Soc* 2011;59(4):2709–13. <http://dx.doi.org/10.3938/jkps.59.2709>.
- [12] Szczykutowicz TP, Qi Z, Chen G-H. A simple image based method for obtaining electron density and atomic number in dual energy CT. In: *Medical imaging 2011: Physics of medical imaging*, vol. 7961. International Society for Optics and Photonics; 2011, p. 79613A. <http://dx.doi.org/10.1117/12.878076>.
- [13] Semerci O, Miller EL. A parametric level-set approach to simultaneous object identification and background reconstruction for dual-energy computed tomography. *IEEE Trans Image Process* 2012;21(5):2719–34. <http://dx.doi.org/10.1109/TIP.2012.2186308>.
- [14] Landry G, Seco J, Gaudreault M, Verhaegen F. Deriving effective atomic numbers from DECT based on a parameterization of the ratio of high and low linear attenuation coefficients. *Phys Med Biol* 2013;58(19):6851–66. <http://dx.doi.org/10.1088/0031-9155/58/19/6851>.
- [15] Wells K, Bradley DA. A review of X-ray explosives detection techniques for checked baggage. *Appl Radiat Isot* 2012;70(8):1729–46.
- [16] Champley KM, Azevedo SG, Member S, Seetho IM, Glenn SM, McMichael LD, et al. Method to extract system-independent material properties from dual-energy X-ray CT. *IEEE Trans Nucl Sci* 2019;66(3):674–86. <http://dx.doi.org/10.1109/TNS.2019.2898386>.
- [17] Rinkel J, Beldjoudi G, Rebuffel V, Boudou C, Ouvrier-buffet P, Gonon G, et al. Experimental evaluation of material identification methods with CdTe X-ray spectrometric detector. *IEEE Trans Nucl Sci* 2011;58(5):2371–7. <http://dx.doi.org/10.1109/TNS.2011.2164266>.
- [18] Beldjoudi G, Rebuffel V, Verger L, Kaftandjian V, Rinkel J. An optimised method for material identification using a photon counting detector. *Nucl Instrum Methods Phys Res A* 2012;663(1):26–36. <http://dx.doi.org/10.1016/j.nima.2011.09.002>.
- [19] Limor Martin. *Enhanced information extraction in multi-energy X-ray tomography for security* [Ph.D. thesis], Boston University; 2014.
- [20] Busi M, Mohan KA, Dooraghi AA, Champley KM, Martz HE, Olsen UL. Method for system-independent material characterization from spectral X-ray CT. *NDT & E Int* 2019;107(August):102136. <http://dx.doi.org/10.1016/j.ndteint.2019.102136>.
- [21] Shikhaliyev PM. Energy-resolved computed tomography: First experimental results. *Phys Med Biol* 2008;53(20):5595–613. <http://dx.doi.org/10.1088/0031-9155/53/20/002>.
- [22] Parsai EI, Shvydka D, Kang J. Design and optimization of large area thin-film CdTe detector for radiation therapy imaging applications. *Med Phys* 2010;37(8):3980–94. <http://dx.doi.org/10.1118/1.3438082>.
- [23] Brambilla A, Ouvrier-Buffet P, Rinkel J, Gonon G, Boudou C, Verger L. CdTe linear pixel X-ray detector with enhanced spectrometric performance for high flux X-ray imaging. *IEEE Trans Nucl Sci* 2012;59(4 PART 3):1552–8. <http://dx.doi.org/10.1109/TNS.2012.2206828>.
- [24] Beldjoudi G, Rebuffel V, Verger L, Kaftandjian V, Rinkel J. Multidimensional data processing methods for material discrimination using an ideal X-ray spectrometric photon counting detector. *IEEE Trans Nucl Sci* 2011;58(6 PART 2):3190–203. <http://dx.doi.org/10.1109/TNS.2011.2171721>.
- [25] Wang X, Meier D, Taguchi K, Wagenaar DJ, Patt BE, Frey EC. Material separation in x-ray CT with energy resolved photon-counting detectors. *Med Phys* 2011;38(3):1534–46. <http://dx.doi.org/10.1118/1.3553401>.
- [26] Rebuffel V, Rinkel J, Tabary J, Verger L. New perspectives of X-ray techniques for explosive detection based on CdTe/CdZnTe spectrometric detectors. In: *Proc. of the int. symp. on digital industrial radiology and computed tomography*, vol. 2; 2011. p. 1–8.
- [27] Wang X, Xu J, Frey EC. Optimization of energy window widths in basis material decomposition using a multi-window photon counting x-ray detector. In: *2007 IEEE nuclear science symposium conference record*, vol. 5. IEEE; 2007, p. 3826–9. <http://dx.doi.org/10.1109/NSSMIC.2007.4436955>.
- [28] A. Brambilla, A. Gorecki, A. Potop CP, Verger L. Basis material decomposition method for material discrimination with a new spectrometric X-ray imaging detector. *J Instrum* 2017;12(8):P08014. <http://dx.doi.org/10.1088/1748-0221/12/08/P08014>.
- [29] Wang AS, Pelc NJ. Optimal energy thresholds and weights for separating materials using photon counting x-ray detectors with energy discriminating capabilities. In: *Medical imaging 2009: Physics of medical imaging*, vol. 7258. International Society for Optics and Photonics; 2009, 725821. <http://dx.doi.org/10.1117/12.811454>.
- [30] Wang AS, Pelc NJ. Sufficient statistics as a generalization of binning in spectral X-ray imaging. *IEEE Trans Med Imaging* 2011;30(1):84–93. <http://dx.doi.org/10.1109/TMI.2010.2061862>.
- [31] Eilbert RF, Krug KD. Dual energy X-ray scanner for detecting contraband. In: *Contraband and cargo inspection technology international symposium proceedings*; 1992. p. 209–17.
- [32] Busi M. *Enhanced Security Screening Using Spectral X-ray Imaging* [Ph.D. thesis], Technical University of Denmark; 2019.
- [33] Kheirabadi M, Bjorholm Dahl A, Lund Olsen U, Mustafa W, Lyksborg M. Multi-spectral x-ray CT: multivariate statistical analysis for efficient reconstruction. In: *Developments in X-Ray Tomography XI*, vol. 1039113. International Society for Optics and Photonics; 2017, p. 38. <http://dx.doi.org/10.1117/12.2273338>.
- [34] Bragg, WH and Peirce S. LXIV. The absorption coefficients of X rays. *Lond Edinb Dublin Philos Mag J Sci* 1914;28(166):626–30.
- [35] Owen E. The absorption of x-rays. *Proc R Soc Lond Ser A Math Phys Eng Sci* 1918;94(664):510–24.
- [36] Richtmyer FK, Warburton FW. The absorption of X-rays by iron, cobalt, nickel and copper. *Phys Rev* 1923;22(6):539–45. <http://dx.doi.org/10.1103/PhysRev.22.539>.
- [37] White D. An analysis of the Z-dependence of photon and electron interactions. *Phys Med Biol* 1977;22(2):219.
- [38] Compton AH, Allison SK, et al. *X-rays in theory and experiment*. New York, NY, USA: Van Nostrand: D. Van Nostrand company, inc.; 1935.
- [39] Mayneord W. The significance of the roentgen. *Acta Int Union Against Cancer* 1937;2:271.
- [40] Spiers FW. Effective atomic number and energy absorption in tissues. *Br J Radiol* 1946;19(218):52–63. <http://dx.doi.org/10.1259/0007-1285-19-218-52>.
- [41] McCullough EC. Photon attenuation in computed tomography. *Med Phys* 1975;2(6):307–20.
- [42] Weber J, van den Berge DJ. The effective atomic number and the calculation of the composition of phantom materials. *Br J Radiol* 1969;42(497):378–83. <http://dx.doi.org/10.1259/0007-1285-42-497-378>.
- [43] Cho ZH, Tsai CM, Wilson G. Study of contrast and modulation mechanisms in X-ray/photon transverse axial transmission tomography. *Phys Med Biol* 1975;20(6):879–89. <http://dx.doi.org/10.1088/0031-9155/20/6/001>.
- [44] Lehmann L, Alvarez R, Macovski A, Brody W, Pelc N, Riederer SJ, et al. Generalized image combinations in dual KVP digital radiography. *Med Phys* 1981;8(5):659–67.
- [45] Williamson JF, Li S, Devic S, Whiting BR, Lerma FA. On two-parameter models of photon cross sections: Application to dual-energy CT imaging. *Med Phys* 2006;33(11):4115–29. <http://dx.doi.org/10.1118/1.2349688>.
- [46] Walter DJ, Tkaczyk EJ, Wu X. Accuracy and precision of dual energy CT imaging for the quantification of tissue fat content. In: *Medical imaging 2006: Physics of medical imaging*, vol. 6142. International Society for Optics and Photonics; 2006, p. 61421G. <http://dx.doi.org/10.1117/12.654669>.
- [47] Langeveld WG. Effective atomic number, mass attenuation coefficient parameterization, and implications for high-energy x-ray cargo inspection systems. *Physics Procedia* 2017;90(November 2016):291–304. <http://dx.doi.org/10.1016/j.phpro.2017.09.014>.
- [48] Dreier ES, Kehres J, Khalil M, Busi M, Gu Y, Feidenhans R, et al. Spectral correction algorithm for multispectral CdTe x-ray detectors. *Opt Eng* 2018;57(5):16. <http://dx.doi.org/10.1117/12.2272935>.
- [49] Goodstitt MM, Christodoulou EG, Larson SC. Accuracies of the synthesized monochromatic CT numbers and effective atomic numbers obtained with a rapid kvp switching dual energy CT scanner. *Med Phys* 2011;38(4):2222–32. <http://dx.doi.org/10.1118/1.3567509>.
- [50] Kim S, Chen J, Cheng T, Gindulyte A, He J, He S, et al. Pubchem 2019 update: Improved access to chemical data. *Nucleic Acids Res* 2019;47(D1):D1102–9. <http://dx.doi.org/10.1093/nar/gky1033>, URL <https://pubchem.ncbi.nlm.nih.gov>.
- [51] Palenstijn WJ, Batenburg KJ, Sijbers J. The ASTRA tomography toolbox. In: *13th international conference on computational and mathematical methods in science and engineering, CMMSE*, vol. 2013. 2013, p. 1139–45, URL <http://www.visionlab.ua.ac.be/sites/default/files/cmmse2013.pdf>.
- [52] Berger M, Hubbell J, Seltzer S, Chang J, Coursey J, Sukumar R, et al. XCOM: Photon cross section database. National Institute of Standards and Technology, Gaithersburg, MD; 2010, <http://dx.doi.org/10.18434/T48G6X>, URL <http://physics.nist.gov/xcom>.
- [53] Nocedal J, Wright SJ. *Numerical optimization*. New York: Springer; 1999.
- [54] Rutherford RA, Pullan BR, Isherwood I. Measurement of effective atomic number and electron density using an EMI scanner. *Neuroradiology* 1976;11(1):15–21. <http://dx.doi.org/10.1007/BF00327253>.
- [55] Phelps ME, Gado MH, Hoffman EJ. Correlation of effective atomic number and electron density with attenuation coefficients measured with polychromatic X rays. *Radiology* 1975;117(3 D):585–8. <http://dx.doi.org/10.1148/117.3.585>.



**Doniyor Jumanazarov** is a Ph.D. fellow at the Department of Physics at Denmark Technical University (DTU), Kongens Lyngby, Denmark. He obtained his BS degree in physics from the National University of Uzbekistan, Tashkent, Uzbekistan, and his MS degree in Molecular Photonics for bio- and nanotechnologies (MONABIPHOT) from the École Normale Supérieure de Cachan, Cachan, France, in 2012 and 2018, respectively.



**Professor, Dr. techn. Henning Friis Poulsen** is employed at DTU Physics since 2012. Henning pioneered several x-ray microscopy methods enabling mapping of materials properties within large samples, and on scales down to nanometers. He heads the 3D Imaging Centre at DTU and is Principal Investigator on a number of European and national projects with the aim of introducing X-ray methods to industry.



**Jakeoung Koo** received his B.Sc. and M.Sc. in Computer Science from Chung-Ang University, South Korea in 2015 and 2017, respectively. He is now a Ph.D. student in Technical University of Denmark (DTU), Kongens Lyngby, Denmark. He is interested in Computed Tomography and Computer Vision.



**Ulrik** is a senior research engineer at DTU's department of Physics since 2013. He obtained his Ph.D. degree in 2009 from Copenhagen University. He is an expert in X-ray instrumentation and specializes in spectral X-ray detectors, data acquisition and processing. Ulrik's current research interest is the use of spectral detectors for security applications for improved reconstruction and material identification.



**Matteo Busi** is a postdoctoral researcher at the Paul Scherrer Institute (Switzerland) since 2019. He was awarded his Ph.D. degree in 2019 from the Technical University of Denmark, for his contributions towards the development and enhancement of spectral X-ray imaging techniques. He is currently researching on the development of novel neutron Bragg edge imaging techniques and respective applications in the material science domain, especially in the field of additive manufacturing.



**Mihai IOVEA**, Engineer in Physics, Senior Research Scientist, Ph.D. in Physics Over 30 years' experience in X-ray Imaging projects research & development for Security and Non-Destructive Testing. Interested in X-ray 2D&3D Tomography and Digital Radiography techniques, such as: dual/multi energy, diffraction, back-scattering applied in for threats detection, high-resolution in-line X-ray scanners for fast industrial non-destructive testing.



## Paper B

**Material classification from sparse spectral X-ray CT using vectorial total variation based on L infinity norm.**

Doniyor Jumanazarov, Jakeoung Koo, Jan Kehres, Henning. F. Poulsen, Ulrik L. Olsen and Mihai Iovea

# Material classification from sparse spectral X-ray CT using vectorial total variation based on L infinity norm

Doniyor Jumanazarov<sup>a,c,\*</sup>, Jakeoung Koo<sup>b</sup>, Jan Kehres<sup>a</sup>, Henning F. Poulsen<sup>a</sup>, Ulrik L. Olsen<sup>a</sup> and Mihai IOVEA<sup>c</sup>

<sup>a</sup>Technical University of Denmark, DTU Physics, 2800 Kgs. Lyngby, Denmark

<sup>b</sup>Technical University of Denmark, DTU Compute, 2800 Kgs. Lyngby, Denmark

<sup>c</sup>ACCENT PRO 2000 s.r.l. (AP2K), Nerva Traian 1, K6, Ap. 26, Bucharest, S3, ROMANIA 031041

## ARTICLE INFO

### Keywords:

Spectral X-ray CT  
Electron density  
Effective atomic number  
Joint reconstruction  
Security screening

## ABSTRACT

The development of energy resolving photon counting detectors (PCD) has paved the way to the Spectral X-ray Computed Tomography (SCT), with which one can simultaneously extract the energy dependence of a material's linear attenuation coefficient (LAC). Spectral CT is proved to be an advanced technique to classify materials based on their physical properties of electron density ( $\rho_e$ ) and effective atomic number ( $Z_{\text{eff}}$ ). However, the application of Spectral CT for material classification in security screening applications may be hindered by the poor image reconstruction quality because of sparse-view (few) projections and the insufficient number of photon counts, which is important to achieve rapid scanning. The image reconstruction quality for each energy bin may also be degraded since the division of photon counts into multiple energy bins naturally leads to higher noise levels. In this work, we explore how to perform accurate Spectral CT reconstructions from such data. We propose to improve Spectral CT by using correlations between multiple energy bins with joint reconstruction. This improvement is realized through  $L_\infty$ -norm-based vectorial total variation ( $L_\infty$ -VTV) regularization. The  $L_\infty$ -VTV is tested on "real life" phantoms consisting of materials in the range of  $6 \leq Z_{\text{eff}} \leq 15$ . From experimental data acquired with a custom laboratory instrument for Spectral CT, we find that the  $L_\infty$ -VTV provides an improved reconstruction, better material classification performance and shorter computation time compared to another state-of-the-art joint reconstruction of total nuclear variation (TNV), and the total variation (TV) regularized and the non-regularized bin-by-bin reconstructions. In a sparse-view case with 7 projections, the  $L_\infty$ -VTV gives the relative deviations of 3.5% for  $\rho_e$  and 2.4% for  $Z_{\text{eff}}$  whereas the TNV and TV lead to deviations of 3.4% and 3.1%, and 3.8% and 4.2%, respectively. The  $L_\infty$ -VTV reconstruction algorithm is now ready for use in security screening applications.

## 1. Introduction


Using sparse-view reconstructions from few projections in X-ray Computed Tomography (CT) Systems can enable rapid scanning which is important for security applications. However, the poor reconstruction quality caused by the sparse data may hinder achieving the desired accuracy in material classification for security screening. Many studies have been done in addressing the sparse data problems either in CT Systems or image processing. The total-variation (TV) introduced by Rudin, Osher, and Fatemi [1] has been effectively used for various image processing problems in noise suppression. TV regularization was shown to provide sharp discontinuities and preserves edges in image reconstruction, promoting sparse gradients of the images. Various TV based reconstruction algorithms have been implemented for sparse-view and limited angle CT [2, 3]. Sidky et al. (2006) [4] implemented a TV-regularized reconstruction in fan-beam CT for different insufficient data problems such as the few-view projections and limited angles. They showed that the TV outperforms the existing reconstruction methods for such data.

The development of energy-resolved, photon counting

detectors (PCD) led to the emergence of Spectral CT, which can simultaneously retrieve the energy dependence of a material's linear attenuation coefficient (LAC). Thus, Spectral CT is just CT with multiple "color" channels. The term channel is referred to as bin in this work. Spectral CT with multiple energy bins may suffer from the fact that narrower energy bins integrate less photons and thus have significantly lower signal to noise ratio (SNR). Therefore, to combat the heavy sparse-view artifacts and improve denoising performance at decreased SNRs in Spectral CT we aim to use the joint reconstruction algorithms. The joint reconstruction algorithm jointly reconstructs the images by simultaneously employing all the multi-energy sinogram data instead of reconstructing each energy bin independently. For image processing problems, Blomgren and Chan (1998) [5] introduced a first definition of vectorial TV (VTV) regularizer that extends the conventional scalar TV into a multi-dimensional frame that considers dependency both in the spatial and spectral dimensions.

The main question when formulating a VTV as a convex regularizer is how exactly to couple color channels. Holt (2014) [6] investigated several VTV types with color image denoising experiments including Total Nuclear Variation (TNV). TNV algorithm uses the nuclear norm in the gradients of images, which is the convex envelope of matrix rank [7]. Holt showed that minimizing the nuclear norm

\*Corresponding author.

 doniyor.jumanazarov@fysik.dtu.dk (D. Jumanazarov); jakoo@dtu.dk (J. Koo); jake@fysik.dtu.dk (J. Kehres); hfpo@fysik.dtu.dk (H.F. Poulsen); u11u@dtu.dk (U.L. Olsen); office@accent.ro (M. IOVEA)  
ORCID(s): 0000-0003-1583-7375 (M. IOVEA)

leads to promoting gradient vectors in different color channels to share common directions, compared to other VTV regularizers of Total Frobenius Variation and Total Spectral Variation. Thus, the TNV leverages the structure coherence of a scanned object sharing the same structure information at various energies. Using simulated data in Spectral CT, Rigie et al. (2015) [8] applied TNV to reconstructing tissue density maps. They showed that TNV is better in suppressing noise and has less edge blurring compared to bin-by-bin TV reconstructions. Even though each energy bin of a spectral CT often has remarkably different noise levels, TNV showed robustness to undesired transfer of individual characteristics to other bins. With experimental data, Rigie et al. (2017) [9] implemented TNV and another VTV algorithm using the Frobenius norm as well as TV in dual-energy CT. They found that both VTV regularized couplings are better at suppressing noise compared to the conventional TV while TNV was still the best regularizer among them. Zhong et al. [10] investigated a TNV reconstruction algorithm by combining energy-dispersive X-ray spectroscopy (EDS) with a more precise high-angle annular dark-field STEM (HAADF-STEM) tomography when the number of tilts is small and photon counts are low. The TNV regularization was more precise in preserving features of reconstructed images compared to the simultaneous iterative reconstruction technique (SIRT) [11] and TV reconstruction algorithms.

Miyata et al. [12] proposed using a  $L_\infty$  norm for defining VTV term. For an image denoising task, they showed that  $L_\infty$ -VTV can efficiently estimate the violation of inter-channel dependency and provide strong coupling among color channels. Duran et al. [13] analyzed several VTV regularizers, by applying different collaborative norms to the discrete gradients of multi-channel images consisting of a 3D matrix, whose dimensions correspond to color channels, the spatial gradients in  $x$  and  $y$ -axis, and the image pixels. For color image denoising tasks, they demonstrated that the  $L_\infty$ -VTV and TNV give the better results to suppress color artifacts compared to the other VTV norms, and the efficiency of particular norm appeared to be dependent on the experimental data considered.

In this work, using experimental data we implement and investigate a  $L_\infty$  norm-based VTV algorithm for Spectral CT with an attention to security screening applications.  $L_\infty$ -VTV uses the infinity (maximum) norm to jointly penalize the maximum image gradient magnitudes over multi energy bins. This joint reconstruction algorithm has a positive weighting parameter that controls the balance between a good fit to energy-resolved sinogram data and a smooth reconstruction. This parameter determines the strength of the regularization term. We use the correlation coefficient to estimate the reconstructed image quality against ground-truth images as a figure of merit (FOM). For each reconstruction algorithm, the reconstructed image quality is estimated for different levels of photon counts as a function of the weighting parameter. The robustness of each algorithm to high noise added to certain energy bins is also tested.

In previous work, we presented the method for system-

independent material classification through attenuation decomposition (SIMCAD) from Spectral CT [14]. The SIMCAD method estimates the system-independent material properties of electron density ( $\rho_e$ ) and effective atomic number ( $Z_{\text{eff}}$ ) from the energy-dependent LACs, independent of the system or the scanner specification, such as the X-ray spectrum. This method employs the attenuation decomposition introduced by Alvarez et al. [15] for the formulation of the method and adopts it for multi-energies.

In this work, applying the SIMCAD method for each reconstruction algorithm we also aim to investigate the performance of material classification by using sparse-view reconstructions as an another FOM. We compare the reconstruction quality and classification performance of  $L_\infty$ -VTV with TNV joint reconstruction algorithm, and TV and SIRT bin-by-bin reconstruction algorithms. This study is based on real experimental data over a common set of materials, measured with a custom laboratory instrument for Spectral CT. We expect that the improvement in the reconstruction quality leads to more accurate extraction of LACs, and therefore to better material classification. The classification performance is estimated as a function of the weighting parameter for each reconstruction algorithm. We also test the robustness of the reconstruction algorithms for noisy projection data. For the experimental validation, we use 20 different materials for the calibration of SIMCAD classification method and 15 additional materials for the ( $\rho_e$ ,  $Z_{\text{eff}}$ ) calculation.

The joint reconstruction algorithms presented in this work can be easily extended to three-dimensional (3D) CT imaging, which is a powerful quantitative tool for exploring complex connections between the features and microstructure of materials in the field of material science [16, 17]. Therefore, the improvement of the distributions of ( $\rho_e$ ,  $Z_{\text{eff}}$ ) in the material through the improved image reconstruction can be useful for studying the complex microstructure of materials. Moreover, the methods introduced in this study can also be applied to data from a variety of spectral imaging techniques such as visible light, electron or neutron tomography.

## 2. Experimental setup. Data processing

### 2.1. Physical properties of materials

Linear attenuation coefficient (LAC) is proportional to a material's electron density [18], which is the number of electrons per unit volume (electron – mole/cm<sup>3</sup>). For a compound or mixture that has the composition of  $N$  total different elements, the electron density can be calculated as

$$\rho_e = \frac{\sum_{i=1}^N \alpha_i Z_i}{\sum_{i=1}^N \alpha_i A_i} \rho. \quad (1)$$

where  $\rho$  is mass density (g/cm<sup>3</sup>),  $A_i$  and  $Z_i$  are atomic mass and atomic number for each element,  $i$ , respectively,  $\alpha_i$  is the number of atoms that have atomic number  $Z_i$ . For compounds, the atomic number is referred to as effective atomic number,  $Z_{\text{eff}}$  and a now classical parameterization proposed

**Table 1**

Parameters of experimental setup. Note that we use 7, 12 and 36 projections in the subsection 5.1, 36 projections in 5.2, 12 projections in 5.3 and 5.4, and 7 and 12 projections in 5.5. The total integration time per projection is 8 seconds in the subsections 5.1 and 5.5, while the integration times are 2 ms, 10 ms and 50 ms in 5.2, and 100 ms in 5.3 and 5.4.

Source parameters	150 kV, 0.5 mA
Focal spot	75 $\mu\text{m}$
Number of pixels	1 $\times$ 640 1D array
Pixel size	0.8 $\times$ 0.8 mm <sup>2</sup>
Detector resolution	6.5% (8 keV at 122 keV)
Number of energy bins	128 (1.1 keV width each)
Number of projections	7, 12, 36
Total integration time per projection	2 ms, 10 ms, 50 ms, 100 ms, 8 s
Source to detector distance (SDD)	701 mm
Source to sample distance (SOD)	500 mm

by [19, 20] is defined as

$$Z_{\text{eff}} = \sqrt[l]{\sum_{i=1}^N r_i Z_i^l}, \quad (2)$$

where  $r_i$  is “relative electron fraction” contribution of an element,  $i$ , which is determined as

$$r_i = \frac{\alpha_i Z_i}{\sum_{j=1}^N \alpha_j Z_j}$$

In previous work [14], for material classification the exponent  $l$  was investigated to tune this value on the best match depending on the materials, source spectrum and system features. The  $l = 8.0$  was found to be the optimal value for classification performance, therefore we choose this value for the calculations of reference  $Z_{\text{eff}}$  values in this work.

## 2.2. Experimental setup and materials

Table 1 lists the parameters of the experimental setup designed for spectral CT measurements. The experiments were performed in the 3D Imaging Center at DTU, Denmark. The X-ray beam was generated by a micro focused X-ray source of the type L12161-07 made by Hamamatsu. The operating parameters were the acceleration tube voltage of 150 kV and the anode filament current of 0.5 mA. A 2-mm-thick aluminum filter was placed in front of the source to remove photons with energies below the detector energy range. The incident beam was collimated to a fan beam by using a JJ X-Ray IB-C80-AIR slit with 5-mm-thick tungsten carbide blades to fully illuminate all the detector pixels while keeping the beam size to a minimum, and thereby to reduce the background radiation composed of scattered and fluorescent photons. The sample placed on the rotation stage was scanned between discrete rotations with different increments over a range of 360 degrees depending on the number of projections. The source to detector distance (SDD) is 701 mm whereas the source to sample distance (SOD) corresponds to 500 mm. Fig. 1 illustrates the experimental setup.

The detector used for the experiments is MultiX ME-100 v2 produced by Detection Technology S.A.S. in Moirans,

France. We employ a system of five detector modules, each module has a 1  $\times$  128 line array of pixels each with the size of 0.8  $\times$  0.8 mm<sup>2</sup>. The number of energy bins is 128 with a width of 1.1 keV each, evenly spaced in the energy range between 20 and 160 keV. The energy resolution of the detector with high X-ray fluxes is 6.5% (8 keV at 122 keV) [21]. The detector is made up of a 3-mm-thick CdTe sensor. Incoming photons pass through a collective cathode of a continuous metal film. The sensor has pixelated anodes on the other side with notably smaller size, which are placed on readout electronics. A single MultiX detector has 128 pixelated anodes (pixels) with a pitch of 800  $\mu\text{m}$  and consists of an array of 4 sensor crystals each with 32 pixels. The detector can operate with integration time from 2 ms to 100 ms (in 10  $\mu\text{s}$  increments). The lower integration time indicates the lower photon counts.

Fig. 2 show the samples scanned and processed through each reconstruction algorithm to estimate the reconstruction quality. Table 2 and Table 3 list the materials used for the calibration step and ( $\rho_e$ ,  $Z_{\text{eff}}$ ) calculation in the material classification described in Section 4, respectively. The reference  $\rho_e$  and  $Z_{\text{eff}}$  values in both tables were calculated by using Eq. (1) and Eq. (2) and the exponent  $l = 8.0$ , respectively. The  $\rho_e$  and  $Z_{\text{eff}}$  values in Table 2 will be used as the reference values in the calibration step of the material classification. Sample dimensions are shown as the diameter for circular samples and as width $\times$ length for rectangular samples. The plastic materials used for the material classification in both tables are polyvinylidene fluoride (PVDF), polyoxymethylene-H (POM-H), polyethylene terephthalate (PET), polytetrafluoroethylene (PTFE), polyoxymethylene-C (POM-C), polymethyl methacrylate (PMMA) and polycarbonate (PC). The most materials listed are explosive or precursor materials, and prohibited in checked-in or carry-on luggage. The materials correspond to the range of effective atomic number,  $6 \leq Z_{\text{eff}} \leq 15$ , which covers most of the materials encountered in security screening [22]. Note that if materials present K-edge absorption in the LAC defined in Eq. (29), the bins with energies lower than the K-edge are truncated making it consistent with the formulation of the

**Table 2**

The list of the materials scanned and processed for the calibration step in material classification, for which the formulation of calibration and the results are presented in the subsections 4.1 and 5.5, respectively. The mass density,  $\rho$  for the plastic materials was measured with uncertainties of  $\pm 0.15\%$ . The mass densities for the rest of materials represent the theoretical values found in PubChem data, [24].

Material	Chemical Formula	Width×length/ Diameter (mm)	$\rho$ (g/cm <sup>3</sup> )	$\rho_e$ (e <sup>-</sup> mol/cm <sup>3</sup> )	$Z_{\text{eff}}$
Graphite	C	12.7	1.8	0.899	6
PC	(CO <sub>3</sub> C <sub>13</sub> H <sub>8</sub> ) <sub>n</sub>	8.2×53.5	1.18	0.610	6.82
PMMA	(C <sub>5</sub> O <sub>2</sub> H <sub>8</sub> ) <sub>n</sub>	40×42	1.18	0.636	7.02
POM-C	(CH <sub>2</sub> O) <sub>n</sub>	9×53.5	1.41	0.753	7.40
PTFE	(C <sub>2</sub> F <sub>4</sub> ) <sub>n</sub>	9×53.3	2.16	1.035	8.70
N,N-Dimethylhydrazine	C <sub>2</sub> H <sub>8</sub> N <sub>2</sub>	67	0.791	0.447	6.44
Ethylenediamine	C <sub>2</sub> H <sub>8</sub> N <sub>2</sub>	67	0.90	0.509	6.44
Acetone 2	C <sub>3</sub> H <sub>6</sub> O	54	0.785	0.432	6.90
Nitrobenzene	C <sub>6</sub> H <sub>5</sub> NO <sub>2</sub>	49	1.20	0.624	7.00
Ethanol 96%	C <sub>2</sub> H <sub>6</sub> O (96%)	67×67	0.798	0.450	7.06
Methanol	CH <sub>3</sub> OH	20	0.792	0.446	7.29
Hydrazine solution	H <sub>4</sub> N <sub>2</sub> (35%)	54	1.0	0.561	7.43
Nitromethane	CH <sub>3</sub> NO <sub>2</sub>	20	1.14	0.597	7.50
Water	H <sub>2</sub> O	20	0.997	0.554	7.78
Water 3	H <sub>2</sub> O	12.7	0.997	0.554	7.78
Hyd. Peroxide 2	H <sub>2</sub> O <sub>2</sub> (50%)	73×74	1.22	0.661	7.83
Magnesium 2	Mg	18	1.74	0.859	12
Aluminum 2	Al	25	2.70	1.3	13
Aluminum 3	Al	20×20	2.70	1.3	13
Silicon	Si	25	2.33	1.161	14

material classification method presented in Section 4. However, the materials used in this work do not possess K-edges within the detector's energy range.

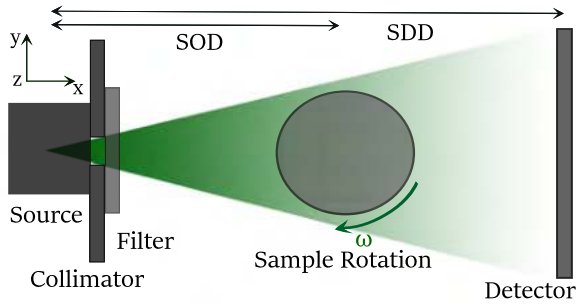


**Figure 1:** The illustration of the experimental setup. SDD and SOD represent the source to detector distance and the source to sample distance, respectively.

### 2.3. Data correction. Rebinning energy bins. Sinogram

The detector requires the correction of the detector's spectral response to achieve a LAC curve that follows the reference attenuation curve [25]. The deviations of the LAC from the reference values occur due to the physical effects in the detector sensor such as charge sharing and weighting potential cross-talk, fluorescence radiation, Compton scattering radiation, pulse pile up and incomplete charge col-

lection. These spectral distortions cannot be completely restored by the correction algorithm at the lower and higher energies. Therefore, we truncate the uncorrected energy bins and set the low- (33.2 keV) and high-energy (132.4 keV) thresholds [14].

The correction of the raw data is followed by rebinning energy channels. In previous work, the material classification performance was tested for 2, 6, 15, 30, 45 and 90 energy bins [14]. The results showed that 30, 45 and 90 energy bins did not improve classification performance compared to 15 energy bins approach, in which energy bins are distributed uniformly between low- and high-energy thresholds with equal width. The reasons for this are firstly that the width of the energy bins becomes narrower than the energy resolution of the detector; Secondly that the detector noise becomes greater as the width of each energy bin becomes narrower when the number of bins increases. Consequently, we use 15 energy bins in this study.

We generate line integrals or sinograms from the photon counts of each energy bin based on Lambert–Beer's law as follows:

$$L_k(\vec{x}) = -\log \frac{I_k(\vec{x})}{I_{0,k}(\vec{x})}, \quad k = 1, 2, 3, \dots, 128; \quad (3)$$

where  $I_{0,k}$  is the flat-field photon counts corresponding to energy bin  $k$ , which is the projection without the sample,  $I_k$  is the measured photon counts for energy bin  $k$  when the material is inserted,  $\vec{x}$  represents the 1D detector pixel array.

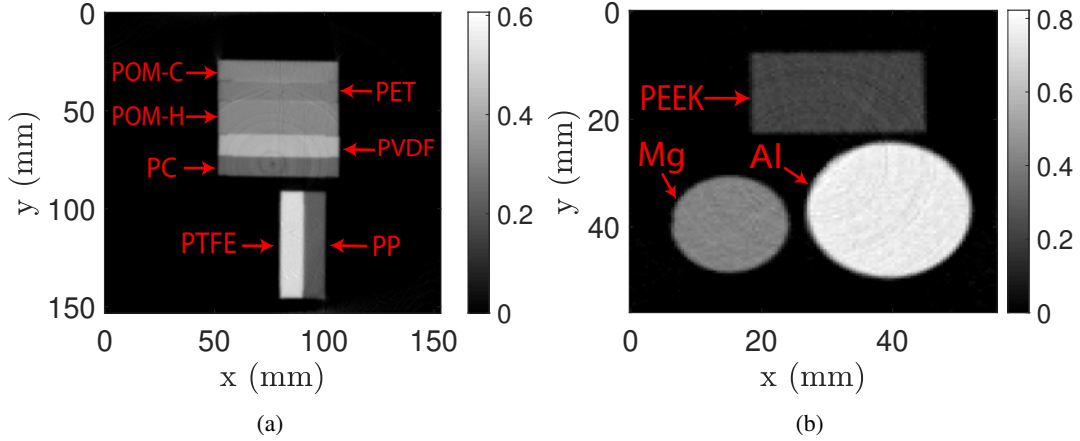


**Figure 2:** Presentation of 2D reconstructions of the samples scanned for the analysis of reconstructed image quality. Both samples are reconstructed with SIRT from 360 projections. The gray scale bars show linear attenuation coefficients (LACs) with the unit of  $\text{cm}^{-1}$ . (a) The sample including the plastics indicated by red arrows, the image corresponds to the energy of 42 keV. This sample is used for the analysis of reconstruction quality for different number of projections, for which the results are presented and discussed in the subsection 5.1. The polypropylene (PP) material is mixed with chemical colorants, which lead to a higher  $Z_{\text{eff}}$  value compared to the pure PP [23]. Therefore, this material is excluded in the estimation of the material classification performances, for which the results are given in the subsection 5.5. (b) The sample including aluminum, magnesium and polyetheretherketone (PEEK) indicated by red arrows. The image is for the energy bin corresponding to 61.9 keV. This sample is used for the analysis, presented and discussed in the subsections 5.2, 5.3 and 5.4.

**Table 3**

The list of all the materials scanned and processed for the  $(\rho_e, Z_{\text{eff}})$  calculation in material classification, for which the formulation of calculation and the results are presented in the subsections 4.2 and 5.5, respectively. The mass density,  $\rho$  for the plastic materials was measured with uncertainties of  $\pm 0.15\%$ . The mass densities for the rest of materials represent the theoretical values found in PubChem data, [24].

Material	Chemical Formula	Width×length/ Diameter (mm)	$\rho$ (g/cm <sup>3</sup> )	$\rho_e$ (e <sup>-</sup> mol/cm <sup>3</sup> )	$Z_{\text{eff}}$
PET	(C <sub>10</sub> H <sub>8</sub> O <sub>4</sub> ) <sub>n</sub>	9×53.5	1.39	0.721	7.09
POM-H	(CH <sub>2</sub> O) <sub>n</sub>	15.5×53.3	1.43	0.763	7.40
PVDF	(C <sub>2</sub> H <sub>2</sub> F <sub>2</sub> ) <sub>n</sub>	9×53.5	1.79	0.896	8.40
PTFE 2	(C <sub>2</sub> F <sub>4</sub> ) <sub>n</sub>	12.7	2.2	1.056	8.70
2-Butanone	C <sub>4</sub> H <sub>8</sub> O	83	0.805	0.447	6.76
Acetone	C <sub>3</sub> H <sub>6</sub> O	20	0.785	0.432	6.90
Methanol 2	CH <sub>3</sub> OH	81	0.792	0.446	7.29
Ethanol 40%	C <sub>2</sub> H <sub>6</sub> O (40%)	67×67	0.947	0.532	7.63
Water 2	H <sub>2</sub> O	51×51	0.997	0.554	7.78
Nitric acid	HNO <sub>3</sub> (65%)	83	1.39	0.714	7.80
Hyd. Peroxide	H <sub>2</sub> O <sub>2</sub> (50 %)	20	1.22	0.661	7.83
Magnesium	Mg	12.7	1.74	0.859	12
Aluminum	Al	25	2.70	1.3	13
Silicon powder	Si	48	0.65	0.324	14
Silicon 2	Si	12.7	2.33	1.161	14

### 3. Reconstruction algorithms

#### 3.1. Problem formulation

In spectral CT, the measurements with  $N$  energy bins consist of  $N$  sinograms  $\mathbf{p}_1, \dots, \mathbf{p}_N \in \mathbb{R}^M$  where  $M$  is the number of detector pixels times the number of projection angles. From the energy-resolved sinograms, we aim to reconstruct the corresponding  $N$  images  $\mathbf{u}_1, \dots, \mathbf{u}_N \in \mathbb{R}^J$  representing the linear attenuation coefficients for each energy

bin  $E_i$  ( $i = 1, 2, \dots, N$ ), where  $J$  is the number of pixels per each image. For notational simplicity, we define the stack of sinograms as a vector  $\mathbf{p} \in \mathbb{R}^{NM}$  and the stack of  $N$  images as  $\mathbf{u} \in \mathbb{R}^{NJ}$  and we denote by  $u_{i,j}$  the attenuation coefficient for the energy bin  $E_i$  on the  $j$ -th pixel ( $j = 1, 2, \dots, J$ ).

The forward-projection to map an image to the sinogram domain can be modeled by a linear operator  $A$  such that  $A\mathbf{u}_i$  estimates a sinogram for each energy bin  $E_i$ . By stacking the same operator for all energy bins, we define the linear oper-

ator  $\mathbf{A}$  on the stack of images  $\mathbf{u}$  such that  $\mathbf{A}\mathbf{u} = \mathbf{p}$ . Then, a typical reconstruction approach is to minimize the data fidelity term defined as the squared reprojection error that is  $l_2$  norm of the difference between the computed ( $\mathbf{A}\mathbf{u}$ ) and the measured sinogram data ( $\mathbf{p}$ ). The data fidelity term can be written as

$$\mathcal{G}(\mathbf{A}\mathbf{u}) = \|\mathbf{A}\mathbf{u} - \mathbf{p}\|_2^2. \quad (4)$$

This data fidelity term is not enough, as data can be highly noisy or obtained from a small number of projection angles. To reconstruct high-quality images, we need a robust regularization scheme, by imposing prior knowledge on the solutions.

One can apply (isotropic) total variation regularization on each energy bin  $E_i$ , independently, which can be written as

$$\mathcal{R}_{\text{TV}}(\mathbf{u}_i) = \sum_{j=1}^J \sqrt{\partial_x u_{i,j}^2 + \partial_y u_{i,j}^2}, \quad (5)$$

where  $\partial_x u_{i,j}$  and  $\partial_y u_{i,j}$  are the gradients of the image  $\mathbf{u}_i$  on the pixel  $j$  with respect to  $x$  and  $y$  axis, respectively. This TV regularization term does not exploit any correlation between the images from different energy bins.

A more robust regularization can be achieved by correlating the gradients of the images from different energy bins. One way to exploit the inter-bin correlations of the image gradients is Total Nuclear Variation (TNV) regularization [8, 13], that is common to all energy bins and defined as the sum of nuclear norm of the Jacobian matrix over all image pixels:

$$\mathcal{R}_{\text{TNV}}(\mathbf{u}) = \sum_{j=1}^J \left\| \begin{pmatrix} \partial_x u_{1,j} & \partial_y u_{1,j} \\ \partial_x u_{2,j} & \partial_y u_{2,j} \\ \vdots & \vdots \\ \partial_x u_{N,j} & \partial_y u_{N,j} \end{pmatrix} \right\|_*, \quad (6)$$

where the nuclear norm  $\|\cdot\|_*$  of the Jacobian matrix including image gradients in pixel, spatial and energy dimension is the sum of its singular values. TNV can be degenerate when there are some outliers in the gradients of the images.

To overcome the disadvantage of TNV, we suggest to use another VTV regularization based on  $L_\infty$  (infinity) norm, which is the sum of the maximum of gradients among  $N$  energy bins over all image pixels, defined as

$$\begin{aligned} \mathcal{R}_{L_\infty\text{-VTV}}(\mathbf{u}) &= \|\mathbf{D}\mathbf{u}\|_{\infty,1,1} \\ &:= \sum_{j=1}^J \left( \max_{1 \leq l \leq N} |\partial_x u_{l,j}| + \max_{1 \leq l \leq N} |\partial_y u_{l,j}| \right), \end{aligned} \quad (7)$$

where  $\mathbf{D}$  is a linear operator for the discrete gradient operations such that  $\mathbf{D}\mathbf{u}$  is a 3D matrix. That is,  $(\mathbf{D}\mathbf{u})_{l,j}$  represents the gradient of the image  $\mathbf{u}_i$  at the pixel  $j$  with respect to  $x$  axis when  $l = 1$  or  $y$  axis when  $l = 2$ . We use the notation  $\|\cdot\|_{\infty,1,1}$ , as it involves applying the  $L_\infty$  norm along

the energy bins dimension, and  $l_1$  norm along the other dimensions with respect to the spatial (pixel) locations and the spatial gradient directions [13]. This  $L_\infty$ -VTV norm correlates the gradients strongly over multiple energy bins, while disallowing some outliers in the sense of the gradient magnitudes. This property will be illustrated in the subsection 5.3.

By combining the data fidelity term (Eq. (4)) and the regularization term  $L_\infty$ -VTV (Eq. (7)), we formulate the optimization problem that we want to solve:

$$\min_{\mathbf{u} \geq 0} \frac{\lambda}{2} \mathcal{G}(\mathbf{A}\mathbf{u}) + \mathcal{R}_{L_\infty\text{-VTV}}(\mathbf{u}), \quad (8)$$

where  $\lambda$  is the weighting parameter between the two terms. Here, we impose the non-negativity constraint on  $\mathbf{u}$ , as linear attenuation coefficients are desired to be non-negative.

### 3.2. Optimization

We describe the optimization of our objective function defined in Eq. (8). Although the objective function is convex, the challenge lies in having the composite operators  $\mathbf{A}$  in the data fidelity term and  $\mathbf{D}$  in the regularization term. To deal with such difficulty, we employ an efficient primal dual algorithm, called Hybrid Gradient Primal Dual method (HGPD) [26]. The basic idea of primal dual algorithms is to reformulate a minimization problem as a minimization-maximization (min-max) problem and aim to find the saddle point. To derive the min-max problem, primal dual algorithms rely on the Fenchel conjugate function [26]  $F^*$  of a convex function  $F$ , defined by,

$$F^*(\mathbf{y}) = \sup_{\mathbf{x}} \langle \mathbf{x}, \mathbf{y} \rangle - F(\mathbf{x}). \quad (9)$$

To use the primal dual algorithm, we introduce two dual variables  $\mathbf{q}$  and  $\mathbf{r}$  corresponding to the operators  $\mathbf{A}$  and  $\mathbf{D}$ , respectively. To rewrite the original minimization problem defined in Eq. (8) as a saddle point problem, we use the Fenchel conjugate function to obtain

$$\mathcal{G}(\mathbf{A}\mathbf{u}) = \max_{\mathbf{q}} \langle \mathbf{A}\mathbf{u}, \mathbf{q} \rangle - \mathcal{G}^*(\mathbf{q}) \quad (10)$$

$$\mathcal{R}_{\text{VTV}}^{L_\infty}(\mathbf{D}\mathbf{u}) = \max_{\mathbf{r}} \langle \mathbf{D}\mathbf{u}, \mathbf{r} \rangle - \mathcal{R}^*(\mathbf{r}) \quad (11)$$

where  $\mathcal{G}^*$  and  $\mathcal{R}^*$  are the conjugate functions of

$$\mathcal{G}(\mathbf{x}) = \frac{1}{2} \|\mathbf{x} - \mathbf{p}\|_2^2, \quad (12)$$

$$\mathcal{R}(\mathbf{X}) = \|\mathbf{X}\|_{\infty,1,1}. \quad (13)$$

Based on Eq. (10) and Eq. (11), we now turn the minimization problem of Eq. (8) into the following saddle point problem

$$\min_{\mathbf{u}} \max_{\mathbf{q}, \mathbf{r}} \langle \mathbf{A}\mathbf{u}, \mathbf{q} \rangle + \langle \mathbf{D}\mathbf{u}, \mathbf{r} \rangle - \mathcal{G}^*(\mathbf{q}) - \mathcal{R}^*(\mathbf{r}) + \delta_+(\mathbf{u}), \quad (14)$$

where  $\delta_+$  is the indicator function for the non-negative constraint, defined by,

$$\delta_+(x) = \begin{cases} x & \text{if } x \geq 0, \\ \infty & \text{if } x < 0. \end{cases} \quad (15)$$

HGPD provides an efficient way to solve the saddle point problem, by alternatively updating the primal and dual variables as follows:

$$\mathbf{u}^{k+1} = \text{prox}_{\delta_+}(\mathbf{u}^k - \tau(\mathbf{A}^T \mathbf{q}^k + \mathbf{D}^T \mathbf{r}^k)) \quad (16)$$

$$\bar{\mathbf{u}} = 2\mathbf{u}^{k+1} - \mathbf{u}^k \quad (17)$$

$$\mathbf{q}^{k+1} = \text{prox}_{\sigma_1 \mathcal{G}^*}(\mathbf{q}^k + \sigma_1 \mathbf{A} \bar{\mathbf{u}}) \quad (18)$$

$$\mathbf{r}^{k+1} = \text{prox}_{\sigma_2 \mathcal{R}^*}(\mathbf{r}^k + \sigma_2 \mathbf{D} \bar{\mathbf{u}}) \quad (19)$$

where  $k$  is the iteration number,  $\tau$  is the step size for the primal variable,  $\sigma_1, \sigma_2$  are the step sizes for the dual variables and prox is the proximal operator [27] defined by

$$\text{prox}_{\sigma f}(\mathbf{x}) = \arg \min_{\mathbf{y}} \frac{1}{2\sigma} \|\mathbf{x} - \mathbf{y}\|_2^2 + f(\mathbf{y}). \quad (20)$$

In Algorithm 1, we provide the whole procedure of optimization, where  $\|\mathbf{A}\|_2$  denotes the operator norm of  $\mathbf{A}$ , which is the largest eigenvalue of  $\mathbf{A}$ . To guarantee the convergence, we carefully choose the step sizes, following [26], based on the operator norms, which can be computed by the power method [28]. The concrete solutions to Eq. (16) and Eq. (18) are provided in Eq. (24) and Eq. (26), respectively. To evaluate Eq. (19), we use the fact that the proximal operator to  $L_\infty$  norm is the projection operator to  $L_1$  unit ball, denoted by  $\Pi_{\|\cdot\| \leq 1}$  [27]. Then, we can write the solution to Eq. (19) as follows:

$$\left(\text{prox}_{\sigma_2 \mathcal{R}^*}(\mathbf{V})\right)_{i,j,l} = \text{sgn}(\mathbf{V}_{i,j,l}) \Pi_{\|\cdot\| \leq 1}(\sigma_2 \|\mathbf{V}_{:,j,l}\|) \quad (21)$$

where sgn is the sign function,  $i$  denotes the index for the energy bin,  $j$  for the pixel index and  $l \in \{1, 2\}$  denotes the index for the gradient with respect to  $x$  or  $y$  axis. The notation  $\mathbf{V}_{:,j,l}$  represents a vector consisting of the elements with respect to the energy bins, given  $j$  and  $l$ . We refer to [13] for a detailed derivation.

To check the convergence, we introduce two residuals  $\mathcal{P}$  and  $\mathcal{D}$  for the primal variables and the dual variables, respectively, as follows:

$$\mathcal{P}^{k+1} = \|(\mathbf{u}^k - \mathbf{u}^{k+1})/\tau - \mathbf{A}^T(\mathbf{q}^k - \mathbf{q}^{k+1}) - \mathbf{D}^T(\mathbf{r}^k - \mathbf{r}^{k+1})\|_1, \quad (22)$$

$$\mathcal{D}^{k+1} = \|(\mathbf{q}^k - \mathbf{q}^{k+1})/\sigma_1 - \mathbf{A}(\mathbf{u}^k - \mathbf{u}^{k+1})\|_1 + \|(\mathbf{r}^k - \mathbf{r}^{k+1})/\sigma_2 - \mathbf{D}(\mathbf{u}^k - \mathbf{u}^{k+1})\|_1. \quad (23)$$

These primal and dual residuals measure the changes of the solutions per iteration for primal and dual variables, respectively. Such residuals are expected to decrease with the iterations. The behaviors of these residuals and the stopping criteria will be discussed in the subsection 3.4.

### 3.3. The definition of correlation coefficient

We estimate the reconstructed image quality through the correlation coefficient,  $r$ , which measures how the reconstructed image  $\mathbf{u}$  is linearly connected to the ground-truth (true) image  $\mathbf{v}$ , and it is expressed as

$$r = \frac{\sum_i (u_i - \bar{u})(v_i - \bar{v})}{\sqrt{\sum_i (u_i - \bar{u})^2 \sum_i (v_i - \bar{v})^2}}, \quad (28)$$

---

#### Algorithm 1 Primal dual updates for solving Eq. (14)

---

Set the step sizes:

$$\tau = \frac{1}{\|\mathbf{A}\|_2 + \|\mathbf{D}\|_2}, \quad \sigma_1 = \frac{1}{\|\mathbf{A}\|_2}, \quad \sigma_2 = \frac{1}{\|\mathbf{D}\|_2}$$

Initialize  $\mathbf{u}^0, \mathbf{q}^0, \mathbf{r}^0$  as zero vectors.

for  $k = 0, 1, 2, \dots$

$$\mathbf{u}^{k+1} = \max(\mathbf{u}^k - \tau(\mathbf{A}^T \mathbf{q}^k + \mathbf{D}^T \mathbf{r}^k), 0) \quad (24)$$

$$\bar{\mathbf{u}} = 2\mathbf{u}^{k+1} - \mathbf{u}^k \quad (25)$$

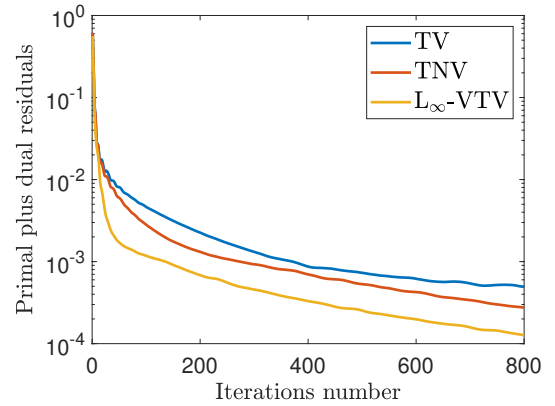
$$\mathbf{q}^{k+1} = \frac{\mathbf{q}^k + \sigma_1(\mathbf{A}\bar{\mathbf{u}} - \mathbf{p})}{1 + \sigma_1} \quad (26)$$

$$\mathbf{r}^{k+1} = \text{prox}_{\sigma_2 \mathcal{R}^*}(\mathbf{r}^k + \sigma_2 \mathbf{D}\bar{\mathbf{u}}) \quad (27)$$


---

where  $\bar{u}$  and  $\bar{v}$  are the mean values, and  $u_i$  and  $v_i$  are the  $i^{\text{th}}$  pixel values of  $\mathbf{u}$  and  $\mathbf{v}$ , respectively. In this work, to compute correlation coefficients the ground-truth images of a sample at multiple energy bins used are synthetically created by assigning the corresponding mean LAC to each energy bin for each material in the sample. The mean LAC for each energy bin is extracted from the attenuation value histogram based on the normal distribution after sample reconstruction with SIRT from 360 projections [14].

### 3.4. Stopping criteria for the iteration number



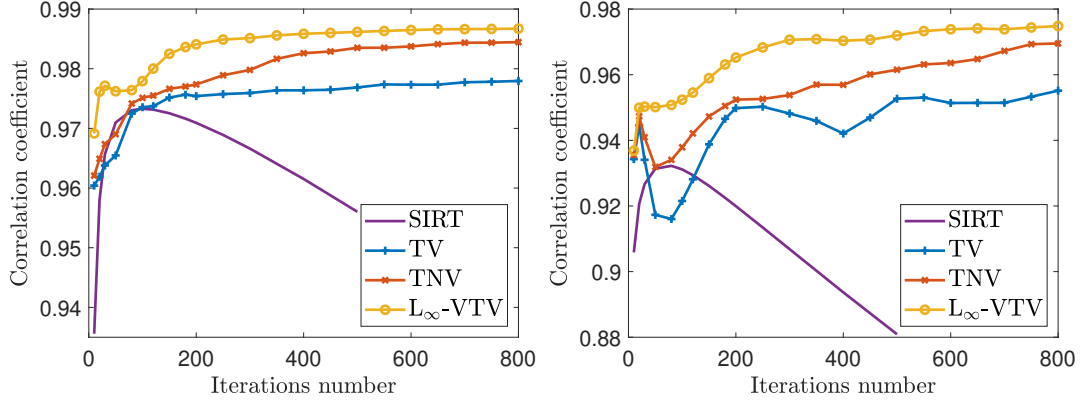
**Figure 3:** The sum of the primal and dual residuals with respect to iteration number for TV, TNV and  $L_\infty$ -VTV. As expected, the residuals decrease with the iterations. To obtain this plot a sample shown in Fig. 2a was scanned with 8 s integration time per projection for 36 projections. The weighting parameter  $\lambda$  defined in Eq. (8) corresponds to the maximum correlation coefficients (shown in Fig. 5) for each reconstruction.

Fig. 3 shows the sum of primal and dual residuals for reconstruction algorithms that decreases as the number of iterations increases for each algorithm, as expected. The convergence of each algorithm is therefore ensured.  $L_\infty$ -VTV converges noticeably faster than TNV and TV whereas TV shows the slowest convergence rate.

We use the correlation coefficient for stopping the iter-



## Material classification from sparse spectral X-ray CT



**Figure 4:** Correlation coefficients as a function of iteration number for 36 (left) and 7 projections (right) for all the algorithms. The weighting parameter  $\lambda$  corresponds to the maximum correlation coefficient (shown in Fig. 5) for each reconstruction algorithm. The correlation coefficients represent the mean values calculated from the coefficients for 15 energy bins used.

**Table 4**

The number of iterations fixed for each algorithm and number of projections.

Projection number	SIRT	TV	TNV	$L_\infty$ -VTV
7	80	550	750	550
12	80	550	600	500
36	100	400	500	400
360	150	400	400	400

ation to define whether or not the algorithms will converge to the ground-truth image. For 7 and 36 projections, Fig. 4 presents how the correlation coefficient changes with the number of iterations for each algorithm. We stop the iteration for SIRT when the correlation coefficient reaches the maximal value. For other algorithms, we use the iteration number at the point when the correlation coefficient and the gradient of the correlation coefficient remain stable. Table 4 shows the number of iterations fixed for each reconstruction algorithm and number of projections used in the reconstruction.

## 4. Method for material classification

The description of the SIMCAD method that estimates  $\rho_e$  and  $Z_{\text{eff}}$  for materials from Spectral CT data is detailed in Jumanazarov et al. [14], and it is briefly repeated in this entire section for the convenience of the reader.

### 4.1. Calibration step

Based on [15], LAC for a material,  $m$ , and for each energy bin can be defined as

$$\mu_m(E_k) = \rho_{e,m} \left( Z_{\text{eff},m}^{n-1} p(E_k) + c(E_k) \right), \quad (29)$$

where  $m = 1, 2, \dots, M$ ,  $k = 1, 2, \dots, K$  with  $M$  being the total number of materials and  $K$  being the number of energy bins used. Note that we use 15 energy bins as discussed in the subsection 2.3.  $p(E_k)$  and  $c(E_k)$  are photoelectric absorption

and Compton scattering basis functions for energy bin  $E_k$ , respectively. The energy-dependent basis functions and the exponent  $n$  are calibrated by using the reference  $\rho_e$  and  $Z_{\text{eff}}$  values, and the same for all the materials estimated.

To optimize the basis functions and  $n$  we define the non-linear objective function as:

$$\min_{0 \leq p_1, c_1, \dots, p_K, c_K, n} \sum_{m=1}^M \sum_{k=1}^K \left( \mu_m(E_k) - \rho_{e,m} (Z_{\text{eff},m}^{n-1} p_k + c_k) \right)^2, \quad (30)$$

where  $p_k = p(E_k)$  and  $c_k = c(E_k)$ . The objective function is optimized by using a nonlinear least square solver based on the trust region method [29]. We impose initial positivity constraints as  $p_k^0 = 0.5$ ,  $c_k^0 = 0.5$  and  $n^0 = 3.6$  for all  $k$ . The classification results are found to be independent from the initial constraints. The classification method can be formulated for any number of energy bins.

### 4.2. Calculation of material features

$\rho_e$  and  $Z_{\text{eff}}$  of an unknown material scanned are estimated by using the calibrated basis functions and the exponent  $n$  and the extracted LACs. We reformulate the LACs defined in Eq. (29) as a linear system equation as follows:

$$\begin{pmatrix} \bar{p} & \bar{c} & & \\ & & \ddots & \\ & & & \bar{p} & \bar{c} \end{pmatrix} \begin{pmatrix} z_1 \\ \rho_{e,1} \\ \vdots \\ z_M \\ \rho_{e,M} \end{pmatrix} = \begin{pmatrix} \bar{\mu}_1 \\ \vdots \\ \bar{\mu}_M \end{pmatrix} \quad (31)$$

where  $z_m$  is a temporary variable inserted instead of  $\rho_{e,m} Z_{\text{eff},m}^{n-1}$  and  $\bar{p} = (p_1, \dots, p_K)^T$ ,  $\bar{c} = (c_1, \dots, c_K)^T$  and  $\bar{\mu}_m = (\mu_m(E_1), \dots, \mu_m(E_K))^T$ . The linear matrix has the size of  $(M \times K)$ -by- $(2 \times M)$  and the number of unknowns is  $2 \times M$ . Using the positivity constraint on the solution we retrieve the vector  $(z_1, \rho_{e,1}, \dots, z_M, \rho_{e,M})$  minimizing the norm in the linear least square problem. From this, the effective atomic numbers are calculated for all the materials estimated

as

$$Z_m = \left( \frac{z_m}{\rho_{e,m}} \right)^{\frac{1}{n-1}}. \quad (32)$$

The accuracy of the material classification is calculated as the percent relative deviation from the reference values for  $\rho_e$  and  $Z_{\text{eff}}$  as:

$$\Delta Z_{\text{eff}}^{\text{rel}} = 100\% \cdot \frac{Z_{\text{eff}}^{\text{est}} - Z_{\text{eff}}^{\text{ref}}}{Z_{\text{eff}}^{\text{ref}}}, \quad (33)$$

$$\Delta \rho_e^{\text{rel}} = 100\% \cdot \frac{\rho_e^{\text{est}} - \rho_e^{\text{ref}}}{\rho_e^{\text{ref}}}, \quad (34)$$

where superscripts est and ref are regarded as the estimated and reference values, respectively. The results obtained with this method of material classification by using the  $L_\infty$ -VTV, TNV and TV reconstruction algorithms are presented in the subsection 5.5.

## 5. Results and discussions

In this section we present and discuss the results obtained with different reconstruction algorithms based on experimental data. The subsections 5.1, 5.2, 5.3 and 5.4 include the results for reconstruction quality studied with the correlation coefficient for each algorithm. The subsection 5.5 presents the material classification results obtained with the SIMCAD method described in Section 4.

### 5.1. Reconstruction results for different numbers of projections

In this subsection, we perform the reconstructions with each algorithm over a set of weighting parameters  $\lambda$  for different number of projections. We now focus on reconstructions from few (7 and 12) projections. Fig. 5 presents the correlation coefficients as a function of weighting parameter computed for the different numbers of projections. Note that a too small value of  $\lambda$  may result in an over-regularized image with blurred edges, while a too large value may give insufficient regularization effects, as notable in Eq. (8). For 7 and 12 projections, the maximal correlation coefficients for bin-by-bin reconstructions of TV and SIRT appear to be noticeably lower compared to the coefficients for the joint reconstructions of TNV and  $L_\infty$ -VTV. In all cases, the maximal correlation coefficient for  $L_\infty$ -VTV reconstruction are clearly larger than the coefficients for TNV and TV reconstructions, while SIRT reconstructions show the lowest values. Fig. 6 compares the TV, the TNV and the  $L_\infty$ -VTV reconstructions for 7, 12 and 36 projections, which are obtained with the corresponding maximal correlation coefficients presented in Fig. 5. In cases of 7 and 12 projections, the TNV and  $L_\infty$ -VTV algorithms appear to have clearly less structural artifacts than the TV reconstruction, which suffers from over-smoothing and more distortion in shape. When comparing  $L_\infty$ -VTV with TNV,  $L_\infty$ -VTV presents more accurate reconstructions with better structure and preserved edges.

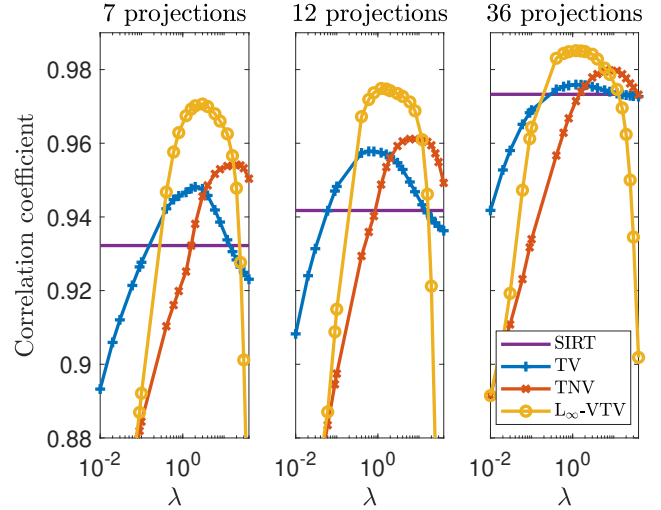


**Figure 5:** The correlation coefficients as a function of weighting parameter  $\lambda$  for 7, 12 and 36 projections, obtained with different reconstruction algorithms. The correlation coefficient determines how the reconstructed image is linearly associated with the ground-truth image, and is defined in Eq. (28). These results are based on scans of the plastics sample shown in Fig. 2a with 8 s integration time per projection. The correlation coefficients represent the mean values calculated from the coefficients for 15 energy bins used. Note the logarithmic scale in the x-axis.

### 5.2. Reconstruction results for different photon counts

In this subsection, we test the robustness of each reconstruction algorithm to different (low) numbers of photon counts using the same sample scanned with integration times of 2 ms, 10 ms and 50 ms. Fig. 7 shows the correlation coefficient evaluating reconstruction quality as a function of weighting parameter for each algorithm. It can be noted from the graphs that the TNV and  $L_\infty$ -VTV reconstructions provide higher maximal correlation coefficients compared to the maximal correlation coefficient for TV. This difference becomes more significant when the integration time is equal to 2 ms. As the integration time decreases, the  $\lambda$  value corresponding to the maximal correlation coefficient also decreases for each reconstruction algorithm, i.e. the reconstruction algorithms need the more regularization to achieve the best reconstruction, as expected. Fig. 8 compares the TV, TNV and  $L_\infty$ -VTV reconstructions corresponding to the maximal correlation coefficients for different integration times. The lowest integration time, 2 ms shows that the TV reconstruction noticeably suffers from blurring and over-smoothing whereas the TNV and the  $L_\infty$ -VTV joint reconstructions appear to be less noisy, sharper and better at preserving the edges. Thus, the joint reconstruction algorithms show better robustness to lower photon counts compared to the bin-by-bin reconstruction, TV. When comparing the  $L_\infty$ -VTV with the TNV, the  $L_\infty$ -VTV presents the reconstructions with noticeably sharper edges and less structural artifacts, which becomes more visible in the cases of 2 ms and 10 ms integration time. The robustness to lower photon

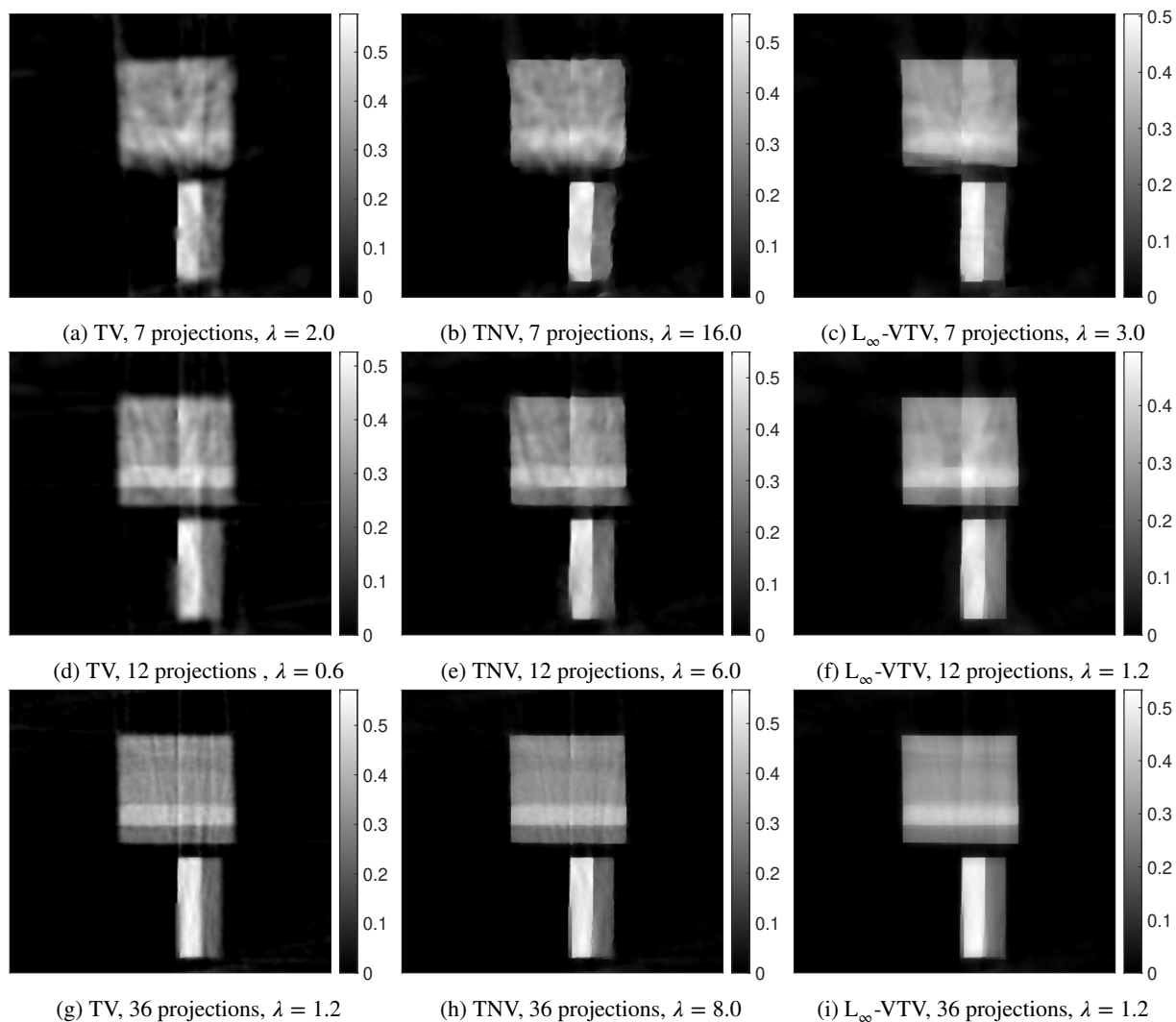


**Figure 6:** TV, TNV and  $L_\infty$ -VTV reconstructions of the plastics sample for 7, 12 and 36 projections corresponding to the X-ray energy of 42 keV. The figure compares the image reconstructions, each obtained with the weighting parameter  $\lambda$  corresponding to maximal correlation coefficients presented in Fig. 5. The composition of the sample is presented in Fig. 2a. The integration time per projection was equal to 8 s. The gray scale bar shows linear attenuation coefficients (LACs) with the unit of  $\text{cm}^{-1}$ .

counts in terms of material classification is important for the industrial applications, because the lower integration time can enable faster data acquisition.

### 5.3. Reconstruction: robustness to significantly higher noise levels in certain energy bins

Some energy bins may suffer from additional noise during scanning. Significant noise in certain energy bins can be caused by metal objects in the sample, which reduce the photon counts leading to photon starvation and create metal artifacts in the reconstructions. Metal artifacts influence primarily the lower energy bins and may be more severe resulting in less reliable characterization of the material properties. To estimate the robustness of the algorithms to such artifacts, we added Gaussian noise to the sinogram data with a standard deviation ( $\sigma$ ) of 0.5, 1.0 and 1.5. The noise is introduced to two specific bins out of 15 energy bins: 48.7 keV and 101.6 keV. Fig. 9 shows the correlation coefficients as

a function of photon energy for each  $\sigma$ , obtained with each reconstruction algorithm. We first found the optimal  $\lambda$  value corresponding to the highest mean correlation coefficient for  $\sigma = 1.5$ , which is calculated from the coefficients for each of 15 energy bins used. We then used this optimal  $\lambda$  to produce correlation coefficients for other  $\sigma$  values for each reconstruction algorithm.

It can be noted from the graphs that there are no interactions between energy bins for TV as expected, whereas TNV and  $L_\infty$ -VTV show correlation between energy bins and have noticeably smaller decreases in correlation coefficient for the affected bins. Thus, the joint reconstruction algorithms compensate for significantly higher noises in specific energy bins by effectively using the unaffected energy bins, for which couplings between energy bins lead to slight decrease in overall reconstruction quality. The figures also show that  $L_\infty$ -VTV in turn outperforms TNV in compensating such increased noise, and significantly improves the re-

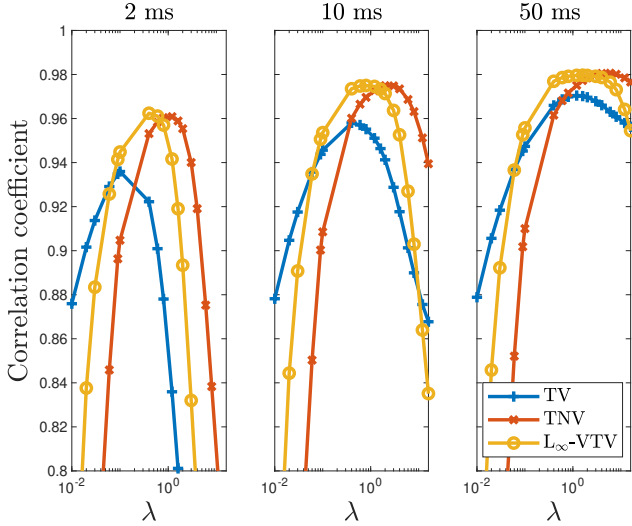


**Figure 7:** Correlation coefficients as a function of weighting parameter  $\lambda$  for integration times of 2 ms, 10 ms and 50 ms, obtained with different reconstruction algorithms. These results are based on scans of the sample shown in Fig. 2b with 36 projections. The correlation coefficients represent the mean values calculated from the coefficients for the 15 energy bins used. Note the logarithmic scale in the x-axis.

construction quality in the lower energy bins. This property of  $L_\infty$ -VTV can be highly important to reduce metal artifacts that mainly affect lower energies.

#### 5.4. The L-curve

L-curve is a plot showing the balance between the regularization term and the respective reprojection error, as the weighting parameter  $\lambda$  changes [30]. The reprojection error is the square root of the data fidelity term expressed in Eq. (4), and summed over all energy bins as  $\| \mathbf{A} \mathbf{u}_\lambda - \mathbf{p} \|_2$ . The regularization term  $\mathcal{R}_{\text{TV}}(\mathbf{u})$  for TV defined in Eq. (5) is computed independently for each energy bin, and summed over all energy bins to plot L-curve. The regularization terms  $\mathcal{R}_{\text{TNV}}(\mathbf{u})$  and  $\mathcal{R}_{L_\infty\text{-VTV}}(\mathbf{u})$  for TNV and  $L_\infty$ -VTV are general for all energy bins, and described in Eq. (6) and Eq. (7), respectively. If the L-curve criterion for a reconstruction algorithm provides a robust estimation of  $\lambda$ , L-curve can be an alternative to correlation coefficient to find the optimal  $\lambda$  without the ground truth image.

Fig. 10 shows the correlation coefficient and the L-curve for each reconstruction algorithm. The optimal  $\lambda$  values theoretically lie on the corner of the L-curve and the values on the flat and vertical parts lead to the reconstructions dominated by over-regularization and under-smoothing, respectively. The L-curve is represented on a log-log scale for the Tikhonov regularization [30]. However, Yang et al. [31] showed that using a linear-linear representation of the L-curve gives a suitable L-shape for TV reconstruction. Similarly, we found that a linear-linear representation makes L-curve better suited for the reconstruction algorithms developed. Note that we use the real experimental data acquired with the phantom presented in Fig. 2b, and few (12) projec-

tions, which may lead to some limitations of the L-curve. Hanke [32] showed that the smoother reconstruction with the Tikhonov regularization leads to a lower accuracy of the estimated  $\lambda$ . Similarly, we found that the TV has such limitation that L-curve criterion leads to noticeable over-regularization, as shown in Fig. 10a. This may be because the TV tends to be over-regularized when using few projections and having low signal-to-noise ratios in the source spectrum which are investigated in the subsections 5.1 and 5.2, respectively. As shown in Fig. 10, when comparing the  $L_\infty$ -VTV with the TNV, the  $L_\infty$ -VTV demonstrates a more accurate estimation of the optimal  $\lambda$  based on the L-curve criterion. Thus, with the  $L_\infty$ -VTV we found the closest match between two weighting parameters corresponding to the maximal correlation coefficient and to the corner of its L-curve.

#### 5.5. Classification performance as a function of $\lambda$

For each reconstruction algorithm we tested the performance of material classification by using the SIMCAD method described in the Section 4. In the case of 7 projections, we artificially introduced Gaussian noise to the experimental data with a standard deviation of  $\sigma = 0.05$  after the spectral correction as described in the subsection 2.3. The reason is that the noise may be added during x-ray generation from the x-ray source in real applications, and we aim to test the robustness of the reconstruction algorithms to such noise for material classification. The noise was added to all the 15 energy bins for all the materials scanned and processed through the calibration step and  $(\rho_e, Z_{\text{eff}})$  calculation. Note that in the subsection 5.3 we added significant noise to specific energy bins to evaluate the reconstruction quality of each reconstruction algorithm and each energy bin, and tested it with one sample.

Fig. 11 presents the relative deviations for  $(\rho_e, Z_{\text{eff}})$  as a function of weighting parameter  $\lambda$  for 7 and 12 projections, and 7 projections with added noise. In the case of 12 projections, the reconstruction algorithms give almost identical results. In the case of 7 projections, the TV shows its lowest deviations of 3.8% for  $\rho_e$  and 4.2% for  $Z_{\text{eff}}$  (at  $\lambda = 16.0$ ), whereas the TNV and  $L_\infty$ -VTV yield the lowest deviations of 3.4% and 3.1% (at  $\lambda = 150.0$ ), and 3.5% and 2.4% (at  $\lambda = 30.0$ ), respectively. These deviations correspond to the optimal weighting parameters, for which both material properties have the lowest overall deviations for each algorithm. In the case of 7 noisy projections, the TV has deviations equal to 4.7% and 5.1% for  $\rho_e$  and  $Z_{\text{eff}}$  (at  $\lambda = 30.0$ ) respectively, while the TNV and  $L_\infty$ -VTV result in the deviations of 4.0% and 3.9% (at  $\lambda = 150.0$ ), and 3.9% and 2.8% (at  $\lambda = 20.0$ ), respectively. Thus, for such sparse-view and noisy projections the joint reconstructions clearly show better classification performance than the bin-by-bin TV reconstruction. When comparing the  $L_\infty$ -VTV with the TNV,  $L_\infty$ -VTV can provide higher classification accuracy. It can be noted from the figure that in the case of 7 noisy projections the  $L_\infty$ -VTV uses the lower  $\lambda$  value to obtain the lowest deviations. The reason may be that the algorithm requires a

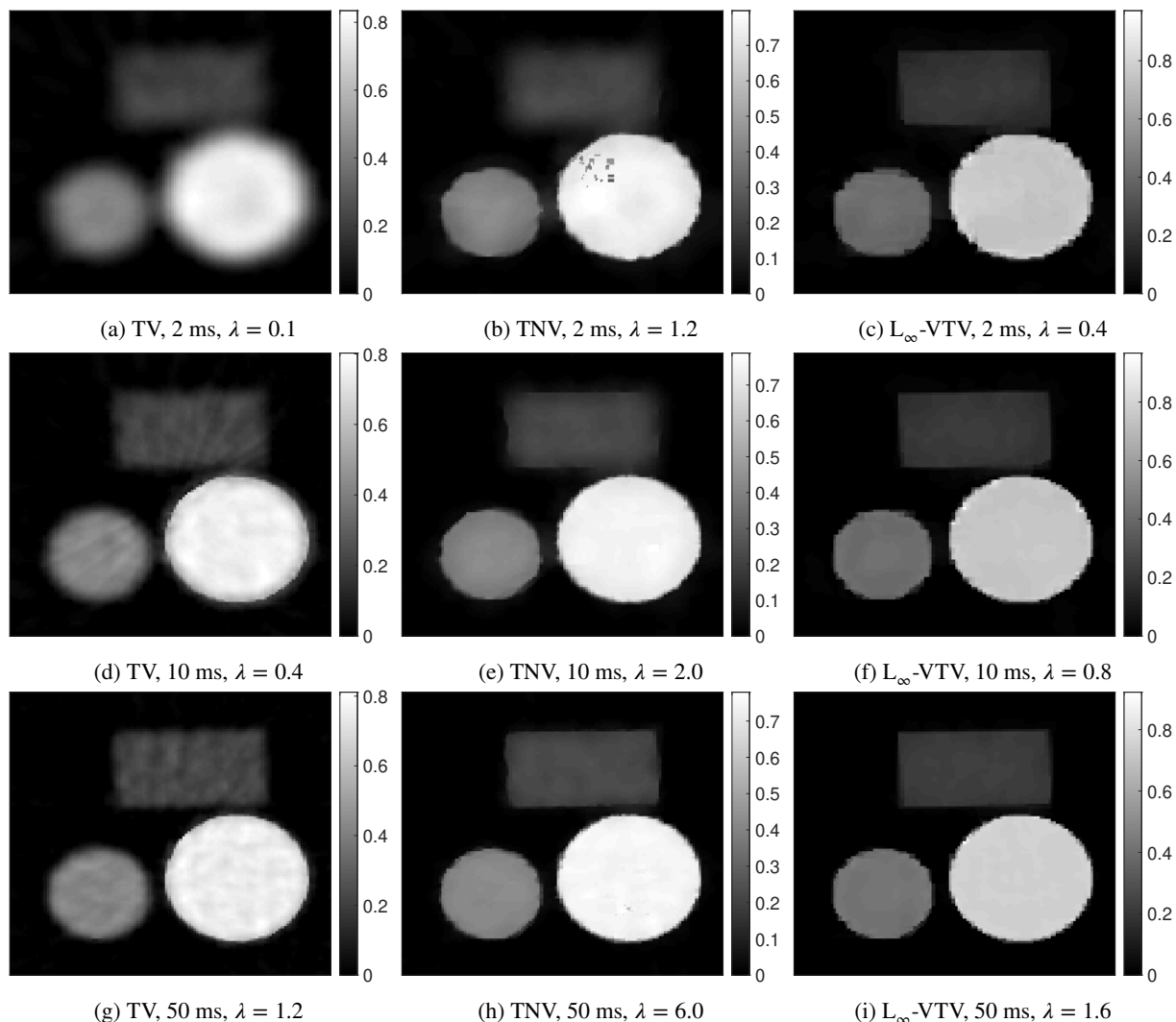


**Figure 8:** TV, TNV and  $L_\infty$ -VTV reconstructions for integration times of 2 ms, 10 ms and 50 ms corresponding to the X-ray energy of 61.9 keV. The figure compares the image reconstructions, each obtained with the weighting parameter  $\lambda$  corresponding to the maximal correlation coefficients presented in Fig. 7. The composition of the sample is presented in Fig. 2b. The number of projections is equal to 36. The gray scale bar shows linear attenuation coefficients (LACs) with the unit of  $\text{cm}^{-1}$ .

stronger regularization term to combat the added noise.

Fig. 12 shows the relative deviations for different materials in the case of 7 projections. The  $L_\infty$ -VTV gives the lowest deviations in both material features for POM-H plastic, which can be a common explosive simulant with similar chemical compositions [33]. Fig. 13 shows the classification performance of the  $L_\infty$ -VTV for different materials as a function of weighting parameter  $\lambda$ , obtained with 7 projections. Thus, the  $L_\infty$ -VTV with  $\lambda$  values between 20.0 and 40.0 can provide the optimal classification performance. We found in our implementation that for material classification the  $L_\infty$ -VTV requires 10.6% and 52.3% shorter computation time compared to the TNV of the state-of-the-art joint reconstruction in Spectral CT and to the TV, respectively.

## 6. Conclusion

We have presented the  $L_\infty$ -VTV joint reconstruction algorithm for Spectral CT with focus on security screening applications. This study is based on the real experimental data acquired with a laboratory X-ray Spectral CT. We tested the  $L_\infty$ -VTV against the state-of-the-art joint reconstruction of the TNV and also the TV and SIRT. We presented the implementation of each algorithm and how the iteration number is fixed based on the correlation coefficient. We use the correlation coefficient to estimate the image quality, which finds how well the reconstructed image is correlated with the ground truth image. We evaluated the reconstruction quality of each algorithm when the image reconstruction is performed from sparse-view projections and low levels of photon counts. As a result, we found that the joint reconstruction algorithms show significantly better image reconstruction compared to bin-by-bin reconstructions. We also

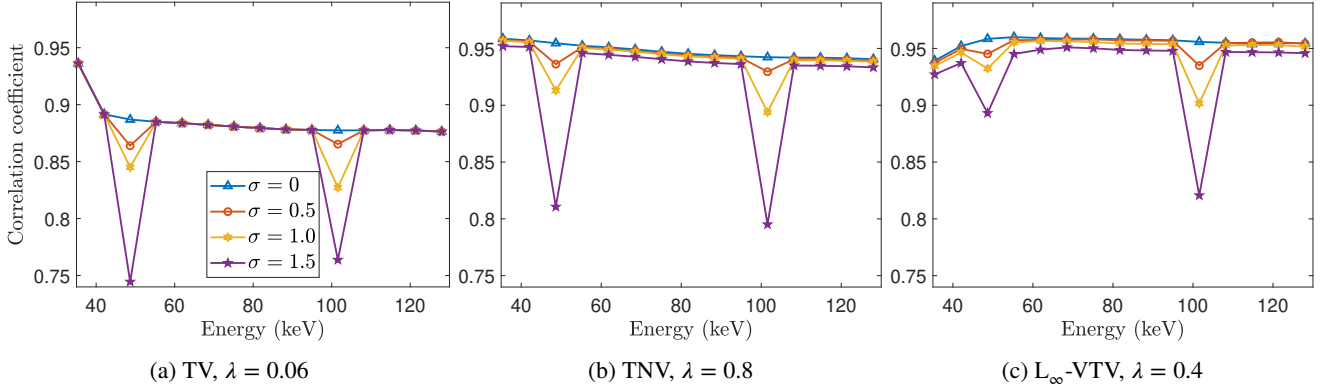


**Figure 9:** Correlation coefficients as a function of photon energy when different high Gaussian noise levels with standard deviation ( $\sigma$ ) of 0.5, 1.0 and 1.5 are added to the certain energies that are 48.7 keV and 101.6 keV. These results are obtained by using the phantom shown in Fig. 2b, being scanned with the integration time of 100 ms and reconstructed from 12 projections.

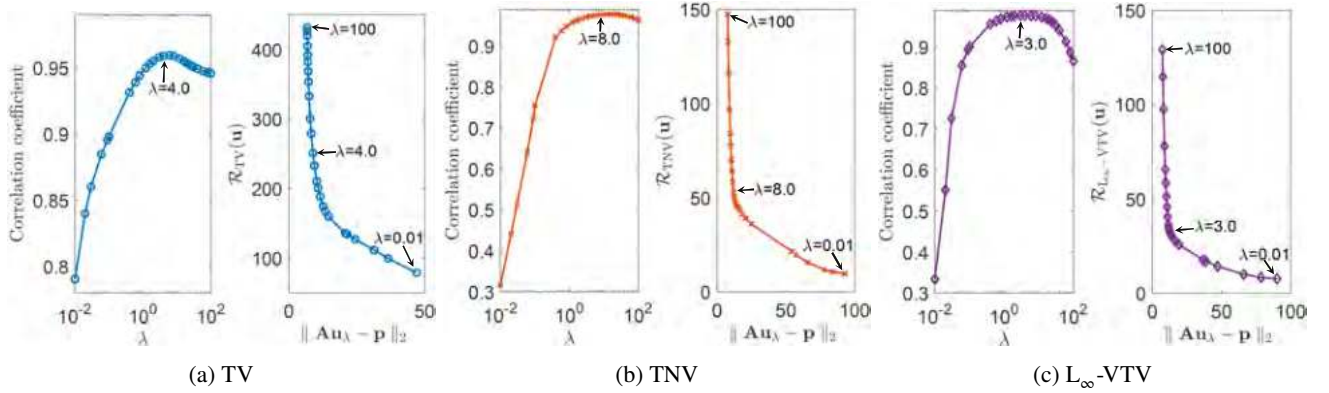


**Figure 10:** The correlation coefficient as a function of weighting parameter  $\lambda$  and L-curve for each reconstruction algorithm. These results are obtained with the sample shown in Fig. 2b, being scanned with the integration time of 100 ms and reconstructed from 12 projections. Note the logarithmic scale in the x-axis for the correlation coefficient.

studied the robustness of each algorithm when significantly higher noise levels are introduced to specific energy bins. The results showed that the joint reconstruction algorithms effectively alleviate such noise with information from unaffected bins and again achieve clearly better reconstructions for all the energy bins compared to the TV. When comparing the  $L_\infty$ -VTV with the TNV in these studies, the  $L_\infty$ -VTV was found to give better reconstruction from few projections and low photon counts, and to compensate more effectively for excess noise. Thus,  $L_\infty$ -VTV correlates the image gradients strongly over different energy bins, resisting outliers in gradient magnitudes. This property can be very useful for handling metal artifacts, which affect mainly the low-energy bins. Furthermore, for each algorithm we studied the L-curve to find the optimal weighting parameter for reconstruction, based on the scanned sample itself without the ground truth image. The  $L_\infty$ -VTV shows a clear correspondence between two optimal weighting parameters obtained with the correlation coefficient and the L-curve. Lastly, we investigated the material classification performance of each reconstruction algorithm by using the SIMCAD method for few and noisy projections, which estimates  $(\rho_e, Z_{\text{eff}})$  of a material from Spectral CT. The broad range of materials have

been used for classifications in the range of  $6 \leq Z_{\text{eff}} \leq 15$ . The joint reconstruction algorithms again show noticeably better performance compared to bin-by-bin reconstructions. The  $L_\infty$ -VTV appears to be more accurate for material classification and to require shorter computation time compared to the TNV. The reconstruction algorithms presented can easily be adapted for 3D CT.

## 7. Data and code availability

The raw and corrected data required to obtain the presented results are available to download from [34]. The implementations of our codes for  $L_\infty$ -VTV and TNV joint reconstruction algorithms are available at <https://github.com/JuliaTomo/XfromProjections.jl>.

## CRediT authorship contribution statement

**Doniyor Jumanazarov:** Conceptualization, Methodology, Software, Formal analysis, Investigation, Data curation, Writing - original draft, Visualization. **Jakeoung Koo:** Methodology, Software, Validation, Formal analysis, Writing - original draft. **Jan Kehres:** Resources, Writing - review and editing. **Henning F. Poulsen:** Writing - review

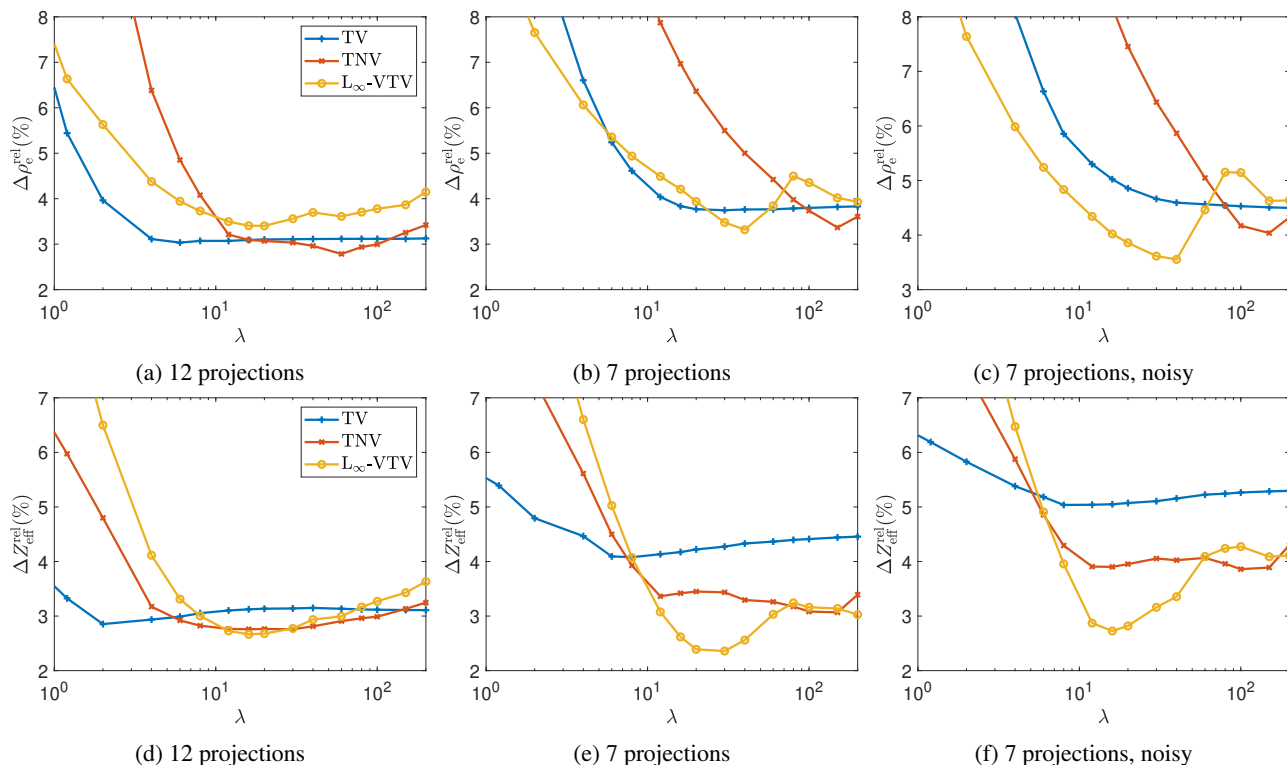


**Figure 11:** The relative deviation for  $(\rho_e, Z_{\text{eff}})$  as a function of weighting parameter  $\lambda$  for 3 cases of 7 and 12 projections, and 7 projections with added Gaussian noise. The first row corresponds to the relative deviations for  $\rho_e$ , and the second row is for  $Z_{\text{eff}}$ . The deviations are the mean values of the absolute deviations for each material listed in Table 3. The SIRT algorithm that is not included in the figure gives significantly higher deviations of 8.4% for  $\rho_e$ , and 2.4% for  $Z_{\text{eff}}$  for 12 projections, and 13.9% and 3.0% for 7 projections, respectively. These results are based on scans of the samples listed in Table 2 and Table 3 used for the calibration step and  $(\rho_e, Z_{\text{eff}})$  calculation, respectively. All the materials are scanned with a total integration time per projection of 8 s. Note the logarithmic scale in the x-axis.

and editing, Supervision. **Ulrik L. Olsen:** Validation, Resources, Data curation, Writing - review and editing, Supervision. **Mihai IOVEA:** Validation, Writing - review and editing, Supervision, Funding acquisition.

## Acknowledgements

This project has received funding from the European Union Horizon 2020 research and innovation programme under the Marie Skłodowska-Curie grant agreement No. 765604 as part of the MULTIscale, Multimodal and Multidimensional imaging for EngineerRING project (MUMMER-ING Innovative Training Network, [www.mummering.eu](http://www.mummering.eu)) and from the EIC FTI program (project 853720).

The authors want to acknowledge also the 3D Imaging Center at DTU, where the experiments have been conducted.

## References

- [1] L. I. Rudin, S. Osher, E. Fatemi, Nonlinear total variation based noise removal algorithms, *Physica D: nonlinear phenomena* 60 (1992) 259–268.
- [2] J. Song, Q. H. Liu, G. A. Johnson, C. T. Badea, Sparseness prior based iterative image reconstruction for retrospectively gated cardiac micro-CT, *Medical Physics* 34 (2007) 4476–4483.
- [3] J. Bian, J. Wang, X. Han, E. Y. Sidky, L. Shao, X. Pan, Optimization-based image reconstruction from sparse-view data in offset-detector CBCT, *Physics in Medicine and Biology* 58 (2013) 205–230.
- [4] E. Y. Sidky, C. M. Kao, X. Pan, Accurate image reconstruction from few-views and limited-angle data in divergent-beam CT, *Journal of X-Ray Science and Technology* 14 (2006) 119–139.
- [5] P. Blomgren, T. F. Chan, Color TV: Total variation methods for restoration of vector-valued images, *IEEE Transactions on Image Processing* 7 (1998) 304–309.
- [6] K. M. Holt, Total Nuclear Variation and Jacobian Extensions of Total Variation for Vector Fields, *IEEE Transactions on Image Processing* 23 (2014) 3975–3989.
- [7] B. Recht, M. Fazel, P. A. Parrilo, Guaranteed minimum-rank solutions of linear matrix equations via nuclear norm minimization, *SIAM review* 52 (2010) 471–501.
- [8] D. S. Rigie, P. J. La Rivière, Joint reconstruction of multi-channel, spectral CT data via constrained total nuclear variation minimization, *Physics in Medicine and Biology* 60 (2015) 1741–1762.
- [9] D. S. Rigie, A. A. Sanchez, P. J. La Rivière, Assessment of vectorial total variation penalties on realistic dual-energy CT data, *Physics in Medicine and Biology* 62 (2017) 3284–3298.
- [10] Z. Zhong, W. J. Palenstijn, J. Adler, K. J. Batenburg, EDS tomographic reconstruction regularized by total nuclear variation joined with HAADF-STEM tomography, *Ultramicroscopy* 191 (2018) 34–43.
- [11] J. Gregor, T. Benson, Computational analysis and improvement of SIRT, *IEEE Transactions on Medical Imaging* 27 (2008) 918–924.
- [12] T. Miyata, Y. Sakai, Vectorized total variation defined by weighted L infinity norm for utilizing inter channel dependency, *Proceedings*

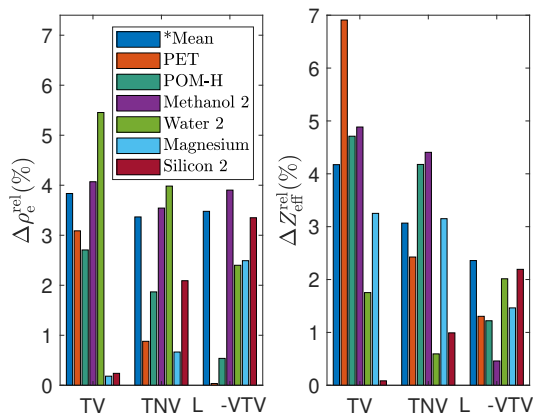


**Figure 12:** The percent relative deviations for  $(\rho_e, Z_{\text{eff}})$  corresponding to the optimal  $\lambda$  values, in which the classification performance for each reconstruction algorithm is the highest as presented in Fig. 11. The reconstructions are performed from sparse-view 7 projections. The mean deviations are calculated from the absolute values of relative deviations for each material listed in Table 3. The deviations for the different materials represent the absolute values.

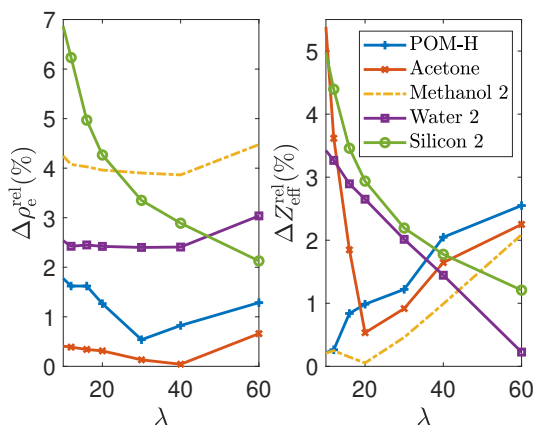


**Figure 13:** The relative deviations for  $\rho_e$  (left) and  $Z_{\text{eff}}$  (right) as a function of weighting parameter  $\lambda$  for the  $L_{\infty}$ -VTV in the case of 7 projections. The deviations are shown as the absolute values.

- International Conference on Image Processing, ICIIP (2012) 3057–3060.

[13] J. Duran, M. Moeller, C. Sbert, D. Cremers, On the Implementation of Collaborative TV Regularization: Application to Cartoon+Texture Decomposition, *Image Processing On Line* 5 (2016) 27–74.

[14] D. Jumanazarov, J. Koo, M. Busi, H. F. Poulsen, U. L. Olsen, M. Iovea, System-independent material classification through X-ray attenuation decomposition from spectral X-ray CT, *NDT and E International* 116 (2020) 102336.

[15] R. E. Alvarez, A. Macovski, Energy-selective reconstructions in X-ray computerised tomography, *Physics in Medicine and Biology* 21 (1976) 733–744.

[16] L. Salvo, M. Suéry, A. Marmottant, N. Limodin, D. Bernard, 3D imaging in material science: Application of X-ray tomography, *Comptes Rendus Physique* 11 (2010) 641–649.

[17] E. Maire, P. J. Withers, Quantitative X-ray tomography, *International Materials Reviews* 59 (2014) 1–43.

[18] A. H. Compton, S. K. Allison, et al., *X-rays in theory and experiment*, New York, NY, USA: Van Nostrand (1935).

[19] Mayneord, WV, The significance of the roentgen, *Acta of the International Union Against Cancer* 2 (1937) 271.

[20] F. W. SPIERS, Effective atomic number and energy absorption in tissues., *The British journal of radiology* 19 (1946) 52–63.

[21] A. Brambilla, P. Ouvrier-Buffet, J. Rinkel, G. Gonon, C. Boudou, L. Verger, CdTe linear pixel X-ray detector with enhanced spectrometric performance for high flux X-ray imaging, *IEEE Transactions on Nuclear Science* 59 (2012) 1552–1558.

[22] M. Ellenbogen, R. Bijjani, Liquids and homemade explosive detection, in: *Optics and Photonics in Global Homeland Security V and Biometric Technology for Human Identification VI*, volume 7306, International Society for Optics and Photonics, 2009, p. 73060Y. doi:10.1117/12.821806.

[23] Busi, Matteo, Enhanced Security Screening Using Spectral X-ray Imaging, Phd thesis, Technical University of Denmark, 2019.

[24] S. Kim, J. Chen, T. Cheng, A. Gindulyte, J. He, S. He, Q. Li, B. A. Shoemaker, P. A. Thiessen, B. Yu, L. Zaslavsky, J. Zhang, E. E. Bolton, PubChem 2019 update: Improved access to chemical data, 2019. URL: <https://pubchem.ncbi.nlm.nih.gov>. doi:10.1093/nar/gky1033.

[25] E. S. Dreier, J. Kehres, M. Khalil, M. Busi, Y. Gu, R. Feidenhans, U. L. Olsen, Spectral correction algorithm for multispectral CdTe x-ray detectors, *Optical Engineering* 57 (2018) 16.

[26] A. Chambolle, T. Pock, A First-Order Primal-Dual Algorithm for Convex Problems with Applications to Imaging, *J. Math. Imaging Vis.* 40 (2011).

[27] H. H. Bauschke, P. L. Combettes, *Convex Analysis and Monotone Operator Theory in Hilbert Spaces*, CMS Books in Mathematics, Springer International Publishing, Cham, 2017. doi:10.1007/978-3-319-48311-5.

[28] L. N. Trefethen, D. Bau, *Numerical Linear Algebra*, Society for Industrial and Applied Mathematics, Philadelphia, 1997.

[29] J. Nocedal, S. J. Wright, *Numerical Optimization*, Springer, New York, 1999.

[30] P. C. Hansen, The L-Curve and its Use in the Numerical Treatment of Inverse Problems, in *Computational Inverse Problems in Electrocardiology*, ed. P. Johnston, *Advances in Computational Bioengineering* 4 (2000) 119–142.

[31] X. Yang, R. Hofmann, R. Dapp, T. van de Kamp, T. d. S. Rolo, X. Xiao, J. Moosmann, J. Kashef, R. Stotzka, TV-based conjugate gradient method and discrete L-curve for few-view CT reconstruction of X-ray in vivo data, *Optics Express* 23 (2015) 5368.

[32] M. Hanke, Limitations of the L-curve method in ill-posed problems, *BIT Numerical Mathematics* 36 (1996) 287–301.

[33] J. Rinkel, G. Beldjoudi, V. Rebuffel, C. Boudou, P. Ouvrier-buffet, G. Gonon, L. Verger, A. Brambilla, Experimental Evaluation of Material Identification Methods With CdTe X-ray Spectrometric Detector, *IEEE Transactions on Nuclear Science* 58 (2011) 2371–2377.

[34] D. Jumanazarov, J. Koo, J. Kehres, H. F. Poulsen, U. L. Olsen, M. IOVEA, Material classification from sparse spectral X-ray CT using vectorial total variation based on L infinity norm [Data set]. Zenodo, 2021. URL: <https://doi.org/10.5281/zenodo.4780625>. doi:10.5281/zenodo.4780625.



**Doniyor Jumanazarov** is a PhD fellow at the Department of Physics at Denmark Technical University (DTU), Kongens Lyngby, Denmark. He obtained his BS degree in physics from the National University of Uzbekistan, Tashkent, Uzbekistan, and his MS degree in Molecular Photonics for bio- and nanotechnologies (MONABIPHOT) from the École Normale Supérieure de Cachan, Cachan, France, in 2012 and 2018, respectively.



**Jakeoung Koo** received his B.Sc. and M.Sc. in Computer Science from Chung-Ang University, South Korea in 2015 and 2017, respectively. He



is now a Ph.D. student in Technical University of Denmark (DTU), Kongens Lyngby, Denmark. His research interests lie in Computed Tomography and Computer Vision.



**Jan Kehres** is a research engineer at DTU Physics. He received his PhD in operando investigation of catalyst nanoparticles using X-ray scattering and continued in this field of research as a postdoctoral researcher. His current field of research is the application of energy-dispersive detector technology for X-ray scattering and advanced imaging modalities with a focus on material identification of illicit materials for security applications. Jan has an extended background in developing instruments in the field of X-Ray science.



Professor, Dr. techn. **Henning Friis Poulsen** is employed at DTU Physics since 2012. Henning pioneered several x-ray microscopy methods enabling multiscale mapping of materials properties from the macroscopic and down to nanometre length scales. He heads the 3D Imaging Centre at DTU and is Principal Investigator on a number of European and national projects with the aim of introducing X-ray methods to industry.



**Dr. Ulrik Lund Olsen** is a senior research engineer at DTU Physics since 2013. He obtained his Ph.D. degree in 2009 from Copenhagen University. He is an expert in X-ray instrumentation and specialises in spectral X-ray detectors, data acquisition and processing. Ulrik's current research interest is the use of spectral detectors for security applications for improved reconstruction and material identification.



**Mihai IOVEA**, Engineer in Physics, Senior Research Scientist, Ph.D in Physics. He has over 30 years' experience in X-Ray Imaging projects research & development for Security and Non-Destructive Testing. Interested in X-ray 2D&3D Tomography and Digital Radiography techniques, such as: dual/multi energy, diffraction, back-scattering applied in for threats detection, high-resolution in-line X-ray scanners for fast industrial non-destructive testing.

## Paper C

**The significance of the spectral correction of photon counting detector response in material classification from spectral x-ray CT.**

Doniyor Jumanazarov, Jakeoung Koo, Henning. F. Poulsen, Ulrik L. Olsen and Mihai Iovea

# PROCEEDINGS OF SPIE

[SPIDigitalLibrary.org/conference-proceedings-of-spie](https://spiedigitallibrary.org/conference-proceedings-of-spie)

## The significance of the spectral correction of photon counting detector response in material classification from spectral x-ray CT

Jumanazarov, Doniyor, Koo, Ja-Keoung, Poulsen, Henning, Olsen, Ulrik, lovea, Mihai

Doniyor Jumanazarov, Ja-Keoung Koo, Henning F. Poulsen, Ulrik L. Olsen, Mihai lovea, "The significance of the spectral correction of photon counting detector response in material classification from spectral x-ray CT," Proc. SPIE 11771, Quantum Optics and Photon Counting 2021, 117710J (18 April 2021); doi: 10.1117/12.2589290

**SPIE.**

Event: SPIE Optics + Optoelectronics, 2021, Online Only

# The significance of the spectral correction of photon counting detector response in material classification from spectral X-ray CT

Doniyor Jumanazarov<sup>a,c</sup>, Jakeoung Koo<sup>b</sup>, Henning F. Poulsen<sup>a</sup>, Ulrik L. Olsen<sup>a</sup>, and Mihai IOVEA<sup>c</sup>

<sup>a</sup>Technical University of Denmark, DTU Physics, 2800 Kgs. Lyngby, Denmark

<sup>b</sup>Technical University of Denmark, DTU Compute, 2800 Kgs. Lyngby, Denmark

<sup>c</sup>ACCENT PRO 2000 s.r.l. (AP2K), Nerva Traian 1, K6, Ap. 26, Bucharest, S3, ROMANIA  
031041

## ABSTRACT

Photon counting imaging detectors (PCD) has paved the way for the emergence of Spectral X-ray Computed Tomography (SCT), which simultaneously measures a material's linear attenuation coefficient (LAC) at multiple energies defined by the energy thresholds. In previous work SCT data was analysed with the SIMCAD method for material classifications. The method measures system-independent material properties such as electron density,  $\rho_e$  and effective atomic number,  $Z_{\text{eff}}$  to identify materials in security applications. The method employs a spectral correction algorithm that reduce the primary spectral distortions from the raw data that arise from the detector response: charge sharing and weighting potential cross-talk, fluorescence radiation, scattering radiation, pulse pile up and incomplete charge collection. In this work, using real experimental data we analyze the influence of the spectral correction on material classification performance in security applications. We use a vectorial total variation ( $L_\infty$ -VTV) as a convex regularizer for image reconstruction of the spectral sinogram. This reconstruction algorithm employs a  $L_\infty$  norm to penalize the violation of the inter energy bin dependency, resulting in strong coupling among energy bins. Due to the strong inter-bin correlation,  $L_\infty$ -VTV leads to noticeably better performance compared to bin-by-bin reconstructions including SIRT and total variation (TV) reconstruction algorithms. The image quality was evaluated with the correlation coefficient that is computed relative to ground-truth images. A positive weighting parameter defines the strength of the  $L_\infty$ -VTV regularization term and thus controls the trade-off between a good match to spectral sinogram data and a smooth reconstruction in both the spatial and spectral dimension. The classification accuracy both for raw and corrected data is analyzed over a set of weighting parameters. For material classification, we used 20 different materials for calibrating the SIMCAD method and 15 additional materials in the range of  $6 \leq Z_{\text{eff}} \leq 15$  for evaluating the classification performance. We show that the correction algorithm accurately reconstructs the measured attenuation curve, and thus gives higher detection rates. We show that using the spectral correction leads to an accuracy increase of 1.6 and 3.8 times in estimating  $\rho_e$  and  $Z_{\text{eff}}$ , respectively.

**Keywords:** Spectral X-ray CT, Material classification, Photon counting X-ray detector, Spectral correction, Joint reconstruction, Security screening

## 1. INTRODUCTION

X-ray radiography and Computed Tomography (CT) widely used for Non-Destructive Testing (NDT) in industrial or laboratory applications give structural images of a material, however do not typically measure material

---

Further author information: (Send correspondence to Doniyor Jumanazarov)

Doniyor Jumanazarov: E-mail: doniyor.jumanazarov@fysik.dtu.dk, Telephone: +40 785402585

Jakeoung Koo: E-mail: jakoo@dtu.dk

Henning F. Poulsen: E-mail: hfpo@fysik.dtu.dk

Ulrik L. Olsen: E-mail: ullu@dtu.dk

Mihai IOVEA: E-mail: office@accent.ro

Quantum Optics and Photon Counting 2021, edited by Ivan Prochazka, Martin Štefaňák,  
Roman Sobolewski, Aurél Gábris, Proc. of SPIE Vol. 11771, 117710J · © 2021 SPIE  
CCC code: 0277-786X/21/\$21 · doi: 10.1117/12.2589290

Proc. of SPIE Vol. 11771 117710J-1

properties such as electron density,  $\rho_e$ , and effective atomic number,  $Z_{\text{eff}}$ .<sup>1,2</sup> The main reason is that the energy dependence of the attenuation is not measured. Security screening systems currently use dual-energy CT (DECT) for material recognition<sup>3-8</sup> with two channels of energy discrimination. However, the dual-energy CT suffer from two main limitations. Firstly, they typically use dual sandwiched energy integrating detectors leading to poor energy separation due to overlapping low- and high-energy spectrums. Secondly, the DECT only measures two different data points in the attenuation spectrum and therefore, only provide limited material classification maps. The development of cadmium telluride (CdTe) energy discriminating imaging detectors has laid groundbreaking step towards multi-energy Spectral CT (SCT) and other energy-resolved imaging modalities.<sup>9-11</sup> These detectors can discriminate the energy of the incident photons enabling the simultaneous collection of the spectrum of the whole range of material's energy-dependent linear attenuation coefficients (LACs) and provide material features. Spectral CT simultaneously measures the energy dependence of a material's LAC using energy resolved photon counting detectors (PCD). Spectral CT is proven to be superior to dual-energy CT for enhancing material recognition.<sup>12</sup> Radiography studies also showed that PCDs have clear advantages over dual-layer sandwich detectors in reducing the false detection rate.<sup>13-15</sup> The poor spectral separation in the dual-layer sandwich detectors was found to be the major reason for the lower performance. This has attracted significant attention in PCDs for material characterization within security applications.<sup>16-18</sup>

DECT Systems typically use an attenuation decomposition method presented by Alvarez et al.<sup>19</sup> for the formulation of an alternative material characterization. It decomposes a material's linear attenuation coefficient (LAC) into photoelectric absorption and Compton scattering basis functions and can define the whole spectral range of the LAC through just two parameters, density,  $\rho$ , and effective atom number,  $Z_{\text{eff}}$ . However, such material identification through the effective LAC using dual-energy sandwich detectors is a system-dependent solution, i.e. depend on source spectrum, filtration, and detector efficiency of the scanner.<sup>20</sup> Recently, Azevedo et al.<sup>21</sup> presented a method that measures  $(\rho_e, Z_{\text{eff}})$  from dual-energy CT called the System-Independent  $\rho_e/Z_{\text{eff}}$  (SIRZ), independent of the scanning instrument, and Champley et al.<sup>22</sup> have improved the method further (SIRZ-2).

Busi et al.<sup>23</sup> have adopted the SIRZ method for Spectral CT with the Spectral  $\rho_e/Z_{\text{eff}}$  Estimation (SRZE) method, which measures both system-independent material features directly from the energy-dependent LACs. However, the SRZE method uses 64 energy bins for the optimal accuracy and gives significantly lower accuracy at two energy bins.

In previous work we presented a novel classification method, named system-independent material classification through attenuation decomposition (SIMCAD),<sup>24</sup> which measures the material features  $(\rho_e, Z_{\text{eff}})$ , independent of the instrument or specifics of the scanner such as the X-ray spectrum, directly from energy resolved LACs in spectral CT. The method uses attenuation decomposition presented by Alvarez et al.<sup>19</sup> for the formulation to adopt it for multiple energies. It was demonstrated with the experimental data that the SIMCAD method can reach the optimal classification performance with optimized bi-energy bins and can give comparable results to the SRZE method. Therefore, the SIMCAD method spends at least 32x shorter time for the tomographic reconstruction after the data acquisition due to a lower number of energy bins used. The speed enables the method well suited for the requirements of rapid scanning for real applications such as check-in baggage control at airports.<sup>25</sup> It is worth noting that even if SIMCAD only used two bins and thus had the same number of data points of the energy spectrum as DECT, the overlap in DECT energy bins does not exist for PCD systems which leads to the improved performance. The above classification methods rely on accurate LAC curves. However, detector effects, such as charge sharing and pulse pileup, strongly distort the measured spectrum of photon-counting x-ray detectors operating under high flux.<sup>26</sup> These effects lead to severe deviation between the measured and the transmitted spectrum, and therefore to a significant decrease in material identification performance when used for both security and industrial applications. Thus, the correction of the detector's spectral response is required to correct the measured LACs. To correct for these distortions, we use a correction algorithm developed by Dreier et al.<sup>27</sup> This is a comprehensive semianalytical correction algorithm that corrects the raw data distorted by charge sharing, weighting potential, pulse pileup, incomplete charge collection, and x-ray fluorescence based on spectral distortion models. With small correction the correction algorithm is could be applied to any photon counting CdTe detector. In this work, we scan 35 different materials with 12 projections and reconstruct using the joint reconstruction method VTV. We analyze the contribution of the correction

algorithm in material identification from sparse (few projections) Spectral CT, because the spectral correction requires additional computation time which is a key factor for security and industrial applications.

## 2. EXPERIMENTAL SETUP AND MATERIALS. DATA CORRECTION ALGORITHM

In this section, we define the system-independent physical properties used to classify materials and LACs. We then present the experimental setup and the samples used to conduct the experiments. Lastly, the detector, data correction and sinogram generation are introduced.

### 2.1 Physical properties of materials

Linear attenuation coefficient (LAC) is proportionally dependent upon a material's electron density.<sup>28</sup> The electron density is the number of electrons per unit volume (electron – mole/cm<sup>3</sup>). For a compound or mixture that consists of  $N$  total different elements, the electron density can be expressed as

$$\rho_e = \frac{\sum_{i=1}^N \alpha_i Z_i}{\sum_{i=1}^N \alpha_i A_i} \rho, \quad (1)$$

where  $\rho$  is mass density (g/cm<sup>3</sup>),  $A_i$  and  $Z_i$  are atomic mass and atomic number for each element,  $i$ , respectively,  $\alpha_i$  is the number of atoms that have atomic number  $Z_i$ . For compounds, the atomic number is referred to as effective atomic number,  $Z_{\text{eff}}$ , which can be classically parameterized as<sup>29,30</sup>

$$Z_{\text{eff}} = \sqrt[l]{\sum_{i=1}^N r_i Z_i^l}, \quad (2)$$

where  $r_i$  is “relative electron fraction” contribution of an element,  $i$ ,

$$r_i = \frac{\alpha_i Z_i}{\sum_{j=1}^N \alpha_j Z_j},$$

In previous work,<sup>24</sup> the exponent  $l$  was studied to optimize the value for the best classification performance for the materials, source spectrum and system features used. The value of  $l = 8.0$  showed the highest accuracy, thus we choose this value for the calculations of reference  $Z_{\text{eff}}$  values in this work.

### 2.2 Decomposition of LAC

For a computed tomography system, Alvarez et al.<sup>19</sup> presented empirically over the range of 30–200 keV that the LAC could be decomposed in the form:

$$\mu(E) = a_1 \frac{1}{E^3} + a_2 f_{\text{KN}}(E), \quad (3)$$

where  $f_{\text{KN}}(E)$  is the Klein-Nishina function

$$f_{\text{KN}}(\varepsilon) = \frac{1 + \varepsilon}{\varepsilon^2} \left( 2 \frac{1 + \varepsilon}{1 + 2\varepsilon} - \frac{\ln(1 + 2\varepsilon)}{\varepsilon} \right) + \frac{\ln(1 + 2\varepsilon)}{2\varepsilon} - \frac{1 + 3\varepsilon}{(1 + 2\varepsilon)^2}, \quad (4)$$

and  $\varepsilon = E/511$  keV ( $\varepsilon = E/m_e c^2$ ) is the reduced energy of the incident photon. The functions  $1/E^3$  and  $f_{\text{KN}}(E)$  represent approximation of the energy dependence of the photoelectric absorption and Compton scattering, respectively. With exception of the absorption edges effect, they further presented that the photoelectric coefficient,  $a_1$  and the Compton scattering coefficient,  $a_2$  could be defined as:

$$a_1 \approx K_1 \frac{\rho}{A} Z^n, \quad a_2 \approx K_2 \frac{\rho}{A} Z \quad (5)$$

where  $K_1$  and  $K_2$  are constants,  $\rho$  is mass density ( $\text{g}/\text{cm}^3$ ),  $A$  is atomic mass and  $Z$  is atomic number.  $n$  is the exponent for photoelectric attenuation (per atom).  $n$  is optimized for each of the classification approaches depending on how many energy bins are used.  $a_1$  and  $a_2$  are expressed with approximation. The insertion of  $a_1$  and  $a_2$  from Eq. 5 into Eq. 3 gives the LAC as:

$$\mu(E) = \frac{Z}{A} \rho (Z^{n-1} p(E) + c(E)), \quad (6)$$

where

$$p(E) = K_1 \frac{1}{E^3}, \quad c(E) = K_2 f_{\text{KN}}(E). \quad (7)$$

$p(E)$  and  $c(E)$  are photoelectric absorption and Compton scattering basis functions, respectively. Inserting Eq. 1 into Eq. 6 we retrieve a parameterized LAC for a compound as

$$\mu(E) = \rho_e (Z_{\text{eff}}^{n-1} p(E) + c(E)). \quad (8)$$

The basis functions are empirically measured through fitting experimental data. In this work, the basis functions and exponent  $n$  are calibrated to retrieve material properties, which is discussed in the next subsection.

### 2.3 Experimental setup and materials

The experiments were conducted in the 3D Imaging Center at DTU, Denmark. The X-ray beam was generated by a Hamamatsu source working under the acceleration voltage and the filament current set to 160 kV and 0.5 mA, respectively. The focal spot is  $75 \mu\text{m}$ . An aluminum filter of 2 mm thickness was mounted after the source to suppress photons with energies lower than the detector energy range. The beam was collimated to a fanbeam using a JJ X-ray IB-80-Air to a height of 0.6mm. Directly in front of the detector a custom built 5mm thick tungsten slit (opening: 0.6mm) minimize photon scattering. The sample was placed on the rotation stage and scanned between discrete rotations with  $30^\circ$  increments over a range of 360 degrees. The source to detector distance (SDD) was set equal to 701 mm whereas the source to sample distance (SOD) was 500 mm. For material classification presented in the subsection 5.3, the total integration time per projection was set to 8 seconds.

The sample scanned for the uses in the subsections 5.1 and 5.2 contains aluminum, magnesium and polyetheretherketone (PEEK) plastic and was scanned with different total integration time per projection varying from 2 ms to 100 ms. This sample is described in Ref. 31. Tab. 1 and Tab. 2 in Appendix A lists the materials used for the calibration as reference materials and estimation of material features, respectively. The tables include the materials' reference  $\rho_e$  and  $Z_{\text{eff}}$  values that were calculated by using Eq. 1 and Eq. 2 respectively. Sample dimension are also presented through width $\times$ length for rectangular samples or diameter for circular samples. The plastics shown in the tables are polymethyl methacrylate (PMMA), polytetrafluoroethylene (PTFE), polyvinylidene fluoride (PVDF), polycarbonate (PC), polyoxymethylene-C (POM-C), polyethylene terephthalate (PET) and polyoxymethylene-H (POM-H). Materials used are commonly found in checked-in luggage, and explosive or precursor materials without K-edge absorption within the detector's energy range and in the range of  $6 \leq Z_{\text{eff}} \leq 15$ .

### 2.4 The detector and data correction for spectral distortion

The detector adopted for the current experiments is MultiX ME-100 v2 manufactured by Detection Technology S.A.S. in Moirans, France. We use a system of five detector modules, each module has a  $1 \times 128$  linear array of pixels sized  $0.8 \times 0.8 \text{ mm}^2$ . The number of energy bins is 128 with a width of 1.1 keV each, evenly distributed in the energy range between 20 and 160 keV. The energy resolution of the detector operating at high X-ray fluxes is 6.5% (8 keV at 122 keV).<sup>11</sup> The detector has a CdTe sensor with 3 mm thickness. Incident photons strike a collective cathode being composed of a continuous metal film. The sensor has pixelated anodes with significantly smaller size, which are located on readout electronics.

The spectral response of photon counting detectors is severely distorted by a range of physical effects occurring inside CdTe sensor crystal. These energy and flux dependent effects decrease the energy resolution of PCDs and induce distortion in measured LAC curves. A X-ray photon absorbed near a pixel border generates electron

charge cloud which may split between neighboring detector pixels. As a result, the high-energy x-ray photon is falsely counted as two photons which have lower energies. This physical phenomenon is called charge sharing. Another phenomenon is related to X-ray fluorescence. Detector sensor materials Cd and Te present K-edges at 26.7 keV and 31.8 keV, respectively. Incoming x-rays at an energy  $E$  can expel K-electrons of CdTe sensor crystal when the photon energy is larger compared to the K-shell binding energies. The vacant K-shells are instantly reoccupied, and the fluorescence K-shell X-ray photons with energy  $E_{\text{fl}}$  are emitted and are in some cases re-absorbed and registered in the detector pixel itself or in adjacent detector pixels (K-escape). As a result, the incoming photons are registered at an energy  $E - E_{\text{fl}}$ , and the consequent peak in the energy spectrum is called K-escape peak. Thus, high-energy x-rays are again recorded at lower energies which leads to a decrease in energy separation and also spatial resolution.

Charge sharing and K-escape are border interactions. Contribution of these phenomena to the overall detector response decreases as the size of the detector pixels increases, which can lead to improved energy discrimination. However, the number of incident X-ray photons striking the same pixel increases in time if the pixel has larger size. This may result in the overlapping of pulses created by two photons, which may be recorded as one photon at a very high energy. This effect is called pulse pile-up. Pulse pile-up can cause non-linear detector counting statistics and eventually detector saturation.<sup>32</sup> The contribution of this effect to the total detector response can be reduced with designing smaller pixels, however, this may result in increased charge sharing and K-escape. Discovering the best size of the detector pixels to steady charge sharing, K-escape and pulse pile-up is very important in making a PCD.

Charge carriers that are counted by one detector pixel may again produce a pulse in the adjacent pixel. This phenomenon is called weighting potential (WP) cross talk and gives rise to the source spectrum at energies lower than 30 keV.<sup>27</sup> Effects such as electronic noise<sup>33</sup> and Compton scattering of the incoming photons in the detector crystal are another problems of PCDs. Both effects have less contributions to the detector signal compared to other effects.

CdTe detectors are also subjected to another challenge that is charge trapping. Some of charge carriers are trapped in crystal lattice defects or impurities, which are non-uniformly distributed.<sup>34</sup> This results in the effect called incomplete charge collection (ICC). The ICC becomes visible in the spectrum at energies higher than 60 keV.<sup>35</sup> The electrons and holes move at drift velocities  $v_e = \mu_e E_e$  and  $v_h = \mu_h E_e$  towards the collective cathode and pixelated anodes, respectively.  $\mu_e$  and  $\mu_h$  are the electron and hole drift mobilities, respectively, and  $E_e$  is the external electric field. The holes drift with significantly smaller mobility than electrons. The electrons have 1000 cm<sup>2</sup>/V of the drift mobility whereas the holes have 80 cm<sup>2</sup>/V.<sup>36</sup> This leads to more severe trapping of the slow holes than electrons. The hole trapping is typically reduced by designing CdTe detector with much smaller pixelated anodes than the crystal thickness. This gives comparatively far less contribution of hole transport to the total signal and, thus, reduces ICC effect.<sup>37</sup> Moreover, the trapped holes create the accumulation of positive charges in the crystal which can change the external electric field distribution over time and distort the characteristics of the charge collection. This effect is called polarization and also can lead to ICC.<sup>34,38</sup> Polarization might cause noticeable ring artifacts in the reconstructed images at higher photon fluxes,<sup>32</sup> and also rapid decrease in signal pulses above a definite high flux rate.<sup>39</sup>

In the correction algorithm, using the simulated detector response matrix the distorted spectrum is first corrected for the flux-independent effects, such as charge sharing, WP cross talk, X-ray fluorescence (escape peaks), Compton scattering and electronic noise. Flux-independent effects are corrected by using an inverse detector response matrix  $\mathbf{M}_C$  of size  $N \times N$ , where  $N$  is the number of energy bins. The raw data is represented as matrix  $\mathbf{I}_R$  of size  $N \times J$ , where  $J$  is the number of detector pixels. The matrix for corrected data for each pixel is obtained by<sup>27</sup>

$$\mathbf{I}_C = \mathbf{M}_C \mathbf{I}_R, \quad (9)$$

The inverse detector response matrix is decomposed into the individual detector response matrices, and it is computed as<sup>27</sup>

$$\mathbf{M}_C = \mathbf{D}_{\text{WP}} \mathbf{D}_E \mathbf{D}_C, \quad (10)$$

where  $\mathbf{D}_{\text{WP}}$ ,  $\mathbf{D}_E$  and  $\mathbf{D}_C$  are the detector response matrices corresponding to WP cross talk, Compton scattering and electronic noise, and charge sharing effects, respectively. The WP cross talk is firstly calculated to correct distortion at low energies. The charge sharing is lastly corrected.



For each pixel's response to X-ray illumination, a Monte Carlo simulation is employed to calculate the total detector response matrix, which is dependent on the incident X-ray energy and location of photon's energy deposition. The location of photon absorption is considered as a function of depth in the sensor under the probability distribution function defined by the reference LACs which are obtained from NIST cross-sections.<sup>40</sup> In the simulation, the escape peaks phenomenon occurring due to X-ray fluorescence is firstly defined, by assuming that the emitted fluorescence photons are directed randomly and absorbed at certain travel distance.  $\mathbf{D}_{WP}$ ,  $\mathbf{D}_E$  and  $\mathbf{D}_C$  detector response matrices are then computed separately based on 2-D histograms of registered and actual incident energy of X-rays in the simulation. In the model of calculating charge sharing, the excited electron cloud is split between two adjacent pixels based on a 1-D Gaussian distribution that is aligned with the detector array. The excited charge cloud can induce current in the adjacent pixels, and the amount of WP cross talk is proportional to the amount of current. A simplified model presented in Ref. 41 is used for calculating WP cross talk, in which the detector is considered as the detector surfaces are composed of two infinite parallel sheets. The model employs the approach of reflected dipole layers (mirror charges), which assumes that WP cross talk is defined as an infinite sum of the WP elementary functions corresponding to the reflected dipole layers distributed at equal distances dependent on the depth of the crystal.

Flux dependent models such as the pulse pileup and incomplete charge collection are then considered for correction. The model presented by Plagnard<sup>42</sup> is employed to correct for the pile-up phenomenon. The pile-up effect of photon with energy  $E_n$  on other whole energies  $E_x$  of the measured spectrum  $I_R(E)$  gives the respective pile-up spectrum  $I_P(E_{nx})$ , which is defined for all the range of  $x$  as<sup>27,42</sup>

$$E_{nx} = E_n + E_x, \quad (11)$$

$$I_P(E_{nx}) = \frac{I_R(E_n)}{I_R(E)_{\max}} C_P I_R(E_x). \quad (12)$$

It is assumed that the two photons with energies  $E_n$  and  $E_x$  in the measured spectrum are recorded as one photon with energy  $E_{nx}$  in the pile-up spectrum.  $C_P$  is a coefficient for defining pile-up probability. Dreier et al.<sup>27</sup> uses an automatic fitting method to compute this coefficient using the spectral LACs of aluminum. The pile-up spectrum is deducted from the measured spectrum, and the result is added to  $\sum_x I_P(E_{nx})$  summed over the whole range of  $x$ . This gives the corrected spectrum  $I_C(E_n)$  of the energy bin  $n$ <sup>27</sup>

$$I_C(E) = I_R(E) - I_P(E), \quad (13)$$

$$I_C(E_n) = I_C(E_n) + \sum_x I_P(E_{nx}). \quad (14)$$

To obtain the whole corrected spectrum, the same modelling is applied for each increment of  $n$  changing from the initial to final values. We refer the reader to Dreier et al.<sup>27</sup> for more details of the correction algorithm.

## 2.5 Sinogram generation

The correction of the raw data is followed by converting the photon counts to line integral or sinogram for each energy bin based on Lambert–Beer's law as follows:

$$L_k(\vec{x}) = -\log \frac{I_k(\vec{x})}{I_{0,k}(\vec{x})}, \quad k = 1, 2, 3, \dots, 128; \quad (15)$$

where  $I_{0,k}$  is the flat-field photon flux corresponding to energy bin  $k$  measured without the sample,  $I_k$  is the measured photon flux for energy bin  $k$  that has passed through the material,  $\vec{x}$  is the 1D detector pixel array.

## 3. IMAGE RECONSTRUCTION METHOD AND LAC EXTRACTION

In this section, we briefly describe the joint reconstruction method we previously presented in Ref.<sup>31</sup> We also present how LAC is extracted, and the data is rebinned into 2 and 15 energy bins between low- and high-energy thresholds. Lastly, we present a tool for analyzing the reconstructed image quality obtained for the raw and corrected data.

### 3.1 Joint reconstruction

In Spectral CT, we measure a stack of energy-resolved sinograms with  $N$  energy bins denoted by  $\mathbf{p}_1, \dots, \mathbf{p}_N \in \mathbb{R}^M$ , with  $M$  being the number of detector pixels multiplied by the number of projection angles. From the spectral sinograms, we target to reconstruct  $N$  respective images of  $\mathbf{u}_1, \dots, \mathbf{u}_N \in \mathbb{R}^J$  for each energy bin  $E_i$ , with  $J$  being the number of pixels for each image. Energy-resolved LACs are retrieved directly from these spectral reconstructions. We denote a stack of spectral sinograms by a vector  $\mathbf{p} \in \mathbb{R}^{NM}$  and a stack of  $N$  reconstructions by  $\mathbf{u} \in \mathbb{R}^{NJ}$  as well as the LAC for the energy bin  $E_i$  on the  $j$ -th pixel by  $u_{i,j}$ .

An operator, known as the forward projection, maps the images onto the sinogram domain and the forward projection is commonly formulated as a linear operator  $\mathbf{A}$  such that  $\mathbf{A}\mathbf{u} = \mathbf{p}$ . Here, we use the same forward-projection operator for each energy bin and  $\mathbf{A}$  is the stack of such operators. This formulation enables comparing the estimation with the sinogram data  $\mathbf{p}$  and we want to minimize the reprojection error (distinction between the synthesized and observed sinogram) in  $L_2$  norm as follows:

$$\mathcal{G}(\mathbf{A}\mathbf{u}) = \frac{1}{2} \|\mathbf{A}\mathbf{u} - \mathbf{p}\|_2^2. \quad (16)$$

To deal with noisy data and a small number of projection angles and obtain better reconstruction taking advantage of multi-spectral dimensionality of reconstructions, we consider a regularization term by imposing a prior knowledge on the solutions. We employ a vectorial total variation scheme called  $L_\infty$ -VTV, which correlates the image gradients using maximum norm over multi energy bins as follows:

$$\mathcal{R}_{\text{VTV}}^{L_\infty}(\mathbf{u}) := \sum_{j=1}^J \left( \max_{1 \leq i \leq N} |\nabla_x u_{i,j}| + \max_{1 \leq i \leq N} |\nabla_y u_{i,j}| \right), \quad (17)$$

where  $u_{i,j}$  represents the image value for  $i$ -th energy bin and  $j$ -th pixel and  $\nabla_x$  and  $\nabla_y$  the gradient operators with respect to  $x$  and  $y$  axis, respectively. We found in our previous work<sup>31</sup> that this  $L_\infty$ -VTV norm correlates the gradients strongly over spectral dimension, rejecting outliers in gradient magnitudes.

We aim to minimize the sum of the data fitting term (Eq. 16) and the regularization term (Eq. 17) with a weighting parameter  $\lambda$  between two terms as follows:

$$\min_{\mathbf{u} \geq 0} \lambda \mathcal{G}(\mathbf{A}\mathbf{u}) + \mathcal{R}_{\text{VTV}}^{L_\infty}(\mathbf{u}), \quad (18)$$

where a non-negativity constraint is imposed on  $\mathbf{u}$  such that the LAC values should be non-negative. We refer to Jumanazarov et al.<sup>31</sup> for details of the optimization of our objective function defined in Eq. 18, and stopping criteria for the number of iterations.

### 3.2 LAC extraction

After energy resolved reconstruction and manual segmentation, for each material and each energy bin the LAC value of a segment is calculated from attenuation value histogram based on normal distribution fitting method within a region of interest (ROI) of a sample.<sup>24</sup> Fig. 1 presents an example of magnesium's spectral LAC calculated both from the raw data and from the data corrected using the correction algorithm as described in the subsection 2.4. the two experimental curves are compared to the reference curve of LAC. The correction algorithm largely restores the LAC towards the reference curve at the low energies, however, fails to correct for additional spectral distortions at lower and higher energies. One reason for this could be because of detector flux variation and photon starvation, i.e. complete attenuation of photons.<sup>27</sup> Energy bins in which the LAC is deviating from the reference values even after applying the correction algorithm are excluded in the later processing by placing low- and high-energy thresholds,  $E_l$  and  $E_h$ .

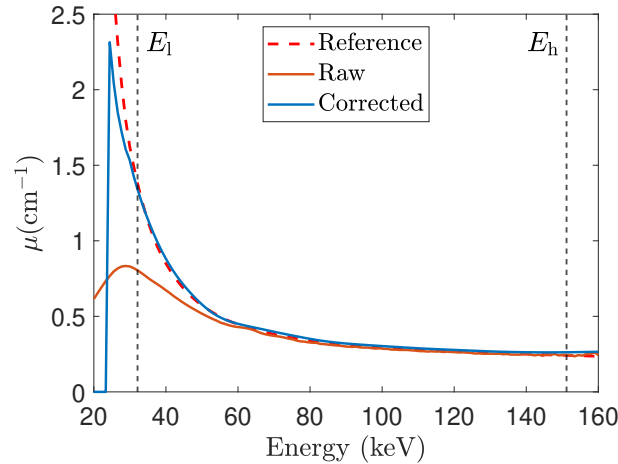


Figure 1: Spectral LAC for magnesium obtained from the raw and corrected data. The reference LACs were obtained by employing NIST cross-sections.<sup>40</sup> The vertical black dash-dotted lines represent the low- and high-energy thresholds,  $E_l$  and  $E_h$  remaining same for all materials estimated.

### 3.3 Rebinning energy bins

In this work, we test the classification performance with approaches using 2 and 15 energy bins, rebinning the corrected data by integrating photon counts between low- (33.2 keV) and high-energy (131.3 keV) thresholds. Each bin in 15 energy bins approach has equal width. The 2 bin approach has a gap between low- and high-energies, which corresponds to interval between 63.0 keV and 79.5 keV. To separate it from a simple rebinning into two bins we refer to it as a bi-energy approach in the remainder of the article. 15 energy bins provide high resolution spectral reconstruction with energy bin widths (6.6 keV) below the detector energy resolution (8 keV) and give measurement of spectral LAC curve of the raw and corrected data, however, spectral distortion of attenuation curve for the raw data is more visible in this approach. With only two energy bins the bi-energy approach are less sensitive to detector artefacts furthermore it integrates more photons into each of the two bins, and consequently are robust to significantly higher noise levels. Finally reconstructing only 2 energy bins makes this approach more computationally efficient. In our previous work,<sup>24</sup> we found that the approaches with energy bin widths below the detector energy resolution did not lead to noticeable improvement in classification performance. Still Spectral CT has a trade-off between spectral binning and noise level and moreover, to match industrial fast scanning application we only use 12 projections. Both aspects may result in more reconstruction artifacts and to compensate for these aspects, we use the joint reconstruction method,  $L_\infty$ -VTV, described in the subsection 3.1. The classification results are presented in the subsection 5.3.

### 3.4 Tool for evaluation of reconstruction quality

We use a correlation coefficient as a tool to measure the quality of reconstruction  $\mathbf{u}$  determining the extent of linear relation to the ground-truth image  $\mathbf{v}$ , defined as

$$r = \frac{\sum_i (u_i - \bar{u})(v_i - \bar{v})}{\sqrt{\sum_i (u_i - \bar{u})^2 \sum_i (v_i - \bar{v})^2}}, \quad (19)$$

where  $\bar{u}$  and  $\bar{v}$  are the mean values, and  $u_i$  and  $v_i$  represent the  $i^{\text{th}}$  pixel values of  $\mathbf{u}$  and  $\mathbf{v}$ , respectively.

We also investigate the L-curve criteria<sup>43,44</sup> on both raw and corrected data. The L-curve criteria is a plot of the 2-norm of maximum gradients,  $\|\mathbf{u}_\lambda\|_{L_\infty\text{-VTV}}$  (Eq. 17), as a function of the 2-norm of the corresponding residual vector,  $\|\mathbf{A}\mathbf{u}_\lambda - \mathbf{p}\|_2$  (Eq. 16), both dependent on weighting parameters. Based on the L-curve, one can find the optimal weighting parameter for a regularized reconstruction method without the ground truth image of a sample. Ideally, the plot appears L-shaped, and the weighting parameters  $\lambda$  corresponding to the point exactly at the knee of the curve represents the optimal  $\lambda$  values. The values on the flat and vertical lines result in over-regularized and under-regularized solutions, respectively. Therefore, when studying a real experimental

sample this graphical tool can be used to find the optimal  $\lambda$  values without using the ground truth image. We use a linear-linear scale for plotting as in Refs. 31, 44. In our previous work,<sup>31</sup> we found the optimal  $\lambda$  value for the corrected data based on the L-curve criterion. In this work, we study how this graphical tool works for the raw data.

We found in our study that using the minimization of the standard deviation within a ROI of a sample as a method to find the optimal weighting parameter  $\lambda$  may lead to over-regularization. We therefore excluded it from estimation of reconstruction quality.

#### 4. METHOD TO MATERIAL CLASSIFICATION

In this section, we briefly give a description of the SIMCAD method presented in detail by Jumanazarov et al.<sup>24</sup> to measure  $\rho_e$  and  $Z_{\text{eff}}$  of materials from Spectral CT.

##### 4.1 Calibration of parameters in LAC

From Eq. 8, LAC for each energy bin can be represented as

$$\mu_m(E_k) = \rho_{e,m} \left( Z_{\text{eff},m}^{n-1} p(E_k) + c(E_k) \right), \quad (20)$$

where  $m = 1, 2, \dots, M$ ,  $k = 1, 2, \dots, K$  with  $M$  being the total number of reference materials and  $K$  being the number of energy bins used for a particular classification approach.  $p(E_k)$  and  $c(E_k)$  are photoelectric absorption and Compton scattering basis functions for energy bin  $E_k$ , respectively, which are calibrated and the same for all materials.

We also optimize the exponent  $n$  together with the basis functions for better measurement. To solve Eq. 20, we set positivity constraints for all basis functions and  $n$ , and formulate the non-linear objective function as:

$$\min_{0 \leq p_1, c_1, \dots, p_K, c_K, n} \sum_{m=1}^M \sum_{k=1}^K \left( \mu_m(E_k) - \rho_{e,m} (Z_{\text{eff},m}^{n-1} p_k + c_k) \right)^2, \quad (21)$$

where  $p_k = p(E_k)$  and  $c_k = c(E_k)$ . To optimize Eq. 21, a nonlinear least square solver is used based on trust region method.<sup>45</sup> Initial constraints were chosen as  $p_k^0 = 0.5$ ,  $c_k^0 = 0.5$  and  $n^0 = 3.6$  for all  $k$ . No particular dependency on the initial constraints was observed. Note that the calibration step is independently performed for the raw and corrected data. The formulation of the classification method is compatible with an arbitrary number of energy bins.

##### 4.2 Calculation of material properties

The calibrated parameters and the measured LAC  $\mu(E_k)$  of an unknown material scanned are used to obtain  $\rho_e$  and  $Z_{\text{eff}}$ . For  $M$ - and  $K$ - total number of unknown materials and energy bins, respectively, Eq. 20 is reformulated as a linear system equation as follows:

$$\begin{pmatrix} \vec{p} & \vec{c} & & & \\ & & \ddots & & \\ & & & \vec{p} & \vec{c} \end{pmatrix} \begin{pmatrix} z_1 \\ \rho_{e,1} \\ \vdots \\ z_M \\ \rho_{e,M} \end{pmatrix} = \begin{pmatrix} \vec{\mu}_1 \\ \vdots \\ \vec{\mu}_M \end{pmatrix} \quad (22)$$

where  $z_m$  is a temporary variable introduced instead of  $\rho_{e,m} Z_{\text{eff}}^{n-1}$  and  $\vec{p} = (p_1, \dots, p_K)^T$ ,  $\vec{c} = (c_1, \dots, c_K)^T$  and  $\vec{\mu}_m = (\mu_m(E_1), \dots, \mu_m(E_K))^T$ . The size of the linear matrix in the above equation is  $(M \times K)$ -by- $(2 \times M)$  and the number of unknowns is  $2 \times M$ . With the positivity constraint on the solution we retrieve the vector  $(z_1, \rho_{e,1}, \dots, z_M, \rho_{e,M})$  that minimizes the norm in the linear least square problem. The effective atomic numbers are then obtained for all materials by

$$Z_m = \left( \frac{z_m}{\rho_{e,m}} \right)^{\frac{1}{n-1}}. \quad (23)$$

The classification accuracy was measured as the percent relative deviation from the reference values of  $\rho_e$  and  $Z_{\text{eff}}$  as follows:

$$\Delta Z_{\text{eff}}^{\text{rel}} = 100\% \cdot \frac{Z_{\text{eff}}^{\text{est}} - Z_{\text{eff}}^{\text{ref}}}{Z_{\text{eff}}^{\text{ref}}}, \quad (24)$$

$$\Delta \rho_e^{\text{rel}} = 100\% \cdot \frac{\rho_e^{\text{est}} - \rho_e^{\text{ref}}}{\rho_e^{\text{ref}}} \quad (25)$$

where superscripts est and ref represent the estimated and reference values, respectively.

## 5. RESULTS AND DISCUSSIONS

### 5.1 Correlation coefficient and L-curve

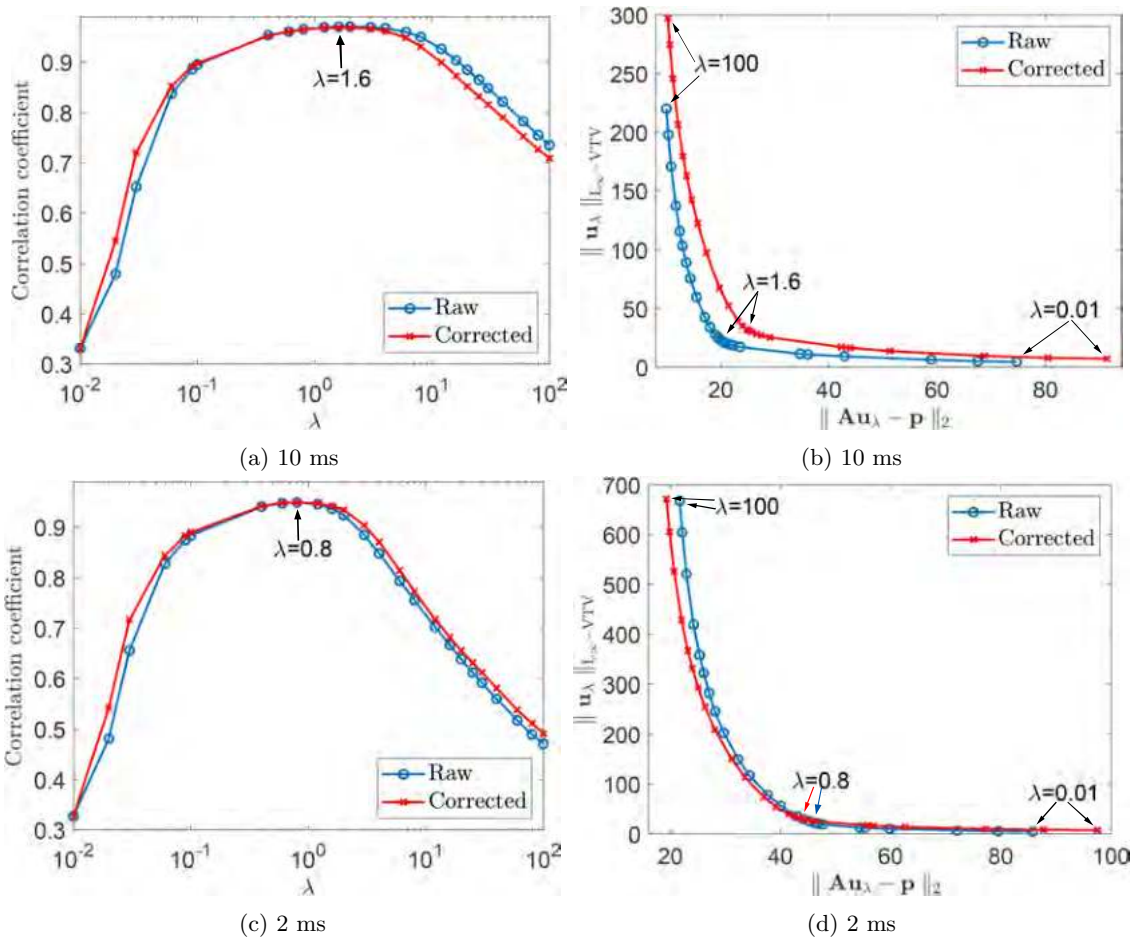


Figure 2: Correlation coefficient as a function of weighting parameter  $\lambda$  (left column) and the L-curves (right column) obtained with the raw and corrected data for 10 ms and 2 ms of integration time. The correlation coefficients represent the mean values calculated from the coefficients for 15 energy bins used. Note the logarithmic scale in the x-axis for correlation coefficients.

The sample for the experiments in this subsection was scanned with 4 different integration times 2 ms, 10 ms, 50 ms and 100 ms. The lower integration time, the lower photon counts. Fig. 2 shows correlation coefficients depending on weighting parameters and L-curve obtained with the raw and corrected data for 10 ms and 2 ms integration time. Based on the correlation coefficients the raw data have similar reconstruction quality as the

corrected data, even with noticeably deviations in the LAC as shown in Fig. 1. For all of total integration times we obtained similar correlation coefficients from the raw and the corrected data. For 10 ms acquisition time, the figure also shows good agreement between the weighting parameter found on the corner of the L-curve and the weighting parameter corresponding to the maximum correlation coefficient. We found that for both the raw and corrected data the vertical parts of the L-curves deviate from initial vertical positions as the total integration time decreases from 100 ms to 2 ms, which was more noticeable in 2 ms case. The raw data with less deflection of vertical lines appears to be slightly more accurate in fitting using the L-curve criterion compared to the corrected data.

## 5.2 Introducing high noise levels to specific energy bins

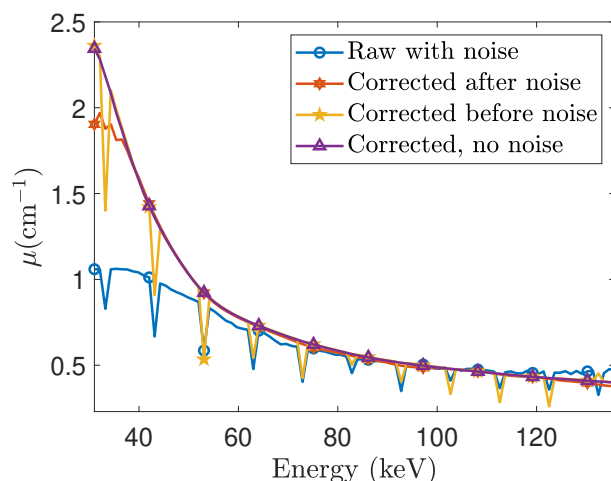


Figure 3: Spectral LAC for aluminum obtained with four different cases of adding high Gaussian noise ( $\sigma = 1.5$ ) to 11 energy bins between the low- and high-energy thresholds; noise is added to the raw data, the correction is performed after and before adding noise, and the correction is performed without adding noise.

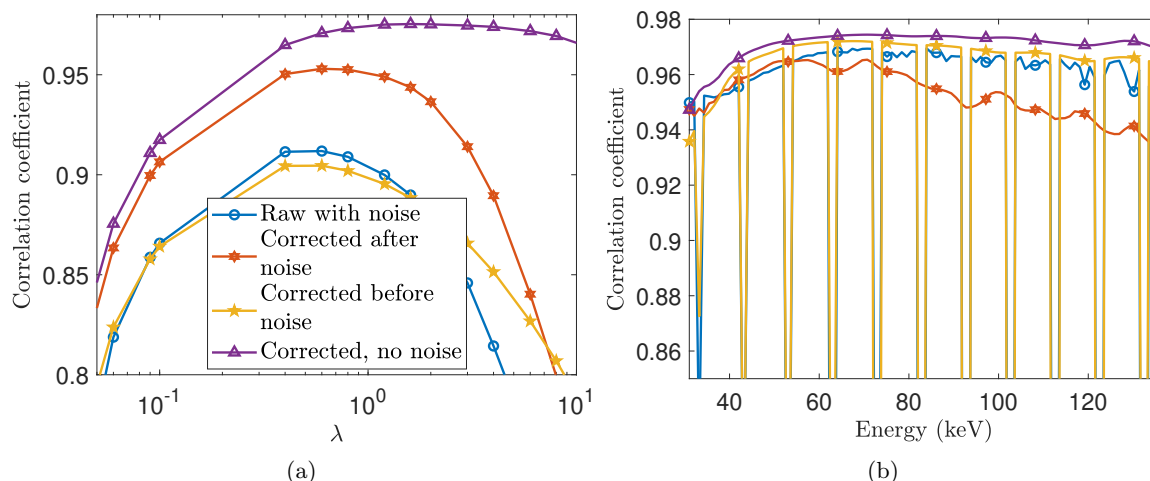


Figure 4: Correlation coefficient as a function of weighting parameter  $\lambda$  (a) and the photon energy between the low- and high-energy thresholds (b) obtained with four such different cases. The correlation coefficients (a) represent the mean values calculated from the coefficients for 96 energy bins used between the low- and high-energy thresholds. Note the logarithmic scale in the x-axis for correlation coefficients (a).

The aim of the joint reconstruction is to correlate intensity shift across the spectral dimensions such that noise in one energy bin blurring a specific edge is corrected by the information in the other channels of the same edge.

The correction algorithm redistributes intensity between energy channels based on the detector response and noise in one channel is thus distributed across the spectrum. We aimed to check the robustness of the combined workflow of correction and reconstruction to this type of noise. Gaussian noise with a standard deviation ( $\sigma$ ) of 1.5 was introduced to 11 energy bins distributed uniformly between 33.2 keV and 132.4 keV. The sample used in this subsection was scanned with 100 ms of the total integration time per projection. We investigated four different cases of added noise; noise is added to the raw data (Raw with noise), noise is added to the raw data and then the data is corrected (Corrected after noise), the raw data is corrected and then noise is added to the data (Corrected before noise) and the raw data is corrected and no noise is added (Corrected, no noise). For all cases sinograms are calculated from the data, reconstructed and manually segmented. Fig. 3 shows energy-resolved LACs from an aluminum segment for each of the 4 cases of added noise. The correction algorithm appears to largely overcome such high noises except it shows some decrease in spectral LAC in the low energy. Adding noise after the spectral correction gives noticeable drops in LACs for the affected energy bins similarly to the case of adding noise to the raw data. Fig. 4 presents correlation coefficients depending on weighting parameter  $\lambda$  and photon energy corresponding to the optimal  $\lambda$  for four such cases. It can be noted from Fig. 4a that the case of correcting before adding noise ( $r = 0.90$  at  $\lambda = 0.6$ ) even gives slightly smaller correlation coefficients compared to the case of noisy raw data ( $r = 0.91$  at  $\lambda = 0.6$ ). The correction algorithm significantly increases reconstruction quality ( $r = 0.95$  at  $\lambda = 0.6$ ) whereas the correction algorithm without added noise gives  $r = 0.97$  at  $\lambda = 1.6$ . The figure also shows that the joint reconstruction method uses lower weighting parameter in the cases of added noises corresponding to increasing the regularization between energy bins. Fig. 4b shows that the correction algorithm after adding noise mostly compensates for the affected bins giving lower overall correlation coefficients whereas the cases of the noisy raw data and the data corrected before adding noise have very sharp drops for such energy bins with added noises.

### 5.3 Material classification

Fig. 5 presents classification results for the bi- and 15 energy bins approaches. Note that we used the materials listed in Tab. 1 and Tab. 2 in Appendix A for the calibration step as the reference materials and for calculation of ( $\rho_e$ ,  $Z_{\text{eff}}$ ) as unknown materials, respectively. We obtained the relative deviations for  $\rho_e$  and  $Z_{\text{eff}}$  as a function of the weighting parameter  $\lambda$  used for the reconstruction. Even though the correlation coefficients for the raw and corrected data were found to be similar as shown in Fig. 2, the corrected data in 15 energy bins approach gives 3.4% for  $\rho_e$  and 2.7% for  $Z_{\text{eff}}$  of relative deviations at  $\lambda = 16.0$  whereas the raw data results in 5.6% and 10.3% at  $\lambda = 4.0$ , respectively. The classification accuracy for the raw data in bi-energy approach was also significantly lower than the corrected data. For bi-energy bins, the relative deviations are 8.0% for  $\rho_e$  and 12.4% for  $Z_{\text{eff}}$  at  $\lambda = 2.0$  for the raw data whereas the corrected data gives 2.6% and 3.9% deviations at  $\lambda = 6.0$ . Thus, the classification accuracy relies on how the measured LAC fits our parameterized LAC defined in Eq. 20. We found that using a bin-by-bin reconstruction method significantly deteriorates classification performance for the raw data.<sup>24</sup>

We tested the robustness of the classification performance for the raw and corrected data by adding Gaussian noise with  $\sigma = 0.15$  to all energy bins and all materials used for the calibration step and calculation of materials features between the low- and high-energy thresholds. Fig. 6 shows the relative deviations for ( $\rho_e$ ,  $Z_{\text{eff}}$ ) as a function of weighting parameter. It can be noted from the graphs that applying the correction algorithm after and before adding noise to the raw data gives similar results, for which the relative deviations are 4.1% for  $\rho_e$  and 3.3% for  $Z_{\text{eff}}$  at  $\lambda = 6.0$ , and 3.8% and 4.0% at  $\lambda = 20.0$ , respectively. In comparison, the raw data with added noise leads to the deviations of 6.5% and 11.1% at  $\lambda = 2.0$ , respectively.

## 6. CONCLUSION

We explored the influence of spectral correction applied to the raw data collected by a PCD. We found the influence on the spectrally resolved LAC curve, the reconstruction quality, the L-curve and the material classification. We used the SIMCAD classification method determining system-independent material properties ( $\rho_e$ ,  $Z_{\text{eff}}$ ). The correlation coefficient were employed to measure reconstruction quality of data acquired with different levels of photon flux, acquisition time and number of bins. We have presented that decreasing the integration time and thus decreasing photon counts, the raw data gave similar correlation coefficients and L-curve properties as the

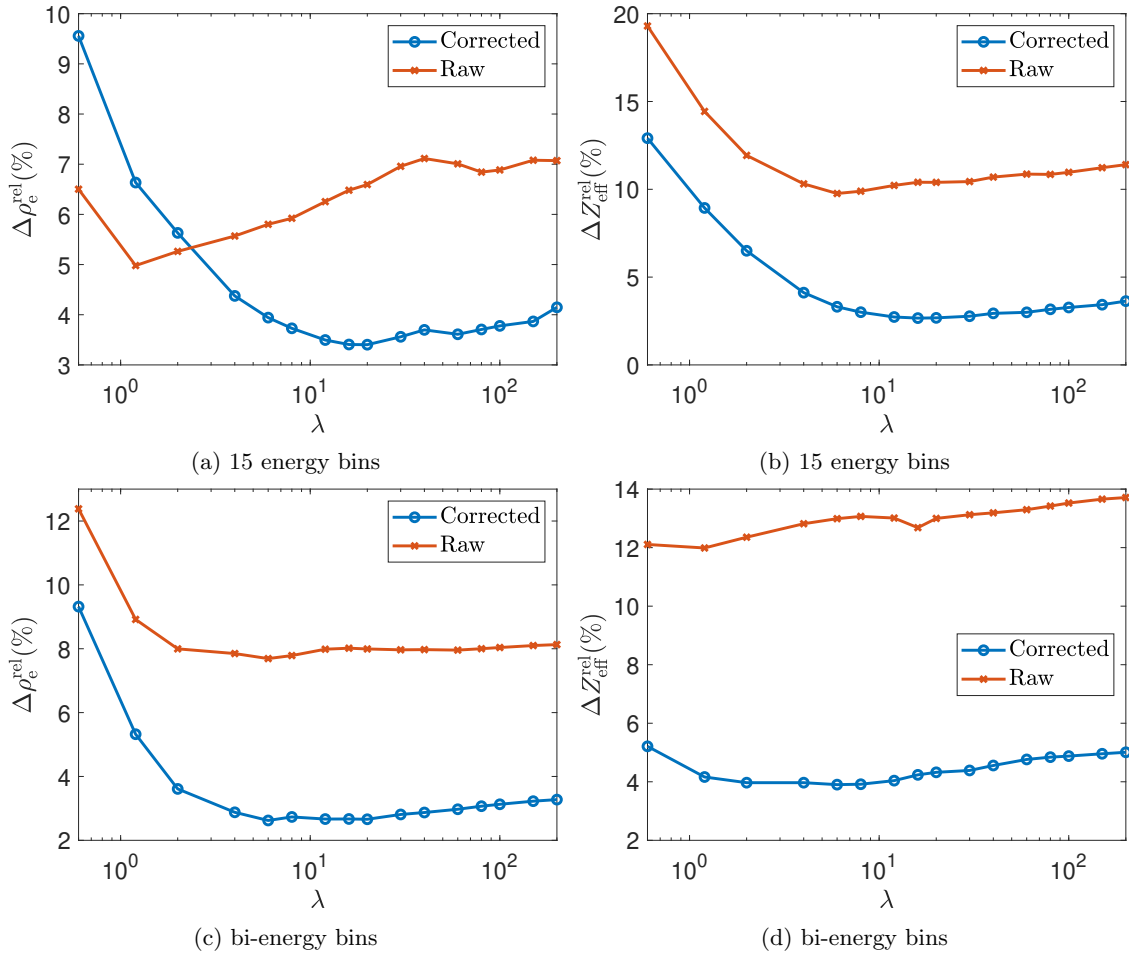


Figure 5: The percent relative deviations as a function of weighting parameter  $\lambda$  for  $\rho_e$  (left column) and  $Z_{\text{eff}}$  (right column) obtained with the raw and corrected data using bi- and 15 energy bins. The deviations are shown as the mean values of the absolute deviations for each material listed in Tab. 2. Note the logarithmic scale in the x-axis.

corrected data. However, very high noise levels introduced to certain energy bins deteriorates reconstruction quality more for the raw data than for data corrected after the noise is added. The correction algorithm showed robustness to such noise in specific energy bins in terms of correcting the noisy spectral LAC. For material classification, we investigated the influence of spectral correction both for high resolution spectral reconstruction where the number of bins exceed the energy resolution of the detector and for computational efficient binning of the spectral dimension into high and low energy bins. We also tested noise conditions for classifications with the raw and corrected data. We found that the correction algorithm significantly enhances the accuracy of the classification performance important for both security and industrial applications where materials are identified from Spectral CT. Since the spectral correction of the detector response could easily be implemented for other types of photon counting detectors, results similar to what is obtained in this study can be expected when the correction algorithm is used for other photon-counting applications and set-ups.

## APPENDIX A. MATERIALS USED FOR CLASSIFICATION

### ACKNOWLEDGMENTS

This project has received funding from the European Union Horizon 2020 research and innovation programme under the Marie Skłodowska-Curie grant agreement No. 765604 as part of the MULTIscale, Multimodal and Multidi-



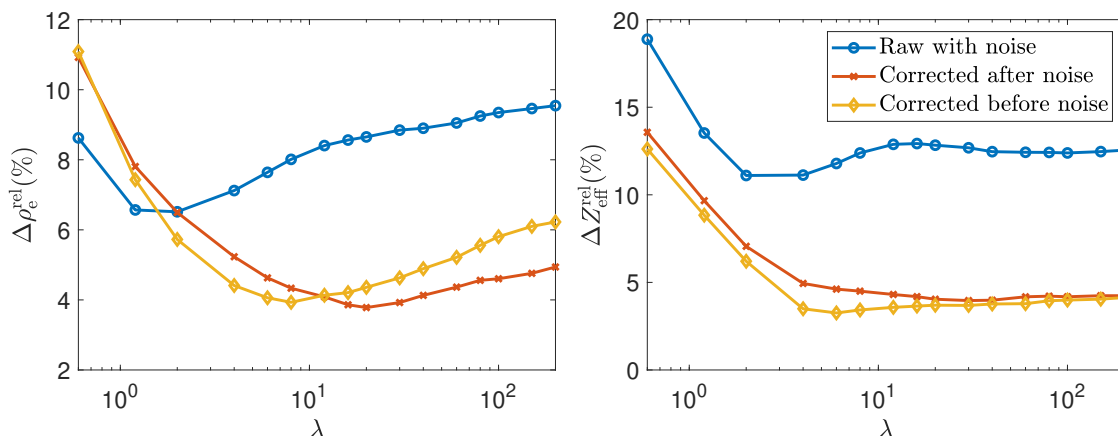


Figure 6: The relative deviations as a function of weighting parameter  $\lambda$  for  $\rho_e$  (left) and  $Z_{\text{eff}}$  (right) obtained with 15 energy bins for the 3 noise cases; noise is added to the raw data, the correction algorithm is applied after and before adding noise. The deviations are shown as the mean values of the absolute deviations for each material listed in Tab. 2. Note the logarithmic scale in the x-axis.

mensional imaging for EngineerRING project (MUMMERING Innovative Training Network, [www.mummering.eu](http://www.mummering.eu)) and from the EIC FTI program (project 853720). The authors want to acknowledge also the 3D Imaging Center at DTU, where the experiments have been conducted.

## REFERENCES

- [1] Martz, H. E., Logan, C. M., Schneberk, D. J., and Shull, P. J., [*X-ray Imaging: fundamentals, industrial techniques and applications*], CRC Press (2016).
- [2] Ying, Z., Naidu, R., and Crawford, C. R., “Dual energy computed tomography for explosive detection,” *Journal of X-Ray Science and Technology* **14**(4), 235–256 (2006).
- [3] Kalender, Willi A and Perman, WH and Vetter, JR and Klotz, E., “Evaluation of a prototype dual-energy computed tomographic apparatus. I. Phantom studies,” *Medical physics* **13**(3), 334–339 (1986).
- [4] Heismann, B. J., Leppert, J., and Stierstorfer, K., “Density and atomic number measurements with spectral x-ray attenuation method,” *Journal of Applied Physics* **94**(3), 2073–2079 (2003).
- [5] Park, J. S. and Kim, J. K., “Calculation of effective atomic number and normal density using a source weighting method in a dual Energy X-ray inspection system,” *Journal of the Korean Physical Society* **59**(4), 2709–2713 (2011).
- [6] Szczykutowicz, T. P., Qi, Z., and Chen, G.-H., “A simple image based method for obtaining electron density and atomic number in dual energy CT,” in [*Medical Imaging 2011: Physics of Medical Imaging*], **7961**, 79613A, International Society for Optics and Photonics (2011).
- [7] Semerci, O. and Miller, E. L., “A parametric level-set approach to simultaneous object identification and background reconstruction for dual-energy computed tomography,” *IEEE Transactions on Image Processing* **21**(5), 2719–2734 (2012).
- [8] Landry, G., Seco, J., Gaudreault, M., and Verhaegen, F., “Deriving effective atomic numbers from DECT based on a parameterization of the ratio of high and low linear attenuation coefficients,” *Physics in Medicine and Biology* **58**(19), 6851–6866 (2013).
- [9] Shikhaliev, P. M., “Energy-resolved computed tomography: First experimental results,” *Physics in Medicine and Biology* **53**(20), 5595–5613 (2008).
- [10] Parsai, E. I., Shvydka, D., and Kang, J., “Design and optimization of large area thin-film CdTe detector for radiation therapy imaging applications,” *Medical Physics* **37**(8), 3980–3994 (2010).
- [11] Brambilla, A., Ouvrier-Buffet, P., Rinkel, J., Gonon, G., Boudou, C., and Verger, L., “CdTe linear pixel X-ray detector with enhanced spectrometric performance for high flux X-ray imaging,” *IEEE Transactions on Nuclear Science* **59**(4 PART 3), 1552–1558 (2012).

Table 1: The list of the materials used for the calibration step as the reference materials for material classification, and their physical properties  $\rho_e$  and  $Z_{\text{eff}}$ . The mass density,  $\rho$  for the plastic materials was measured with uncertainties of  $\pm 0.15\%$ . The mass densities for the rest of materials represent the theoretical values found in PubChem data.<sup>46</sup>

Material	Chemical Formula	Width×length/ Diameter (mm)	$\rho$ (g/cm <sup>3</sup> )	$\rho_e$ (e <sup>-</sup> mol/cm <sup>3</sup> )	$Z_{\text{eff}}$
Graphite	C	12.7	1.8	0.899	6
PC	(CO <sub>3</sub> C <sub>13</sub> H <sub>8</sub> ) <sub>n</sub>	8.2×53.5	1.18	0.610	6.82
PMMA	(C <sub>5</sub> O <sub>2</sub> H <sub>8</sub> ) <sub>n</sub>	40×42	1.18	0.636	7.02
POM-C	(CH <sub>2</sub> O) <sub>n</sub>	9×53.5	1.41	0.753	7.40
PTFE	(C <sub>2</sub> F <sub>4</sub> ) <sub>n</sub>	9×53.3	2.16	1.035	8.70
N,N-Dimethylhydrazine	C <sub>2</sub> H <sub>8</sub> N <sub>2</sub>	67	0.791	0.447	6.44
Ethylenediamine	C <sub>2</sub> H <sub>8</sub> N <sub>2</sub>	67	0.90	0.509	6.44
Acetone 2	C <sub>3</sub> H <sub>6</sub> O	54	0.785	0.432	6.90
Nitrobenzene	C <sub>6</sub> H <sub>5</sub> NO <sub>2</sub>	49	1.20	0.624	7.00
Ethanol 96%	C <sub>2</sub> H <sub>6</sub> O (96%)	67×67	0.798	0.450	7.06
Methanol	CH <sub>3</sub> OH	20	0.792	0.446	7.29
Hydrazine solution	H <sub>4</sub> N <sub>2</sub> (35%)	54	1.0	0.561	7.43
Nitromethane	CH <sub>3</sub> NO <sub>2</sub>	20	1.14	0.597	7.50
Water	H <sub>2</sub> O	20	0.997	0.554	7.78
Water 3	H <sub>2</sub> O	12.7	0.997	0.554	7.78
Hyd. Peroxide 2	H <sub>2</sub> O <sub>2</sub> (50%)	73×74	1.22	0.661	7.83
Magnesium 2	Mg	18	1.74	0.859	12
Aluminum 2	Al	25	2.70	1.3	13
Aluminum 3	Al	20×20	2.70	1.3	13
Silicon	Si	25	2.33	1.161	14

- [12] Wang, X., Meier, D., Taguchi, K., Wagenaar, D. J., Patt, B. E., and Frey, E. C., “Material separation in x-ray CT with energy resolved photon-counting detectors,” *Medical Physics* **38**(3), 1534–1546 (2011).
- [13] Rinkel, J., Beldjoudi, G., Rebuffel, V., Boudou, C., Ouvrier-buffet, P., Gonon, G., Verger, L., and Brambilla, A., “Experimental Evaluation of Material Identification Methods With CdTe X-ray Spectrometric Detector,” *IEEE Transactions on Nuclear Science* **58**(5), 2371–2377 (2011).
- [14] Beldjoudi, G., Rebuffel, V., Verger, L., Kaftandjian, V., and Rinkel, J., “Multidimensional data processing methods for material discrimination using an ideal X-ray spectrometric photon counting detector,” *IEEE Transactions on Nuclear Science* **58**(6 PART 2), 3190–3203 (2011).
- [15] Beldjoudi, G., Rebuffel, V., Verger, L., Kaftandjian, V., and Rinkel, J., “An optimised method for material identification using a photon counting detector,” *Nuclear Instruments and Methods in Physics Research, Section A: Accelerators, Spectrometers, Detectors and Associated Equipment* **663**(1), 26–36 (2012).
- [16] Rebuffel, V., Rinkel, J., Tabary, J., and Verger, L., “New perspectives of X-ray techniques for explosive detection based on CdTe/CdZnTe spectrometric detectors,” in [*Proc. of the Int. Symp. on Digital Industrial Radiology and Computed Tomography*], **2**, 1–8 (2011).
- [17] Limor Martin, *Enhanced information extraction in multi-energy X-ray tomography for security*, phd thesis, Boston University (2014).

Table 2: The list of the materials used for the calculation of  $(\rho_e, Z_{\text{eff}})$  in material classification, and their physical properties  $\rho_e$  and  $Z_{\text{eff}}$ . The mass density,  $\rho$  for the plastic materials was measured with uncertainties of  $\pm 0.15\%$ . The mass densities for the rest of materials represent the theoretical values found in PubChem data.<sup>46</sup>

Material	Chemical Formula	Width×length/ Diameter (mm)	$\rho$ (g/cm <sup>3</sup> )	$\rho_e$ (e <sup>-</sup> mol/cm <sup>3</sup> )	$Z_{\text{eff}}$
PET	(C <sub>10</sub> H <sub>8</sub> O <sub>4</sub> ) <sub>n</sub>	9×53.5	1.39	0.721	7.09
POM-H	(CH <sub>2</sub> O) <sub>n</sub>	15.5×53.3	1.43	0.763	7.40
PVDF	(C <sub>2</sub> H <sub>2</sub> F <sub>2</sub> ) <sub>n</sub>	9×53.5	1.79	0.896	8.40
PTFE 2	(C <sub>2</sub> F <sub>4</sub> ) <sub>n</sub>	12.7	2.2	1.056	8.70
2-Butanone	C <sub>4</sub> H <sub>8</sub> O	83	0.805	0.447	6.76
Acetone	C <sub>3</sub> H <sub>6</sub> O	20	0.785	0.432	6.90
Methanol 2	CH <sub>3</sub> OH	81	0.792	0.446	7.29
Ethanol 40%	C <sub>2</sub> H <sub>6</sub> O (40%)	67×67	0.947	0.532	7.63
Water 2	H <sub>2</sub> O	51×51	0.997	0.554	7.78
Nitric acid	HNO <sub>3</sub> (65%)	83	1.39	0.714	7.80
Hyd. Peroxide	H <sub>2</sub> O <sub>2</sub> (50 %)	20	1.22	0.661	7.83
Magnesium	Mg	12.7	1.74	0.859	12
Aluminum	Al	25	2.70	1.3	13
Silicon powder	Si	48	0.65	0.324	14
Silicon 2	Si	12.7	2.33	1.161	14

- [18] A. Brambilla, A. Gorecki, A. Potop, C. P. and Verger, L., “Basis material decomposition method for material discrimination with a new spectrometric X-ray imaging detector,” *Journal of Instrumentation* **12**(8), P08014 (2017).
- [19] Alvarez, R. E. and Macovski, A., “Energy-selective reconstructions in X-ray computerised tomography,” *Physics in Medicine and Biology* **21**(5), 733–744 (1976).
- [20] Wells, K. and Bradley, D. A., “A Review of X-ray Explosives Detection Techniques for Checked Baggage,” *Applied Radiation and Isotopes* **70**(8), 1729–1746 (2012).
- [21] Azevedo, S. G., Martz, H. E., Aufderheide, M. B., Brown, W. D., Champley, K. M., Kallman, J. S., Roberson, G. P., Schneberk, D., Seetho, I. M., and Smith, J. A., “System-Independent Characterization of Materials Using Dual-Energy Computed Tomography,” *IEEE Transactions on Nuclear Science* **63**(1), 341–350 (2016).
- [22] Champley, K. M., Azevedo, S. G., Member, S., Seetho, I. M., Glenn, S. M., McMichael, L. D., Smith, J. A., Kallman, J. S., Brown, W. D., and Martz, H. E., “Method to Extract System-Independent Material Properties From Dual-Energy X-Ray CT,” *IEEE Transactions on Nuclear Science* **66**(3), 674–686 (2019).
- [23] Busi, M., Mohan, K. A., Dooraghi, A. A., Champley, K. M., Martz, H. E., and Olsen, U. L., “Method for system-independent material characterization from spectral X-ray CT,” *NDT & E International* **107**(August), 102136 (2019).
- [24] Jumanazarov, D., Koo, J., Busi, M., Poulsen, H. F., Olsen, U. L., and Iovea, M., “System-independent material classification through X-ray attenuation decomposition from spectral X-ray CT,” *NDT and E International* **116**(July), 102336 (2020).
- [25] Kheirabadi, M., BJORHOLM DAHL, A., LUND OLSEN, U., MUSTAFA, W., and LYKSBERG, M., “Multispectral x-ray CT: multivariate statistical analysis for efficient reconstruction,” in [*Developments in X-Ray Tomography XI*], **1039113**, 38, International Society for Optics and Photonics (2017).
- [26] Taguchi, K. and Iwanczyk, J. S., “Vision 20/20: Single photon counting x-ray detectors in medical imaging.,” *Medical physics* **40**(10), 100901 (2013).

- [27] Dreier, E. S., Kehres, J., Khalil, M., Busi, M., Gu, Y., Feidenhans, R., and Olsen, U. L., “Spectral correction algorithm for multispectral CdTe x-ray detectors,” *Optical Engineering* **57**(5), 16 (2018).
- [28] Compton, A. H., Allison, S. K., et al., “X-rays in theory and experiment,” *New York, NY, USA: Van Nostrand* (1935).
- [29] Mayneord, WV, “The significance of the roentgen,” *Acta of the International Union Against Cancer* **2**, 271 (1937).
- [30] SPIERS, F. W., “Effective atomic number and energy absorption in tissues,” *The British journal of radiology* **19**(218), 52–63 (1946).
- [31] Jumanazarov, D., Koo, J., Poulsen, H. F., Olsen, U. L., and Iovea, M., “Material classification from sparse spectral X-ray CT using vectorial total variation based on L infinity norm,” *Submitted to NDT & E International* (2021).
- [32] Flohr, T., Petersilka, M., Henning, A., Ulzheimer, S., Ferda, J., and Schmidt, B., “Photon-counting CT review,” *Physica Medica* **79**(October), 126–136 (2020).
- [33] Brambilla, A., Ouvrier-Buffet, P., Gonon, G., Rinkel, J., Moulin, V., Boudou, C., and Verger, L., “Fast CdTe and CdZnTe semiconductor detector arrays for spectroscopic X-ray imaging,” *IEEE Transactions on Nuclear Science* **60**(1), 408–415 (2013).
- [34] Persson, M., Huber, B., Karlsson, S., Liu, X., Chen, H., Xu, C., Yveborg, M., Bornefalk, H., and Danielsson, M., “Energy-resolved CT imaging with a photon-counting silicon-strip detector,” *Physics in Medicine and Biology* **59**(22), 6709–6727 (2014).
- [35] Eisen, Y. and Horovitz, Y., “Correction of incomplete charge collection in CdTe detectors,” *Nuclear Inst. and Methods in Physics Research, A* **353**(1-3), 60–66 (1994).
- [36] McGregor, D. S. and Hermon, H., “Room-temperature compound semiconductor radiation detectors,” *Nuclear Instruments and Methods in Physics Research, Section A: Accelerators, Spectrometers, Detectors and Associated Equipment* **395**(1), 101–124 (1997).
- [37] Barrett, H. H., Eskin, J., and Barber, H., “Charge transport in arrays of semiconductor gamma-ray detectors,” *Physical Review Letters* **75**(1), 156 (1995).
- [38] Toyama, H., Higa, A., Yamazato, M., Maehama, T., Ohno, R., and Toguchi, M., “Quantitative analysis of polarization phenomena in CdTe radiation detectors,” *Japanese Journal of Applied Physics, Part 1: Regular Papers and Short Notes and Review Papers* **45**(11), 8842–8847 (2006).
- [39] Bale, D. S. and Szeles, C., “Nature of polarization in wide-bandgap semiconductor detectors under high-flux irradiation: Application to semi-insulating Cd<sub>1-x</sub>Zn<sub>x</sub>Te,” *Physical Review B - Condensed Matter and Materials Physics* **77**(3), 1–16 (2008).
- [40] Berger, M.J., Hubbell, J.H., Seltzer, S.M., Chang, J., Coursey, J.S., Sukumar, R., Zucker, D.S., and Olsen, K., “XCOM: Photon Cross Section Database,” (2010).
- [41] Guerra, P., Santos, A., and Darambara, D. G., “Development of a simplified simulation model for performance characterization of a pixellated CdZnTe multimodality imaging system,” *Physics in Medicine and Biology* **53**(4), 1099–1113 (2008).
- [42] Plagnard, J., “Comparison of measured and calculated spectra emitted by the X-ray tube used at the Gustave Roussy radiobiological service,” *X-Ray Spectrometry* **43**(5), 298–304 (2014).
- [43] Hansen, P. C., “The L-Curve and its Use in the Numerical Treatment of Inverse Problems,” in *Computational Inverse Problems in Electrocardiology*, ed. P. Johnston, *Advances in Computational Bioengineering* **4**, 119–142 (2000).
- [44] Yang, X., Hofmann, R., Dapp, R., van de Kamp, T., Rolo, T. d. S., Xiao, X., Moosmann, J., Kashef, J., and Stotzka, R., “TV-based conjugate gradient method and discrete L-curve for few-view CT reconstruction of X-ray in vivo data,” *Optics Express* **23**(5), 5368 (2015).
- [45] Nocedal, J. and Wright, S. J., [*Numerical Optimization*], Springer, New York (1999).
- [46] Kim, S., Chen, J., Cheng, T., Gindulyte, A., He, J., He, S., Li, Q., Shoemaker, B. A., Thiessen, P. A., Yu, B., Zaslavsky, L., Zhang, J., and Bolton, E. E., “PubChem 2019 update: Improved access to chemical data,” (2019).

## Paper D

**Method for system-independent material classification through basis material decomposition from spectral X-ray CT.**

Doniyor Jumanazarov, Jakeoung Koo, Henning. F. Poulsen, Ulrik L. Olsen and Mihai Iovea

# Method for system-independent material classification through basis material decomposition from spectral X-ray CT

Doniyor Jumanazarov<sup>a,c,\*</sup>, Jakeoung Koo<sup>b</sup>, Henning F. Poulsen<sup>a</sup>, Ulrik L. Olsen<sup>a</sup> and Mihai IOVEA<sup>c</sup>

<sup>a</sup>Technical University of Denmark, DTU Physics, 2800 Kgs. Lyngby, Denmark

<sup>b</sup>Technical University of Denmark, DTU Compute, 2800 Kgs. Lyngby, Denmark

<sup>c</sup>ACCENT PRO 2000 s.r.l. (AP2K), Nerva Traian 1, K6, Ap. 26, Bucharest, S3, ROMANIA 031041

## ARTICLE INFO

### Keywords:

Spectral X-ray CT  
Data processing methods;  
Quantitative X-ray characterization  
Photon counting detectors  
Security screening

## ABSTRACT

We present a method for material classification in spectral X-ray Computed Tomography (CT) using energy-resolved, photon-counting detectors (PCD), with which one can simultaneously measure the energy dependence of a material's linear attenuation coefficient (LAC). The method uses a basis material decomposition for the multi-energy LAC measurements and accurately estimates effective atomic number ( $Z_{\text{eff}}$ ) of a material. The decomposition is based on the fact that the material's LAC can be represented as the sum of multiple basis materials with respective equivalent thicknesses. The measured spectra in PCDs working under high flux is distorted by a range of detector artifacts such as charge sharing and pulse pile up. These physical effects lead to distortions of the measured LAC curves, therefore we use a spectral correction algorithm for these distortions.

We use the different materials in the range of  $6 \leq Z_{\text{eff}} \leq 15$  for experimental validation, which are scanned with a MultiX ME-100 v2 line array PCD. We show that using spectral correction algorithm before the material decomposition classification method decrease the relative deviation in  $Z_{\text{eff}}$  to 2.4% from 5.2% when spectral correction is not used.

## 1. Introduction

Conventional X-ray computed tomography (CT) for laboratory or industrial applications measures the distribution of the averaged linear attenuation coefficients (LAC) within an object. One reason is that it neglects polychromaticity of radiation generated by an X-ray source, which integrates photons over the broad energy range and results in the averaged quantity of LAC. Material classification in conventional single energy CT is just based on the contrast between different materials that arises due to the difference of the averaged LACs. However, various materials may have overlapping averaged LACs measured within the wide energy range, which significantly limit the classification accuracy. This is because the dependence of the LAC on the energy, and also on material features like electron density,  $\rho_e$ , and effective atomic number,  $Z_{\text{eff}}$  is neglected. Some research showed that the overlapping LACs cause a decrease in contrast of soft human tissues with different  $\rho_e$  or  $Z_{\text{eff}}$  [1–3], which means that the quantitative characterization based on  $\rho_e$  and  $Z_{\text{eff}}$  is desired.

An accurate measurement of  $\rho_e$  and  $Z_{\text{eff}}$  is very useful in radiotherapy and medical diagnosis [4–8], and security field [9]. Alvarez et al. [10] alternatively presented that the LAC can be decomposed into energy- and material-dependent components, which can be defined by photoelectric absorption and Compton scattering interactions, and density,  $\rho$ , and  $Z_{\text{eff}}$ , respectively. This led to the emergence of Dual-energy CT, which can retrieve a map of both  $\rho_e$

and  $Z_{\text{eff}}$ , and is the state-of-the-art method for the material characterization in medical and security applications [3, 11–19]. The dual-energy CT is usually performed with a single source spectrum (i.e. single acquisition) using dual-energy sandwich detectors. However, the dual-energy CT has the main limitation that low- and high-energy spectrums measured by dual-energy sandwich detectors are overlapping resulting in lower energy separation, and thereby limiting classification performance. Moreover, the dual-energy CT still measures the averaged LACs at overlapping low- and high-energies, and therefore material classification with the dual-energy CT is dependent on the system, i.e. on source spectrum, filtration, and detector efficiency [20].

The development of cadmium telluride (CdTe) photon-counting detectors (PCD) has laid the foundation for Spectral CT [21, 22]. This technique is also known as multi-energy X-ray CT in the literature. PCDs can separate different energies of the incident photons and simultaneously measure a spectrum of energy-dependent material features by using the selected thresholds to assemble and digitize the photon counts. This has generated large interest in PCDs within diagnostic and radiation therapy imaging [23, 24]. With single acquisition, spectral CT employing a PCD can quantitatively obtain a material's LAC at several energies, and is found to have a large potential to improve material separation compared to dual-energy CT [25]. As a result spectral CT has drawn significant research attention from medical [26–31] and security fields [32–34]. X-ray radiography investigations in explosive detection presented that PCDs reveal superiority over dual-layer sandwich detectors that have relatively poorer energy separation ability in enhancing material characterization [35–38].

In previous study we showed a novel classification method,

\*Corresponding author.

✉ doniyor.jumanazarov@fysik.dtu.dk (D. Jumanazarov);  
jakeoung@gmail.com (J. Koo); hfpo@fysik.dtu.dk (H.F. Poulsen);  
ullu@dtu.dk (U.L. Olsen); office@accent.ro (M. IOVEA)  
ORCID(s): 0000-0003-1583-7375 (M. IOVEA)

namely system-independent material classification through attenuation decomposition (SIMCAD) [39], independent of the instrument or its specifics like the source spectrum. From spectral CT measurements, the SIMCAD method decomposes LACs into energy- and material-dependent components based on the model presented by Alvarez et al. [10], and accurately estimates the material properties,  $\rho_e$  and  $Z_{\text{eff}}$ , representing the measured and decomposed LACs at multiple energies. Using the experimental data it was shown that this method obtains the best classification performance with optimized bi-energy bins. This is because the low- and high-energy bins are separated by a gap of certain energy width that makes them non-overlapping and improves the performance. Another factor that contributes to classification improvement is that the position of the gap is optimized keeping the low- and high-energy thresholds constant to find the best classification.

Using MultiX ME100 PCD in spectral CT, Brambilla et al. [33] presented a material identification method, which relies on basis material decomposition that a material's LAC can be described as a linear combination of the LACs of selected basis materials with respective equivalent thicknesses [40–42]. PCDs operating under high flux suffer from the spectrum distortions that physical interactions such as charge sharing and weighting potential cross-talk, fluorescence radiation, Compton scattering, pulse pile up and incomplete charge collection significantly distort the raw data collected. These spectral distortions cause a strong deviation of the extracted LACs from actual attenuation curve [43]. Therefore, Brambilla et al. [33] used a calibration step to register the detector's response for different combinations of thicknesses of the basis materials superposed on each other. The thicknesses of basis materials for which the detector's response function matches with the measurement are found using a maximum likelihood solution relying on the assumption that photon counts in each energy bin are distributed based in a Poisson law. They calculated material's  $Z_{\text{eff}}$  from the equivalent thicknesses obtained by the calibration step using polyethylene (PE) and polyvinyl chloride (PVC) as basis materials. The equivalent thicknesses for the detector responses of the materials corresponding to the intermediate or external equivalent thicknesses were found by interpolation or extrapolation, respectively. However, using the calibration step may be to a system-dependent solution because of the dependence on source spectrum when recording the detector's responses. Su et al. using synthesized simulation data from spectral CT investigated material discrimination performance based on basis material decomposition model for different number of energy bins and different exposure parameters per projection (in milliamp-seconds, mA · s). They found that with both projection domain and image domain techniques one could quantitatively discriminate iron from calcium, potassium and water by choosing the appropriate number of energy bins and the exposure parameters, being different for each technique [44].

In this work, using the experimental data we present a method for material classification that estimates  $Z_{\text{eff}}$  of a

material based on basis material decomposition (BMD) in spectral CT. The BMD method offers a system-independent solution because we use a correction algorithm presented by Dreier et al. [43] that corrects for severe spectral distortions when applying to the raw data and gives the corrected LACs. This allows us to directly use the corrected LACs for estimations instead of using the calibration step presented by Brambilla et al. [33]. In previous study [45], we presented that the distorted LACs lead to a significant decrease in material classification performance estimated by the SIMCAD method, and the correction algorithm is required to improve the performance. In this work, we aim to test the robustness and accuracy of the BMD method for different materials with a broad range of  $Z_{\text{eff}}$ . We use sparse-view reconstructions from just 12 projections that would enable rapid scanning and low dose imaging desired for security and medical applications, respectively. In comparison, 350–450 projections are usually employed by cone beam CT systems in most diagnostic imaging applications such as the head scanning, breast and extremities [46]. However, a fewer number of projections will reduce image reconstruction quality because of the sparser sampling of the data [47]. In the present work, to achieve improved image quality at few projections we use the joint reconstruction regularization, vectorial total variation based on  $L_\infty$  norm ( $L_\infty$ -VTV), which utilizes additional information in the spectral dimension of sinogram data [45]. The BMD will be compared to another classification method, the SIMCAD for inspecting a wide range of materials.

## 2. Theory

### 2.1. Linear attenuation coefficient

When x-ray photons are sent to a material, some part of the photons interact with the material's particles and their energy might be scattered or absorbed. The dominant interactions are photoelectric effect and Compton scattering within the detector's energy range in our study. A quantity of this scattering and absorption is named the linear attenuation coefficient (LAC), denoted by  $\mu$ . The rest of photons transmit through the material without interaction with the material's particles. The quantity of photons passed through the material is dependent on the photon energy, and the density, atomic number and the thickness of the material. The Beer Lambert law can describe the LAC for a homogeneous material and for energy bin  $E_k$  as follows:

$$I(\vec{x}, E_k) = I_0(\vec{x}, E_k)e^{-\mu(E_k)d}, \quad k = 1, 2, 3, \dots, K; \quad (1)$$

where  $I(E_k)$  is the photon flux transmitted through the material, and  $I_0(E_k)$  is the flat-field photon flux, i.e. the projection measured by the detector without the sample. The latter also represents the source spectrum or the system's spectral response.  $\mu(E_k)$  is the LAC for energy bin  $E_k$ , and  $d$  is the thickness of the X-ray path through the material.  $\vec{x}$  is referred to the 1D linear detector pixel array.  $K$  denotes the total number of energy bins used. In conventional and dual-energy CT, the polychromatic nature of the X-ray beam is ne-

glected, and therefore the image reconstruction gives an averaged LAC. Differently from dual-energy CT, spectral CT measures the LAC at multiple energy bins, and this fact can enable more accurate decomposition of the LACs to energy- and material-dependent components. From this, we expect better material classification.

## 2.2. Decomposition to photoelectric effect and Compton scattering

For a CT system, Alvarez et al. [10] presented empirically within the energy region of 30–200 keV that the LAC can be represented in two dimensions that approximate two main physical interactions as:

$$\mu(E) = a_1 \frac{1}{E^3} + a_2 f_{\text{KN}}(E), \quad (2)$$

where  $f_{\text{KN}}(E)$  is the Klein-Nishina function [10], the functions  $1/E^3$  and  $f_{\text{KN}}(E)$  approximate the energy dependence of the photoelectric effect and Compton scattering, respectively.  $a_1$  and  $a_2$  are the material-dependent coefficients of the decomposition. In previous work, using this model of attenuation decomposition being adjusted for spectral CT we presented a novel classification method, the SIMCAD that can efficiently estimate both material properties ( $\rho_e$ ,  $Z_{\text{eff}}$ ) directly from spectral LAC measurements [39]. The method was tested in the range of  $6 \leq Z_{\text{eff}} \leq 23$ .

## 2.3. General model of decomposition

The LAC can be represented with a more general mathematical formulation, which decomposes the LAC to multiple dimensions of x-ray attenuation space for energy bin  $E_k$  as [48, 49]

$$\mu(E_k) = a_1 f_1(E_k) + a_2 f_2(E_k) + \dots + a_N f_N(E_k), \quad (3)$$

where  $a_i$  are the material-dependent coefficients,  $f_i(E_k)$  are energy-dependent basis functions ( $i = 2, 3, \dots, N$ ,  $k = 2, 3, \dots, K$ ), and  $N$  and  $K$  are the total number of components, i.e. dimensionality of the LACs, and energy bins, respectively. The basis functions can be just a mathematical formulation without a physical interpretation.

## 2.4. Singular Value Decomposition

Alvarez (1982) [48] explored how to efficiently quantify the dimensionality of the LAC vector space (Eq. 3) based on the Singular Value Decomposition (SVD) theorem, a tool from matrix algebra. For dual-energy CT systems and for biological materials within the energy region of medical diagnosis, they found that the LAC decomposition to linear vector space with just two components yields sufficient accuracy. Additionally, they noticed that if the energy region has a discontinuity in the LAC due to a K-edge material like iodine contrast agent, now three basis functions are needed to accurately fit the vector space model of the LAC. Using synthetic spectral CT data, Eger et al. [50] investigated the dimensionality of the spectral LAC decomposition for a set of explosive and non-explosive materials for security applications between 10 keV and 150 keV. They studied

a broad range of different materials with overall number of 124. Based on the SVD decomposition, they concluded that two dimensional linear vector space representation of the LAC is not sufficient for accurate approximation of the spectral LACs, and more energy-dependent basis functions and material-dependent coefficients are needed for better material classification. Our assumption for the reason is that some of the materials may have K-edge discontinuity in the LAC, which may be expected for materials encountered in security screening. From Spectral CT measurements, Busi et al. [51] also performed a SVD analysis with innocuous and threat materials in the range of  $5 \leq Z_{\text{eff}} \leq 10$  with an attention to security screening applications. They used the filtered back projection algorithm with 360 projections for image reconstruction. From SVD decomposition, they found that the first two singular vectors are sufficient to find a good approximation for the spectral LACs of all the materials used. Thus, the dimensionality is mostly dependent on the range of materials and the energy range.

The SVD is applied to the matrix  $A$ , whose columns are the measured LAC curves of all the materials with dimensions ( $K \times M$ ) at multiple energy bins.  $K$  and  $M$  are the total number of energy bins and materials estimated, respectively. The SVD of the matrix  $A$  targets to retrieve a group of optimal linearly independent vectors that can approximate the measured LAC, and is defined as [48, 52]

$$A = \begin{bmatrix} \mu_1(E_1) & \mu_2(E_1) & \dots & \mu_N(E_1) \\ \mu_1(E_2) & \mu_2(E_2) & \dots & \mu_N(E_2) \\ \vdots & \vdots & \ddots & \vdots \\ \mu_1(E_K) & \mu_2(E_K) & \dots & \mu_N(E_K) \end{bmatrix} = U D V^T, \quad (4)$$

where  $D$  is a diagonal matrix, whose diagonal elements are the singular values  $\sigma_i$  of  $A$ , and the columns of  $U$  and  $V$  are composed of the left and right singular vectors, respectively. The left singular vectors can be called the optimal basis set functions [48], which consist of linearly independent vectors  $u_i(E)$ . The magnitude of each singular value  $\sigma_i$  characterizes how the corresponding optimal basis set function  $u_i$  relatively contributes to the decomposition model in Eq. 3 or Eq. 5. The optimal basis set functions can alternatively be considered as a group of energy-dependent basis functions in Eq. 3 that can represent the spectral LACs of materials [50].

We also performed the analysis to estimate the dimensionality of LACs for the set of our materials and detector's energy range based on SVD decomposition, for which the results are given in the subsection 4.1.

We also analyzed the dimensionality of LAC vector space for the set of our materials and energy range using the SVD, for which the results are presented in the subsection 4.2.

## 2.5. Basis material decomposition

As an alternative way to the general attenuation decomposition, a material can also be decomposed into a linear combination of multiple basis materials with respective equivalent thicknesses for each energy bin,  $E_k$ , which can be



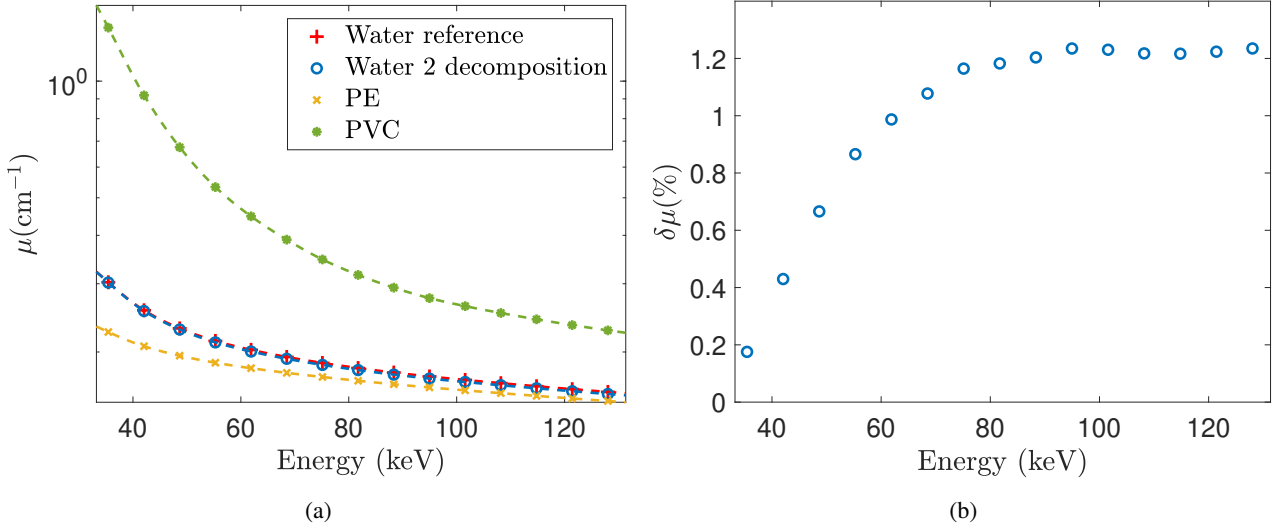


**Figure 1:** Spectral LAC decomposition for water 2 sample introduced in Tab. 1. (a) Basis material decomposition computed from 15 energy bins. The reference LACs of water, PE and PVC are obtained from NIST database [54]. Note logarithmic scale in the y-axis. (b) Percent relative deviations of the attenuation decomposition with respect to the reference LACs at each energy bin.

written as [40–42, 53]

$$\mu(E_k) = h_1\mu_1(E_k) + h_2\mu_2(E_k) + \dots + h_N\mu_N(E_k), \quad (5)$$

where  $h_i$  and  $\mu_i(E_k)$  ( $i = 2, 3, \dots, N$ ;  $k = 2, 3, \dots, K$ ) represent the equivalent thickness and LAC of a basis material  $i$  at energy bin  $E_k$ , respectively.  $N$  and  $K$  represent the number of basis materials, (or the dimensionality of the LAC) and energy bins, respectively. Note that the number of basis materials  $N$  should be smaller than or equal to the number of energy bins  $K$ , otherwise the above equation would be under-determined.

Fig. 1a shows basis material decomposition of the energy resolved LACs, exemplified for water. Using experimental data, and PE and PVC basis materials, we first obtained equivalent thicknesses  $h_{\text{PE}}$  and  $h_{\text{PVC}}$  using Eq. 10, and then represented the LACs by linear combination of basis materials based on Eq. 5. Fig. 1b presents how the basis material decomposition is accurate with respect to the reference LACs, shown as the percent relative deviations at multiple energy bins.

The basis material decomposition has an advantage over the photoelectric absorption–Compton scattering model that one can accurately approximate the LAC of materials with K-edge absorption by including another basis material that has a K-edge within the energy region used [33, 48]. How many basis materials are required to accurately define the decomposed LAC of the material is an important question in terms of classification. Using experimental data we analysed the classification accuracy versus the number of basis materials in the LAC (Eq. 5), for which the results are given in the subsection 4.2.

### 3. Methods

#### 3.1. Material features under investigation

X-ray attenuation mechanism is related to a material's electron density [55], which is the number of electrons per unit volume (electron – mole/ $\text{cm}^3$ ). For a compound composed of  $N$  total different elements  $i$  each with a number of atoms,  $\alpha_i$ , the electron density is expressed as follows

$$\rho_e = \frac{\sum_{i=1}^N \alpha_i Z_i}{\sum_{i=1}^N \alpha_i A_i} \rho, \quad (6)$$

where  $\rho$  is mass density,  $Z_i$  and  $A_i$  denote atomic number and atomic mass of an element  $i$ . For compounds, the atomic number is referred to as effective atomic number,  $Z_{\text{eff}}$ , dependent on the atomic numbers of the elements in the compound and on their corresponding quantities. Mayneord (1937) [56] and Spiers (1946) [57] proposed a now classical parameterization of  $Z_{\text{eff}}$ , defined as

$$Z_{\text{eff}} = \sqrt[l]{\sum_{i=1}^N r_i Z_i^l}, \quad (7)$$

where  $r_i$  is the relative electron fraction of each element:

$$r_i = \frac{\alpha_i Z_i}{\sum_{j=1}^N \alpha_j Z_j},$$

where  $\alpha_i$  is the number of atoms that have the same atomic number  $Z_i$ . The exponent  $l$  is a free parameter that is adjusted depending on the energy range, materials and system features. This exponent typically varies between 2.94 and 3.8 stemming from experimental fits for various CT systems [42]. In our previous work [39], when estimating the classification performance with the SIMCAD method we found

that  $l = 8.0$  appeared to be the optimal value for the set of our materials, source spectrum and system features. Therefore, in this work to calculate reference  $Z_{\text{eff}}$  values of the materials listed in Tab. 1, required for  $Z_{\text{eff}}$  estimation technique presented in the subsection 3.7, we employ the value of  $l = 8.0$ .

### 3.2. Experimental setup and materials

The experiments were carried out in the 3D Imaging Center at DTU, Denmark. The X-ray beam was produced by a micro focused Hamamatsu source. The operating parameters of the source such as the acceleration tube voltage and the anode filament current were 150 kV and 0.5 mA, respectively. A 2-mm-thick aluminum filter was inserted in front of the source to suppress photons with energies under the detector's energy range. The incoming beam was collimated to a fan beam by employing a JJ X-Ray IB-C80-AIR slit with 5-mm-thick tungsten carbide blades to irradiate the full detector area. The slit decreases the background radiation of scattered and fluorescent photons by maintaining the beam size to a minimum. The sample was mounted on the rotation stage and the scans were performed between discrete rotations with  $30^\circ$  increments over a range of 360 degrees because we use 12 projections for reconstructions. The source to detector distance is 701 mm while the source to sample distance is set to 500 mm.

We used MultiX ME-100 v2 PCD for the experiments that is manufactured by Detection Technology S.A.S. in Moirans, France. The detector consists of a system of five detector modules, each module possesses a  $1 \times 128$  linear array of  $0.8 \times 0.8 \text{ mm}^2$  pixels. The detector can measure with 128 energy bins with a width of 1.1 keV each, evenly distributed between 20 and 160 keV energy range. The detector working under high X-ray fluxes provides the energy resolution of 6.5% (8 keV at 122 keV) [22]. The integration time of the detector can change from 2 ms to 100 ms (in 10  $\mu\text{s}$  increments). In this work, the total integration time per projection is set to 8 seconds for classification performance estimations.

Tab. Table 1 lists the materials tested in this work and their reference  $Z_{\text{eff}}$  values that were computed by using Eq. 7 and the exponent  $l = 8.0$ . Sample dimensions are described through width $\times$ length for rectangular samples or diameter for circular samples. The plastics presented in the tables are polycarbonate (PC), polymethyl methacrylate (PMMA), polyoxymethylene-C (POM-C), polytetrafluoroethylene (PTFE), polyethylene terephthalate (PET), polyoxymethylene-H (POM-H) and polyvinylidene fluoride (PVDF).  $Z_{\text{eff}}$  values of materials generally found in a passenger luggage mostly changes between 7 and 8. Most organic materials are related to this region [9]. The plastics were selected for estimations because their chemical compositions show resemblance to several explosives, e.g. POM can be regarded as an explosive simulant [36]. The most human organs and tissues change between  $6 \leq Z_{\text{eff}} \leq 15$  [58–61] within the detector's energy region, which represent the similar  $Z_{\text{eff}}$  variation as the materials

used in the work. One reason may be that the major abundant elements in various human tissues and polymers are composed of H, C, N, and O [8]. The classification of these materials used is thereby an efficient gauge for an instrument's capacity to quantitatively classify materials in medical and security fields. Note that none of the materials tested have absorption edges in the energy range of the detector, otherwise we would need to use one or multiple K-edge basis materials to fit the basis material decomposition model, as described in the subsection 2.5.

Fig. 2 presents just two "real life" phantoms (samples) among all the phantoms that were scanned and processed through the BMD classification method, as examples.

### 3.3. Basis materials used for the study of LAC dimensionality based on classifications

In this work, we perform classifications with the different number of basis materials in the decomposition. In other words, we study the dimensionality of LACs based on classifications. Tab. 2 lists all the used basis materials with reference density and  $Z_{\text{eff}}$ . Tab. 3 shows the basis materials for each LAC dimensionality study. Note that for classifications we use only the theoretical LACs for all the basis materials, taken from NIST database [54]. The classification results obtained with respect to the number of basis materials are given in the subsection 4.2, where we find that two basis materials give the best classification performance. Therefore, we use two basis materials, PE and PVC, for classifications in the subsections 4.3, 4.4 and 4.6.

### 3.4. Data correction and setting low- and high-energy thresholds

Physical effects such as charge sharing and weighting potential cross-talk, fluorescence radiation, scattering radiation, pulse pile up and incomplete charge collection severely distort the measured spectra of a Cadmium telluride (CdTe) PCD working under high flux. These effects being related to energy and flux decrease the detector's energy resolution and lead to large deviations in the extracted LACs of materials from theoretical values. As a result the spectral distortions will significantly decrease classification performance [45]. The correction of the detector's spectral response is therefore needed to accurately extract the LACs. We employed the correction algorithm introduced by Dreier et al. [43] to correct for these distortions, of which we refer the reader to for further details. Fig. 3 shows the spectral LACs of water obtained with the raw and corrected data. The reference LAC curve is also shown for comparison. The correction algorithm significantly corrects the deviated LAC from the raw data at the low energies, however, cannot correct the deviated LACs at lower and higher energy bins. This may be due to detector's flux variation and photon starvation, i.e. complete attenuation of photons at these energies, which are excluded by setting low- (33.2 keV) and high-energy (132.4 keV) thresholds,  $E_l$  and  $E_h$  that remain the same for all the materials used in the measurements.

**Table 1**

The list of the materials used for classifications and their respective reference  $Z_{\text{eff}}$  values computed with Eq. 7. The mass density,  $\rho$  for the plastics was estimated with uncertainties of  $\pm 0.15\%$ . The rest of mass density values are taken from PubChem database [62].

Index	Material	Chemical Formula	Width×length/ Diameter (mm)	$\rho$ (g/cm <sup>3</sup> )	$Z_{\text{eff}}$
1	Graphite	C	12.7	1.8	6
2	N,N-Dimethylhydrazine	C <sub>2</sub> H <sub>8</sub> N <sub>2</sub>	67	0.791	6.44
3	Ethylenediamine	C <sub>2</sub> H <sub>8</sub> N <sub>2</sub>	67	0.90	6.44
4	PC	(C <sub>16</sub> H <sub>14</sub> O <sub>2</sub> ) <sub>n</sub>	8.2×53.5	1.18	6.82
5	Acetone 2	C <sub>3</sub> H <sub>6</sub> O	54	0.785	6.90
6	Nitrobenzene	C <sub>6</sub> H <sub>5</sub> NO <sub>2</sub>	49	1.20	7.00
7	PMMA	(C <sub>5</sub> O <sub>2</sub> H <sub>8</sub> ) <sub>n</sub>	40×42	1.18	7.02
8	Ethanol 96%	C <sub>2</sub> H <sub>6</sub> O (96%)	67×67	0.798	7.06
9	Methanol	CH <sub>3</sub> OH	20	0.792	7.29
10	POM-C	(CH <sub>2</sub> O) <sub>n</sub>	9×53.5	1.41	7.40
11	Hydrazine solution	H <sub>4</sub> N <sub>2</sub> (35%)	54	1.0	7.43
12	Nitromethane	CH <sub>3</sub> NO <sub>2</sub>	20	1.14	7.50
13	Water	H <sub>2</sub> O	20	0.997	7.78
14	Water 3	H <sub>2</sub> O	12.7	0.997	7.78
15	Hyd. Peroxide 2	H <sub>2</sub> O <sub>2</sub> (50%)	73×74	1.22	7.83
16	PTFE	(C <sub>2</sub> F <sub>4</sub> ) <sub>n</sub>	9×53.3	2.16	8.70
17	Magnesium 2	Mg	18	1.74	12
18	Aluminum 2	Al	20×20	2.70	13
19	2-Butanone	C <sub>4</sub> H <sub>8</sub> O	83	0.805	6.76
20	Acetone	C <sub>3</sub> H <sub>6</sub> O	20	0.785	6.90
21	PET	(C <sub>10</sub> H <sub>8</sub> O <sub>4</sub> ) <sub>n</sub>	9×53.5	1.39	7.09
22	Methanol 2	CH <sub>3</sub> OH	81	0.792	7.29
23	POM	(CH <sub>2</sub> O) <sub>n</sub>	12.7	1.42	7.40
24	POM-H	(CH <sub>2</sub> O) <sub>n</sub>	15.5×53.3	1.43	7.40
25	Ethanol 40%	C <sub>2</sub> H <sub>6</sub> O (40%)	67×67	0.947	7.63
26	Water 2	H <sub>2</sub> O	51×51	0.997	7.78
27	Nitric acid	HNO <sub>3</sub> (65%)	83	1.39	7.80
28	Hyd. Peroxide	H <sub>2</sub> O <sub>2</sub> (50 %)	20	1.22	7.83
29	PVDF	(C <sub>2</sub> H <sub>2</sub> F <sub>2</sub> ) <sub>n</sub>	9×53.5	1.79	8.40
30	PTFE 2	(C <sub>2</sub> F <sub>4</sub> ) <sub>n</sub>	12.7	2.2	8.70
31	Magnesium	Mg	12.7	1.74	12
32	Aluminum	Al	25	2.70	13
33	Silicon	Si	12.7	2.33	14

**Table 2**

The list of the basis materials used for classifications, and their  $Z_{\text{eff}}$  values calculated with Eq. 7. The mass densities are from in PubChem data [62].

Basis material	Chemical Formula	$\rho$ (g/cm <sup>3</sup> )	$Z_{\text{eff}}$
Polyethylene (PE)	(C <sub>2</sub> H <sub>4</sub> ) <sub>n</sub>	0.93	5.79
Polyacetylene (PAc)	(C <sub>2</sub> H <sub>2</sub> ) <sub>n</sub>	0.4	5.89
Polypyrrole (PPy)	(C <sub>4</sub> H <sub>5</sub> N) <sub>n</sub>	0.97	6.22
Polymethyl methacrylate (PMMA)	(C <sub>5</sub> O <sub>2</sub> H <sub>8</sub> ) <sub>n</sub>	0.94	7.02
Polyoxymethylene (POM)	(CH <sub>2</sub> O) <sub>n</sub>	1.42	7.40
Polyvinyl Chloride (PVC)	(C <sub>2</sub> H <sub>3</sub> Cl) <sub>n</sub>	1.406	15.71

### 3.5. Energy rebinning step

After the spectral corrections are applied to the spectra of each projection of the CT scan, the data is rebinned by summing photon counts between low- (33.2 keV) and high-energy (132.4 keV) thresholds. A higher number of

energy bins can give better resolution, but also results in higher noise levels in each bin. This is because the signal-to-noise ratio (SNR) in each energy bin is proportional to the square root of the expected number of photons [65]. Spectral CT thus has a compromise between hiring more energy bins

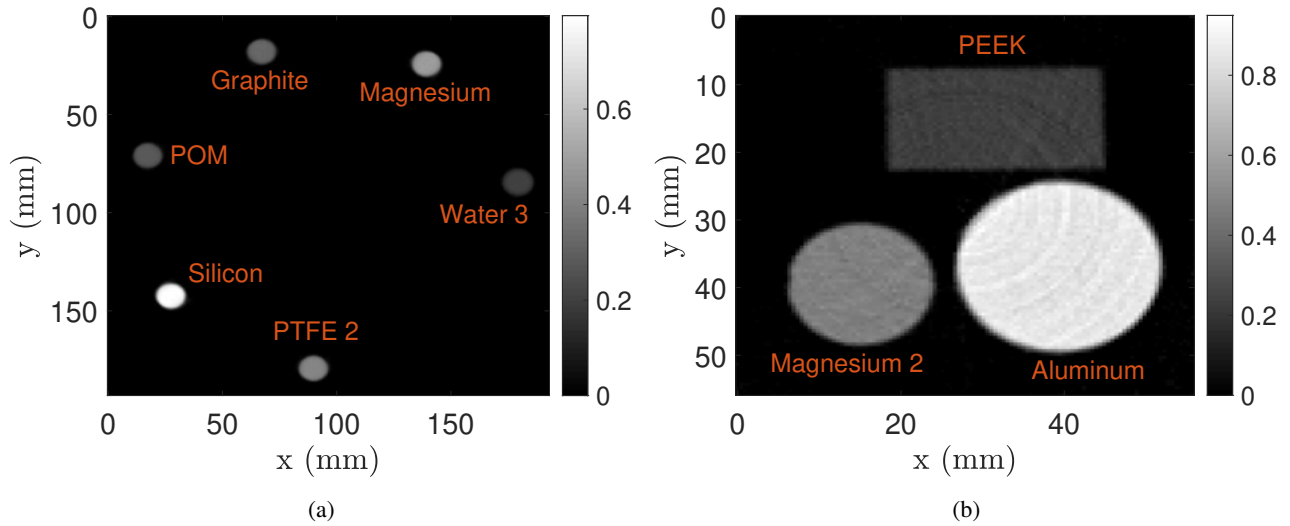


**Figure 2:** Presentation of just two "real life" phantoms among all the phantoms scanned, as examples. The materials in both phantoms used for the classification performance estimation are listed in Tab. 1. These 2D reconstructions were performed with the simultaneous iterative reconstruction technique (SIRT) [63] from 360 projections for presentation (at 55.3 keV X-ray energy). The gray scale bars represent the LACs with the unit of  $\text{cm}^{-1}$ . (a) This phantom was taken from the authors of Ref. [64] to test it on our classification method. (b) This phantom was scanned with the different integration times of 2 ms, 10 ms, 50 ms and 100 ms, for which the results are presented in the subsection 4.2. PEEK represents polyetheretherketone.

**Table 3**

The basis materials for each LAC dimensionality study based on classification performance. Note that in each case we use PVC with the highest  $Z_{\text{eff}}$  value among all the basis materials, whose  $f_{\text{PVC}}$  fraction is used for classifications as explained in the subsection 3.7.

Dimensionality of the LACs	Basis materials
2	PE, PVC
3	PE, PPy, PVC
4	PE, PPy, POM, PVC
5	PE, PAc, PPy, POM, PVC
6	PE, PAc, PPy, PMMA, POM, PVC

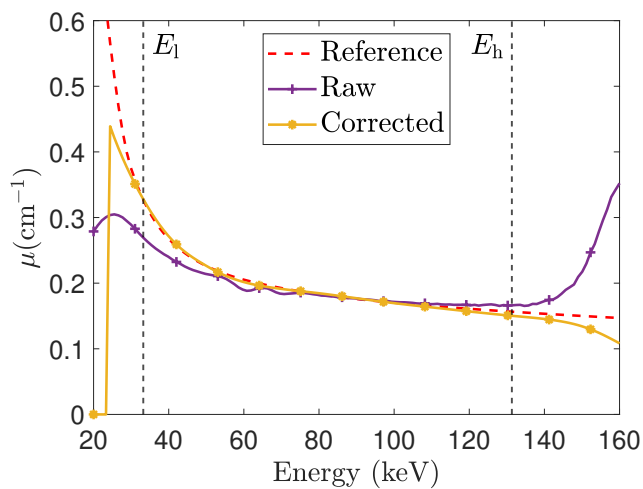


**Figure 3:** Spectral LACs for water calculated from the raw and corrected data. The reference LACs were taken from NIST database [54]. The vertical black dash-dotted lines show the low- and high-energy thresholds,  $E_1$  and  $E_h$ .

and having a higher SNR. Moreover, the classification performance is dependent on the trade-off between the energy bin width and detector's spectral resolution [39]. Therefore, we study the classification performance with 2 (bi-), 15 and 90 energy bins. A source spectrum is sampled for 2 energy bins approach such that 2 separate bins has a gap between low- and high-energies, whose higher and lower boundaries correspond 63.0 keV and 79.5 keV, respectively. To differentiate 2 energy bins from conventional overlapping dual-energies in dual-energy CT, we refer to them as bi-energy bins in the remainder of the paper. 90 energy bins were formed just by collecting all the bins between low- and high-energy thresholds without integration of photon counts. The merging for 15 energy bins approach is done by rebinning the data from 90 energy bins to increase photons statistics. 15 energy bins are uniformly distributed with equal energy bin width within the detector's energy range.

The classification results for all the multiple energy bins approaches analyzed in our study are presented in the subsection 4.3, where we find that 15 energy bins give the best

classification performance. Therefore, we use 15 energy bins for estimations in the subsections 4.1, 4.2, 4.4, 4.5 and 4.6.

### 3.6. Reconstruction algorithm and LAC extraction

To achieve rapid scanning useful for security applications, we employ only 12 projections for estimations. To improve the reconstruction quality from such sparse data, we use the joint reconstruction algorithm called a vectorial total variation scheme,  $L_\infty$ -VTV [45]. This algorithm jointly reconstructs the LACs by using correlations between multiple energy bins. Using  $L_\infty$ -VTV regularization, it is possible to augment the available data of each bin with extra information from another bins. The  $L_\infty$ -VTV uses a L-infinity norm that jointly penalizes the violation of the inter-bin relations, leading to strong couplings between bins. The algorithm uses a weighting parameter  $\lambda$  determining the strength of the regularization term.  $\lambda$  regulates the trade-off between a good fit to the sinogram data and reconstruction smoothness in both the spatial and spectral domain. In application, the value of  $\lambda$  should be selected carefully to have a desired image reconstruction. A too small value may result in an over-regularization with blurred edges, whereas a too large value may give insufficient regularization results. Therefore, we estimate classifications for a set of  $\lambda$  values to examine the impact of this factor.

After performing reconstructions, the mean LAC value of a segment is extracted from the LAC histogram based on the normal distribution fitting. A region of interest (ROI) in the reconstruction is selected with manual segmentation technique, being employed for all materials.

### 3.7. Curve fitting and calculation of $Z_{\text{eff}}$

Brambilla et al. [33] showed that there is dependence between  $Z_{\text{eff}}$  of the estimated material and quantity of equivalent thickness of the basis material with the highest  $Z_{\text{eff}}$  among all the basis materials used. In particular, the fraction for PVC, denoted by  $f_{\text{PVC}}$ , increased monotonically with increasing  $Z_{\text{eff}}$  values of estimated materials. The curve of this dependence can thus be fitted by a polynomial model of degree 3 as [33]

$$Z_{\text{eff}} = c_0 + c_1 \cdot f_{\text{PVC}} + c_2 \cdot f_{\text{PVC}}^2 + c_3 \cdot f_{\text{PVC}}^3, \quad (8)$$

where  $c$  is a set of polynomial regression coefficients that are estimated. The PVC fraction can be calculated by [33]

$$f_{\text{PVC}} = \frac{h_{\text{PVC}}}{\sum_{i=1}^N h_i}, \quad (9)$$

where  $h_i$  is equivalent thickness of basis material  $i$ , and  $i = 2, 3, \dots, N$  with  $N$ - being the total number of basis materials.

Fig. 4 presents the dependence between  $Z_{\text{eff}}$  and  $f_{\text{PVC}}$  fraction, which is fitted by Eq. 8. The reference materials (blue circles) corresponding to indexes from 1 to 18 in Tab. 1 were used to obtain interpolated and extrapolated points (plus signs), which can be used to estimate  $Z_{\text{eff}}$  values. The reference and estimated materials used for classification studies in the subsections 4.2, 4.3 and 4.4 correspond

to indexes from 1 to 18, and from 19 to 33 in Tab. 1, respectively.

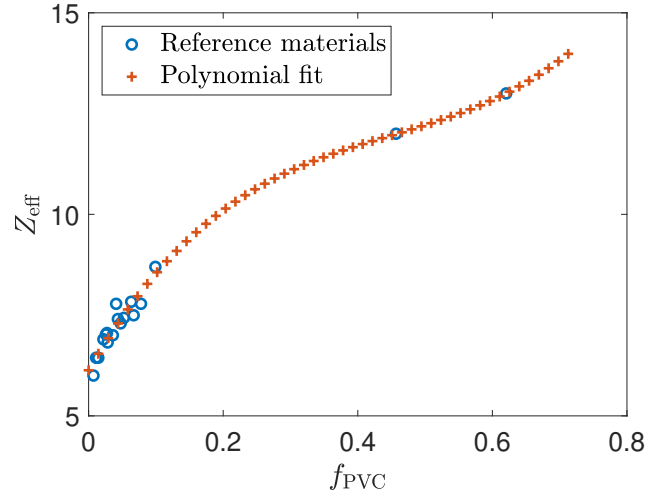


**Figure 4:**  $Z_{\text{eff}}$  as a function of PVC fraction,  $f_{\text{PVC}}$ , obtained with PE and PVC basis materials, and 15 energy bins.

As mentioned previously, Brambilla et al. [33] employed the calibration step to estimate the equivalent thicknesses based on maximum likelihood function. For this step, the detector's response was recorded as a function of the real thicknesses of PE and PVC basis materials superposed on each other. In comparison, we correct the distorted LACs using the spectral correction algorithm presented in the subsection 3.4, and thereby estimate the equivalent thicknesses from Eq. 10. To retrieve equivalent thickness  $h_i$  of each basis material, we reformulate Eq. 5 as a linear system of equations as

$$(\vec{\mu}_1 \quad \dots \quad \vec{\mu}_N) \begin{pmatrix} h_1 \\ \vdots \\ h_N \end{pmatrix} = \begin{pmatrix} \mu(E_1) \\ \vdots \\ \mu(E_K) \end{pmatrix} \quad (10)$$

where  $\vec{\mu}_i = (\mu_i(E_1), \dots, \mu_i(E_K))^T$ , and  $k = 2, 3, \dots, K$  with  $K$ - being the total number of energy bins used.  $\mu_i(E_k)$  designates the LAC of the basis material  $i$  at energy bin  $E_k$ , and  $\mu(E_k)$  represent the measured LACs of the estimated material. In the latter equation, the size of the linear matrix on the left hand side is  $K$ -by- $N$  and the number of unknowns is  $N$ . Note that both the minimum numbers of energy bins and basis materials used in this work are equal to two as discussed in the subsections 3.5 and 3.3, respectively. We use a linear least square solver called **lsqnonneg** function in MATLAB<sup>®</sup> with the positivity constraint on the solution. This gives the vector of equivalent thicknesses  $(h_1, \dots, h_N)$  that minimizes the norm.

Eq. 8 can thus be employed to compute  $Z_{\text{eff}}$  of unknown materials by interpolating or extrapolating the curve of  $Z_{\text{eff}}$  with respect to  $f_{\text{PVC}}$  fraction, as shown in Fig. 4. The classification performance was estimated as the percent relative deviation based on the reference values of  $Z_{\text{eff}}$ , defined as

$$\Delta Z_{\text{eff}}^{\text{rel}} = 100\% \cdot \frac{Z_{\text{eff}}^{\text{est}} - Z_{\text{eff}}^{\text{ref}}}{Z_{\text{eff}}^{\text{ref}}}, \quad (11)$$

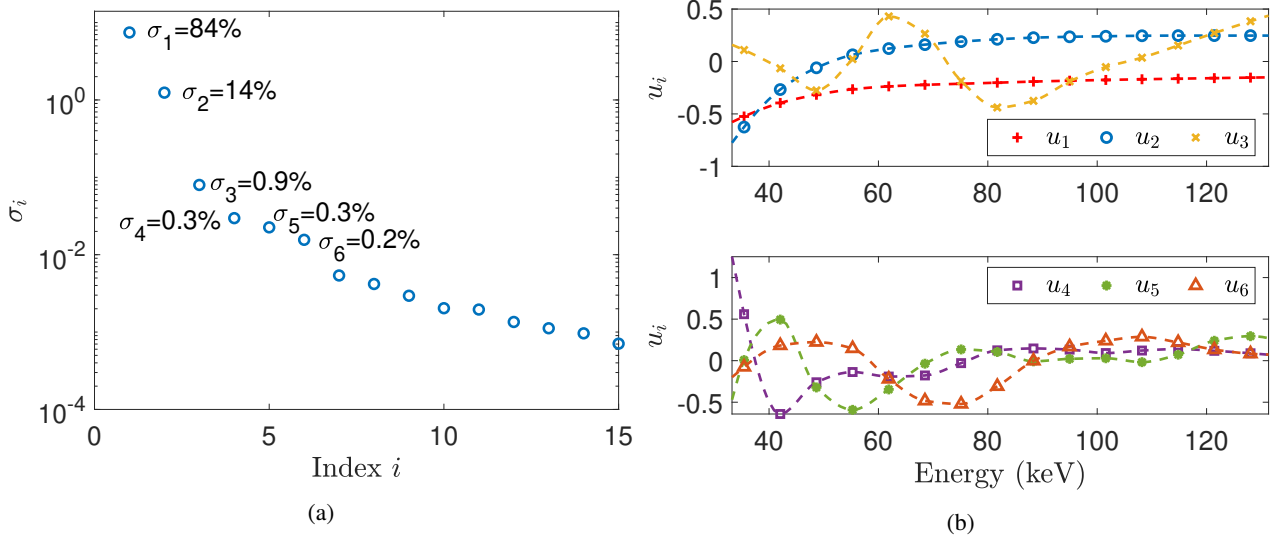


**Figure 5:** Singular Value Decomposition examination of the matrix whose columns contain the extracted LACs of all the materials listed in Tab. 1. (a) Singular values  $\sigma_i$ . Note logarithmic scale in the y-axis. (b) The first six optimal basis set functions  $u_i$  corresponding to the first six singular values  $\sigma_i$ . The scale is in arbitrary units.

where superscripts est and ref indicate the estimated and reference values, respectively.

## 4. Results and discussions

### 4.1. LAC dimensionality analysis based on Singular Value Decomposition

Fig. 5a presents the first singular values  $\sigma_i$  indicating the decomposition accuracy versus the number of dimensions of the LAC space, and Fig. 5b shows the first six optimal basis set functions. The results are obtained by the corrected LACs of all the materials listed in Tab. 1, computed from the data corrected using the correction algorithm as presented in the subsection 3.4. Based on singular values we can conclude that the first two optimal basis set functions can yield precise approximations of the spectral LACs, as expected. That may be because the materials used in this study do not have K-edge discontinuities within the energy range used. Moreover, the rest of optimal basis set functions may be influenced by noise and the characteristic K-edge peaks  $K_{\alpha_1}$  (59.3 keV) and  $K_{\beta_1}$  (67.2 keV) of tungsten inside the X-ray source. The latter may have decreased detector resolution and thereby led to the LAC variations around the energies of K-edge peaks that are visible in Fig. 3. These findings are similar to what have been reported by Busi et al. [51]. However, in our study the first two optimal basis set functions  $u_1, u_2$  are clearly different from the photoelectric and Compton scattering basis functions. This phenomenon is similar to the one observed by Eger et al. [50].

SVD-based analysis based on the singular values of the LACs shows that the dimensionality of LACs is thus estimated at two for the set of our materials and energy range.

### 4.2. Classification performance as a function of basis materials used

The basis materials used for each classification case using the different number of basis materials ( $N$  defined in Eq. 5) in the decomposition were listed in Tab. 3. In this subsection, we compare the classification performance of each case and find the most accurate dimensionality of LACs suitable for the set of our materials, source spectrum and system feature. The classification results presented in this subsection are obtained by the corrected LACs of estimated materials, computed from the data corrected using the correction algorithm. Fig. 6 highlights the relative deviations for  $Z_{\text{eff}}$  with respect to weighting parameter  $\lambda$  values for each dimensionality. The deviations increase as the number of basis materials increases. 2 basis materials give the lowest deviation of 2.4% (at  $\lambda = 60$ ) whereas 5 basis materials provide the highest deviation of 4.4% (at  $\lambda = 30$ ). The deviation is 4.1% (at  $\lambda = 30$ ) for 6 basis materials.

The reason for the increase in the relative deviations with the the number of basis materials may be because the  $f_{\text{PVC}}$  fraction for the most materials significantly decreases as the numbers of basis materials increase, as shown in Fig. 7a. We also estimated how  $f_{\text{PVC}}$  fraction for PEEK in the sample presented in Fig. 2b changes with the number of basis materials.  $f_{\text{PVC}}$  fraction for each number of basis materials is computed using Eq. 10, based on extracted LACs of PEEK. We scanned the sample with the different integration times (per projection) of 2 ms, 10 ms, 50 ms and 100 ms. The resulting reconstruction images from 2 ms and 10 ms have much higher noise levels due to the short data acquisition time. Fig. 7b presents the mean  $f_{\text{PVC}}$  fraction values calculated from such different integration times for each number of basis materials, shown with respective percent relative error bars. The plot shows that the higher numbers of basis materials increase cause an overall decrease in the mean  $f_{\text{PVC}}$

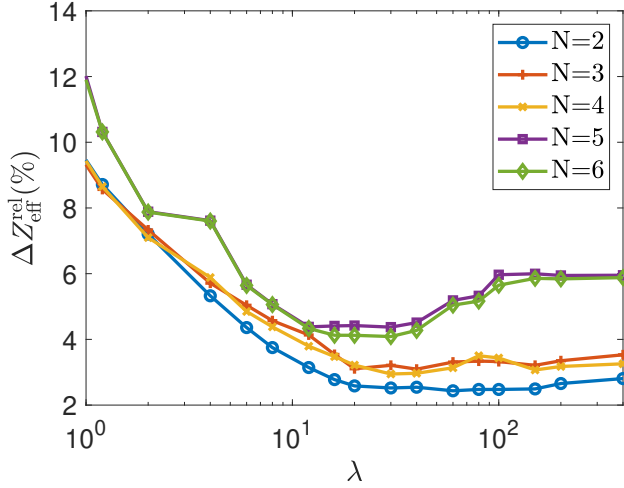


**Figure 6:** The percent relative deviations for  $Z_{\text{eff}}$  as a function of weighting parameter  $\lambda$ , obtained with the different numbers of basis materials  $N$ . The deviations are shown as the mean values of the absolute deviations for each estimated material, corresponding to indexes from 19 to 33 in Tab. 1. Note the logarithmic scale in the x-axis.

fraction and the respective relative error, i.e. in robustness to high noise in image reconstruction. Even though 2 basis materials give the lowest relative error of 21% in  $f_{\text{PVC}}$  fraction calculation among all the numbers of basis materials, this error is still significantly high. This may be due to that LACs extracted from the measurements of 2 ms and 10 ms integration times can be significantly noisy. Thus, as the number of basis materials is larger, the respective  $f_{\text{PVC}}$  fraction changes significantly with respect to high noise levels.

The BMD method thus achieves the best classification performance with just two basis materials, PE and PVC, which are used for classifications in the subsections 4.3, 4.4 and 4.6.

### 4.3. Classification performance as a function of the number of energy bins used

How a source spectrum is sampled for bi-, 15 and 90 energy bins was described in the subsection 3.5. The classification results shown in this subsection are retrieved by the corrected LACs of estimated materials based on the correction algorithm. Fig. 8 presents the percent relative deviations for  $Z_{\text{eff}}$  as a function of weighting parameter  $\lambda$ , for these energy bins approaches. The plot shows that bi- and 90 energy bins give the lowest mean deviations of 4% (at the optimal value of  $\lambda = 6$ ) and 3.2% (at  $\lambda = 150$ ), respectively, whereas 15 energy bins produce the lowest mean deviation of 2.4% (at  $\lambda = 60$ ). Thus, using 90 energy bins does not improve but rather deteriorates classification performance compared to 15 bins approach. This may be due to that 90 energy bins have energy bin widths of 1.1 keV, which is noticeably lower than the detector's energy resolution of 8 keV, while 15 energy bins have energy bin widths of 6.6 keV; Secondly hiring more energy bins leads to the more detector noise. A similar phenomenon was previously observed by Jumanazarov et al.

[39], with the SIMCAD classification method.

We discarded photon counts in the gap between non-overlapping bi-energy bins, which could help to improve the classification performance [66, 67]. Moreover, the gap width was selected as 16.5 keV (with the boundaries at 63.0 keV and 79.5 keV), being greater than the detector's energy resolution, and thus another factor for the improvement. Nevertheless, bi-energy bins resulted in the poorest performance among all the multiple energy bins approaches estimated. One reason may be that using radiography data Beldjoudi et al. [37, 38] presented that the energy thresholds should be optimized when few energy bins are used for material identification. Based on this report, using experimental data from spectral CT Jumanazarov et. al [39] optimized the classification performance for the position of the energy separation gap in the bi-energy bins approach while preserving the low- and high-energy thresholds and the gap width over the whole energy range. As a result, they achieved the best classification performance with just bi-energy bins, investigating classification performance as a function of the number of energy bins used. However, because in this study we focus on testing the novel classification method against a limited number of projection angles and noisy conditions desired for security and medical applications, we use the  $L_{\infty}$ -VTV joint reconstruction that helps to improve reconstruction quality [68]. Therefore, in this work optimizing the method for bi-energy bins with respect to the gap's position in a source spectrum as well as weighting parameter  $\lambda$  would be complicated.

Thus, the BMD method achieves the best classification performance with 15 energy bins approach, which is employed for estimations in the subsections 4.1, 4.2, 4.4, 4.5 and 4.6.

### 4.4. Comparing performances of the raw and corrected data

The uncorrected and corrected LACs obtained by the raw data and the data corrected using the correction algorithm, respectively, were described in the subsection 3.4, exemplified for water. Fig. 9 compares the percent relative deviations in  $Z_{\text{eff}}$  for the raw and corrected data, with respect to weighting parameter  $\lambda$ . As expected, the uncorrected LACs of estimated materials leads to the significantly larger deviation of 5.2% (at  $\lambda = 12.0$ ), whereas the corrected LACs achieves the deviation of 2.4% (at  $\lambda = 60.0$ ). Moreover, the deviations produced by the raw data are not stable with respect to weighting parameter, and slight changes in  $\lambda$  value result in the increased deviations. Thus, the correction for the detector's spectral distortions is required to significantly increase the accuracy of the BMD characterization method.

### 4.5. Adding significantly high noise levels to specific energies

Certain energies may be affected by additional noise during data acquisition. Metal objects can result in such high noise levels, which heavily attenuate photons causing photon starvation and generate metal artifacts in the image re-

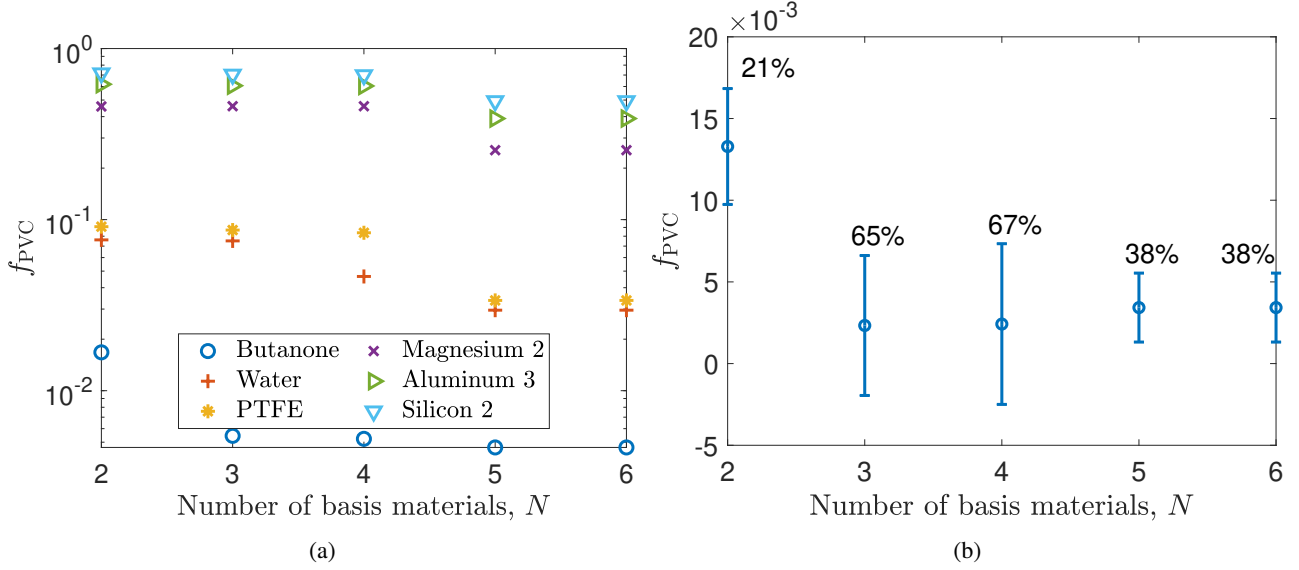


**Figure 7:**  $f_{PVC}$  fraction with respect to the numbers of basis materials. (a)  $f_{PVC}$  values are shown for the different materials from the list in Tab. 1. Note the logarithmic scale in the y-axis. (b) The mean  $f_{PVC}$  values with the respective relative error bars are calculated from the different integration times of 2 ms, 10 ms, 50 ms and 100 ms, related to PEEK in the sample shown in Fig. 2b.

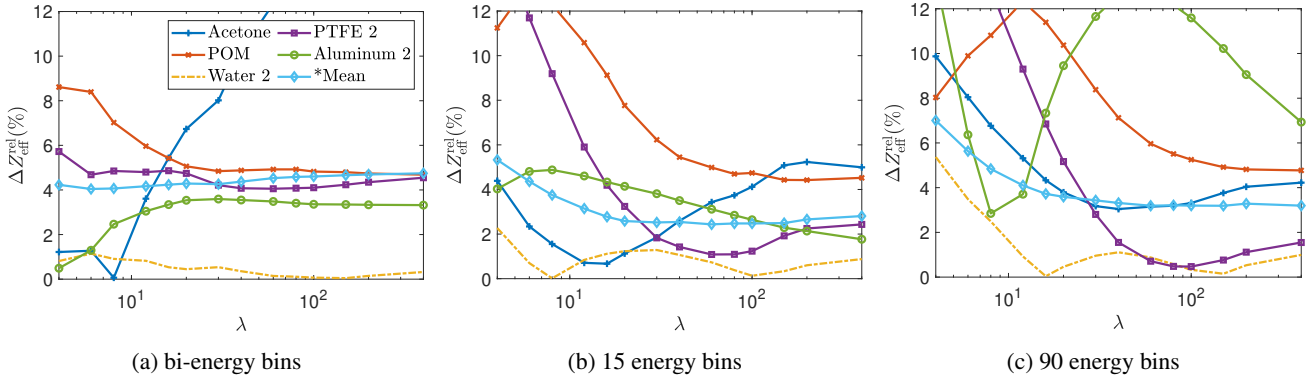


**Figure 8:** The percent relative deviations for  $Z_{eff}$  as a function of weighting parameter  $\lambda$ , obtained with bi-, 15 and 90 energy bins. \*The mean deviation was calculated from absolute values of relative deviations for the estimated materials, corresponding to indexes from 19 to 33 in Tab. 1. Note the logarithmic scale in the x-axis.

construction. Compared to medical applications, in security field a broader range of materials with metals tend to be more commonly scanned. Metal artifacts mainly affect lower energies and may severely decrease the classification performance. To evaluate the robustness of the classification method to such artifacts, normally distributed (Gaussian) noise was added 12 specific energies (among 90 energies), with zero mean and standard deviation  $\sigma = 1.25$ , i.e. 125% noise. These noisy energies were distributed each with equal energy width between low- and high-energy thresholds, to which such noise levels are added as well.

Such noise levels are added to the X-ray spectra of all the projections with the sample being inserted, excluding the flat field measurement. After adding the noise, the spectral correction algorithm is applied to correct the spectral distortions. Fig. 10a shows the raw and spectral corrected X-ray spectra of the flat field measurement ( $I_0$ ) and the first pro-

jection ( $I_1$ ) of the CT scan, exemplified for water 2 sample.  $I_1$  raw spectrum indicates significantly high noise levels in noisy energies.  $I_1$  corrected spectrum shows that the correction of the detector's spectral response smooths the noise with a significant reduction of standard deviation.

After adding the noise, the data was rebinned from 90 energies to 15 energy bins to reconstruct LACs from such noisy data. Fig. 10b presents the noisy raw LACs and the noisy corrected LACs, which represent LACs being reconstructed from the raw and corrected data after adding such noise levels, respectively. For comparison, the reference and noiseless corrected LACs (corrected without adding noise) are shown as well. The noisy corrected LACs still deviate from the noiseless corrected LACs with a significant drop at most energy bins. This indicates that even though the correction algorithm smooths the spectrum with the added noise in specific energies (as shown in Fig. 10a), it cannot elimi-



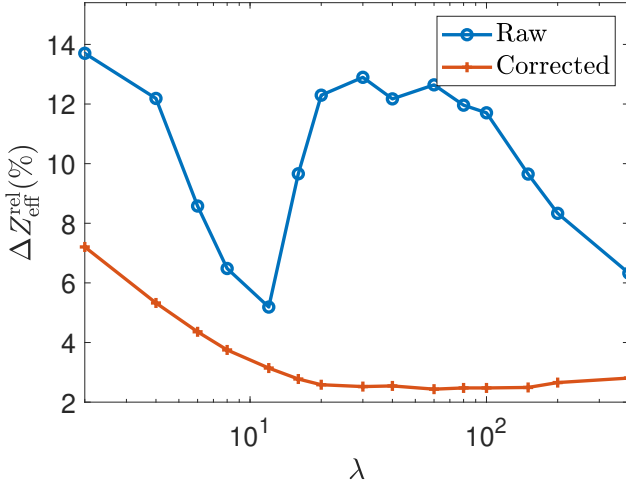


**Figure 9:** The percent relative deviations for  $Z_{\text{eff}}$  as a function of weighting parameter  $\lambda$ , obtained with the raw and corrected data. The deviations are shown as the mean values of the absolute deviations for the estimated materials, corresponding to indexes from 19 to 33 in Tab. 1. Note the logarithmic scale in the x-axis.

nate the noise completely, but redistributes between different energy channels. The noiseless corrected LACs are also noticeably below the reference LACs especially at high-energy channels that are affected by measurement noise (introduced during the data acquisition) in the experimental data due to low photon statistics.

The reconstructions of the LACs presented in Fig. 10b are performed with the  $L_{\infty}$ -VTV algorithm. Both the noisy raw and noisy corrected LACs are reconstructed using weighting parameter  $\lambda = 6$ , being the optimal value for BMD classification performance as shown in Fig. 12a. Based on the classification performance, similarly  $\lambda = 60$  is applied for the extraction of the noiseless corrected LACs. The  $L_{\infty}$ -VTV joint reconstruction also contributes to correlation of intensity shift across the spectrum such that noise in one energy causing blur in a certain edge is compensated by the information in the other bins of the same edge [45, 68].

Fig. 11 shows the histograms of the noiseless and noisy corrected LACs at the energy of 128 keV, both being assigned to the LACs shown in Fig. 10b. The plots show that the high noise levels added to specific energies lead to significant decreases and increases in attenuation values for some pixels within a segment of the sample. Overall, the mean LACs extracted based on the normal distribution decrease for all energy bins (see the noisy corrected LACs in Fig. 10b), even though photon counts in some energies increase after adding the noise, as shown in Fig. 10a. The reason for decreases in the mean LACs may be due to that the reconstruction quality is degraded severely after adding such high noise levels, leading to the presence of more pixels with the significantly decreased LACs.

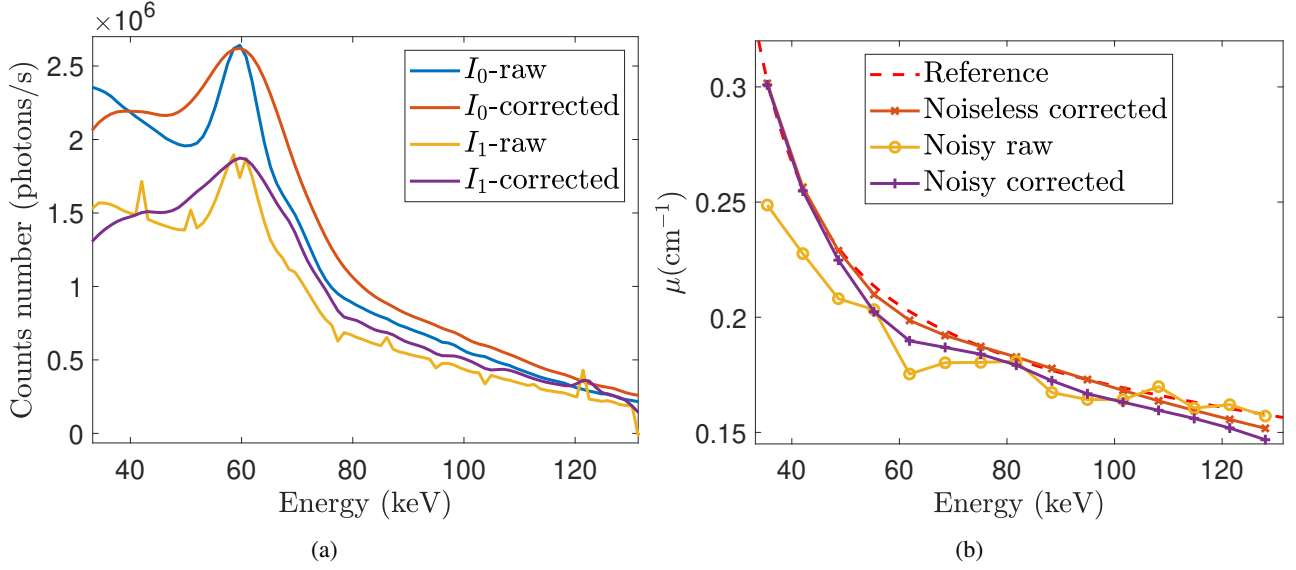
#### 4.6. Comparing BMD with SIMCAD

In the subsection 4.5 we added significantly high noise levels to specific energies in the raw dataset, examining the X-ray spectra and LACs of water 2 sample. In this subsection, we add similar noise levels to similar specific energies in the raw data of all the materials listed in Tab. 4. We then apply the spectral correction algorithm to the noisy raw data, and hereafter rebin the data from 90 energies into 15 energy bins. We extract LACs from such noisy corrected data after energy rebinning. Our aim is to compare classification performances of BMD and SIMCAD method presented by Jumanazarov et al. [39]. We classify the materials in Tab. 4 from the noiseless and noisy corrected data. The LACs obtained by the noiseless and noisy corrected data were demonstrated in Fig. 10b, exemplified for water 2 sample.

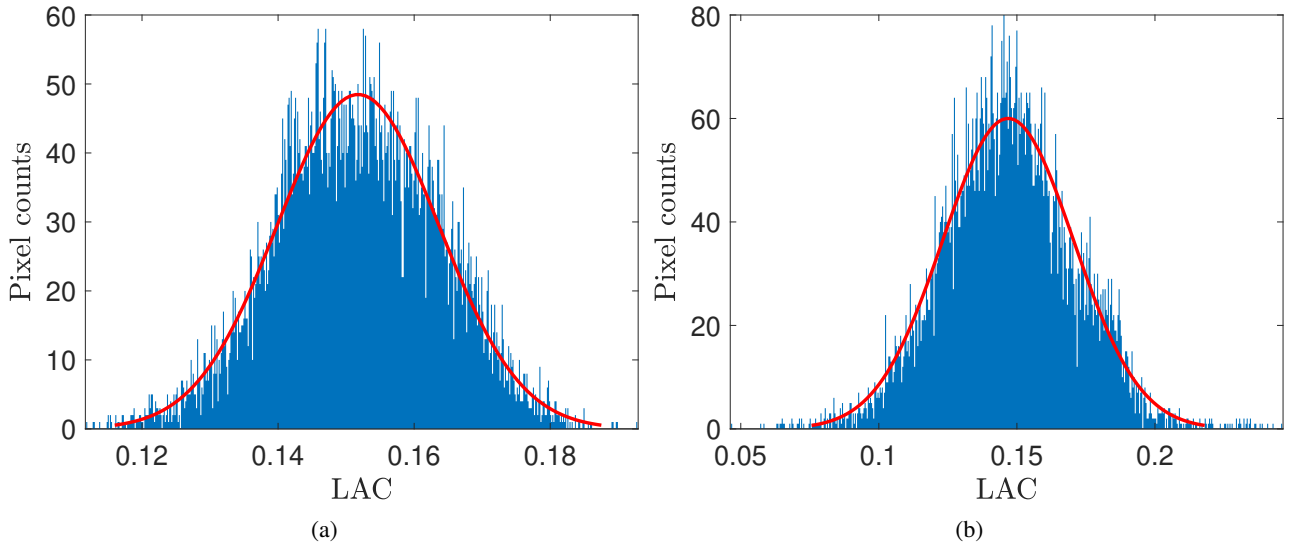
The classification performances of both methods under noiseless and noisy conditions depend on the combined workflow of the correction algorithm and the joint reconstruction. The artifacts in reconstructions due to limited number of projections are handled by the latter. We use  $L_{\infty}$ -VTV joint reconstruction algorithm and just 12 projections for both methods. The curve fitting (presented in the subsection 3.7) and calibration steps for the BMD and SIMCAD, respectively, were performed using all the materials shown in Tab. 1, from the noiseless corrected LACs.

Fig. 12a shows the percent mean relative deviations for  $Z_{\text{eff}}$  of the BMD and SIMCAD methods at the different weighting parameters  $\lambda$ . With the noiseless corrected data, the BMD reaches the maximal classification performance with the deviation of 2.3% (at  $\lambda = 60.0$ ), while the SIMCAD reaches it with the deviation of 2.7% (at  $\lambda = 16.0$ ). With the noisy corrected data, for the BMD and SIMCAD these deviations are 4.6% (at  $\lambda = 6.0$ ) and 5.4% (at  $\lambda = 8.0$ ), respectively. Fig. 12b shows the relative deviations for  $\rho_e$  obtained with the SIMCAD using the noiseless and noisy corrected data, for which the mean deviations are 2.5% (at  $\lambda = 16.0$ ) and 6.1% (at  $\lambda = 8.0$ ), respectively. Compared to the SIMCAD, the BMD thus reaches 17.4% improved accuracy with the noiseless corrected data. Under noisy conditions, the SIMCAD appears to be more stable with respect to  $\lambda$  compared to the BMD, for which slightly lower or higher  $\lambda$  values lead to noticeably higher deviations. On the other hand, the SIMCAD results higher deviations under such noisy conditions. Tab. 4 compares the deviations obtained by the noiseless and noisy corrected data of each method for the different materials. The results in the table are from in Fig. 12a corresponding to the the optimal  $\lambda$  values. Under noisy conditions, the BMD and SIMCAD show the deviations of  $-4.6\%$  and  $-6.1\%$  for PET, respectively, and the deviations are  $-11.0\%$  and  $-13.9\%$  for magnesium, respectively. It is noteworthy that the BMD shows better robustness to such high noise levels for inspecting plastics in the range of  $6 \leq Z_{\text{eff}} \leq 9$ .

The main advantage of the SIMCAD is its capability to estimate both material properties,  $\rho_e$  and  $Z_{\text{eff}}$ . However, the BMD has an outstanding advantage that it can classify a broader range of  $Z_{\text{eff}}$ , including materials with K-edge



**Figure 10:** X-ray spectra and energy resolved LACs, exemplified for water 2 sample introduced in Tab. 1. (a) X-ray source spectra before and after applying spectral correction algorithm for the flat field ( $I_0$ ) and the first projection data ( $I_1$ ). The number of counts per second shown is summed over all detector pixels. (b) Energy resolved LACs obtained by the raw and corrected data, when high noise levels are added to specific energies between low- and high-energy thresholds. The reference and noiseless corrected (without adding noise) LACs are also presented for comparison.



**Figure 11:** The histograms of LACs of water 2 sample presented with a Gaussian peak fit (red line), both corresponding to the LACs shown in Fig. 10b at the energy of 128 keV. The pixel counts denote the number of pixels within a region of interest (ROI), each having the respective LACs presented on the x-axis. (a) The histogram of the noiseless corrected LACs (corrected without adding noise). (b) The histogram of the noisy corrected LACs (corrected after adding noise).

discontinuities in their LACs. For this purpose, the BMD method uses basis materials that at least one basis material should have a K-edge absorption within the detector's energy region to represent the extracted LACs with a K-edge [33, 48]. It is important to note that  $Z_{\text{eff}}$  range of basis materials should cover  $Z_{\text{eff}}$  range of estimated materials. Otherwise, the value of  $f_{\text{PVC}}$  fraction of the estimated material would become larger than one, for which the extrapolation would lead to lower accuracy in fitting  $Z_{\text{eff}}$  (see the subsection 3.7). A similar phenomenon was reported by Brambilla

et al. [33]. The SIMCAD cannot estimate materials that have K-edges in their LACs between detector's energy region [39]. This is because this method uses an attenuation decomposition model based on photoelectric absorption and Compton scattering interactions, whose energy-dependent components (i.e. basis functions) are smooth [10], being not capable to approximate a discontinuity in the LACs of estimated materials. One solution could be to truncate the energy bins below the edge, however this would limit the energy range, and thereby may decrease the classification

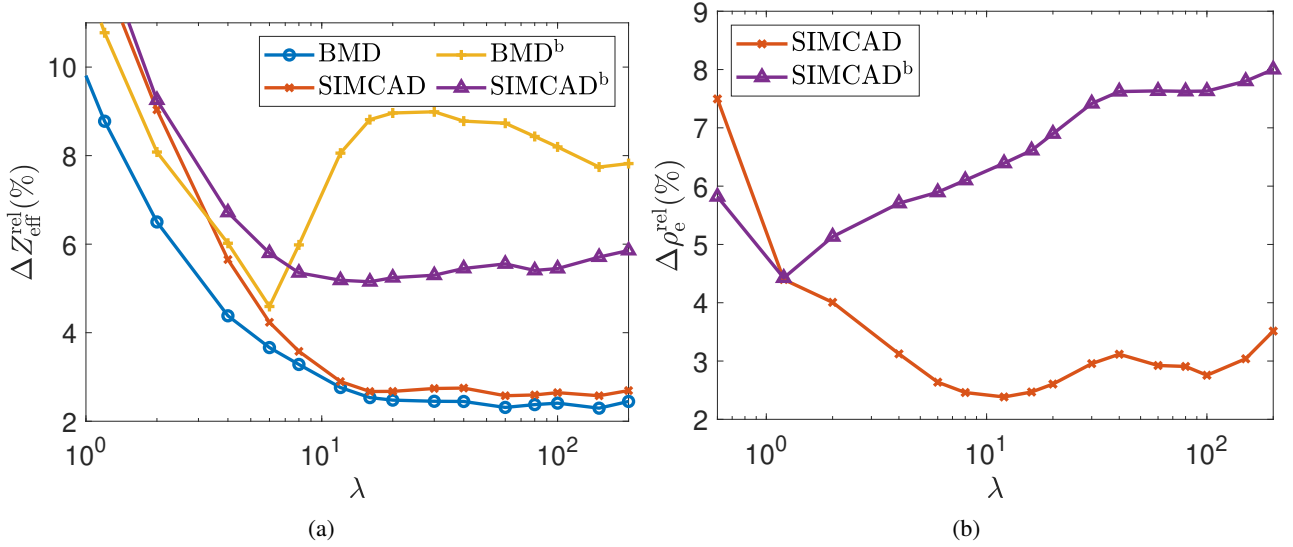


**Figure 12:** The percent relative deviations for  $Z_{\text{eff}}$  (a) and  $\rho_e$  (b) as a function of weighting parameter  $\lambda$ , obtained by the BMD and SIMCAD methods. The BMD does not estimate  $\rho_e$ . <sup>b</sup>The deviations are obtained from the noisy corrected data in which how the noise is introduced is described in the subsection 4.5. The deviations are shown as the mean values of the absolute deviations for each estimated material listed in Tab. 4. Note the logarithmic scale in the x-axis.

**Table 4**

The percent relative deviations for  $Z_{\text{eff}}$  and  $\rho_e$  with the reference values that are calculated using Eqs. 7 and 6, respectively. The deviations for each method correspond to the maximal classification performance presented in Fig. 12a. <sup>a</sup>The mean values were calculated from absolute values of each column. <sup>b</sup>The deviations are obtained from the noisy corrected data in which how the noise is added is described in the subsection 4.5. Note that the BMD does not estimate  $\rho_e$ .

Material	$Z_{\text{eff}}^{\text{ref}}$	BMD $\Delta Z_{\text{eff}}^{\text{rel}}(\%)$	SIMCAD $\Delta Z_{\text{eff}}^{\text{rel}}(\%)$	BMD <sup>b</sup> $\Delta Z_{\text{eff}}^{\text{rel}}(\%)$	SIMCAD <sup>b</sup> $\Delta Z_{\text{eff}}^{\text{rel}}(\%)$	$\rho_e^{\text{ref}}$	SIMCAD $\Delta \rho_e^{\text{rel}}(\%)$	SIMCAD <sup>b</sup> $\Delta \rho_e^{\text{rel}}(\%)$
PMMA	7.02	1.3	-0.4	-0.03	0.4	0.636	1.8	2.0
PTFE	8.70	3.0	4.0	2.1	-1.3	1.035	3.2	7.1
PVDF	8.40	4.3	3.9	3.5	0.3	0.896	-3.1	-0.6
PC	6.82	0.2	-2.0	-4.2	-2.9	0.610	-1.9	-1.2
POM-C	7.40	0.9	0.4	-0.3	-2.5	0.753	3.9	5.0
PET	7.09	0.1	-1.3	-4.6	-6.1	0.721	2.8	7.4
POM-H	7.40	1.7	0.3	1.6	0.6	0.763	2.4	2.6
Acetone	6.90	-4.1	-2.6	-5.2	-4.7	0.432	0.9	4.6
Hyd. Peroxide	7.83	-4.7	-4.9	-9.3	-11.5	0.661	2.5	5.8
Methanol	7.29	-1.8	-2.6	-0.2	0.2	0.446	1.5	6.1
Water	7.78	-4.5	-4.7	-10.9	-13.1	0.554	0.5	8.3
Nitromethane	7.50	-5.6	-6.6	-9.3	-10.9	0.597	1.1	6.2
Aluminum	13	-1.8	-2.9	-5.3	-7.8	1.3	1.8	8.0
Silicon	14	0.7	3.5	1.4	-4.2	1.161	-4.8	9.2
Magnesium	12	0.2	-0.1	-11.0	-13.9	0.859	-4.8	17.2
Mean <sup>a</sup>	-	2.3	2.7	4.6	5.4	-	2.5	6.1

accuracy.

## 5. Conclusion

We have presented the BMD method for material classification from system-independent physical parameter  $Z_{\text{eff}}$  with Spectral CT measurements. We showed that the correction for the detector's spectral distortions aids in reconstruction of the LACs, as they are brought much closer to

the reference LACs. Therefore, using the correction algorithm is required to achieve desired classification results. We explored the influence of the number of basis materials on the performance of the method. As a result, we found the method to be most accurate employing just two basis materials. We observed that the use of a correction algorithm suppresses most detector response artifacts from the LAC, and classification even with two basis materials is presented

to require the correction. The BMD requires a curve fitting step using a set of reference materials to define the relation between  $Z_{\text{eff}}$  values of reference materials and the fraction from the decomposed LAC expression. We also investigated the performance of the method as a function of the number of energy bins rebinned. It was demonstrated that 90 energy bins with energy bin widths lower than the detector's energy resolution did not enhance classifications further, and we saw that the method gives most accurate results with 15 energy bins.

In contrast to another state-of-the-art method, the SIMCAD [39], the BMD can provide higher accuracy with 17.4% improvement in terms of estimating relative deviations from the expected reference  $Z_{\text{eff}}$  values. In addition, the BMD appeared to give better robustness to high noise levels in certain energy bins. However, the SIMCAD has the main advantage that it can map  $Z_{\text{eff}}$  against  $\rho_e$  on a chart, estimating both material properties and suggesting a complete way to distinguish materials. It is also noteworthy that because the BMD method uses an attenuation decomposition model based on basis materials' LACs, it can be applicable to estimate a larger range of  $Z_{\text{eff}}$  materials with K-edges within detector's energy region [33, 48].

The method has been tested in the range of  $6 \leq Z_{\text{eff}} \leq 15$ . This range of atomic numbers include most of the materials commonly found in a passenger luggage [9], and most of human organs and tissues [58–61]. We inspected the performance of the method for few projections important for security applications where rapid scanning is required. We found that the relative deviations were lower than 5.6% for all the samples, with a mean deviation of 2.3% for  $Z_{\text{eff}}$ . For future experiments, we will explore the robustness of the method to materials with a larger range of  $Z_{\text{eff}}$ , and with the presence of K-edge absorption.

## 6. Data and code availability

The raw and spectral corrected data required to reproduce these findings are available to download from [69]. The developed code for  $L_{\infty}$ -VTV joint reconstruction algorithm is available at <https://github.com/JuliaTomo/XfromProjections.jl>.

## CRedit authorship contribution statement

**Doniyor Jumanazarov:** Conceptualization, Methodology, Software, Formal analysis, Investigation, Data curation, Writing - original draft, Visualization. **Jakeoung Koo:** Software, Formal analysis. **Henning F. Poulsen:** Writing - review and editing, Supervision. **Ulrik L. Olsen:** Validation, Resources, Data curation, Writing - review and editing, Supervision. **Mihai IOVEA:** Validation, Writing - review and editing, Supervision, Funding acquisition.

## Acknowledgements

This project has received funding from the European Union Horizon 2020 research and innovation programme

under the Marie Skłodowska-Curie grant agreement No. 765604 as part of the MULTISCALE, Multimodal and Multidimensional imaging for EngineerRING project (MUMMER-ING Innovative Training Network, [www.mummering.eu](http://www.mummering.eu)) and from the EIC FTI program (project 853720).

The authors want to acknowledge also the 3D Imaging Center at DTU, where the experiments have been conducted.

## References

- [1] Z. Qi, J. Zambelli, N. Bevins, G. H. Chen, Quantitative imaging of electron density and effective atomic number using phase contrast CT, *Physics in Medicine and Biology* 55 (2010) 2669–2677.
- [2] M. D. Agrawal, D. F. Pinho, N. M. Kulkarni, P. F. Hahn, A. R. Guimaraes, D. V. Sahani, Oncologic applications of dual-energy CT in the abdomen, *Radiographics* 34 (2014) 589–612.
- [3] H. W. Goo, J. M. Goo, Dual-energy CT: New horizon in medical imaging, *Korean Journal of Radiology* 18 (2017) 555–569.
- [4] M. Antoniassi, A. L. Conceição, M. E. Poletti, Study of effective atomic number of breast tissues determined using the elastic to inelastic scattering ratio, *Nuclear Instruments and Methods in Physics Research, Section A: Accelerators, Spectrometers, Detectors and Associated Equipment* 652 (2011) 739–743.
- [5] M. Bazalova, E. E. Graves, The importance of tissue segmentation for dose calculations for kilovoltage radiation therapy, *Medical Physics* 38 (2011) 3039–3049.
- [6] M. Kurudirek, Effective atomic numbers and electron densities of some human tissues and dosimetric materials for mean energies of various radiation sources relevant to radiotherapy and medical applications, *Radiation Physics and Chemistry* 102 (2014) 139–146.
- [7] H. Manjunatha, Comparison of effective atomic numbers of the cancerous and normal kidney tissue, *Radiation Protection and Environment* 38 (2015) 83.
- [8] H. C. Manjunatha, L. Seenappa, Pocket formula for mass attenuation coefficient, effective atomic number, and electron density of human tissues, *Nuclear Science and Techniques* 30 (2019).
- [9] M. Ellenbogen, R. Bijjani, Liquids and homemade explosive detection, in: *Optics and Photonics in Global Homeland Security V and Biometric Technology for Human Identification VI*, volume 7306, International Society for Optics and Photonics, 2009, p. 73060Y. doi:10.1117/12.821806.
- [10] R. E. Alvarez, A. Macovski, Energy-selective reconstructions in X-ray computerised tomography, *Physics in Medicine and Biology* 21 (1976) 733–744.
- [11] E. Kalender, Willi A and Perman, WH and Vetter, JR and Klotz, Evaluation of a prototype dual-energy computed tomographic apparatus. I. Phantom studies, *Medical physics* 13 (1986) 334–339.
- [12] B. J. Heismann, J. Leppert, K. Stierstorfer, Density and atomic number measurements with spectral x-ray attenuation method, *Journal of Applied Physics* 94 (2003) 2073–2079.
- [13] Z. Ying, R. Naidu, C. R. Crawford, Dual energy computed tomography for explosive detection, *Journal of X-Ray Science and Technology* 14 (2006) 235–256.
- [14] J. S. Park, J. K. Kim, Calculation of effective atomic number and normal density using a source weighting method in a dual Energy X-ray inspection system, *Journal of the Korean Physical Society* 59 (2011) 2709–2713.
- [15] T. P. Szyzykutowicz, Z. Qi, G.-H. Chen, A simple image based method for obtaining electron density and atomic number in dual energy CT, in: *Medical Imaging 2011: Physics of Medical Imaging*, volume 7961, International Society for Optics and Photonics, 2011, p. 79613A. doi:10.1117/12.878076.
- [16] O. Semerci, E. L. Miller, A parametric level-set approach to simultaneous object identification and background reconstruction for dual-energy computed tomography, *IEEE Transactions on Image Processing* 21 (2012) 2719–2734.
- [17] G. Landry, J. Seco, M. Gaudreault, F. Verhaegen, Deriving effective

- atomic numbers from DECT based on a parameterization of the ratio of high and low linear attenuation coefficients, *Physics in Medicine and Biology* 58 (2013) 6851–6866.
- [18] H. E. Martz, C. M. Logan, D. J. Schneberk, P. J. Shull, *X-ray Imaging: fundamentals, industrial techniques and applications*, CRC Press, 2016.
- [19] S. Ohira, H. Washio, M. Yagi, T. Karino, K. Nakamura, Y. Ueda, M. Miyazaki, M. Koizumi, T. Teshima, Estimation of electron density, effective atomic number and stopping power ratio using dual-layer computed tomography for radiotherapy treatment planning, *Physica Medica* 56 (2018) 34–40.
- [20] K. Wells, D. A. Bradley, A Review of X-ray Explosives Detection Techniques for Checked Baggage, *Applied Radiation and Isotopes* 70 (2012) 1729–1746.
- [21] P. M. Shikhaliyev, Energy-resolved computed tomography: First experimental results, *Physics in Medicine and Biology* 53 (2008) 5595–5613.
- [22] A. Brambilla, P. Ouvrier-Buffet, J. Rinkel, G. Gonon, C. Boudou, L. Verger, CdTe linear pixel X-ray detector with enhanced spectrometric performance for high flux X-ray imaging, *IEEE Transactions on Nuclear Science* 59 (2012) 1552–1558.
- [23] D. Shvydka, X. Jin, E. I. Parsai, Performance of Large Area Thin-Film CdTe Detector in Diagnostic X-Ray Imaging, *International Journal of Medical Physics, Clinical Engineering and Radiation Oncology* 02 (2013) 98–109.
- [24] E. I. Parsai, D. Shvydka, J. Kang, Design and optimization of large area thin-film CdTe detector for radiation therapy imaging applications, *Medical Physics* 37 (2010) 3980–3994.
- [25] X. Wang, D. Meier, K. Taguchi, D. J. Wagenaar, B. E. Patt, E. C. Frey, Material separation in x-ray CT with energy resolved photon-counting detectors, *Medical Physics* 38 (2011) 1534–1546.
- [26] M. Joshi, D. A. Langan, D. S. Sahani, A. Kambadakone, S. Aluri, K. Procknow, X. Wu, R. Bhotika, D. Okerlund, N. Kulkarni, D. Xu, Effective atomic number accuracy for kidney stone characterization using spectral CT, *Medical Imaging 2010: Physics of Medical Imaging* 7622 (2010) 76223K.
- [27] K. Taguchi, J. S. Iwanczyk, *Vision 20/20: Single photon counting x-ray detectors in medical imaging.*, *Medical physics* 40 (2013) 100901.
- [28] N. G. Anderson, A. P. Butler, Clinical applications of spectral molecular imaging: Potential and challenges, *Contrast Media and Molecular Imaging* 9 (2014) 3–12.
- [29] A. Potop, V. Rebuffel, J. Rinkel, A. Brambilla, F. Peyrin, L. Verger, Investigation of the polynomial approach for material decomposition in spectral X-ray tomography using an energy-resolved detector, *Medical Imaging 2014: Physics of Medical Imaging* 9033 (2014) 90333I.
- [30] C. O. Schirra, B. Brendel, M. A. Anastasio, E. Roessl, Spectral CT: A technology primer for contrast agent development, *Contrast Media and Molecular Imaging* 9 (2014) 62–70.
- [31] P. M. Shikhaliyev, Soft tissue imaging with photon counting spectroscopic CT, *Physics in Medicine and Biology* 60 (2015) 2453–2474.
- [32] Limor Martin, Enhanced information extraction in multi-energy X-ray tomography for security, Phd thesis, Boston University, 2014.
- [33] A. Brambilla, A. Gorecki, A. Potop, C. Paulus, L. Verger, Basis material decomposition method for material discrimination with a new spectrometric X-ray imaging detector, *Journal of Instrumentation* 12 (2017) P08014.
- [34] Busi, Matteo, Enhanced Security Screening Using Spectral X-ray Imaging, Phd thesis, Technical University of Denmark, 2019.
- [35] V. Rebuffel, J. Rinkel, J. Tabary, L. Verger, New perspectives of X-ray techniques for explosive detection based on CdTe/CdZnTe spectrometric detectors, in: *Proc. of the Int. Symp. on Digital Industrial Radiology and Computed Tomography*, volume 2, 2011, pp. 1–8.
- [36] J. Rinkel, G. Beldjoudi, V. Rebuffel, C. Boudou, P. Ouvrier-buffet, G. Gonon, L. Verger, A. Brambilla, Experimental Evaluation of Material Identification Methods With CdTe X-ray Spectrometric Detector, *IEEE Transactions on Nuclear Science* 58 (2011) 2371–2377.
- [37] G. Beldjoudi, V. Rebuffel, L. Verger, V. Kaftandjian, J. Rinkel, Multidimensional data processing methods for material discrimination using an ideal X-ray spectrometric photon counting detector, *IEEE Transactions on Nuclear Science* 58 (2011) 3190–3203.
- [38] G. Beldjoudi, V. Rebuffel, L. Verger, V. Kaftandjian, J. Rinkel, An optimised method for material identification using a photon counting detector, *Nuclear Instruments and Methods in Physics Research, Section A: Accelerators, Spectrometers, Detectors and Associated Equipment* 663 (2012) 26–36.
- [39] D. Jumanazarov, J. Koo, M. Busi, H. F. Poulsen, U. L. Olsen, M. Iovea, System-independent material classification through X-ray attenuation decomposition from spectral X-ray CT, *NDT and E International* 116 (2020) 102336.
- [40] R. Alvarez, E. Seppi, A comparison of noise and dose in conventional and energy selective computed tomography, *IEEE Transactions on Nuclear Science* 26 (1979) 2853–2856.
- [41] S. J. Riederer, C. Mistretta, Selective iodine imaging using K-edge energies in computerized x-ray tomography, *Medical Physics* 4 (1977) 474–481.
- [42] L. Lehmann, R. Alvarez, A. Macovski, W. Brody, N. Pelc, S. J. Riederer, A. Hall, Generalized image combinations in dual kvp digital radiography, *Medical physics* 8 (1981) 659–667.
- [43] E. S. Dreier, J. Kehres, M. Khalil, M. Busi, Y. Gu, R. Feidenhans, U. L. Olsen, Spectral correction algorithm for multispectral CdTe x-ray detectors, *Optical Engineering* 57 (2018) 16.
- [44] T. Su, V. Kaftandjian, P. Duvauchelle, Y. Zhu, A spectral X-ray CT simulation study for quantitative determination of iron, *Nuclear Instruments and Methods in Physics Research, Section A: Accelerators, Spectrometers, Detectors and Associated Equipment* 894 (2018) 39–46.
- [45] D. Jumanazarov, J. Koo, H. F. Poulsen, U. L. Olsen, M. Iovea, The significance of the spectral correction of photon counting detector response in material classification from spectral x-ray CT, in: *Quantum Optics and Photon Counting 2021*, volume 11771, International Society for Optics and Photonics, SPIE, 2021, pp. 60 – 76. URL: <https://doi.org/10.1117/12.2589290>. doi:10.1117/12.2589290.
- [46] Z. Zhao, G. J. Gang, J. H. Siewerdsen, Noise, sampling, and the number of projections in cone-beam CT with a flat-panel detector, *Medical Physics* 41 (2014).
- [47] A. N. Van Daatselaar, P. F. Van Der Stelt, J. Weenen, Effect of number of projections on image quality of local CT, *Dentomaxillofacial Radiology* 33 (2004) 361–369.
- [48] R. E. Alvarez, *Energy Dependent Information in X-Ray Imaging : Part 1 . The Vector Space Description*, unpublished, year (1982).
- [49] L. A. Lehmann, R. E. Alvarez, *Energy selective radiography: a review*, *Digital Radiography: Selected Topics* New York: Plenum (1986) 145–188.
- [50] L. Eger, S. Do, P. Ishwar, W. C. Karl, H. Pien, A learning-based approach to explosives detection using multi-energy X-ray computed tomography, *ICASSP, IEEE International Conference on Acoustics, Speech and Signal Processing - Proceedings* (2011) 2004–2007.
- [51] M. Busi, J. Kehres, M. Khalil, U. L. Olsen, Effective atomic number and electron density determination using spectral x-ray CT 1099903 (2019) 2.
- [52] D. Skillicorn, *Singular Value Decomposition (SVD), Understanding Complex Datasets* (2021) 71–112.
- [53] P. Sukovic, N. H. Clinthorne, Penalized weighted least-squares image reconstruction for dual energy X-ray transmission tomography, *IEEE Transactions on Medical Imaging* 19 (2000) 1075–1081.
- [54] K. Berger, M.J., Hubbell, J.H., Seltzer, S.M., Chang, J., Coursey, J.S., Sukumar, R., Zucker, D.S., and Olsen, *XCOM: Photon Cross Section Database*, 2010. URL: <http://physics.nist.gov/xcom>. doi:10.18434/T4866X.
- [55] A. H. Compton, S. K. Allison, et al., *X-rays in theory and experiment*, New York, NY, USA: Van Nostrand (1935).
- [56] Mayneord, WV, The significance of the roentgen, *Acta of the International Union Against Cancer* 2 (1937) 271.
- [57] F. W. SPIERS, Effective atomic number and energy absorption in tissues., *The British journal of radiology* 19 (1946) 52–63.
- [58] Shivaramu, Effective atomic numbers for photon energy absorp-

- tion and photon attenuation of tissues from human organs, *Medical Dosimetry* 27 (2002) 1–9.
- [59] M. A. Zenobio, T. A. Silva, M. S. Tavares, E. G. Zenobio, Effective atomic number of human enamel and dentin within a photo energy range from 10 to 200 keV (2011).
- [60] M. M. Goodsitt, E. G. Christodoulou, S. C. Larson, Accuracies of the synthesized monochromatic CT numbers and effective atomic numbers obtained with a rapid kVp switching dual energy CT scanner, *Medical Physics* 38 (2011) 2222–2232.
- [61] H. C. Manjunatha, B. Rudraswamy, Study of effective atomic number and electron density for tissues from human organs in the energy range of 1 keV–100 GeV, *Health Physics* 104 (2013) 158–162.
- [62] S. Kim, J. Chen, T. Cheng, A. Gindulyte, J. He, S. He, Q. Li, B. A. Shoemaker, P. A. Thiessen, B. Yu, L. Zaslavsky, J. Zhang, E. E. Bolton, PubChem 2019 update: Improved access to chemical data, 2019. URL: <https://pubchem.ncbi.nlm.nih.gov>. doi:10.1093/nar/gky1033.
- [63] J. Gregor, T. Benson, Computational analysis and improvement of SIRT, *IEEE Transactions on Medical Imaging* 27 (2008) 918–924.
- [64] M. Busi, K. A. Mohan, A. A. Dooraghi, K. M. Champley, H. E. Martz, U. L. Olsen, Method for system-independent material characterization from spectral X-ray CT, *NDT & E International* 107 (2019) 102136.
- [65] D. J. Schroeder, *Astronomical optics*, Elsevier, 1999.
- [66] A. S. Wang, N. J. Pelc, Optimal energy thresholds and weights for separating materials using photon counting x-ray detectors with energy discriminating capabilities, in: *Medical Imaging 2009: Physics of Medical Imaging*, volume 7258, International Society for Optics and Photonics, 2009, p. 725821. doi:10.1117/12.811454.
- [67] A. S. Wang, N. J. Pelc, Sufficient statistics as a generalization of binning in spectral X-ray imaging, *IEEE Transactions on Medical Imaging* 30 (2011) 84–93.
- [68] D. Jumanazarov, J. Koo, J. Kehres, H. F. Poulsen, U. L. Olsen, M. Iovea, Material classification from sparse spectral X-ray CT using vectorial total variation based on L infinity norm, Submitted for publication (2021).
- [69] D. Jumanazarov, J. Koo, J. Kehres, H. F. Poulsen, U. L. Olsen, M. IOVEA, Material classification from sparse spectral X-ray CT using vectorial total variation based on L infinity norm [Data set]. Zenodo, 2021. URL: <https://doi.org/10.5281/zenodo.4780625>. doi:10.5281/zenodo.4780625.



**Donyor Jumanazarov** is a PhD fellow at the Department of Physics at Denmark Technical University (DTU), Kongens Lyngby, Denmark. He obtained his BS degree in physics from the National University of Uzbekistan, Tashkent, Uzbekistan, and his MS degree in Molecular Photonics for bio- and nanotechnologies (MONABIPHOT) from the École Normale Supérieure de Cachan, Cachan, France, in 2012 and 2018, respectively.



**Jakeoung Koo** received his B.Sc. and M.Sc. in Computer Science from Chung-Ang University, South Korea in 2015 and 2017, respectively. He is now a Ph.D. student in Technical University of Denmark (DTU), Kongens Lyngby, Denmark. His research interests lie in Computed Tomography and Computer Vision.



Professor, Dr. techn. **Henning Friis Poulsen** is employed at DTU Physics since 2012. Henning pioneered several x-ray microscopy methods enabling multiscale mapping of materials properties from the macroscopic and down to nanometre length scales. He heads the 3D Imaging Centre at

DTU and is Principal Investigator on a number of European and national projects with the aim of introducing X-ray methods to industry.



**Dr. Ulrik Lund Olsen** is a senior research engineer at DTU Physics since 2013. He obtained his Ph.D. degree in 2009 from Copenhagen University. He is an expert in X-ray instrumentation and specialises in spectral X-ray detectors, data acquisition and processing. Ulrik's current research interest is the use of spectral detectors for security applications for improved reconstruction and material identification.



**Mihai IOVEA**, Engineer in Physics, Senior Research Scientist, Ph.D in Physics. He has over 30 years' experience in X-Ray Imaging projects research & development for Security and Non-Destructive Testing. Interested in X-ray 2D&3D Tomography and Digital Radiography techniques, such as: dual/multi energy, diffraction, back-scattering applied in for threats detection, high-resolution in-line X-ray scanners for fast industrial non-destructive testing.